

Short range ordering and microstructure
property relationship in
amorphous alloys

Dissertation
zur Erlangung des Doktorgrades
der Mathematisch-Naturwissenschaftlichen Fakultäten
der Georg-August-Universität Göttingen

vorgelegt von
Ahmed Shariq
aus Lahore, Pakistan

Göttingen 2006

D7

Referent: Prof. Dr. Reiner Kirchheim

Korreferent: Prof. Dr. Hans Hofsäss

Tag der mündlichen Prüfung:

*In the name of Allah, Most Gracious,
Most Merciful*

CONTENTS

CHAPTER 1

MOTIVATION.....	1
-----------------	---

CHAPTER 2

AMORPHOUS ALLOYS & METALLIC GLASSES	4
---	---

2.1 INTRODUCTION	4
2.2 GLASS FORMING ABILITY (GFA)	7
2.3 THERMODYNAMICS OF UNDERCOOLED MELT	8
2.4 NUCLEATION	10
2.4.1 Homogeneous nucleation	10
2.4.2 Heterogeneous nucleation.....	12
2.5 TRANSFORMATION KINETICS	14
2.6 INSIGHT INTO THE PROPERTIES OF AMORPHOUS ALLOYS AND METALLIC GLASSES.....	16

CHAPTER 3

INVESTIGATED MATERIALS.....	18
-----------------------------	----

3.1 $Zr_{53}Co_{23.5}Al_{23.5}$ AMORPHOUS ALLOYS	18
3.1.1 $Zr_{53}Co_{23.5}Al_{23.5}$ bulk amorphous alloy	19
3.1.2 $Zr_{53}Co_{23.5}Al_{23.5}$ Glassy Splats.....	20
3.2 $Fe_{40}Ni_{40}B_{20}$ GLASSY RIBBONS	22
3.3 $Pd_{55}Cu_{23}P_{22}$ BULK METALLIC GLASS.....	23
3.4 $Zr_{41.2}Ti_{13.8}Cu_{12.5}Ni_{10}Be_{22.5}$ BULK METALLIC GLASS.....	24

CHAPTER 4

EXPERIMENTAL METHODS AND TECHNIQUES.....	25
--	----

4.1 DIFFERENTIAL SCANNING CALORIMETRY (DSC)	26
4.2 X-RAY DIFFRACTION.....	27
4.3 FIELD ION MICROSCOPY AND ATOM PROBE TOMOGRAPHY.....	28
4.3.1 Field Ion Microscopy	28
4.3.2 Atom Probe Tomography	31
4.3.3 Measurement conditions for different samples analysed.....	33
4.4 TAP SAMPLE PREPARATION	33
4.5 DUAL BEAM FOCUSED ION BEAM/ SCANNING ELECTRON MICROSCOPY (FIB/SEM)	35
4.6 ADDITIONAL ANALYSIS METHODS	41
4.6.1 Transmission Electron Microscopy.....	41
4.6.2 Superconducting Quantum Interference Device (SQUID).....	42

CHAPTER 5

AMORPHOUS STRUCTURE AND STRUCTURE RESOLVING TOOLS	43
---	----

5.1 AMORPHOUS STRUCTURE	43
5.1.1 Pair and Radial Distribution Functions.....	43
5.1.2 Structural models	46
5.2 TAP DATA TREATMENT FOCUSED ON BOTH STERIC AND COMPOSITIONAL CONSIDERATIONS.....	47
5.2.1 Next Neighbourhood Evaluation Module.....	47
5.2.2 Cluster search Module	52
5.2.3 “Radial Distribution Function” Module.....	53

5.3	TAP DATA TREATMENT MAINLY ON COMPOSITIONAL CONSIDERATIONS	54
5.3.1	<i>Composition profile</i>	54
5.3.2	<i>Frequency distribution & a comparison with the binomial distribution</i>	55
5.3.3	χ^2 - Test.....	56
CHAPTER 6		
RESULTS AND DISCUSSION		57
6.1	Pd ₅₅ Cu ₂₃ P ₂₂ BULK AMORPHOUS ALLOYS	57
6.1.1	<i>Thermal characterization by DSC</i>	57
6.1.2	<i>Structural characterization by TAP microscopy</i>	58
6.1.3	<i>Next Neighbourhood Evaluation Module</i>	60
6.1.4	<i>Radial Distribution Functions</i>	64
6.1.5	<i>Discussion</i>	65
6.1.6	<i>Conclusion</i>	70
6.2	Fe ₄₀ Ni ₄₀ B ₂₀ GLASSY RIBBONS	71
6.2.1	<i>Thermal characterization by DSC</i>	71
6.2.2	<i>Diffraction study by X-Rays</i>	71
6.2.3	<i>Structural characterization by TAP microscopy</i>	72
6.2.4	<i>Next Neighbourhood Evaluation Module</i>	75
6.2.5	<i>Discussion</i>	77
6.2.6	<i>Conclusion</i>	84
6.3	Zr ₅₃ Co _{23.5} Al _{23.5} AMORPHOUS ALLOYS	84
	<i>Results and Discussion</i>	84
6.3.1	<i>As cast Zr₅₃Co_{23.5}Al_{23.5} bulk amorphous alloys</i>	84
6.3.2	<i>Heat treated Zr₅₃Co_{23.5}Al_{23.5} bulk amorphous alloys</i>	89
6.3.3	<i>Magnetic properties of the as cast and heat treated Zr₅₃Co_{23.5}Al_{23.5} bulk samples</i>	91
6.3.5	<i>Zr₅₃Co_{23.5}Al_{23.5} metallic glass (splat quenched)</i>	98
6.3.6	<i>Reconsidering microstructural investigations of the as cast Zr₅₃Co_{23.5}Al_{23.5} bulk amorphous alloys</i>	104
6.3.7	<i>Microstructural investigations by APT</i>	107
6.3.8	<i>Conclusion</i>	112
CHAPTER 7		
SUMMARY AND OUTLOOK		114
APPENDIX A		
VITRELOY 1 (Zr_{41.2}Ti_{13.8}Cu_{12.5}Ni₁₀Be_{22.5}) BULK METALLIC GLASS.....		117
	<i>Microstructural characterization by TAP microscopy</i>	117
	<i>Discussion</i>	119
	<i>Conclusions</i>	120
APPENDIX B		
RADIAL DISTRIBUTION FUNCTION CALCULATED BY TAP		122
APPENDIX C		
NEXT NEIGHBOURHOOD EVALUATION AS FUNCTION OF AVERAGE ATOMIC VOLUME....		125
BIBLIOGRAPHY		127

Chapter 1

Motivation

The scientific and technological novelty of amorphous alloys and metallic glasses makes them superior in many ways to other commercially-viable materials. These materials have the properties of liquids in terms of their lack of long range order that is unprecedented for structural metals and the properties of solids in terms of stability. The intriguing facts that they are plastic at high temperature rendering them to process technology similar to that possessed by plastics and more rigid at lower temperature by exhibiting the strength twice than commercial titanium alloys. Unique structural features in these regimes and transition between the two regimes play a critical role in understanding conspicuous properties of these materials. The commercial interests however developed on such amorphous alloys not only due to the superior mechanical properties but owing to better magnetic properties. Sensors for electronic article surveillance have become a large application for amorphous materials.

Many of the potential structural applications are though restricted due to the fact that these materials lack ductility despite offering remarkably high yield strength and elastic limits. That incites for a better understanding of the microstructure property relationship in this class of materials. Delving the microstructure of amorphous materials is rather a nontrivial undertaking and leads to the short range ordering with structural correlation in sub-nanometre range.

The present work is a step to address the microstructure property relationship in addition to reveal the short range ordering in glassy materials. This work enunciates the first microstructural investigations on the $Zr_{53}Co_{23.5}Al_{23.5}$ glassy materials that exhibit the highest glass forming ability among its variant. For this purpose, different characterization tools such as differential scanning calorimetry, X-ray diffraction technique, high resolution transmission electron microscopy, analytical transmission electron microscopy, tomographic atom probe and computer assisted field ion image tomography has been utilized. The magnetic properties of this alloy system are also revealed during the course of this research work exploiting superconducting quantum interference device. Furthermore, subsequent

effects of crystallization kinetics after different heat treatments on the magnetic properties are also investigated in detail. Different experiments depict that the magnetic properties of the $Zr_{53}Co_{23.5}Al_{23.5}$ glassy materials can be enhanced by the presence of the crystalline phase(s). Superior magnetic properties after the heat treatment have been found for both as cast $Zr_{53}Co_{23.5}Al_{23.5}$ glassy material and as quenched metallic glass, though are much superior in the later case.

The absence of any translational periodicity in the amorphous structure means that a statistical description of the structure is inevitable. A Fourier inversion of the scattering data obtained in reciprocal space, from conventional scattering experiments using X-rays, electrons, or neutrons, enables eliciting the short range order. For a monoatomic amorphous materials diffraction provides adequate amount of obtainable structural information. The situation exacerbates for multicomponent systems that incites to incorporate different scattering techniques for a complete structural information. In order to combat this, an effort has been made during this work to utilize tomographic atom probe (TAP) for elucidating the interatomic relationship for different elements in real space. We present a new processing tool for the TAP data (i.e., next neighbourhood evaluation tool) that evinces the atomic positions and chemical nature of the neighbouring atoms regardless the number of constituent elements. It enables to elucidate the interatomic elemental correlation solely exploiting tomographic atom probe. These are first kind of investigations to unfold the next neighbourhood atomic correlation for amorphous materials by the tomographic atom probe.

The next neighbourhood evaluation (NNE) module processed on TAP data for the $Pd_{55}Cu_{23}P_{22}$ bulk amorphous alloy reveal the first ten next neighbours for all elemental correlations. The subsequent atomic positions can be correlated to assign the atoms responsible for the coordination peaks in typical radial distribution functions obtained from scattering techniques. An intriguing fact is also revealed that the atomic distribution of first ten next neighbours follows a certain steric order irrespective of their chemical nature. Furthermore, $Fe_{40}Ni_{40}B_{20}$ metallic glass ribbons are also investigated in the as quenched state and for a heat treated state in order to reveal the incipient structural changes. The NNE module is further processed on the TAP data to reveal the subsequent structural changes in a range of sub-nanometre, a primordial stage to crystallization.

Chapter 2 describes the essential theoretical background for the physical description of amorphous alloys and metallic glasses. This chapter also sheds some light on the commercial applications for such unique class of materials. Chapter 3 provides the bibliographical review of the investigated materials. Moreover, details of the sample preparation are provided in this chapter. In chapter 4, a brief introduction of some of the experimental techniques utilized during this work is given. It also unveils different experimental parameters used for different characterization tools for each material analysed. Chapter 5 deals with the intriguing structural details of the glassy materials, as well as, describes in detail the statistical tools for the TAP data interpretation that are utilized during this research work for

evincing the amorphous structure. The detailed description of the next neighbourhood evaluation module is also given in this chapter. The experimental results are interpreted and discussed in chapter 6. Chapter 7 summarizes this work and additionally provides an outlook to further useful investigations.

Chapter 2

Amorphous Alloys & Metallic Glasses

Historically, solid state physics is attributed to crystal physics. Yet, one of the most active and emerging field in the solid state physics deals with the study of non crystalline solids i.e., solids in which arrangement of the atoms lacks the slightest vestige of long range order. This chapter is dedicated to general, however, brief description of amorphous alloys and metallic glasses, description of glass forming ability followed by describing different salient thermodynamic attributes of such materials and finally summing up, by introducing some of the unique properties these materials exhibit.

2.1 Introduction

A solid alloy having a liquid like atomic structure is called a metallic glass, or alternatively an amorphous metallic alloy. Metallic glasses are rapidly quenched liquids produced by avoiding crystallization; whereas (bulk) amorphous alloys are alloys which can be produced by conventional cooling techniques in bulk dimensions. Certain metallic alloys on drastically cooling below the melting temperature, don't crystallize and can be further cooled down such that no phase transformation occurs. The viscosity η of the undercooled melt is a strong function of the temperature and hence, increased rapidly towards the glass transition temperature by more than ten to fifteen orders of magnitude. The glass transition temperature (T_g) is empirically defined as the temperature at which the viscosity of the melt reaches to 10^{13} poise and thereafter the system behaves like solid. Albeit, the conspicuous properties on offer by the metallic glasses [Duwez76], the requirement of ultra high cooling rates ($\sim 10^6 \text{ Ks}^{-1}$) [Greer95] restricts the specimen geometry to thin ribbons, foils and powders with at least one dimension having thickness of micrometers ensuring a high cooling rate. The pioneering investigations by Inoue lead to new multicomponent alloy systems with much lower critical cooling rates required for amorphous structure [Inoue88]. His work triggered a research on amorphous alloys in new directions and results in a number of new bulk amorphous alloy system (with dimensions in millimetres, in comparison to the metallic glasses) as reviewed elsewhere [Inoue00].

Thermodynamically metallic glasses and amorphous alloys are metastable states. The term metastable was enunciated by a German physical chemist, Wilhelm Ostwald in 1893. A metastable state is one in internal equilibrium, that is, within the range of configurations to which there is access by continuous change, the system has lowest possible free energy [Cahn96], larger fluctuations however will urge the system to attain the stable equilibrium state.

Let us envisage a liquid cooled into the crystalline or a glassy state. Fig. 2.1 shows schematically the changes in different properties of the system as a function of temperature [Cahn96] where temperature regime can be divided into three regions i.e., region A, B & C. The melt is essentially in equilibrium at the higher temperatures i.e., range A. The equilibrium freezing temperature¹ serves as a boundary between ranges A and B. In range B, the melt is thermodynamically undercooled and if a critical nucleus is provided it will crystallize drastically, which is an energetically favourable state (Fig. 2.1 d). Fig. 2.1 b shows that at higher temperatures in this range the liquid has a low viscosity; hence, crystallization can only be avoided by cooling extremely fast, giving no time for nucleus formation. At the lowest temperatures in this range the liquid viscosity increases rapidly with the decrease in temperature. The crystalline structure can still be avoided even in the presence of nuclei because low atomic mobility suppresses crystal growth. In range B, the viscosity varies over some ten to fifteen orders of the magnitude. Albeit, the viscosity increases in range B, the atomic mobility is still adequate enough for the liquid to remain in configurational equilibrium.

Fig. 2.1 a, illustrates that contrary to the glass formation, crystallization involves a discontinuous change in properties. The intriguing fact for glass formation is that crystallization can occur only in range B, and if it is avoided by cooling, range C is reached. Range C is essentially defined by the glass transition temperature T_g .

Below T_g the viscosity is high enough to virtually seize the atomic mobility, thereby, no configurational changes occur any more. Consequently, the supercooled melt congealed into a rigid glass, having a structure that corresponds to frozen-in liquid structure. In range C, the properties of the glass have rather weak temperature dependence, roughly matching the behaviour of the crystal. Intriguingly, T_g is not a thermodynamically defined temperature but determined wholly by kinetic considerations, hence, is different for different cooling rates. The glass has a lower viscosity or high diffusivity, and greater specific volume and internal energy when quenched at faster rate (Fig. 2.1 a, curve 1). However, for relatively slower cooling rates (such as curve 2) though still enough to avoid crystallization, the supercooled melt configurations can stay in equilibrium even to a lower temperature, reducing the glass transition temperature from $(T_g)_1$ to $(T_g)_2$. The slower quenching rates entail a smaller volume (higher density) and higher viscosity for the glass. A glass in general is not in an internal equilibrium and hence relaxes structurally to a more stable equilibrium state whenever atoms attain appreciable mobility. On annealing glasses densify and evolve towards an ideal glassy state as represented by the extrapolation of the equilibrium properties, shown on Fig. 2.1 b.

¹ The equilibrium freezing temperature can be different to that of equilibrium melting temperature T_E , however to avoid complicity and for the sake of consistency in this thesis, it will be referred as melting temperature.

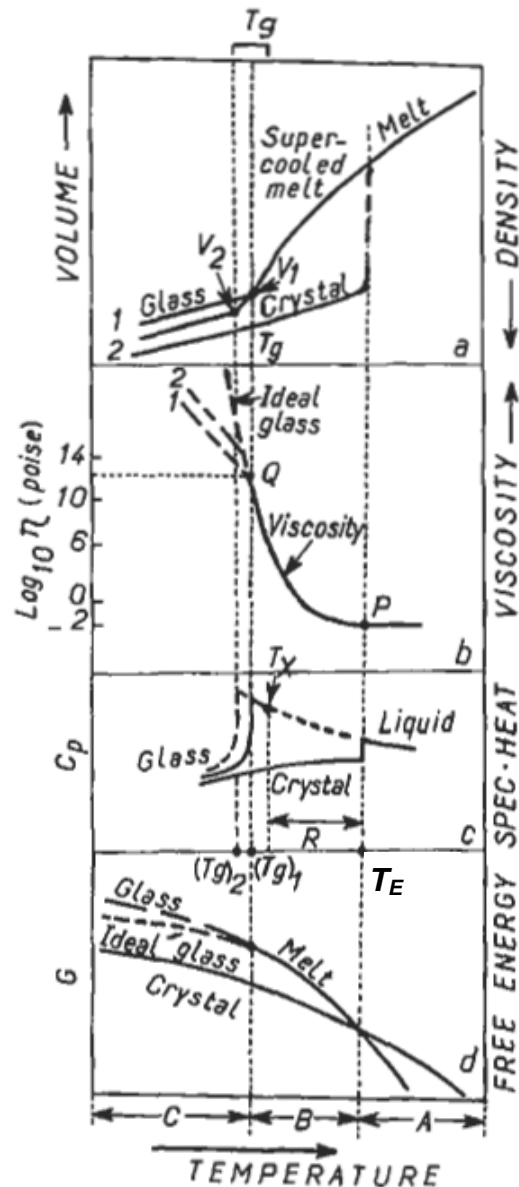


Fig. 2.1 A schematic illustration of possible thermodynamic states of alloys. The vertical axis shows Gibbs free energy, the horizontal, a parameter representing changes in structure[Cahn96].

Fox has introduced the concept of free volume [FOX51]. Free volume is the unfilled space between the atoms or molecules which is in excess of that what would exist even in an ideal close packing. As evident from Fig. 2.1 a, a faster quenched glass (1) has a lower density than a more slowly quenched one (2) or, in other terms, “1” has a larger free volume than “2”. The smaller the free volume, the more sluggish is any structural rearrangement. The extent of free volume is relatively higher in the metallic glasses as compared to bulk amorphous alloys.

Fig. 2.1c depicts that a metallic glasses exhibit a large step in specific heat at T_g , which for a glass-forming liquid alloy is significantly greater than that of the corresponding crystalline solid. The larger specific heat is attributed to the loss of entropy on cooling. Integration of liquid and solid specific heats over the temperature interval between T_E and T_g shows that the heat of crystallization of the glass

at T_g should be significantly less than the latent heat of melting at T_E . Glass-forming alloys typically show a strongly negative heat of mixing of their components.

2.2 Glass Forming Ability (GFA)

The prime requirement for the glass formation from a liquid state is to suppress essentially nucleation and growth of crystalline phase in the supercooled region as described in above section. The glass transition temperature T_g is a salient feature in rapidly quenched alloys. Albeit, it is rather a well defined temperature, the kinetic dependence of T_g make it vulnerable to the cooling rates and thereby results in a slight change in T_g [Chen69]. There is a considerable interest on devising criteria for forming glasses based on temperature dependent attributes of metallic glasses and amorphous alloys such as glass transition temperature T_g , crystallization-onset temperature T_x , the liquidus temperature T_E , etc. Turnbull divulged a ratio, widely adapted as reduced glass transition temperature T_{rg} ; a ratio between glass transition temperature T_g and the liquidus temperature T_E of an alloy, is used as a criterion to determine the glass forming ability (GFA) of an alloy [Turnbull49]. According to Turnbull criterion, a liquid having a $T_{rg} = 2/3$ becomes increasingly sluggish in crystallization within laboratory time scale and can only crystallize with in a very narrow temperature range [Turnbull69]. Such a liquid congeals to solid glass even for relatively slow cooling rates. Albeit, the recent investigations shows a slight deviation from this value in certain amorphous systems, Turnbull criterion for the suppression of crystallization in undercooled melts remains one of the best “rule of thumb” for prediction of glass formation ability of an alloy system [Johnson99].

Inoue enunciated another parameter i.e., supercooled liquid region ΔT_x , the temperature interval between T_g and T_x [Inoue00]. Larger the supercooled region is, the greater is the glass forming ability. The recent progress also sees the imperative critical cooling rates for metallic glasses i.e., 10^6 Ks^{-1} demoted by several order of magnitudes to 0.1 Ks^{-1} for new bulk amorphous systems [Inoue00].

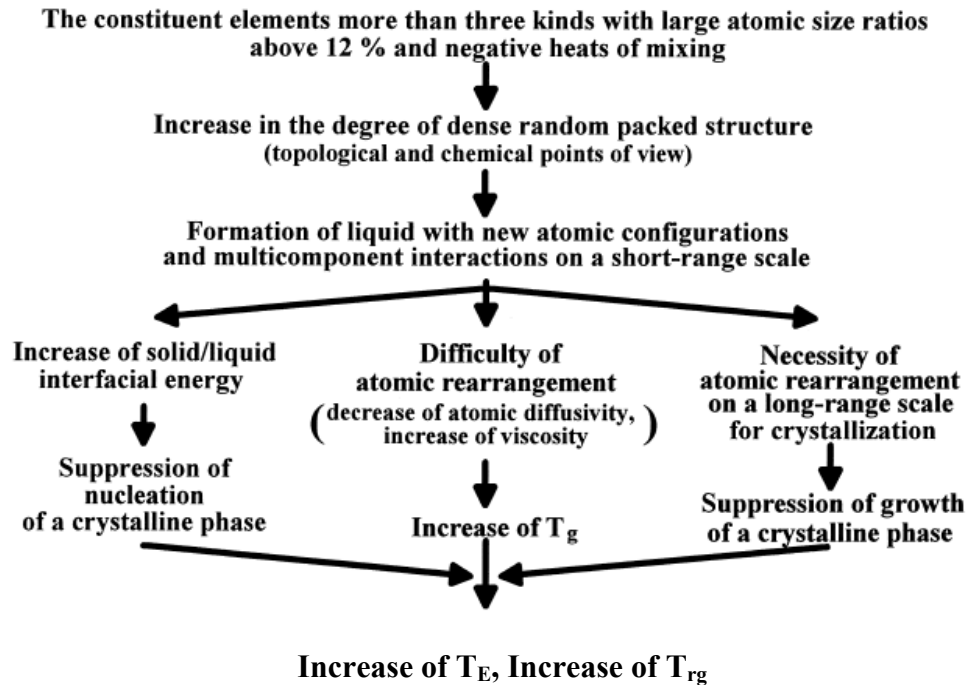
The development of plausible predictive models for identification of GFA of different alloy families and the composition range remains under intensive debate in the scientific community. Recently, Inoue enunciated an empirical consideration for predicting GFA as shown in the Table 2.1 [Inoue95].

Three major contributing factors to the aforementioned empirical rule are atomic size mismatch of the constituent elements, high negative heat of mixing, and multicomponent alloy system. Table 2.1 illustrates hierarchal influence of aforementioned factors on the glass transition temperature T_g , melting temperature T_E and subsequently on reduced glass transition temperature T_{rg} .

The addition of more components in a bid to increase GFA is also known as “confusion principle” [Greer95]. The critical radius of a crystalline nucleus increases in a multicomponent system that suppresses further the nucleation and growth process. In addition, as the order of a structure goes from elemental to binary, ternary and higher order, the number of new structure types diminishes. Hence, atomic mismatch inhibit considerably the crystal nucleation, which need long range diffusion to occur. The suggested relative ratio of atomic radii larger than 12% tends to result in a dense packing of

different elements and essentially forbid any atomic long range rearrangement restricting only to a short range order in such multicomponent system.

Table 2.1 Mechanisms for the stabilization of supercooled liquid and high glass forming ability for multicomponent alloys which satisfy the empirical rule [Inuo00]



2.3 Thermodynamics of undercooled melt

The Gibbs free energy G for pure metals depends exclusively on pressure P and temperature T . At a constant pressure, the temperature dependent Gibbs free energy can be enunciated as:

$$G(T) = H(T) - TS(T) \quad (2.1)$$

Where H is the enthalpy and S is the entropy of the system. Fig. 2.2 schematically illustrates the temperature dependent G at constant pressure for a liquid phase L and two solid phases i.e., a metastable solid phase α and a stable solid phase γ . Owing to the higher entropy of the liquid than solid, the $G(T)$ curve intersect at characteristic temperatures which define the melting temperatures of the solid phases i.e., T_E^α and T_E^γ [Herlach94]. Smaller Gibbs free energy of the liquid phase than the solid phases at higher temperatures makes the liquid state more stable than the others. Cooling the system below the melting temperature of the α phase i.e., T_E^α , the solid α phase becomes stable. Albeit, the α phase is stable in this temperature regime, other solid phases i.e., γ phase and the glassy state can be metastable. The thermodynamical driving force for the solidification of the formation of the metastable γ phase can be provided by essentially undercooling the melt exceeding the temperature difference of the equilibrium melting points of the two solid phases α and γ

($\Delta T = T_E^\alpha - T$). However, if the undercooling is extended beyond the glass transition temperature T_g , the undercooled melt freezes to the metastable amorphous phase.

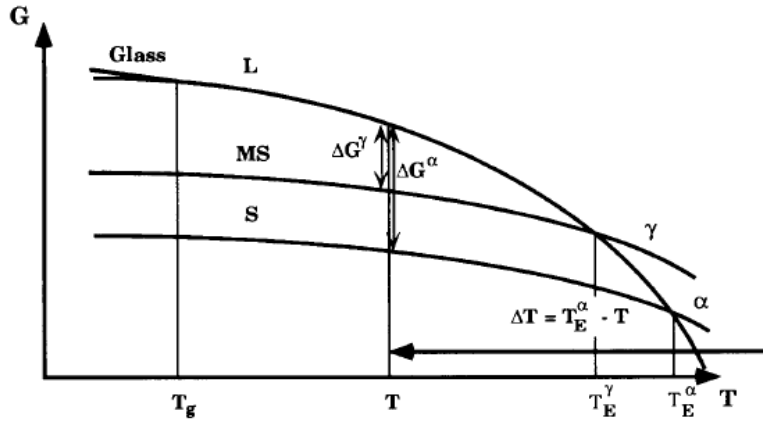


Fig. 2.2 Gibbs free energy as a function of temperature for liquid phase (L) and two solid phases i.e., a metastable solid phase (MS) α and a stable solid (S) phase γ . The intersection of Gibbs free energies of solid phase with the liquid phase represents the respective equilibrium melting points [Herlach94].

The negative difference of the free energies between the liquid and the solid, $\Delta G = G_s - G_l < 0$ provides the thermodynamic driving force for the crystallization of the solid phase. Using the elementary thermodynamics the Gibbs free energy difference can be expressed as:

$$\Delta G(T) = \Delta H(T) - T\Delta S(T) \quad (2.2)$$

Where, ΔH and ΔS are the differences of the enthalpy and entropy. These two thermodynamic entities are determined by the differences of the specific heat, ΔC_p between liquid and solid states, and the enthalpy of fusion, ΔH_f , and the entropy of fusion, ΔS_f . Where, T_E is the equilibrium melting temperature. The enthalpy and entropy differences can be expressed as:

$$\Delta H(T) = \Delta H_f - \int_T^{T_E} \Delta C_p(T) dT \quad (2.3)$$

$$\Delta S(T) = \Delta S_f - \int_T^{T_E} \frac{\Delta C_p(T)}{T} dT \quad (2.4)$$

$$\Delta H_f = T_E \Delta S_f \quad (2.5)$$

By inserting the above values in Eq. 2.2:

$$\Delta G = \frac{\Delta H_f \Delta T}{T_E} - \int_T^{T_E} \Delta C_p(T) dT + T \int_T^{T_E} \frac{\Delta C_p(T)}{T} dT \quad (2.6)$$

Where $\Delta T = T_E - T$ represent the magnitude of undercooling.

Dubey calculated a temperature dependent Gibbs free energy difference as under [Dubey94]:

$$\Delta G(T) = \frac{\Delta H_f \Delta T}{T_E} - \frac{\Delta C_p(T_E) \Delta T^2}{2T} \left[1 - \frac{\Delta T}{6T} \right] \quad (2.7)$$

2.4 Nucleation

Formation of small solid particle in the liquid phase, called Nuclei, and the process itself is named as nucleation, can occur either by the homogeneous nucleation or heterogeneous nucleation. When the nuclei initiates from a foreign particle it is called heterogenous nucleation otherwise homogeneous nucleation.

2.4.1 Homogeneous nucleation

Fisher and Turnbull introduced the liquid-solid phase transition [Turnbull49]. Consider liquid of a certain volume at a temperature ΔT below the T_E having the Gibbs free energy G_1 . At a certain time, atoms will approach statistically to distances comparable to the interatomic spacing in the crystals, forming a small sphere of solid cluster. The free energy of the system thereby will change to G_2 as given by:

$$G_2 = V_s G_v^s + V_l G_v^l + A_{sl} \gamma_{sl} \quad (2.8)$$

Where V_s is the volume of the solid sphere, V_l is the volume of the liquid, A_{sl} is the solid liquid interfacial area, G_v^s and G_v^l are the Gibbs free energy per unit volume for the solid and liquid respectively, and γ_{sl} solid liquid interfacial free energy.

The Gibbs free energy of the pure liquid without any solid is given by:

$$G_1 = (V_s + V_l) G_v^l \quad (2.9)$$

The formation of solid, hence results in the change of free energy ($\Delta G = G_2 - G_1$) of the system as given below:

$$\Delta G = -V_s \Delta G_v + A_{sl} \gamma_{sl} \quad (2.10)$$

Where $\Delta G_v = G_v^l - G_v^s$ for a certain undercooling ΔT , ΔG_v can also be expressed as [Porter01]:

$$\Delta G_v = \frac{L_v \Delta T}{T_E} \quad (2.11)$$

Where L_v is the latent heat of fusion per unit volume.

For $T < T_E$ the free energy of the crystalline (solid) phase is lower than liquid phase. Albeit the free energy change ΔG_v is negative, the solid state is not obtained spontaneously at melting temperature rather than a certain undercooling is necessary. It is because of the positive contribution due to the creation of solid liquid interface. The interface, being a defect, contributes an excess energy to the system. Assuming a spherical new solid phase, of radius r , then Eq. 2.10 becomes:

$$\Delta G(r) = -\frac{4\pi}{3}r^3(\Delta G_v) + 4\pi r^2\gamma_{sl} \quad (2.12)$$

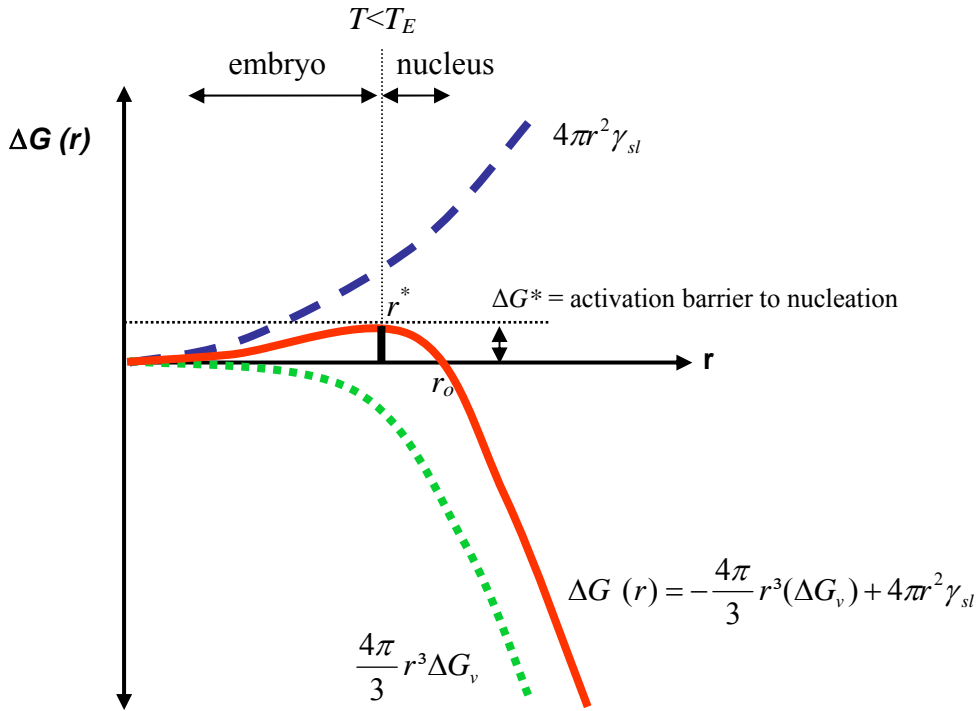


Figure 2.3 Nucleation of spherical solid nuclei from a pure liquid

The free energy change during the nucleation is lucidly illustrated in Fig. 2.3. The volume contribution is proportional to r^3 , on the other hand interface contribution is proportional to r^2 , that leads to a positive maximum for $\Delta G(r)$ value (i.e., ΔG^* at a critical radius r^*), which forms an activation barrier against the crystallization. For clusters with radius $r < r^*$, the interface to volume ratio is large, so interface contribution dominates, hence, will naturally dissolve lowering the free energy and for cluster with radius $r > r^*$, system will lower free energy by growing. Subcritical clusters ($r < r^*$) are called embryos, on the other hand clusters with radius ($r > r^*$) are called nucleus. To form nucleus, the free energy ΔG_{hom}^* must be added (activation energy). Once the nucleus has grown beyond the r_o , it represents the stable form of the system, hence, starting crystallization.

The differentiation of Eq. 2.12 results in:

$$r^* = \frac{2\gamma_{sl}}{\Delta G_v} \quad (2.13)$$

The critical free energy difference requires forming a nucleus of critical size r^* is calculated by substituting Eq. 2.13 in Eq. 2.12:

$$\Delta G_{\text{hom}}^* = \frac{16\pi\gamma_{sl}^3}{3(\Delta G_v)^2} \quad (2.14)$$

Substituting value of ΔG_v from Eq. 2.11 in the above two equation gives:

$$r^* = \left(\frac{2\gamma_{sl}T_E}{L_v}\right) \frac{1}{\Delta T} \quad (2.14)$$

and

$$\Delta G_{\text{hom}}^* = \left(\frac{16\pi\gamma_{sl}^3T_E^2}{3L_v^2}\right) \frac{1}{(\Delta T)^2} \quad (2.15)$$

Eqs. 2.14 and 2.15 show the dependence of the critical nucleus radius r^* and ΔG_{hom}^* on the undercooling. For small undercooling the critical nucleus size r^* will be large enough that there will be no chance of forming a stable nucleus. However, with the increase in the undercooling both, critical nucleus size r^* and ΔG_{hom}^* decreases consequently the probability of clusters reaching the critical nucleus size r^* is getting high.

2.4.2 Heterogeneous nucleation

Eq 2.13 flaunts the dependence of homogenous nucleation on the interfacial energy and Gibbs free energy difference, depicting that homogeneous nucleation depends exclusively on the thermodynamic properties of the respective material. Homogenous nucleation is therefore an intrinsic process. The expression for ΔG_{hom}^* exhibits that nucleation can yet occur even for a smaller undercooling, by reducing the interfacial contribution which can effectively be achieved if the nucleus forms in contact with a foreign phase. In practice, it is very difficult to under cool the liquid to higher degrees without avoiding nucleation. It is because the container/mould wall, any foreign particles such as inhomogeneities in the melt, any metal oxide at melt surface or even a mote in the melt essentially provide a potential nucleation site. Hence, heterogeneous nucleation plays a dominate role in the nucleation process. Heterogeneous nucleation is an extrinsic process and can be influenced by the experimental conditions. Equilibrium of the interfacial tensions is illustrated in Fig. 2.4 and can mathematically be expressed as:

$$\gamma_{ml} = \gamma_{sm} - \gamma_{sl} \cos \theta \quad (2.16)$$

Where indices m, l and s represents mould, undercooled melt and solid (crystal embryo) respectively. The volume of a heterogeneous nucleus of a critical size r^* is always smaller than that of the counter part i.e., for homogeneous nucleus of the same critical radius. Formation of an embryo (as a result of heterogeneous nucleation) will be associated with an excess free energy:

$$\Delta G_{\text{het}} = -V_s \Delta G_v + A_{sl} \gamma_{sl} + A_{sm} \gamma_{sm} - A_{sm} \gamma_{ml} \quad (2.17)$$

Where, V_s is the volume of crystal embryo, A_{sl} and A_{sm} are areas of solid/liquid and solid/mould interfaces and γ_{sl} , γ_{sm} and γ_{ml} are the free energies of the solid/liquid, solid/mould and mould/liquid interfaces. The contribution of the first two interfaces is positive as arises from interfaces created due to the nucleation process. However, the contribution of the third interfacial energy is negative because the mould/liquid interfacial contribution disappears under the spherical cap. Correspondingly, the activation energy to form a critical heterogeneous nucleus is reduced by a factor $S(\theta)$ and is given as under:

$$\Delta G_{het} = \left\{ -\frac{4\pi}{3} r^3 (\Delta G_v) + 4\pi r^2 \gamma_{sl} \right\} S(\theta); \quad 0 \leq S(\theta) \leq 1 \quad (2.18)$$

Where;

$$S(\theta) = \frac{(2 + \cos \theta)(1 - \cos \theta)^2}{4} \quad (2.19)$$

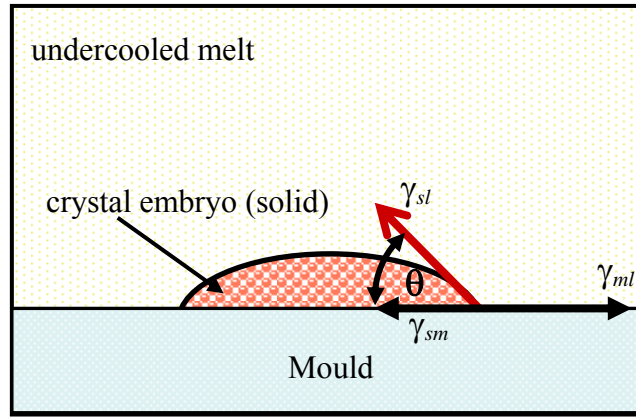


Figure 2.4 Nucleation at the mould wall (heterogeneous nucleation)

The function $S(\theta)$ depends only on θ , hence, termed as a shape factor. Eq. 2.18 is the same as for the homogenous nucleation (i.e., Eq. 2.12) except the reducing factor $S(\theta)$. Differentiating Eq. 2.18 gives:

$$r_{het}^* = \frac{2\gamma_{sl}}{\Delta G_v} \quad (2.20)$$

and, subsequently,

$$\Delta G_{het}^* = \frac{16\pi\gamma_{sl}^3}{3(\Delta G_v)^2} S(\theta)$$

Therefore, the activation energy barrier against the heterogeneous nucleation, ΔG_{het}^* is smaller than ΔG_{hom}^* by the shape factor $S(\theta)$. Albeit the ΔG^* decreases, the critical nucleus radius r^* is unaffected by heterogeneous nucleation. Combining Eqs 2.12 & 2.18 gives:

$$\Delta G_{het}^* = \Delta G_{hom}^* S(\theta) \quad 0 \leq S(\theta) \leq 1 \quad (2.21)$$

Above expression i.e., Eq. 2.21 divulges that the wetting behaviour of the melt on the mould surface has a palpable effect on the activation energy ΔG_{het}^* and thereby, on the undercooling. The lower the wetting angle, the lower will be the activation threshold. For a special case when $\theta = 180^\circ$ i.e.,

virtually no wetting, the presence of foreign particle will not influence the nucleation barrier, hence, $S(\theta) = 1$ and $\Delta G_{het}^* = \Delta G_{hom}^*$. The opposite case is complete wetting i.e., $S(\theta) = 0$, so that the activation energy is zero, hence, no undercooling is required and the melt will solidify as soon as the temperature reaches the melting temperature. Contrary to the assumption that the mould wall is flat, generally it contains cracks or crevices. The solid phase of the sample can be stabilized on such cracks or hollow regions without any significant undercooling.

The subsequent growth of the nuclei leads to a crystal and is determined largely by the atomic structure of the growing interface. At the melting temperature there may be a constant migration of atoms at the interface between the solid and liquid phases, but yet there is no net crystal growth. For crystal growth to take place at the interface some undercooling is required, so that more atoms are added into the interface. The undercooling at the interface essentially provides the requisite driving force to bias the kinetic processes at the interface in the freezing direction. The greater the interfacial cooling, greater is the driving force for the crystal growth, consequently, higher is the rate of solidification. The growth rate is dependent only on the interface temperature and the actual growth form depends on the thermal conditions in the liquid ahead of the interface [Haasen96].

2.5 Transformation Kinetics

The crystal growth velocity is very high in pure alloys and in simple miscible alloys, so that the crystallization takes place ubiquitously after the formation of the first nuclei. For steady state, nucleation frequency can be expressed as follows [Steinhardt83]:

$$\ln t = \ln\left(\frac{V_p \Omega(T)}{N}\right) + \frac{16\pi\gamma^3}{3K_B T (\Delta G)^2} S(\theta) \quad (2.22)$$

Where N is number of nuclei in a melt of volume V_p , K_B is boltzmann constant, and $\Omega(T)$ is temperature dependent parameter. The so-called Time Temperature Transformation (TTT) diagram (also known as Time Temperature Nucleation TTN) can be drawn using the Eq. 2.22. Such TTT plots give essential information about the time frame and the extent of undercooling required forming first nuclei.

Fig. 2.5 illustrates the nucleation's time and temperatures dependence for homogenous nucleation (hom), heterogeneous nucleation of a metastable phase (met) and heterogeneous nucleation of a stable phase (het) [Herlach94]. At temperatures just below the melting temperature, system kinetics is controlled by the activation energy ΔG^* , whereas at low temperatures down to the glass transition temperature, the temperature dependent diffusion dominates. All curves in the Fig. 2.5 approach the glass transition temperature at which the viscosity becomes very high (typically the order of 10^{13} poise), hereafter the remaining undercooled melt freezes into amorphous state. The widths of such TTT curves are mainly determined by the activation energy ΔG^* , on the other hand position of the

nose depends on both activation energy ΔG^* and number of potential nucleation sites. The curves bearing the arrows depict the cooling rates of the melt. The crossing point of the cooling rates with that of TTT curves gives the extent of undercooling and time at which nucleation will take place.

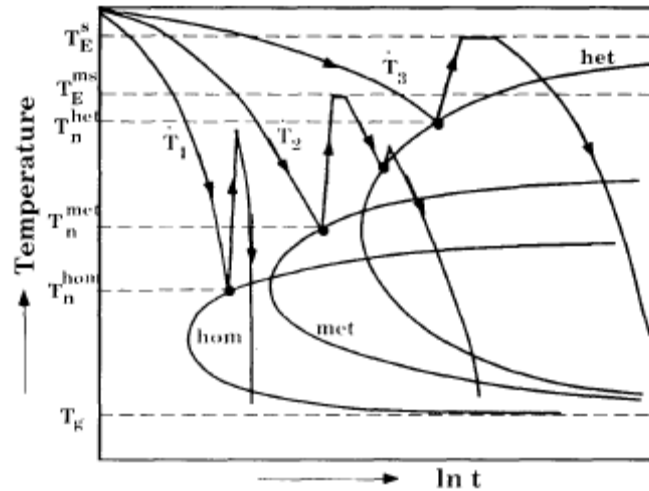


Figure 2.5 illustrates the temperature time transformation diagram for homogeneous nucleation (hom) and heterogeneous nucleation of a stable (het) and a metastable (met) phase. In the cooling rates, recalescence profiles corresponds to the hypercooling (hom), crystallization of a metastable phase (met) having melting temperature T_E^{ms} and of a stable phase having melting temperature $T_E^s \cdot T_g$ denotes the glass transition temperature.

Each atom in the melt is a potential nucleation site for homogeneous nucleation, however for heterogeneous nucleation the atoms at the interface of the foreign surface are potential nucleation sites. This explains the position of the nose of “hom” curve in TTT at shorter times than others. Fig. 2.5 lucidly illustrates that the cooling rate will effect the phase selection in the undercooled melt. For a moderate cooling rate, \dot{T}_3 , a stable phase will nucleate heterogeneously. A further increase in the cooling rate to \dot{T}_2 will change the scenario and the nucleation of a metastable phase is expected. The temperature rise during recalescence will consequently increase the temperature of the system to the melting temperature of the respective metastable phase. During the subsequent cooling the primary nucleated metastable phase might transform into a stable solid [Chuang86a, b]. Yet an increase in the cooling rate to \dot{T}_1 will lead to the homogeneous nucleation, however, as the undercooling limit (for homogeneous nucleation) exceeds the hypercooling limit in many cases, the temperature rise owing to the recalescence will not be enough to rise the temperature of the melt to the melting temperature. If the cooling rate is high enough to avoid any intersection with the nucleation curves in the TTT diagram, it will lead to formation of a metallic glass. Its energetic state will correspond to an undercooled melt which falls out of local equilibrium at the glass transition temperature consequently the liquid like structure is frozen in. In the absence of heat of crystallization, the temperature time profile will be continuous, without showing typical features of recalescence as described above. Hence, the essential requirement of metallic glass formation is a complete bypass of the nucleation process.

2.6 Insight into the properties of amorphous alloys and metallic glasses

Bulk amorphous alloys have a density difference of 0.5% than their crystalline counter parts, in egregious contrast to metallic glasses for which it reaches to almost 2% as reported earlier [Chen80, Masumato82, Masumato76]. Such a small differences of bulk amorphous alloys to their crystalline counter parts indicates that these materials flaunt higher density randomly packed atomic configuration. Albeit, having smaller density differences, upon annealing the density of the bulk amorphous alloys increase systematically to a structurally relaxed glass and eventually to the crystals. The new bulk amorphous alloys with wider supercooled regions allow studying temperature dependent viscosity in these ranges. Johnson delved to show that viscosity follow the Vogel-Flucher-Tammann equation:

$$\eta = \eta_o \cdot \exp\left(\frac{DT_o}{T - T_o}\right) \quad (2.23)$$

Where D is called fragility index and T_o is the Vogel-Flucher-Tammann temperature (at which η diverges). Angell has distinguished between strong and fragile glasses, based on the dependence of viscosity on T_g/T [Angell95]. Most of the metallic glasses are fragile contrary to that of silica and silicates which are strong glasses. The fragility index D has a value of 2 for fragile glasses and 100 for strong glasses. Where as for BMG's D varies from 20 to 25.

Bulk metallic glasses possess high yield strength and very high elastic limit. The Hookean elastic strain, a metallic glass can support in tension or in bending is almost double to that of a commercially available crystalline material. Metallic glasses have very high fracture strength coupled with 2–3% of elastic strain. Conventional aluminium, titanium alloys and steels can sustain 1–2% of elastic strain. Albeit, good yield strength and high elastic limit, their applications are restricted owing to low plasticity. Toughness of the glasses can be improved by hindering propagation of shear bands and by introducing multiple pinning centres either by introducing foreign particle in the amorphous matrix i.e., to form an extrinsic composite or by partial crystallization of the amorphous matrix so that to provide a strong interface reinforcement to matrix.

Many metallic glasses flaunt exceptionally good corrosion properties. Absence of defects and structural homogeneity in amorphous alloys obviates creation of electrolytic micro-cell and thereby increases the corrosion resistance. Pang has enunciated that the corrosion loss in 6N HCl at 298K is about 105 times larger for 304 stainless steels than for P containing bulk amorphous alloys [Pang02]. Fe-Cr-P-C ribbons are used as active element in electromagnetic filters to remove rust from the water; a higher corrosion resistance ensured longer life of the filter elements [Kawashima85].

Commercial interests developed in using metallic glasses and amorphous/nanocrystalline composites based on their superior soft magnetic properties. Sensors for electronic article surveillance have become a large application for amorphous materials. Nano-composites developed still sustain their soft magnetic properties; intriguingly flaunt higher saturation magnetization and lower

magnetostriction than the pure amorphous material. The first widely studied alloy from this group is $\text{Fe}_{73.5}\text{Cu}_1\text{Nb}_3\text{Si}_{13.5}\text{B}_9$ FINEMET [Yoshizawa88], which at present is already used in practice. The energy loss in transformers can be reduced to a factor of almost 2/3 just by replacing crystalline Fe-Si based cores to amorphous materials. Other applications for ferromagnetic metallic glasses are switch-mode power supplies, magnetic amplifiers, ground fault interrupters, sensors and magnetic shielding [Smith93]. Albeit, metallic glasses and amorphous show good soft ferromagnetic properties, better hard magnetic properties of certain amorphous composites has already been enunciated. Fig 2.6 illustrates a time frame for progress in improvement of hard magnetic properties of complex magnetic materials [Bracchi04].

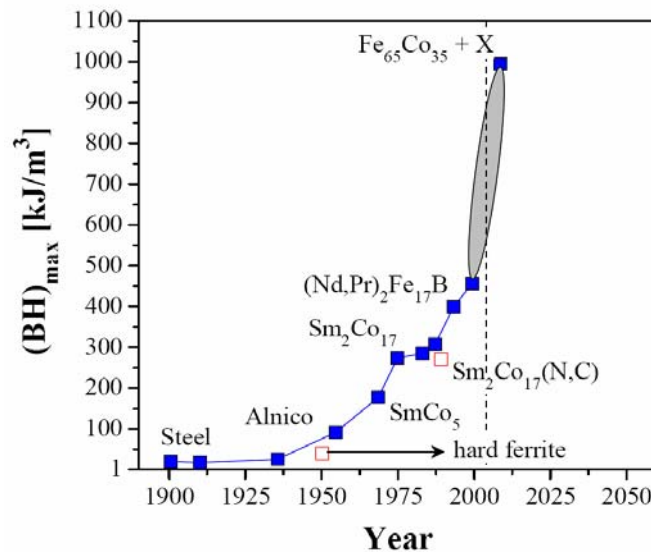


Fig. 2.6 Progress of improved magnetic properties of amorphous structure over the last century. The shaded area shows hypothetical trend improved by additives in Fe-Co amorphous alloys.

The remarkable leap in improvement of properties is observed in last 20 years or so, with the introduction of SmCo- based and FeCo based alloys that usually consist of two or more phases showing high coercivity and pinning effects of main magnetic phases. The continued developments in new metallic glasses and amorphous alloys (even complex composite) incite new application for such unique materials. The properties of BMG's and metallic glasses are reviewed in detail elsewhere [Ashby06, Schneider01, Inoue99].

Chapter 3

Investigated Materials

This chapter deals mainly with the bibliographical review of the investigated material and in addition summarizes the methodology of sample preparation. All three possible states of matter i.e., vapour, liquid and solid have been successfully utilized to achieve vitrification of diversified elemental compositions using different methodologies, such as, melt quenching, amorphization by ball milling, thermal deposition, chemical decomposition, irradiation, solid state diffusional amorphization, etc. However, quenching from vapour and melt are commercialized owing to the ease in controlling different crucial parameters. The details of these preparation techniques are summarized elsewhere [Liebermann83, Duwez76, Cahn96]. During the course of this work melt quenching/casting are utilized to attain metallic glasses and bulk amorphous alloys.

3.1 $Zr_{53}Co_{23.5}Al_{23.5}$ Amorphous Alloys

During the past decades, there have been considerable efforts on the fundamental understanding of structure, atomic and electronic transport properties as well as further exploration of mechanical, magnetic and chemical properties of amorphous materials. The unique properties exhibited because of their novel structure, promises for numerous potential engineering applications. The research interests in Zr-based metallic glasses were stimulated by the discovery of Zr-Cu-Al amorphous alloy with a good glass forming ability (GFA) by Inoue [Inoue91,93].

Amorphous alloys exhibit an interesting combination of mechanical properties. A lack of translation periodicity results in comparatively higher tensile strengths as compared with crystalline materials in which dislocation are created and propagated through the crystalline lattice resulting in a drastic drop in strength against the theoretically measured strength. However, the lack of ductility and brittle nature of amorphous alloys are main drawbacks which restricts many structural applications. Recent efforts on improving the plasticity have been focused on fabricating metallic glass composites. A variety of

BMG composites have been formed by the introduction of reinforcing crystalline phase in the glassy matrix.

Another approach can be producing a glass-glass composite with enhanced mechanical properties. Palpable interest has been developed to fabricate the glassy composite structure as glass-glass composite or glass-crystal composite with improved mechanical and physical properties. Heilmaier have enunciated such Zr-based glass matrix composite amorphous alloys [Heilmaier00]. Mechanical properties of Zr-Al-Co based amorphous systems both in glassy ribbons and bulk amorphous states have been reported by Inoue [Zhang04b]. Addition of the Cu to Zr-Al-Co leads to a higher tensile strength and subsequently, better mechanical properties.

To shed more light on the glass forming ability in amorphous alloys, an alternate approach adapted, though under intensive debate, is exploiting Fermi surface-Brillion zone (Fs-Bz) interaction [Nagel75]. The Fermi surface-Brillion zone (Fs-Bz) interaction, denoted as $2k_f \approx k_p$, where k_f is the momentum of the electrons at the Fermi level and k_p is the width of pseudo-Brillion zone; an important stabilization mechanism analogous to the Mott-Jones formulation of Hume-Rothery rules in crystalline alloys. The conduction electron concentration per atom (e/a) ratio revealed to be a universal feature of many electronically simple and transition metal containing alloys. The e/a criteria has been utilized to reveal high GFA in multicomponent systems in Al-Ni-Zr and Al-Cu-Ni-Zr systems [Wang03, Chen03]. Utilizing the aforementioned criteria Zhang has depicted the composition optimization of Zr-Co-Al bulk metallic glasses with largest GFA exhibiting by $Zr_{53}Co_{23.5}Al_{23.5}$ alloy system that have the highest thermal stability [Zhang04].

Albeit, the aforementioned mechanical properties and the studies based on the electronic structure of Zr-Al-Co amorphous alloys have been reported, rather recently, no intention has been given to the magnetic properties of such class of the system. Moreover, no systematic investigations on the detailed microstructure have been done. The present work addresses these very issues to reveal the microstructure of Zr-Al-Co alloys and their respective magnetic properties. In addition, effects of the heat treatment on subsequent magnetic properties are also investigated. To study the microstructural behaviour and magnetic properties the alloy system with the largest GFA reported; has been chosen i.e., $Zr_{53}Co_{23.5}Al_{23.5}$ alloy system.

3.1.1 $Zr_{53}Co_{23.5}Al_{23.5}$ Bulk Amorphous Alloy

$Zr_{53}Co_{23.5}Al_{23.5}$ bulk glassy alloys were prepared in Department of Materials Engineering¹, Dalian University of Technology, Dalian, P. R. China. The setup for sample preparation at Dalian university is shown in Fig. 3.1 and Fig. 3.2 illustrates corresponding schematic drawing. The rods of 3 mm diameter were produced by arc melting of pure Zr, Al and Co in an argon atmosphere, followed by Cu mould suction casting (Fig. 3.3c). Further details about the sample preparation are described elsewhere [Wang04, Zhang04].

¹ In collaboration with Dr. C. Dong and Dr. J. Qiang



Figure 3.1 Vacuum arc melting furnace for Cu mould suction casting in Department of Materials Engineering, Dalian University of Technology, Dalian, P. R. China².

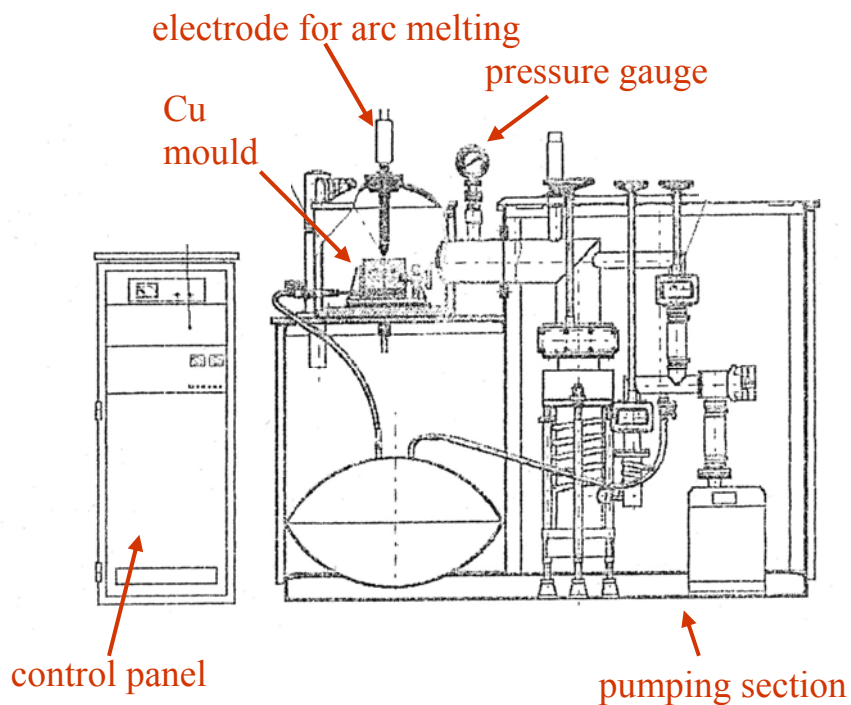


Figure 3.2 Schematic illustration of the Vacuum arc-melting furnace.

3.1.2 $Zr_{53}Co_{23.5}Al_{23.5}$ Glassy Splats

$Zr_{53}Co_{23.5}Al_{23.5}$ splat metallic glasses were produced in I. Physikalisches Institut, Universität Göttingen, Germany. The main advantage of using splat quenching over Cu mould suction casting is higher cooling rates (i.e., $\approx 10^6 \text{ Ks}^{-1}$). To prepare splats of a desired composition, a master alloy was produced from pure elements by arc melting in small pieces.

² Dr. W. Qing has kindly provided these sketches.

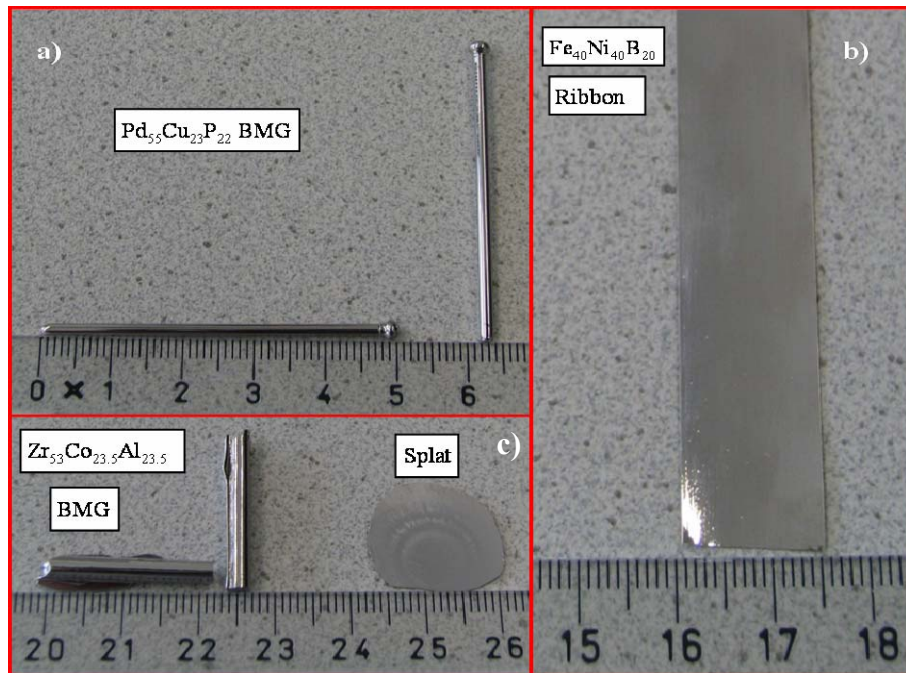


Figure 3.3 Pictures of different glassy samples characterized during the course of this research work; (a) $\text{Pd}_{55}\text{Cu}_{23}\text{P}_{22}$ bulk metallic glass, (b) $\text{Fe}_{40}\text{Ni}_{40}\text{B}_{20}$ glassy ribbon, and (c) $\text{Zr}_{53}\text{Co}_{23.5}\text{Al}_{23.5}$ bulk metallic glass and splat sample.

Fig 3.4 illustrates the set up for splat quenching device (Buehler GmbH). The master alloy is then melted in induction coil in Ar environment. The chamber is flushed with Ar several times before melting to obtain an oxygen free atmosphere.

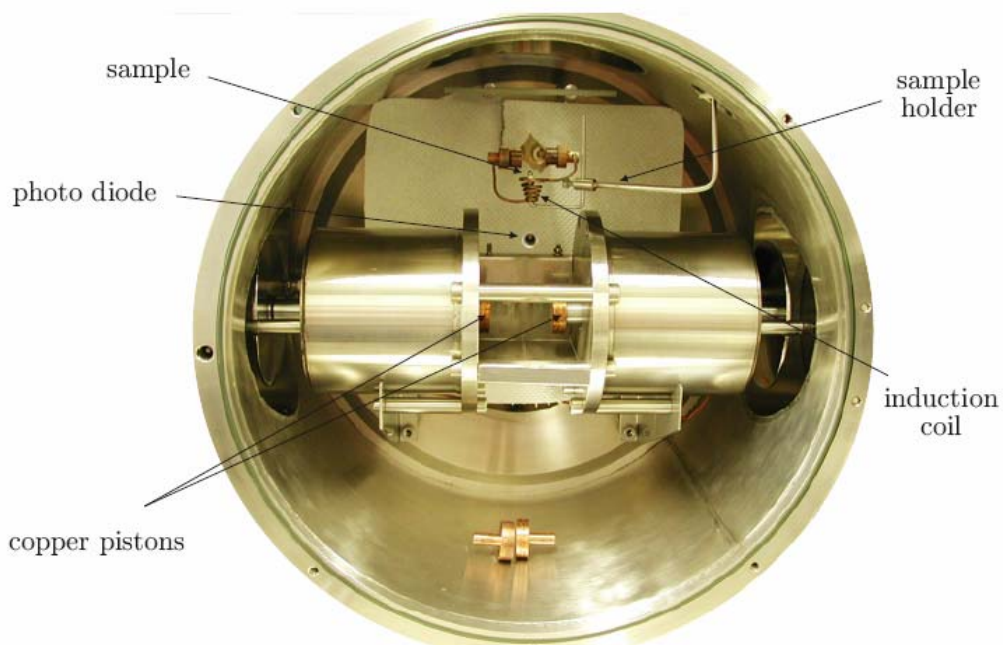


Figure 3.4 Sketch of splat quenching device at I. Physikalisches Institut, Universität Göttingen, Germany [Bracchi04].

The induction coils not only increase the temperature of the sample to melting temperature by energy dissipation but also produce eddy current, coupled with the external induction field, provide a force

high enough to balance the gravitational force on the small samples. Hence, molten specimen can levitate with out any external support. Thereafter, the sample is dropped freely, by switching off the current to the induction coils. A light diode trigger two Cu pistons against each other trapping the melt and quenching results in a splat foil (hereafter, will be called splat) having a thickness about 30 μm . A $\text{Zr}_{53}\text{Co}_{23.5}\text{Al}_{23.5}$ splat metallic glass is shown in Fig. 3.3c.

3.2 $\text{Fe}_{40}\text{Ni}_{40}\text{B}_{20}$ Glassy Ribbons

Fe-Ni-B metallic glasses have been studied intensively in the past decades owing to their excellent soft magnetic properties; leading to a number of industrial applications [Luborsky80]. In addition to their good magnetic properties, a reasonable amount of research is also devoted to mechanical properties of these alloys. Prime interest develops because even slight partial crystallization ends the useful life of the material: palpable loss in high permeability and low coercivity [Walter78, Greer82]. Albeit there is subsequent loss in magnetic properties after annealing, ductile-brittle transition is also reported even for annealing below crystallization temperatures [Chen76, Lewis79, Piller82].

Different rationales include excess free energy volume that anneals out during annealing thereby making plastic deformation even more difficult [Li77] alongside the structural relaxation phenomenon upon annealing. Structural relaxation causes a topological change in short range order i.e., changes in bond distances and bond angles as well as change in chemical short range order i.e., exchange in chemically different neighbours. The present study on the $\text{Fe}_{40}\text{Ni}_{40}\text{B}_{20}$ metallic glasses both for the as quenched state and heat treated state (1 hour at 350°C) below the crystallization temperature deal with the aforementioned issue; mainly utilizing the NNE module to elicit any information on the short range ordering.

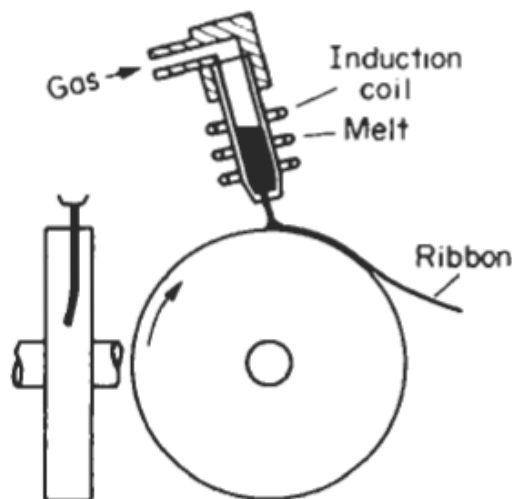


Figure 3.5 Sketch illustrating two side views for melt spinning [Cahn96].

$\text{Fe}_{40}\text{Ni}_{40}\text{B}_{20}$ glassy ribbons were kindly provided by Vacuumschmelze GMBH. The set up for producing the ribbons is pretty similar to the one; shown in Fig. 3.5, where the piston assembly is replaced by a rotatable copper wheel along with an extension to collect the ribbon. The induction coil is no more in the spiral shape, and contains a glass tube containing the master alloy. The expulsion of

molten alloy as a jet through an orifice and subsequent impingement of the jet on a rotating copper wheel ensures high cooling rates ($\approx 10^6 \text{ Ks}^{-1}$) and that results in a continuous glassy ribbon. A 15 mm wide $\text{Fe}_{40}\text{Ni}_{40}\text{B}_{20}$ glassy ribbon is shown in Fig. 3.3b having a thickness around 30 μm . Further details about the sample preparation by melt spinning can be found in literature [Cahn96].

3.3 $\text{Pd}_{55}\text{Cu}_{23}\text{P}_{22}$ Bulk Metallic Glass

Pd- based glasses are an important class of bulk amorphous alloys particularly owing to ease in vitrification by fluxing techniques [He98]. Earlier, Chen has divulged a Pd based alloy system having composition $\text{Pd}_{40}\text{Ni}_{40}\text{P}_{20}$ [Chen74] having 1-3 mm thickness. Thereafter, introduction of the fluxing techniques to eliminate heterogeneous nucleation enabled to produce centimetre sized glasses. Since then, a number of variants of Pd-based alloys have been investigated for their structural, thermodynamic and magnetic behaviour [Shen98, Wilde94, Harms03, Miller03, Vennström04]. Albeit, the interest in general properties, these alloys were conspicuous for the better understanding of the underlying physics of bulk amorphous structures.

$\text{Pd}_{55}\text{Cu}_{23}\text{P}_{22}$ amorphous alloy has been investigated during the course of this research work in order to divulge any information on the topological and chemical short range order in this amorphous system essentially to elucidate the atomic distances between neighbouring atoms utilizing the atom probe tomography (APT). He has enunciated the composition for the formation of bulk amorphous alloys in Pd-Cu-P systems especially with a thickness of 7 mm as depicted in Fig. 3.6 [He98]. Albeit, the glass formation range is wider for different variants of Pd-Ni-P alloy system, Pd-Cu-P system is an ideal candidate for the TAP investigations for the absence of any overlap among the constituent elements. Hence, it offered no complexity in assigning correctly the chemical nature of constituent elements during the TAP data treatment.

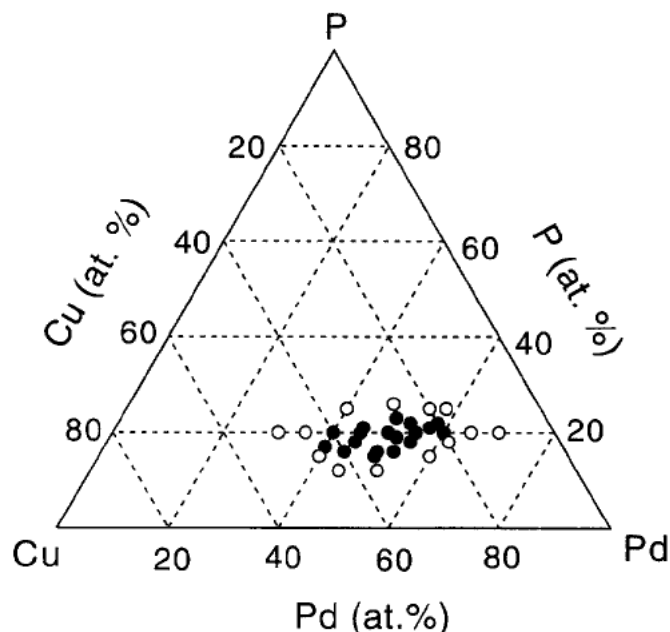


Figure 3.6 illustrates bulk glass formation range in Pd-Cu-P systems. Filled circles denotes the formation of glassy rods with a diameter of at least 7 mm [He98].

The Pd₅₅Cu₂₃P₂₂ bulk amorphous alloys were produced as a 2 mm diameter rod with the length of almost 50 mm at Los Alamos National Laboratory, MST Division, Los Alamos, USA. The amorphization was enhanced by using fluxing techniques [Drehman82]. A detailed description of sample preparation is reported elsewhere [He98]. The Pd₅₅Cu₂₃P₂₂ bulk amorphous rods are shown in Fig. 3.3a.

3.4 Zr_{41.2}Ti_{13.8}Cu_{12.5}Ni₁₀Be_{22.5} Bulk Metallic Glass

Palpable thermal stability against crystallization in the deeply undercooled liquid region of recently developed bulk amorphous alloys, instigate new dimensions to the research on amorphous structure. The extended supercooled region in newly developed bulk metallic glasses triggered a large number of experiments performed to study the glassy structure in supercooled region to understand the underlying physical phenomenon in this aforementioned range. Peker and Johnson have developed a Zr_{41.2}Ti_{13.8}Cu_{12.5}Ni₁₀Be_{22.5} bulk metallic glass, BMG, with excellent GFA and processability that has become the most widely used commercial bulk metallic glass (BMG) with the trade name of Vitreloy 1 (Vit1) [Peker93]. Both, interests in fundamental sciences of BMGs and ease in availability incited us to start investigations on such sort of alloys utilizing state of art APT.

Vitreloy-1 (Zr_{41.2}Ti_{13.8}Cu_{12.5}Ni₁₀Be_{22.5}) bulk amorphous alloy was also characterized mainly by Tomographic atom probe. It was produced by making a master alloy from the constituents (purity > 99.9 %) utilizing arc melting in argon atmosphere. The ingot was re-melted in a silica tube of inner diameter 10 mm (vacuum $\approx 10^{-5}$ mbar) followed by water quenching. The resultant cooling rate was high enough to form a 10 mm diameter amorphous Vitreloy-1 rod.

Chapter 4

Experimental Methods and Techniques

During the course of this research work, the differential scanning calorimetry is utilized to study the thermal transitions and related attributes of the investigated amorphous systems. To reveal the crystallographic nature, X-ray diffraction has been carried out though the information extracted is limited to microscopic scale. The main disadvantage of the X-ray diffraction studies is its inability to reveal fine scale nano-composite structure due to limited resolution. Hence, structural characterizations are carried out exploiting the advanced characterization tools such as high resolution transmission microscopy (HRTEM) and tomographic atom probe.

The main advantage of the high resolution transmission electron microscope is its ability to reveal the microstructural details even in the sub-nanometre range. Different analytical setups enhance the functionality of the TEM by allowing rather a quantitative analysis than qualitative. The main drawback of the TEM analysis is the lack of stereological information. Hence, tomographic atom probe is used to gain the three dimensional information in real space. Moreover, it allows quantifying different phases in addition to study the phase morphology in detail that is restricted in TEM because of the larger electron beam specimen interaction. Recently developed statistical tools for the TAP data, even allow revealing the interatomic and elemental relationship with the resolution in angstrom which is extremely difficult to reveal from other characterization techniques. Main drawback of the TAP analysis is tedious specimen preparation and difficulty in analyzing brittle samples.

The description of methods and techniques used for the structural, thermodynamical and magnetic characterization of the amorphous alloys and metallic glasses are discussed in this chapter. The brief description about the theory of the methodology is followed by the description of the measurement devices.

4.1 Differential Scanning Calorimetry (DSC)

One of the fundamental concepts of modern sciences and the basis of thermodynamics is the connection between heat and energy. An entire class of materials analysis techniques is based on the ability to transfer heat to a material and monitor the effects. This class of techniques is known as thermal analysis. Differential Scanning Calorimetry (DSC) is a convenient and highly accurate method for performing thermal analysis on a wide variety of materials. Phase transformation temperatures, enthalpies of transformation and thermal transitions hysteresis data of a sample can be determined by measuring the heat flow of the sample compared to a reference material. DSC is a technique for measuring the energy necessary to establish a nearly zero temperature difference between a substance and inert reference material, as the two specimens are subjected to identical temperature regimes in an environment heated or cooled at a controlled rate.

The Perkin-Elmer DSC7 instrument is used for the thermal characterization of metallic glasses and amorphous alloys in the present study. A schematic representation of this instrument is shown in Fig. 4.1. The temperature difference is kept equal to zero by placing the temperature sensors, Pt resistor thermometers into a bridge circuit. Any imbalance is used to drive a heater in the appropriate sample or reference portion of the cell. The power required to keep the bridge circuit in balance is proportional to the change in heat capacity or enthalpy occurring. The reaction is endothermic if the power is supplied to the sample and exothermic when it is supplied to the reference.

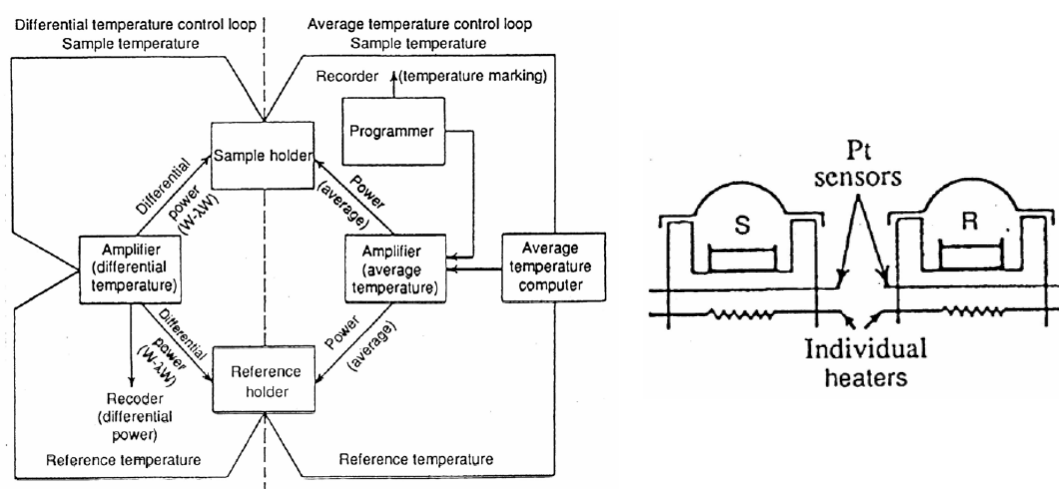


Figure 4.1 A schematic representation of the power compensating DSC instrument and its operation [Watson64].

Al pan containing 5-20 mg of the sample of investigated material were crimped together with an Al lid using a specially designed crimping tool. Empty Al pans were used as reference material for all DSC measurements. The flow of Ar gas is maintained during the DSC scan to avoid any oxidation. During a heating cycle of the DSC analysis the same heating power is supplied to both furnaces via a control unit as shown in the Fig. 4.1 to achieve a preset mean temperature at a desirable heating rate. A heating rate of 0.33 K/s is used for all the DSC measurements.

For an ideal symmetry, the temperature of both furnaces containing sample “S” and reference “R” remains the same. However, as a result of any sample reaction a temperature difference is established between two furnaces. The DSC 7 compensates this difference by increasing or decreasing proportionally the heating power. The heat capacity of the sample can be mathematically expressed as: Heat capacity = Heat flow/ heating rate i.e.,

$$C_p = \frac{dQ/dt}{dT/dt} = \frac{dQ}{dT} \quad (4.1)$$

The results can now be presented as a plot of the differential heat flow between the reference and sample cell as a function of temperature. When there are no thermodynamic chemical processes occurring, the heat flow difference between the sample and reference varies only slightly with the temperature, and shows up as a flat or very shallow base line on the plot. However, an exothermic or endothermic process within the sample results in a significant deviation in the difference between the two heat flows. The result is a peak in the DSC curve. Generally, the differential heat flow is calculated by subtracting the sample heat flow from the reference heat flow called base line. In the present investigations the base line was obtained by rerunning the DSC scan with the same sample under same conditions knowing that no additional reaction occurs in the interested temperature range. The splat and ribbons of the metallic glasses were cut into the appropriate shape and cleaned with acetone before the DSC measurements. The rods of the bulk samples were cut into the discs with the thickness of 1 mm using an electric discharge machine (EDM) followed by wet grinding on the both sides of the discs to get rid of any oxide layer formed during the cutting process. These discs were then cleaned in acetone prior to the DSC measurements.

4.2 X-Ray Diffraction

X-ray diffraction is one of the most important tools of solid-state science as a matter of the fact that it constitutes a powerful and readily available method for determining atomic arrangements in matter. These techniques cover various investigations, including qualitative and quantitative phase identification and analysis, differentiating between crystalline and amorphous materials, determination of the crystalline structure (crystal axes, size and shape of the unit cell, positions of the atoms in the unit cell), determination of the orientation of single crystals, determination of the texture of polygrained materials, measurement of strain and small grain size, measurement of various kinds of randomness, disorder, and imperfections in crystals and determination of radial distribution functions for amorphous solids and liquids. The German physicist von Laue in 1912 first determined that X-rays diffract from the periodic arrangement of atoms in a crystal, exactly analogous to the diffraction of visible light from a grating. Based on the work of von Laue, W. H. and W. L. Bragg showed in 1913 that diffraction from a crystal is described by the equation now known as Bragg's law:

$$n\lambda = 2d \sin \theta \quad (4.2)$$

Where n is order of the reflection, d is interplanar spacing, θ is one half of the diffraction angle and λ is wavelength (Fig. 4.2). Diffraction experiments require X-ray wavelengths of the order of the interatomic spacing to produce interference, and hence typical wavelength ranges are 0.07-0.2 nm. Theory of X-ray diffraction is well explained elsewhere [Cullity67].

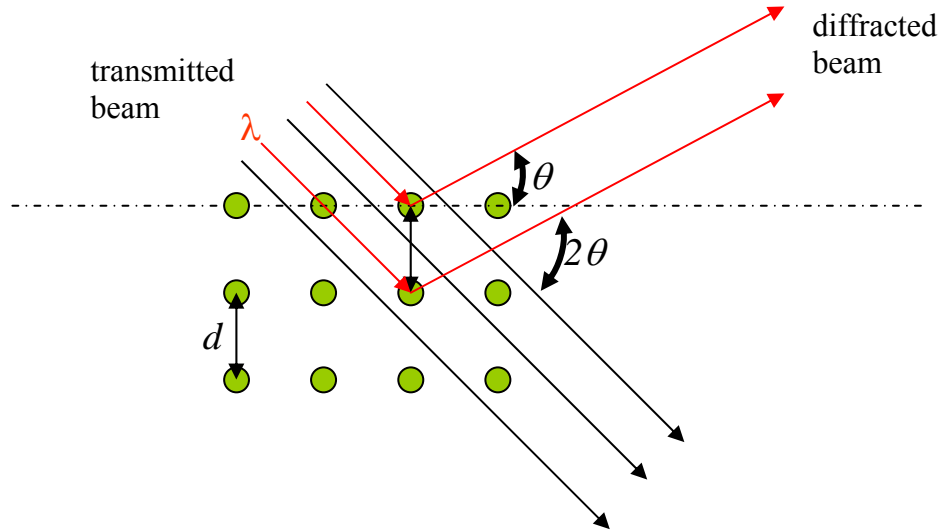


Figure 4.2 Diffraction of x-rays by a crystal.

Diffraction measurement in the present work are carried out on the X'Pert MRD diffractometer instrument equipped with the CoK_α source having $\lambda = 0.179$ nm. The measurements were carried out with a voltage of 40 KV, a current of 30 mA and measurement angle 2θ varies from 20-100.

4.3 Field Ion Microscopy and Atom Probe Tomography

The tomographic atom probe equipped with the field ion microscopy is a powerful microanalysis tool enabling imaging and chemical analysis with extremely high spatial resolution less than 1 nm [Miller96]. Imaging is done by field ionization of inert gas atoms, while chemical analysis is attained due to the field evaporation and time of flight mass spectroscopy. Hence, it is essentially a combination of two techniques, field ion microscopy (FIM) and mass spectroscopy with single ion sensitivity. The tomographic atom probe in short is a unique technique having atomic resolution, ability to detect all elements and a low noise level. There are some drawbacks as well such as tedious sample preparation and the analysis is destructive in nature. One should also be aware of the fact that the results from atom probe represent a very small volume of the examined material.

4.3.1 Field Ion Microscopy

The concept of atoms was introduced in the 5th century B.C. but it was not developed into scientific theories until the 20th century. Prof. Erwin Müller, a German Physicist, for the first time in the history observed the position of an individual atom with field emission microscopy (FEM). It was FEM that

lead to the development of field ion microscopy (FIM), comparatively more effective method with the better resolution. The basic principle of FIM is depicted in Fig. 4.3.

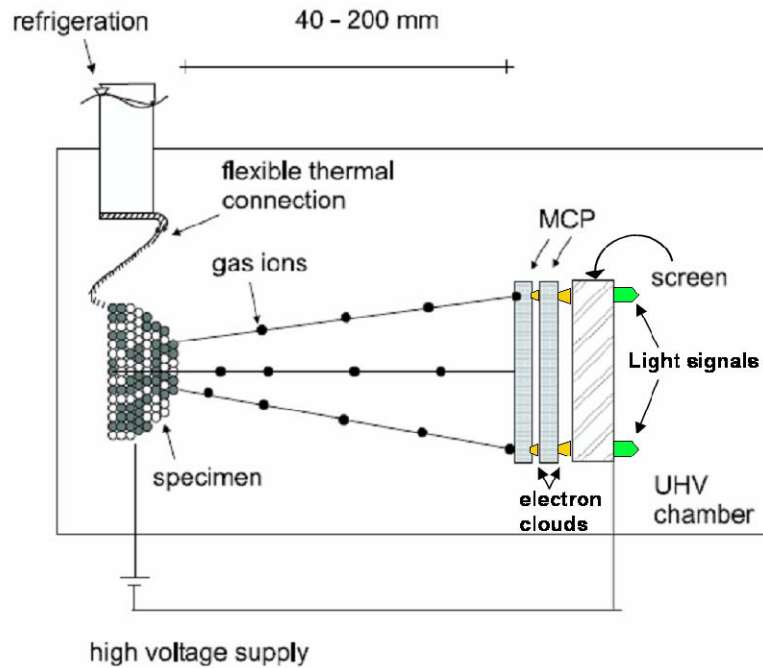


Figure 4.3 Schematic illustration of the principle of field ion microscopy (FIM) [alkassab03 with minor modifications].

It essentially consists of a vacuum chamber filled with small amounts ($\sim 10^{-3}$ Pa) of an imaging gas such as Ne, He or Ar. The sample in the form of an extremely sharp needle having an end radius of about 10-100 nm is mounted in an electrically insulated holder along the axis of the chamber in front of an assembly of microchannel plates (MCP) and phosphor screen at a distance of about 40-200 mm. A high positive voltage (2-20 kV) is applied on the specimen, and a strong field is produced on the very tip of the sample. The gas molecules near the specimen apex get polarized because of the strong field and are drawn towards the needle surface. Upon reaching at the surface, gas atoms lose their kinetic energy by thermal accommodation and get adsorbed (field adsorbed) on protruding atoms because of the local high field regions (Fig. 4.4). When the distance between the next coming gas atom and protruded adsorbed atoms at the specimen surface approaches to few tenths of a nanometer (known as ionization zone), electrons from the gas atom tunnels through the surface potential barrier into a vacant energy level in the specimen, leaving behind an ionized gas atom. This process is called “field ionization”. These ions are repelled from the specimen towards the MCP where they generate electron clouds. These electron clouds in turn illuminate the phosphor screen giving a highly magnified replicate image of the surface atoms where they were ionized.

For a hemispherical shaped tip the surface atoms located on the ledges or kinks at the edges of different stacks of the lattice planes protrude from the surface. The probability of electron tunnelling is maximum at the most protruding atoms on the tip of the needle and a narrow beam of ions (formed on such atoms) continuously hitting the screen results in a bright spot on the screen. These trajectories of

ions will follow a path normal to the surface of specimen. The phenomenon of the image formation on the tip of the specimen is shown in the Fig. 4.4.

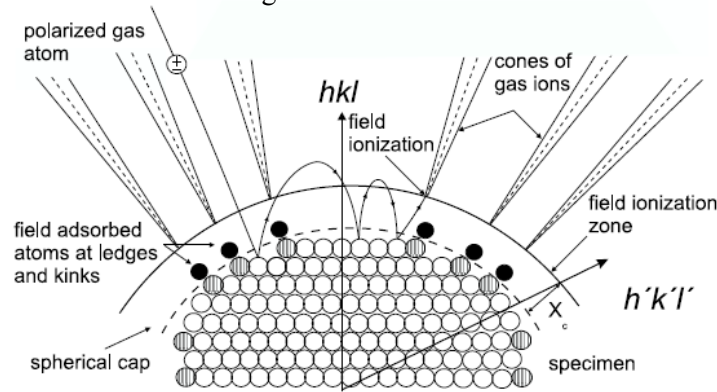


Figure 4.4 Schematic drawing of the field ionization process of the gas atoms [alkassab03]

The intersection of the hkl atomic layers with the hemispherical tip may give rise to an image and concentric rings are observed for each stack of hkl atomic layers in the FIM image. Such rings are more evident for the FIM images of the pure metals or diluted alloys having a simple unit cell such as cubic centered or cubic face centered. However, amorphous materials and metallic glasses don't show such characteristic rings in the FIM imaging.

The field on the apex of the needle is given by:

$$F_o = \frac{V}{k_f r_t} \quad (4.3)$$

Where F_o is the field at apex, V_o is the voltage applied, r_t is the apex radius of the specimen and k_f is a geometry factor. The electric field required for field ionization of inert gases is in the range of 20-45 Vnm^{-1} . As the field is inversely proportional to the apex radius, a radius of 10-100 nm is required to produce ionization at any applied voltage less than 20kV.

The magnification, η of the image is the ratio of the specimen to screen distance to the apex radius of the specimen, as given below:

$$\eta = \frac{R}{\xi r_t} \quad (4.4)$$

Where η is the magnification of image, R is the distance between specimen and phosphor screen and ξ is the image compression factor with a typical value of about 1.5. For a typical value of r_t (35 nm) and R (50 mm) the magnification approaches to about one million. The magnification can be easily controlled by adjusting R , the distance between the specimen and the screen. Image resolution is a function of different variables such as lateral thermal velocity of image gas ions, uncertainty in tangential momentum of these ions and ionization zone above a given surface atom. In terms of image spot size δ , image resolution is expressed as:

$$\delta = \left[\delta_o^2 + \frac{2\xi h r_t k_f^{1/2}}{\pi (2meV_o)^{1/2}} + 16k_f \left(\frac{\xi^2 r_t^2}{eV_o} \right) \varepsilon_t \right]^{1/2} \quad (4.5)$$

Where δ_o is the diameter of ionization zone above a given atom ~ 0.2 nm, m is the mass of image gas ion and ε_t is the transverse thermal energy of image gas atom at the time of its ionization. Thus resolution is mainly determined by δ_o and ε_t which depend on temperature. At sufficiently low temperatures as lateral thermal velocity of the image gas is very low, δ_o dominates but as the temperature is raised ε_t becomes increasingly important resulting in a remarkable decrease in resolution. Therefore, the specimen is kept at cryogenic temperature around 10 – 50 K to get best resolution with neon or helium image gas. In addition a low temperature also helps to increase the evaporation field above the ionization field, which is necessary for the function of the atom probe.

4.3.2 Atom Probe Tomography

The atom probe tomography is based on the process of field evaporation. Ionic states of the atoms are generally metastable with respect to the neutral state in matter. However, when a high electric field is applied the ionic state becomes increasingly stable. When the removal of an atom by thermal activation over a reduced thermal barrier becomes possible, field evaporation can take place. A time of flight mass spectrometer and a position sensitive detector are connected with the FIM to convert it into a tomographic atom probe. The image gas which was used for the FIM imaging is pumped out from the vacuum chamber to achieve ultra high vacuum conditions ($\sim 10^{-7}$ Pa). The specimen is subjected to a high DC voltage to which very short pulses are applied. During a pulse atoms from the specimen surface are ionized and repelled out towards the detector. The applied pulse triggers a clock that stops when an ion hit the detector, giving time of flight (t) of an ion i.e. the time required for an ion to travel from the specimen to the detector. Assuming that ions are instantaneously accelerated to their final velocity the following relation between the flight time (t) and the mass-to-charge ratio (m/n) can be derived:

$$\frac{m}{n} = 2e(V_o + v) \left(\frac{t}{d} \right)^2 \quad (4.6)$$

Where $\frac{m}{n}$ is the mass-to-charge ratio of the detected ion, e is the elementary charge, V is the total voltage i.e., $(V_o + v)$, V_o is the standing DC voltage, v is the pulse voltage t is the time of flight and d is the distance an ion travels from the specimen to the detector.

During the TAP analysis, atoms from the specimen surface are removed layer by layer resulting in a gradual increase of the tip radius. Thereby, changing the magnification during the analysis, the analyzed volume will, therefore, be a truncated cone rather than a cylindrical volume. Equation 4.3 shows that the electric field strength is inversely proportional to the radius of the tip. Hence, during the analysis, as the radius is increased, higher and higher voltage is required to achieve a fixed field evaporation rate. Normally the voltage is automatically regulated as the experiment proceeds.

The 3-D atom probe in Göttingen is equipped with the detector developed by Blavette et al. [Bostel89, Blavette93]. At a distance of 450 mm from the specimen tip an assembly of MCP of the Z stack type of MCP and a 10 x 10 anode array device are located. The schematic drawing of the system is shown in Fig. 4.6.

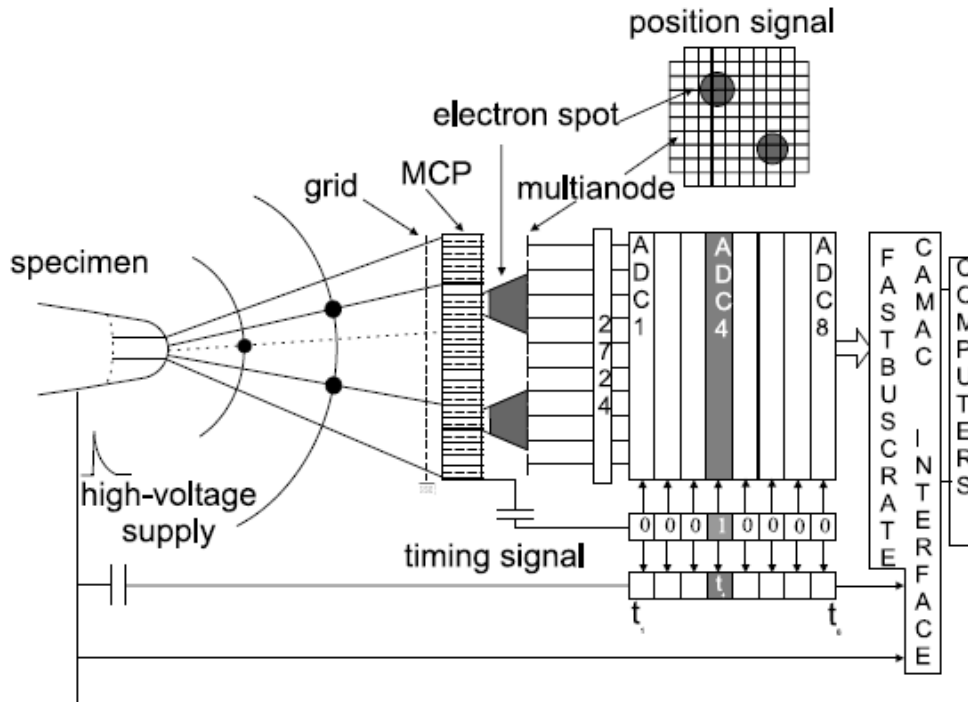


Figure 4.6 Schematic sketch of the tomographic atom probe (TAP) [alkassab03].

During the field evaporation, the evaporated ions hit the MCP generating an electron cloud. This cloud triggered 3-5 anodes on the anode array. From the distribution of the charge on the triggered anodes, the x and y coordinates of the respective ion are calculated using equation 4.7, after measuring the centre position of the electron cloud (x_a, y_a):

$$x = \frac{x_a}{\eta}, \quad y = \frac{y_a}{\eta} \quad (4.7)$$

Where the magnification η can be calculated using equation 4.4. However, the magnification changes during the course of field evaporation, as the radius of the specimen increases. It is impractical to measure the radius of the specimen after every event of ion evaporation; an estimate has to be made. Equation 4.3 is used to make estimation of the radius of specimen and then x and y coordinates are calculated. The z position is determined from the order in which the ion hit the detector. For each ion impacting the detector, the position of the ion in the z direction is the increment by an amount z_i , which is given as:

$$z_i = \frac{\Omega_i}{\zeta A_d} = \frac{\Omega_i}{V_i^2} \left[\frac{(RkF)^2}{\zeta d_x d_y \zeta^2} \right] \quad (4.8)$$

Where Ω_i is the atomic volume of the i^{th} ion, V_i is the effective voltage applied to the specimen to field evaporate the i^{th} ion. A_d is the effective area and ζ is the detection efficiency of the detector. The z position of the n^{th} atom is hence, the sum of z increments of all the atoms detected before the n^{th} atom:

$$z = \sum_{i=1}^{n-1} z_i \quad (4.9)$$

In practice, some corrections have to be made before z positioning the atoms, details of which are given elsewhere [Miller00]. Computer stores the information for each detected ion such as mass, position, etc., in a data file. AVS (Advanced visualization system) program is used to read out the data and for atomic reconstruction. In addition different statistical tools can be applied details of which are described in chapter 5.

4.3.3 Measurement conditions for different samples analysed

The experimental conditions such as measurement temperature, pulse fraction and pulse frequency for APFIM analysis were different for different investigated materials (depending on the sample brittleness) details of which are summarized in table 4.1,

Table 4.1 Summary of different experimental parameters for the TAP analysis.

	Imaging gas	Temperature [K]	Pulse fraction [%]	Frequency [Hz]	Vacuum [mbar]
Vit1 BMG	Ne	100, 60 and 50	15	2000	$5.0 \cdot 10^{-10}$
Pd₅₅Cu₂₃P₂₂ BMG	Ne	30	20	2000	$5.0 \cdot 10^{-10}$
Fe₄₀Ni₄₀B₂₀ glassy ribbons	Ne	60	22.5	2000	$5.0 \cdot 10^{-10}$
Zr₅₅Co_{23.5}Al_{23.5} BMG	Ne	35-55	20	2000	$5.0 \cdot 10^{-10}$

4.4 TAP Sample Preparation

Bulk amorphous alloys were cut into rods of approximately 0.3 x 0.3 x 10 mm using an electric discharge machine. Contrarily, metallic glasses (ribbons/splat) square shaped rods were produced by mechanical polishing. Thereafter, the rods were electropolished to produce needles with a tip radius < 100 nm. Electropolishing was carried out in two steps. The set up for conventional electropolishing is shown in Fig. 4.11. In step one, a thin layer of an electrolyte (e.g., 25 % perchloric acid in glacial acetic acid for Zr based metallic glass) floating on a dense but chemically inert liquid (trichloroethylene), was used to produce a neck in middle of the rod. Step one was designed to remove the material rapidly. It is advisable to move the specimen up and down slowly during this process to avoid preferential attack of the air-electrolyte interface and also to facilitate forming a good tapered necked region. The applied voltage was in the range of 10-20 V DC. The exact voltage depends on the constituent of the specimen. After electropolishing, the rod was cleaned in methanol. In step two the necked region was completely dipped in 2% perchloric acid in ethyleneglycol-monobutylether and a voltage in a range of 5-10 V DC was applied. In this step, material was continuously removed until the

weight of the lower half caused the needle to break giving two samples for atom probe analyses. Both needles were cleaned with methanol. Both steps were carried out at room temperature. The selection of the electrolyte for each step depends on the sample to be analysed. Table 4.2 shows the electrolytes used for the TAP sample preparation for different amorphous alloys along with the applied voltage for each step.

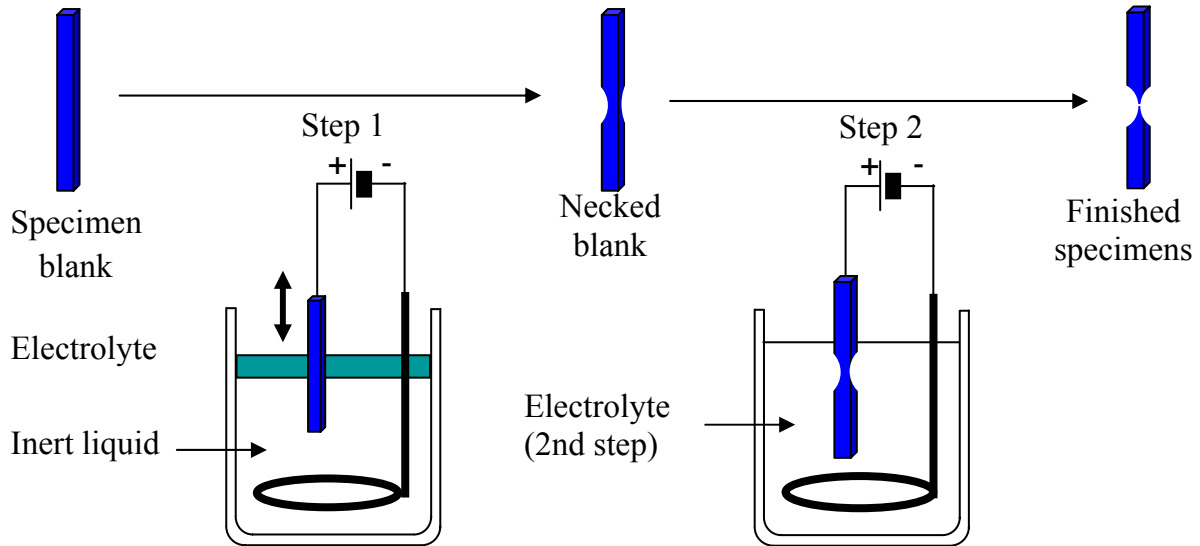


Figure 4.11 A typical two-steps electropolishing procedure. In step one, a necked region is produced (by electropolishing the needle in a thin layer of electrolyte floating on the inert liquid). A continued polishing in step two gives two needles with very sharp tips.

One of the challenges, in a successful TAP analysis, is having a very sharp specimen free of surface contaminations that might induce brittleness. This becomes even more critical in the case of bulk metallic glasses which are well known for their brittle nature. The conventional electropolishing method as described above leaves a complex oxide layer enveloping the outer surface of the tip making the specimen even more brittle, such a layer is shown in the Fig. 4.12 [Shariq06a]. Zr- and Pd-based amorphous alloys were further fabricated using focused ion beam milling to get rid of such contaminations, described in detail in the next section.

Table 4.2 Summary of different parameters used for the chemical etching of the TAP samples.

Alloy	Stage 1		Stage 2	
	Electrolyte	Voltage	Electrolyte	Voltage
Pd₅₅Cu₂₃P₂₂	25% Perchloric acid in glacial acetic acid floating on trichloroethylene	5-10V DC	2% Perchloric acid in ethlenemono-butylether	2-8 V DC
Fe₄₀Ni₄₀B₂₀	10% Perchloric acid in ethanol floating on trichloroethylene	3-10 V DC	-	-
Zr₅₃Co_{23.5}Al_{23.5}	25% Perchloric acid in glacial acetic acid floating on trichloroethylene	5-10V DC	2% Perchloric acid in ethylene-monobutylether	2-8 V DC

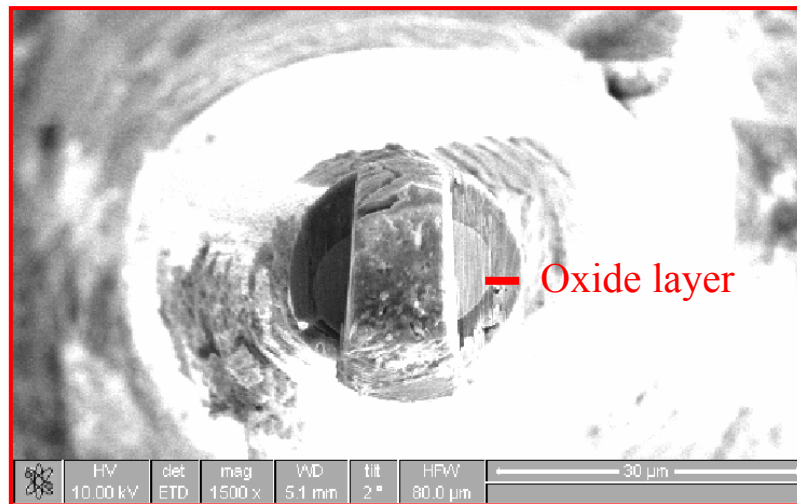


Figure 4.12 Top view of a TAP tip after milling from two sides, shows thick oxide layer covering the samples outer surface [Shariq06a].

4.5 Dual Beam Focused Ion Beam/ Scanning Electron Microscopy (FIB/SEM)

A high resolution dual beam FIB/SEM system is a unique precision machining tool that can be used to modify, in addition, to gather information from the surface of the specimen at submicrometer resolution. It allows producing microstructures with an ease and a greater control that would be difficult, if not extremely difficult to create otherwise, in addition to analyze and image structures at high spatial resolution. A FIB also makes it possible to create a TEM and TAP specimen at an arbitrary location in the surface of a macroscopic object with a precision not attainable yet by any other means. For these reasons, FIB systems have revolutionized failure analysis in the semiconductor industry and are having an increasing impact on materials analysis in general. However one of the main draw back of the specimen preparation exploiting FIB is damage to the specimen surface with each ion impinging on it though a careful handling and working at low voltage limits it just to first 20-30 nm range (that differs from material to material).

The FEI Nova™ 600 Nanolab dual beam (FIB/SEM) instrument with gallium ions at Institute für Materialphysik, Göttingen, Germany was used for the sample preparation both for TEM and TAP during this study.

Working Principle

Krohn developed a liquid-metal ion sources (LMIS) for the use in space that eventually lead to development of the focused ion beam technique [Krohn61]. A FIB system carries a strong resemblance to a SEM. During this research work ion milling was the prime focus for sample preparation, hence, described in detail rather than well established SEM principle. FIB consists of a field emission liquid metal ion (FE-LMI) source, which is used for generation of the gallium ion, as an incident beam. It essentially consists of a liquid metal supported on a blunt; however, heat-able field emitter, and a pointed wire usually having an end radius of about 5 μm (see Fig. 4.14).

When a high voltage extraction potential is applied to the emitter, the liquid metal is drawn into a conical shape and ions are produced by a field evaporation process at the cone apex, which has a radius around 5 nm. Thereafter, the ion beam is focused/scanned on the sample surface using different lenses and a scanning coil. The interaction of the sample with the ion beam generates a number of signals i.e., sputtered atoms, secondary electrons, secondary ions, x-rays and some more effects as shown in the Fig. 4.14c. Sputtering is the primary cause of the actual modification of the material surface. Other signals generated can be utilized for imaging possibilities.

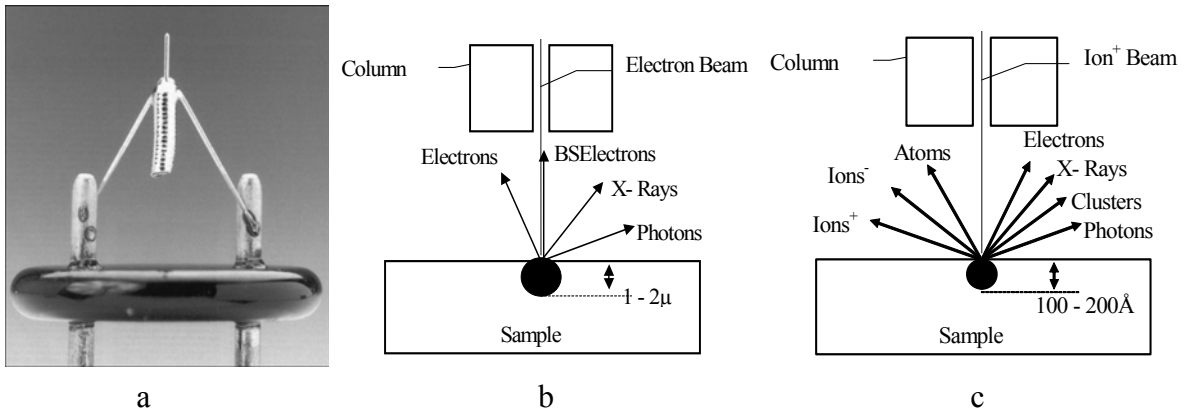


Figure 4.14 (a) LIMS along with a reservoir of gallium, (b) interaction of the sample with electron beam and (c) ion beam [Courtesy of FEI Company].

Fig. 4.15 illustrates the position of the sample for milling with respect to the electron beam. Prior to the milling, the sample should be adjusted to eucentric height, which for this machine is 5 mm. The eucentric height is the point of coincidence of the electron and ion beams.

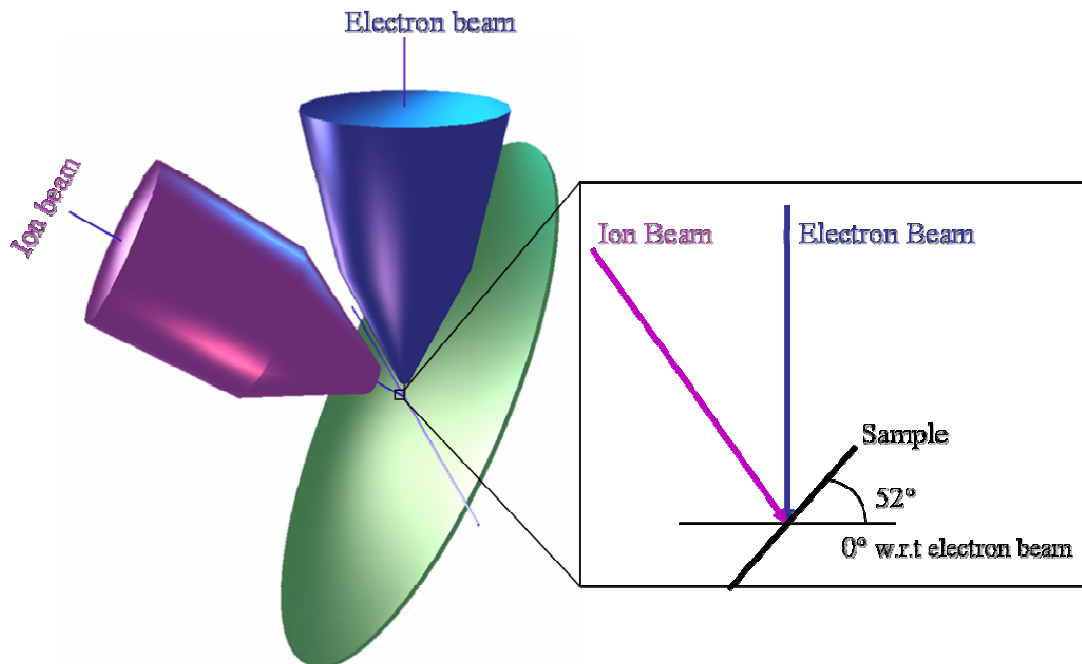


Figure 4.15 Schematic diagram showing the position of the sample with respect to the FIB and SEM column. Ion milling position is 52° whereas; 5 mm is the eucentric height, a point where two beams coincide [Courtesy of FEI Company].

Different parameters can be used to control the source brightness, source intensity, source energy distribution and some others details which can be found in some text books [Orloff02, Giannuzzi04]. The ion beam always cause damage to the specimen surface which can be reduced to a great extent by using electron beam (especially for aligning the instrument) and a lower voltage for the final stages of sample preparation. In addition, the electron beam allows monitoring the condition/status of the specimen even during ion-milling.

A gas injection system allows the deposition of a chemical compound (Pt in our case) on the sample surface. A gas, usually an organometallic compound, decomposes after the interaction with the Ga ions. The volatile organic impurities are released and removed by the FIB's vacuum system, leaving behind the desired metal deposited on the surface of the sample. Both beams, i.e., electron and ion can be used to decompose the organometallic gas resulting in a finer, however, slower or coarse but faster, deposition. A thin Pt layer was deposited before the TEM sample cut out to decrease the extent of sample damage during sample preparation.

TEM sample preparation by FIB

Thin transparent foils suitable for a number of TEM related investigations can be successfully produced using FIB technique [Giannuzzi04, 99, Orloff02].

The TEM samples from the $Zr_{55}Co_{23.5}Al_{23.5}$ bulk and splat samples were fabricated using ion milling. Fig 4.16 illustrates different steps of the ion milling for the sample preparation. The sample surface is coated with a 3 μm Pt layer to avoid severe surface damage to the sample because of the accelerated Ga ions (see Fig. 4.16a). This layer comprises of a primary electron beam deposited Pt layer followed by a coarser ion beam deposited layer. Two reference crosses are ion milled for pattern recognition during the automated milling process. Thereafter, 12 x 3 μm^2 thin lamella is prepared (as shown in the Fig. 4.16b) by trench milling on its both sides. The lamella is then cut free at its base and at both sides apart from one edge. The Omni probe is then inserted for careful handling and lifting out the lamella. The end of the Omni probe is Pt welded with one edge of the lamella and after Pt welding; the remaining part of the lamella is cut free. The Omni probe is retract and the lamella is then welded on a special Cu holder by Pt deposition, as shown in the Fig. 4.16d. Fig. 4.16e shows a sample ready for the TEM analysis.

TAP sample preparation by FIB

Recently, FIB has been utilised to make TAP samples from a wide range of materials [Larson98, 99, Miller05, Shariq06a]. During the course of this research work, FIB has been utilized for, a) final finishing of the TAP tips produced by conventional electropolishing techniques and (b) for making TAP samples from the $Zr_{55}Co_{23.5}Al_{23.5}$ splat samples.

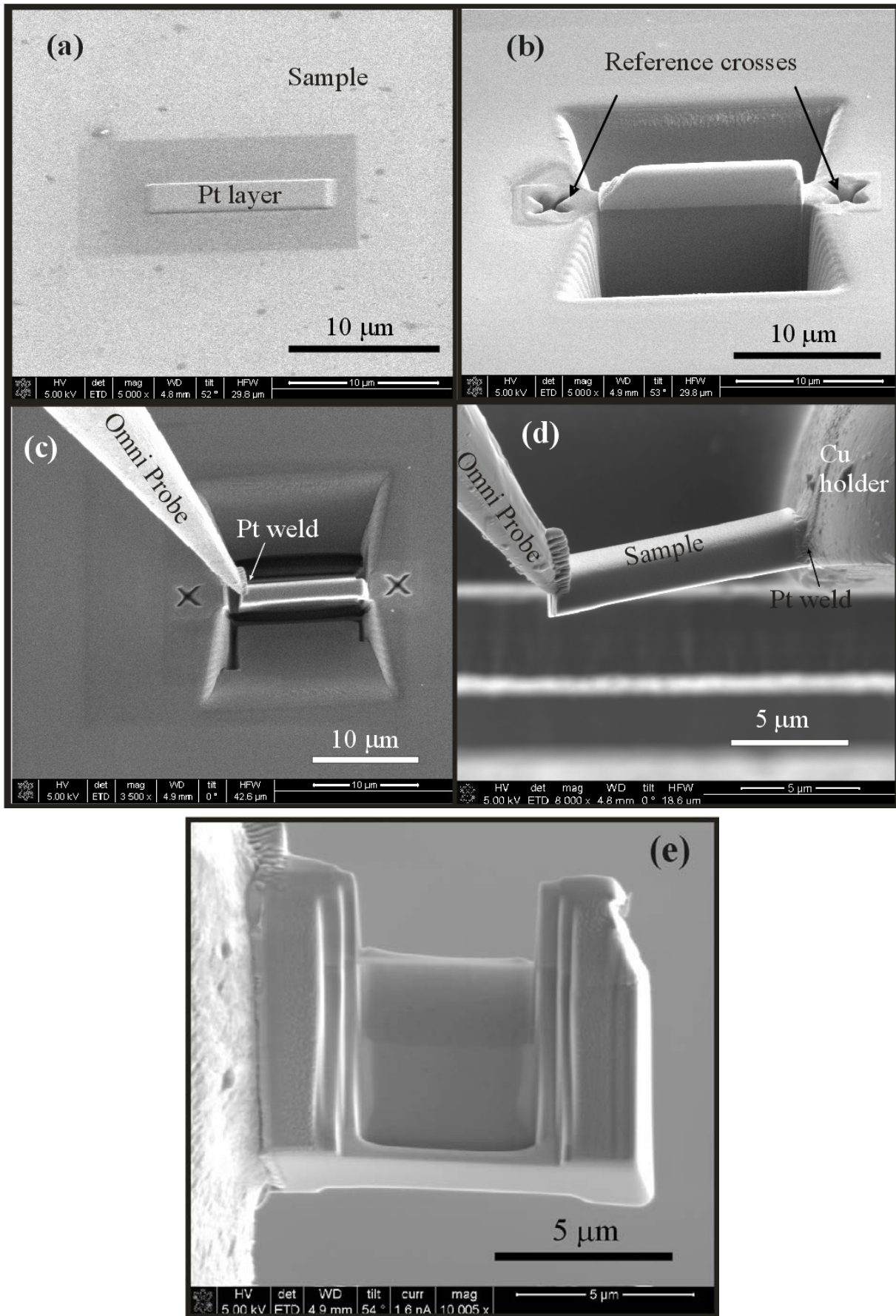


Figure 4.16 Different steps for the TEM sample preparation [Shariq06a].

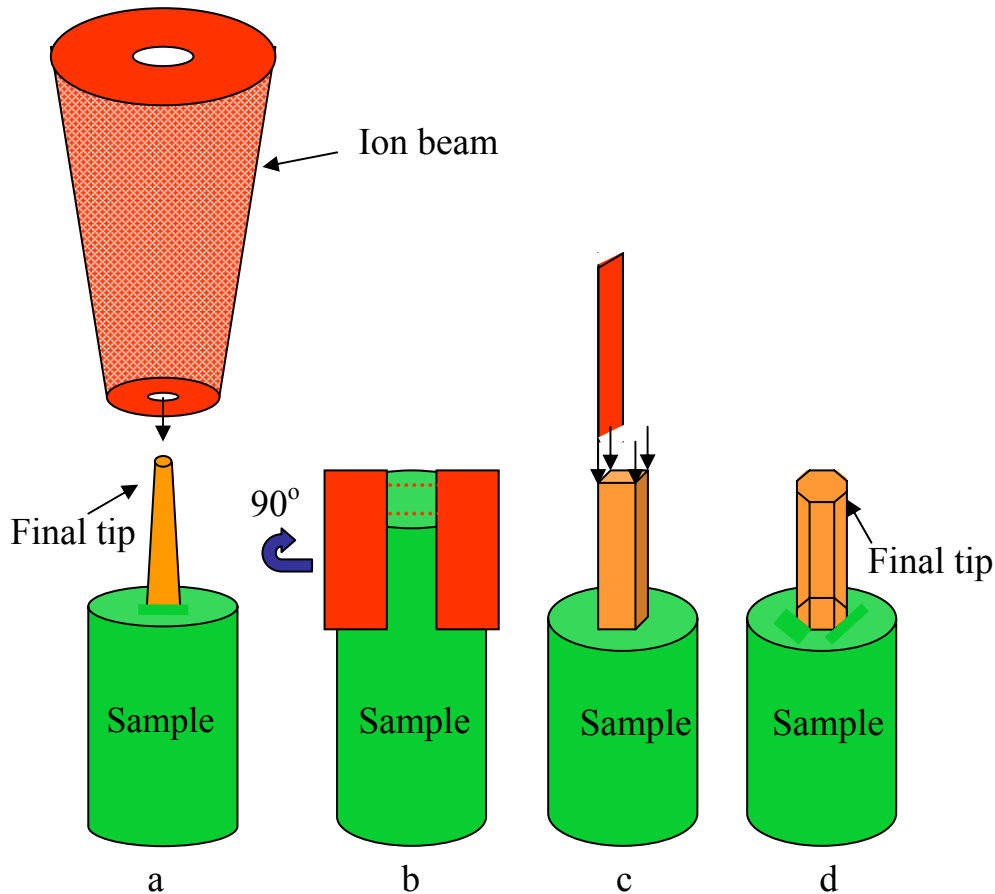


Figure 4.17 Different steps of the ion milling, (a) annular milling, (b) rectangular milling from the side of the tip, after side cuts the sample is rotated at 90° and followed by cut on the remaining two sides, (c) leaving a square blank on the top of the tip. Milling further the corners of the square, (d) an octagonal blank, can either be used as it is or final annular milling using a low voltage ion beam.

a) Final finishing of the electropolished TAP tips

The conventional electropolishing methods some times leave a complex oxide layer enveloping the outer surface of the tip that makes the sample even more brittle and difficult to analyse by TAP. Fig. 4.18a shows an electropolished tip of $Zr_{55}Co_{23.5}Al_{23.5}$ bulk sample, entirely covered by an oxide. A rectangular cross-section, as shown in the Fig. 4.17b has been used to remove this contaminated layer. Fig. 4.18b illustrates the thickness of the contaminated layer. The sample is, thereafter, rotated at 90° and continued rectangular milling gives an oxide free blank on the very top of the specimen. The annular ion milling, illustrated in the Fig. 4.17a, is used to get a final tip, as shown in the Fig. 4.18d with a diameter < 111 nm.

b) TAP tips by lift out

The TAP samples from metallic glass ribbons or splat are fabricated using the lift out method. The initial steps for getting a blank from the metallic glass sample are similar to the one for making a TEM lamella, as described above.

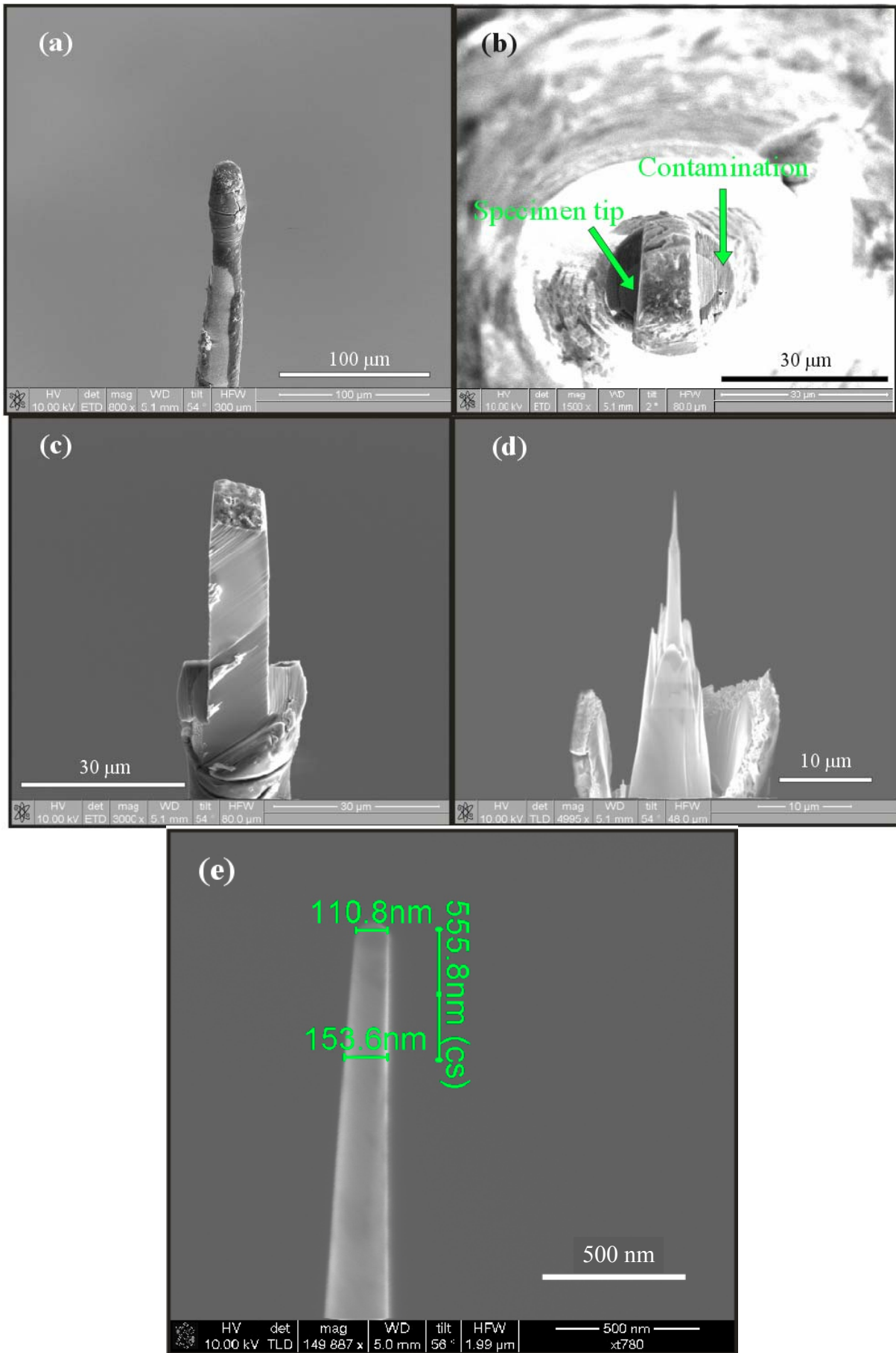


Figure 4.18 Different steps for the TAP sample preparation [Shariq06a].

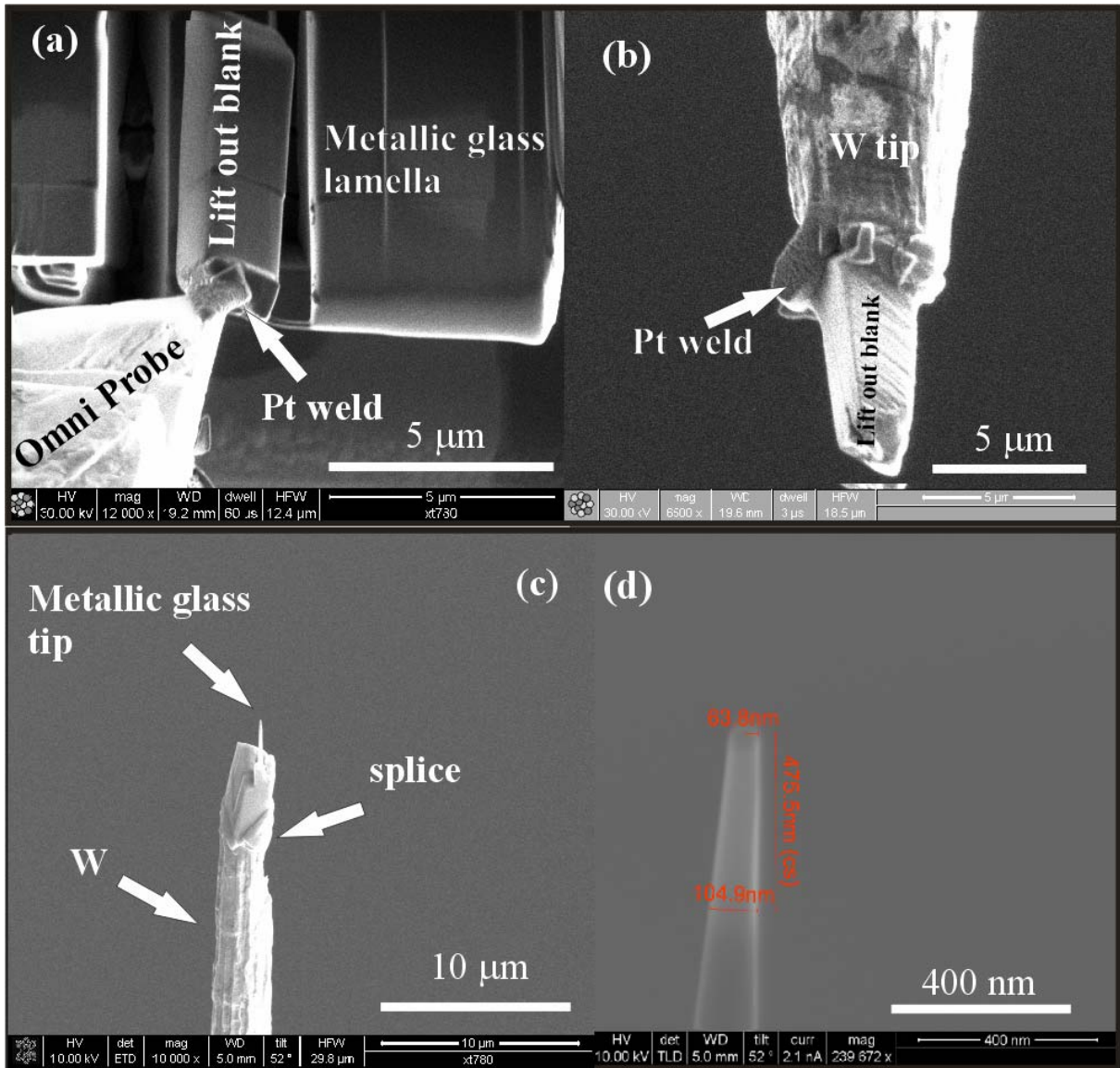


Figure 4.19 Different steps for the TAP sample preparation [Shariq06a].

Later, instead of putting the lamella on a Cu holder, it is welded on a W tip as illustrated in the Fig. 4.19b. After the Pt welding from all four sides, the square blank on the W tip is milled by cutting the sides of the square to have an octagonal blank as shown in Fig. 4.17d. Such sample can be used as it is or can further be milled by using a 10 KV ion beam, just to mill away the first 800-900 nm part to get a hemispherical tip with the requisite radius (i.e., < 100 nm).

4.6 Additional Analysis Methods

4.6.1 Transmission Electron Microscopy

Philips EM 420 ST TEM working at 120 KV equipped with a Noran system six, EDX system at the Institute für Materialphysik, was used for conventional transmission electron microscopy i.e., TEM imaging, electron diffraction and EDX analysis. However for high resolution electron microscopy,

Philips CM 200 FEG-UT TEM was utilized, working at 200 kV in the IV. Physikalisches Institut, Universität Göttingen. The main advantage of the later instrument is high resolution.

The analytical transmission electron microscopy i.e., EFTEM and EDX scans was carried out by utilizing the Gatan Imaging Filter (GIF) fitted to a Philips CM200 FEG equipped with a LINK EDX system in Experimental Physics department in Chalmers University of Technology, Göteborg, Sweden.

4.6.2 Superconducting Quantum Interference Device (SQUID)

The magnetic properties of the $Zr_{55}Co_{23.5}Al_{23.5}$ bulk and splat samples, in as cast/quenched state and for different heat treated conditions, were measured using the superconducting quantum interference device (SQUID). The SQUID magnetometer is the most sensible and best known commercial device for the characterization of the magnetic materials. The Quantum Design MPMS-5s⁴, in the I. Physikalisches Institut, Universität Göttingen, was used to perform magnetic measurements. Helium in the liquid state ($T \leq 4.2K$) is used for effectively cooling down the sample to low temperatures. The working principle of the SQUID is described in detail elsewhere [McElfresh94, Bracchi04]. The samples used for X-ray diffraction (§ 4.2) were also used for the SQUID magnetic measurements.

⁴ Mr. Dmitriy Bogdanov is kindly acknowledged for operating the SQUID.

Chapter 5

Amorphous structure and Structure resolving tools

This chapter mainly deals with the description of the atomic structure of amorphous materials, which is a nontrivial undertaking for a number of reasons. Firstly, the extensively used terminology for defining a structure in solid state physics, a unit cell, essentially for an amorphous structure lead to one containing an infinitely large number of atoms means a statistical description of the structure is inevitable. Secondly, the absence of any translational periodicity simply leaves out any possibility utilizing features associated with the mathematical treatment of, say, diffraction. Finally, the ambiguous picture of the structure of an amorphous solid exacerbate by the fact that for both microscopic and macroscopic levels, it essentially depends on the very minute details of the preparation procedures. In addition, this chapter is also dedicated to description of different modules used for structural description utilizing the TAP data. The raw data can be presented in different ways, e.g. as mass spectrum, time spectrum, composition profile, ladder diagram and cumulative diagram [Miller00, 89, 96]. The most common and frequently used modules are discussed very briefly; the modules developed and implemented such as Next Neighbourhood Evaluation (NNE) module during the present work are discussed in detail. The data treatment can be divided into two groups:

- Treatment focused on both steric and compositional considerations.
NNE module, Cluster search module and RDF module
- Treatment focused mainly on compositional considerations.
Compositional profile, Frequency distribution, χ^2 - test and Variation parameter.

5.1 Amorphous Structure

5.1.1 Pair and Radial Distribution Functions

The salient feature of an amorphous state is that it has, in essence, no microstructure and atoms are arranged more or less randomly, howbeit, there may exists regions of local order (SRO)⁵ owing to

⁵ Short range order

constraints imposed by the closed packing of atoms as the melt solidifies. Shortly, bulk amorphous alloys and metallic glasses are characterized by the absence of atomic long range order but possess topological and chemical short range ordering with a structural correlation length in the order of atomic distances [O'Handley87]. The topological structure describes the arrangement of atoms according to the constraint of filling the three dimensional space, while the chemical structure describes the mutual arrangement of the atoms of different components of the alloy system. Various scattering techniques i.e, X-ray, neutron and electron diffraction techniques have been used to address this issue. X-ray diffraction, though, is the most popular and extensively used for the structural analysis of the amorphous state. Diffraction occurs when the Bragg equation is satisfied, resulting in well-known diffraction patterns having sharp intensity peaks for crystalline structure. For amorphous materials, the unordered assemblages of atoms, however, interact with radiation in such a way as to produce a dispersed and nondistinctive pattern.

The most convenient description from the scattering experiments is the atomic pair distribution function, $g(r)$, define as the probability of finding another atom at a distance, r , from the origin atom taken as the point $r = 0$ [Waseda80, Ohsaka98].

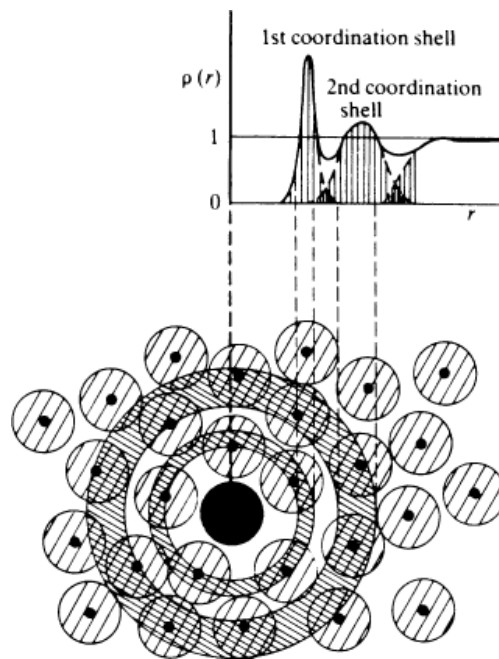


Figure 5.1 Schematic illustration of the structural origin of certain features in the density function $\rho(r)$ for an amorphous solid [Elliott90].

For a homogeneous system having an average number density, $\rho_o = N/V$ for N number of atoms, the probability of finding another atom at a distance r from an origin atom corresponds to:

$$\rho(r) = \rho_o g(r) \quad (5.1)$$

Albeit, the information given by $\rho(r)$ is only one-dimensional (Fig. 5.1), it is quantitative information on the amorphous systems obtained by three dimensional averaging procedures and as such, is one of the most important pieces of information in the study of amorphous materials. As a matter of the fact that the interatomic distances cannot be smaller than the atomic core diameters, hence,

$$g(r)_{r \rightarrow 0} = 0$$

For larger separations i.e., increasing r values; the correlation of atomic positions decreases and $\rho_o g(r)$ approaches to ρ_o , consequently:

$$g(r)_{r \rightarrow \infty} = 1$$

Thereby, system behaves as a structureless continuum. The radial distribution function, RDF, is used more frequently in description of amorphous structures. This function is defined as average number of atoms at distances between r and $r + dr$ from a given origin atom, is given as [Dixmier76]:

$$J(r) = 4\pi r^2 \rho_o g(r) = 4\pi r^2 \rho(r) \quad (5.2)$$

To elaborate the structural features, a reduced radial distribution function is calculated as given below:

$$G(r) = 4\pi r^2 [\rho(r) - \rho_o] \quad (5.3)$$

Radial distribution functions, RDF, pay no regard to atom type, and hence, partial radial distribution functions, PRDFs, are calculated for each elemental correlation. The RDFs can be obtained by Fourier inversion of the scattering data obtained in reciprocal space, from conventional scattering experiments using X-rays, electrons, or neutrons (Wagner83). Albeit, diffraction provides maximum amount of obtainable structural information for a monoatomic amorphous material, the information for multicomponent systems is much less easily interpretable. For a materials containing, n , elements, a total of $n(n+1)/2$ distinct pair correlation functions are needed to fully describe the structure. For this reason, different scattering techniques should be incorporated to describe the structure. Though, a combination of different scattering experiments enabled to calculate reduced radial distribution functions and hence, partial reduced radial distribution functions for simple binary metallic glasses, the task becomes increasingly complex for amorphous alloys containing more than two constituent elements.

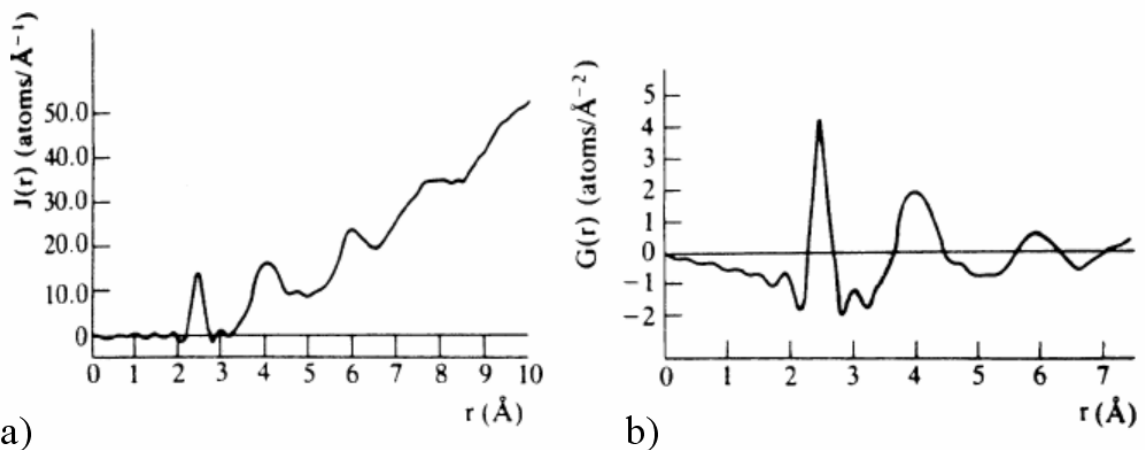


Figure 5.2 Structural correlation functions obtained by x-ray diffraction for sputtered a -Ge films (a) RDF; (b) reduced RDF [Temkin73]

An example of RDF and consequently, RRDF of amorphous a -Ge film is illustrated in Fig. 5.2 [Temkins73]. The first peak in the radial distribution function indicates the nearest neighbour separation and integrating the first peak along with appropriate geometrical factors yields the average

coordination number. The coordination number, Z , which is defined as the number of atoms surrounding an origin atom at a particular distance corresponding to the following relation:

$$Z = \int_{r_1}^{r_2} 4\pi r^2 \rho(r) dr \quad (5.4)$$

where r_1 and r_2 corresponds to the inner and outer radii of the shell under consideration. The coordination numbers are typically in the range 11.5 to 14.5, indicating that metallic glasses are densely packed, as would also be indicated by an extrapolation of liquid properties. Though, valuable information is received from RDFs, they provide no information on the angular distribution of interatomic vectors.

5.1.2 Structural models

The first structural model suggested for metallic glasses was most probably based on the hypothesis that the structure of metallic glasses constitutes microcrystallites. An anstaz, that suggests, the glass is nothing else than a polycrystalline solid having very small grain size. However, early work by Cargill showed evidently that the microcrystallite model does not corroborate with RDFs of glasses [Cargill70]. Other, adapted structural models based on either the dense random packing, DRP, model of Bernal [Bernal64], or the local-coordination model of Gaskell [Gaskell79].

Bernal enunciated a relatively simple model exploiting the DRP of hard spheres of same diameter and it was based on physical measurements with steel balls kneaded in a rubber bag. The structure can thereby be considered to be made up of only five simple polyhedra as shown in Fig. 5.3. The DRP has some geometrical links with the continuous random network model [Zachariasen32] familiar for oxide glasses. When amorphous structures are composed of more than one element, the Bernal model is generally not adequate due to atomic size differences and chemical short-range ordering.

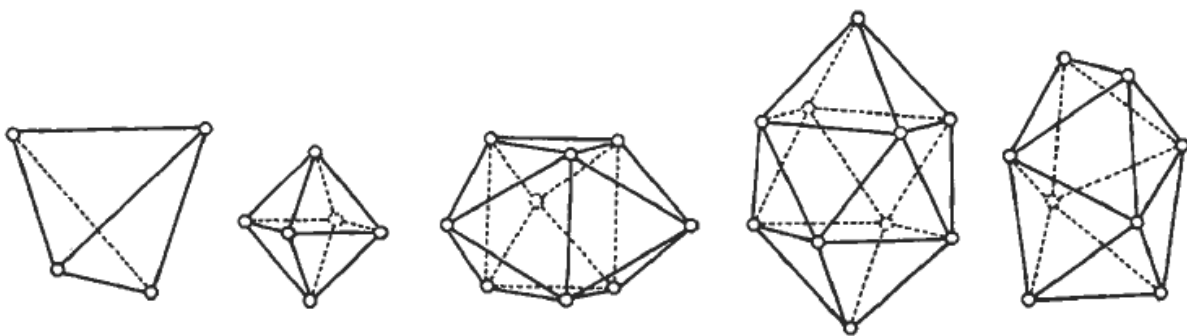


Figure 5.3 Polyhedra formed by dense random packing of hard spheres, according to Bernal [Cahn96].

Polk extends Bernal's model to a transition metal-metalloid (TM) glasses, which suggested that the metalloid sits in the larger interstices of the DRP array of the metal atoms [Polk70]. However, in the DRP structure, the number of holes having appropriate size to accommodate all the metalloid atoms was far too small in the typical glass forming range composition. Gaskell enunciated a model for metal-metalloid glasses called local coordination model [Gaskell79]. This model essentially deals with constraining the nearest neighbour coordination (typically nine nearest neighbour metal atoms) to

trigonal prisms⁶ (Fig. 5.3), and is analogous in crystalline compounds of similar composition. A varying atomic size ratio will determine the ways in which the trigonal prismatic units are linked to each other as illustrated in Fig. 5.4. Gaskell proposes that the glass structure is a non-periodic array of such prisms. Computer models assembled accordingly and then relaxed under appropriate atomic potentials give rather good fits to measured distribution functions. The second nearest neighbour metal-metal distance in measured PRDFs can correspond distinctly to one or the other of the distances expected from the types of linkage in Fig. 5.4. Thereby, suggesting considerable medium-range structural orders in addition to the short-range order; evident from prisms network.

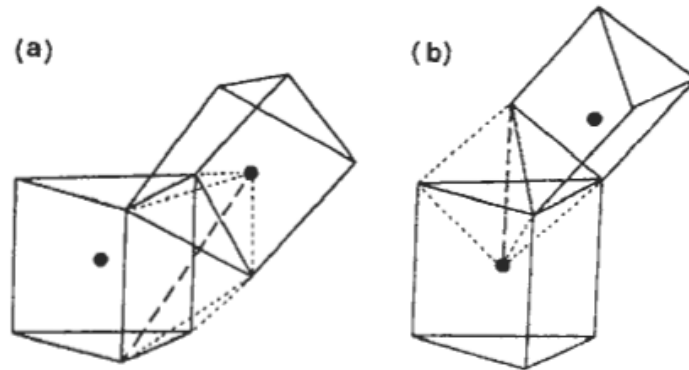


Figure 5.4 Packing of trigonal prisms as found in (a) Fe_3C and (b) Fe_3P . Each prism has a metalloid atom at its centre. The long-dashed line indicates the second-nearest metalloid-metal distance in each case [Gaskell83].

Dubois suggested a chemical twinning model, a step further to the local coordination model (some what analogous to crystalline twinning process) [Dubois85a], who enunciated that trigonal prismatic coordination can also be applied to many metal-metal compounds. According to the model, glass-forming ability should be greatest for coexistence of competing types of twinning in the alloy. This idea has been used in developing new glass forming compositions in aluminium-based alloys [Dubois85a]. Moreover, strong icosahedral component in the nearest neighbour configurations are also reported in structural studies of amorphous state. A sub-class of aluminium-based systems shows somewhat icosahedral coordination. Though, on annealing some aluminium-based glasses form non-icosahedral crystalline phases that are explained by the chemical twinning model for glasses in a good agreement with the RDFs. A detailed study of structural models is reported elsewhere [Finny83].

5.2 TAP data treatment focused on both steric and compositional considerations

5.2.1 Next Neighbourhood Evaluation Module

The atomic structure is the basis for understanding the nature of all states of matter. The lack of periodicity in glassy structures pushes scientists to use statistical tools for the description of the structure of amorphous alloys. The structural information of amorphous alloys can best be represented

⁶ giving six nearest neighbours; with three more, slightly further away in the next trigonal prism.

in terms of a radial distribution function (RDF). The complex nature of the calculations for multi-component systems makes it rather difficult to elucidate any experimental results, in particular for the estimation of the partial distribution of the different species in such alloys. Furthermore, RDF's give only spherical averaged information on correlations in atom positions without specifying the unique atom positions and chemical identities of atoms for amorphous materials especially for multi-component systems. During the course of this work a new algorithm is developed to extract information about the next neighbourhood atomic vicinity from the TAP data. This algorithm is utilized to specify atom positions and chemical identities of atoms for amorphous materials which are difficult to access alone from RDF's. Using this algorithm, solely TAP experiments enabled us to find all possible correlations for different elements of multi-component systems.

Next Neighbourhood Evaluation (NNE) algorithm

The Next Neighbourhood Evaluation (NNE) algorithm is very similar to the one used for the radial distribution function (section 5.2.3). Fig. 5.5 shows a schematic representation of the processing of the NNE algorithm.

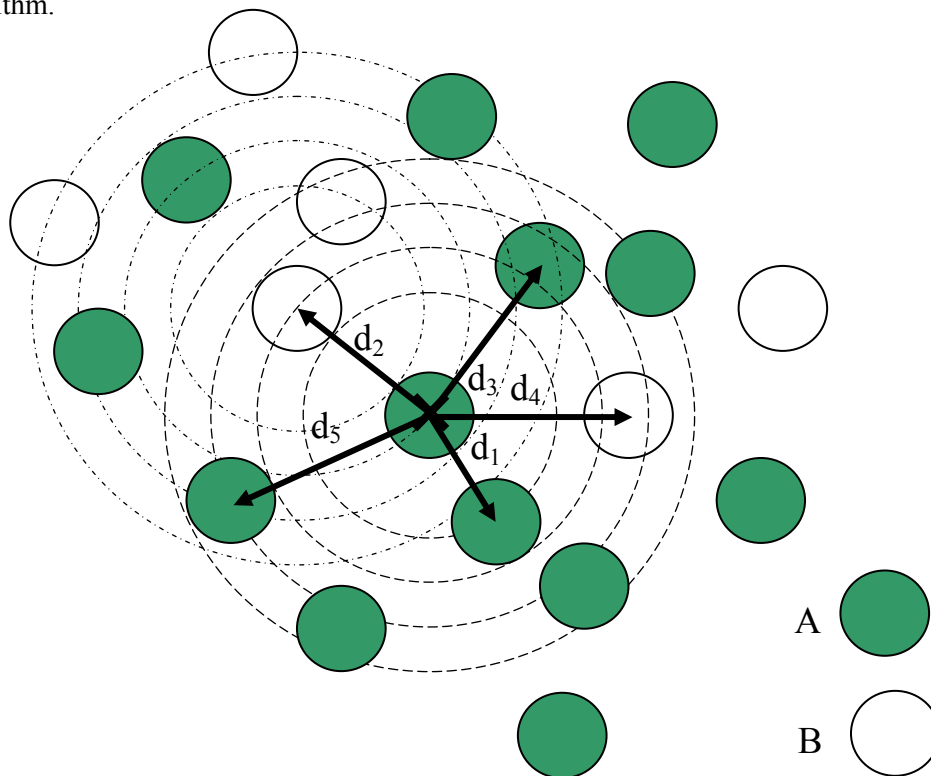


Figure 5.5 Basic principles for the calculation of next neighbourhood evaluation module.

Atom A with a cross in the centre is chosen as a start atom of a specified volume. Then, the distances and chemical nature from this atom to every other atom in the selected volume are calculated. The neighbouring limit can be chosen to be 1000 or 1500 atoms. These distances are then listed in the ascending order, along with the relative chemical nature to that of the start atom. Similarly, the next atom is then selected as a start atom (atom B in the centre of the dot-dashed circles in Fig. 5.5) and the

same procedure is repeated until the whole selected volume is processed. The distances and chemical nature of the neighbours of all atoms are then summarized in a table containing information of the first 1000 or 1500 neighbours of each atom. The experimental histogram of any neighbour can be then drawn. The distance for the maximum of such histogram gives us the maximum probability of finding an atom.

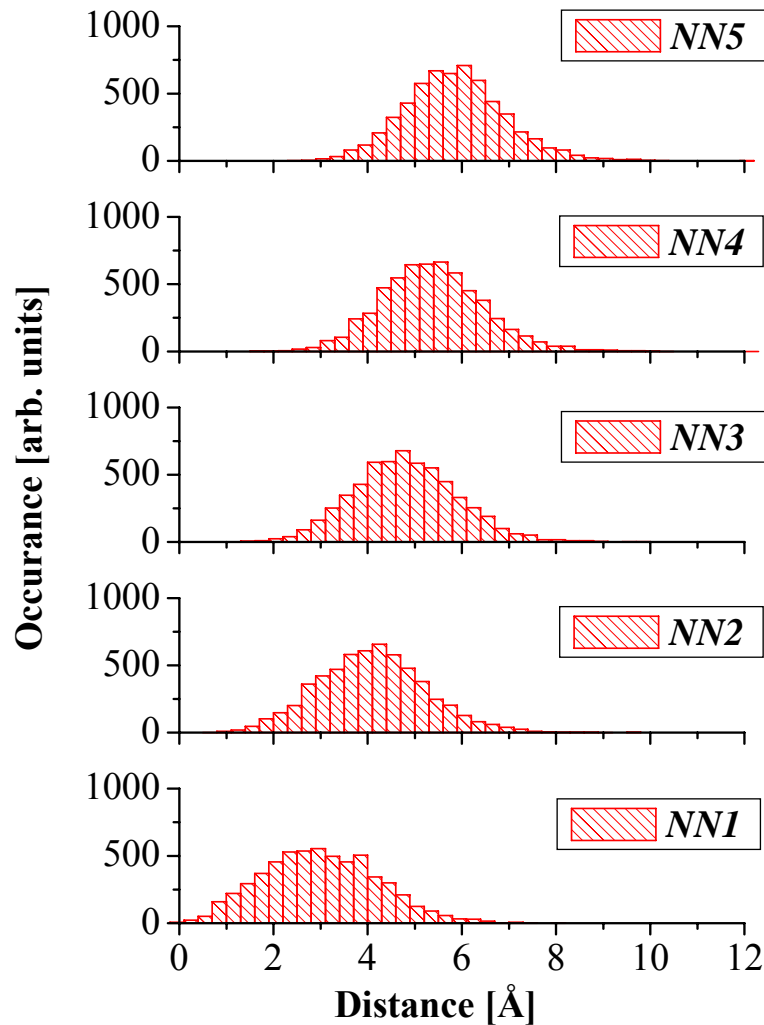


Figure 5.6 Histogram calculated using NNE algorithm for $\text{Pd}_{55}\text{Cu}_{23}\text{P}_{22}$ bulk amorphous alloy showing the distance distribution of first five next neighbours for Cu-Cu correlation.

Fig. 5.6 illustrates the histogram for Cu-Cu elemental correlation in the analysed volume of $\text{Pd}_{55}\text{Cu}_{23}\text{P}_{22}$. The experimental histograms are drawn for the first five neighbours, chosen for simplicity. In the histograms, the distribution of the distances of the next neighbouring atoms are denoted as NN_i . The occurrence of the distances for all neighbours follows a Gaussian distribution. This distribution provides the information about the probability of finding the first five neighbouring Cu atoms at certain distances. This figure also reflects the experimental errors in positioning where the peaks are broadened considerably in comparison to the expected ideal peak distribution. Since, the interatomic distances in a given reconstructed volume may as well depend on the detection efficiency, a slight shift in the position of the peak may also occur, as a consequence.

If $p(r)$ is a true distribution of the 1st next neighbour distance and $p^o(r)$ is its apparent distribution due to the experimental broadening, then the relation can be described mathematically as:

$$p^o(r) = \int d^3 r' s(\bar{r} - \bar{r}') p(r') \quad (5.5)$$

Where, $s(\bar{r} - \bar{r}')$ represents the experimental broadening of the atomic distribution. As a matter of fact, two atoms cannot occupy a position less than their average diameter, the distribution of the 1st neighbour should start from a critical distance r_c rather than from 0 as shown in Fig. 5.7 for 1st next neighbour (NN1). Another important parameter is the value of the full width at half maximum (FWHM). The experimental broadening, $s(\bar{r} - \bar{r}')$ leads to a higher value of the FWHM than reality. One of the major factors leading to the experimental broadening is detection efficiency (i.e., 50%). Higher detection efficiency will result in higher number of atoms in total, to which the averaged NNs will be more precise, as represented by the ideal distribution in the Fig. 5.7. Nevertheless, the peak positions in these distribution plots give important information about the distances of the next neighbours.

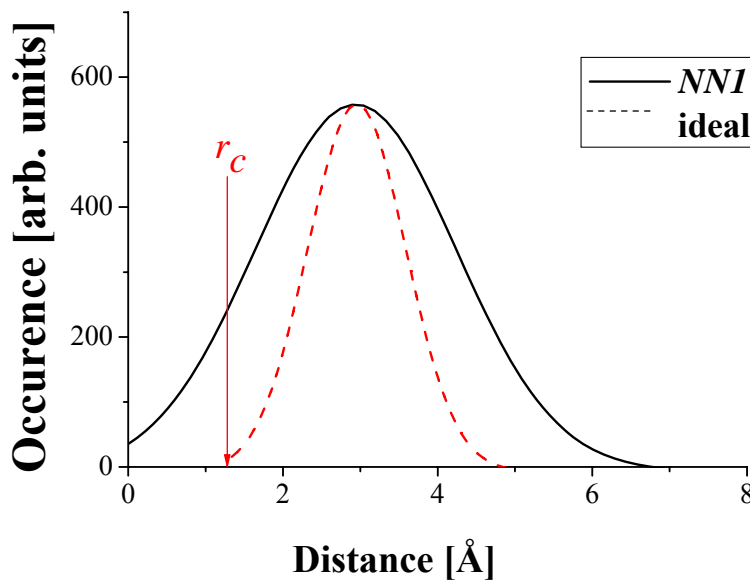


Fig. 5.7 Schematic illustration of the experimental next neighbour's distribution broadening and an ideal distribution for the first next neighbour.

The Gaussian fit for all five next neighbours for Cu-Cu correlation, as depicted in the histograms in Fig. 5.6, gives the probability of finding first five neighbouring Cu atoms at certain distances and are illustrated in Fig. 5.8. This figure is a reproduction of Fig. 5.6, after a Gaussian fit. The maximum of this peak gives us the maximum probability of finding relative Cu atoms which is the same as the average of all the distances of the first neighbour atoms. Similarly, the distribution of the next neighbouring atoms for other elemental correlations can be calculated by processing this algorithm.

The full width at half maximum (FWHM) shows the following trend;

$$\text{FWHM for } NN1 > NN2 > NN3 > NN4 > NN5$$

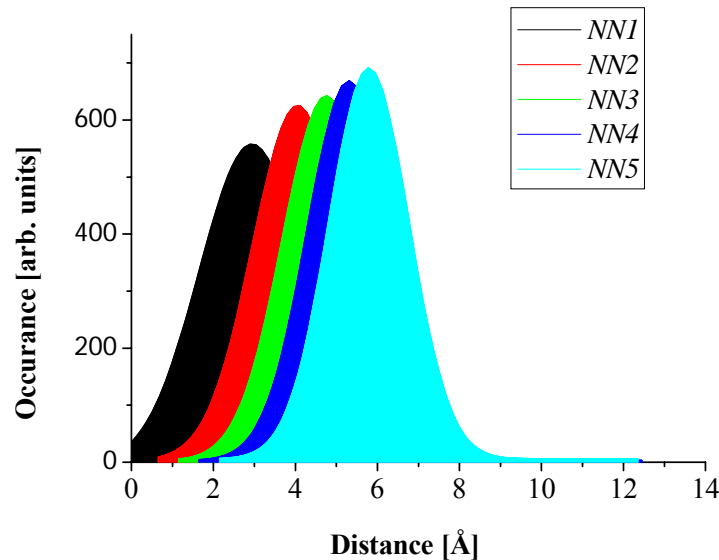


Figure 5.8 The distance distribution of first five next neighbours for Cu-Cu correlations after Gaussian fit. The distances assigned as $NN1$ shows the distance distribution of next neighbouring atom for the Cu-Cu correlation. The probability of finding the first five next neighbours are presented here.

This relation reveals that the distribution for $NN5$ has the smallest error among all of them. The experimental limitations in TAP analysis (i.e., detection efficiency, depth and lateral resolution, localised effect of field evaporation, etc.) result in smearing individual next neighbouring atomic distributions leading to strong overlapping (Fig. 5.6). This comparison also provides plausible explanation of the inability to reveal any detailed structure in the RDFs⁷ due to the pronounced overlaps in NN 's atomic distributions. Albeit, there is no problem in differentiating individual NN distributions which is evident from Fig. 5.6 (experimental histograms), the smearing effect however pose greater uncertainty in differentiating coordination shells in the RDFs. Similarly it is possible to make a comparison of FWHM among the different correlations. The distances of maximum occurrence of each distribution give the maximum probability of finding a respective atom at those distances.

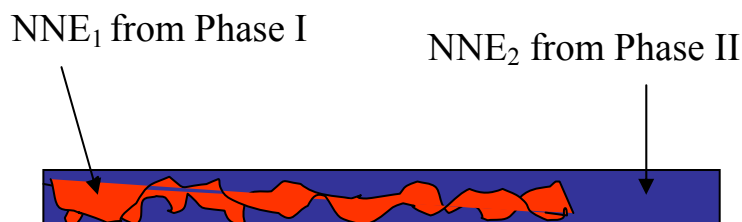


Figure 5.9 Schematic illustration of the sampling effect of two phase structure on the overall NNE.

A careful selection of the analysed volume is needed for NNE module. The NNE results will be different for two different phases as shown in the Fig. 5.9. The net NNE_{av} will be different than both NNE_1 and NNE_2 . Therefore, other statistical tools should be utilized (e.g., χ^2 -test) to see if the sample is random solid solution or not. Particularly, for amorphous alloys if the sample is heat treated even

⁷ Described in detail in chapter 6 § 1.4.

below the crystallization temperature, there can be a change in the short range ordering that can affect the NNE_{av} value. Apart from the selection criteria of the analysed volume, different experimental parameters such as F_oK_f factors and atomic volume Ω_{av} [Miller89] can also affect the NNE value. A detailed comparison of the next neighbouring atomic distances calculated by processing the NNE algorithm on atomic reconstructions for different F_oK_f factors and for different average atomic volumes (Ω_{av}) is described in the next chapter. A wrong Ω_{av} and F_oK_f parameters can result in a shift of all distributions to higher or lower distances. Moreover, an analysis with the high noise level also lead to a wrong NN evaluation. Positions of other atoms are effected in the analysis with the high noise level, even if the noise is deselected using the AVS program.

Comparison with typical radial distribution function

The best explanation for these results will be making a comparison with well established radial distributions known from different diffraction techniques. Fig. 5.1 illustrates a typical radial distribution function for amorphous alloys showing 1st and 2nd coordination shells. However, in the case of NNE instead of cumulative shell, exact distances of each next neighbour contributing to respective coordination shell can be described. Hence, $NN1$, $NN2$ and/or $NN3$ are contributing to the 1st coordination shell and the remaining ones ($NN4$, $NN5$ etc..) can be a part of next coordination shell. Hence, this algorithm not only provides the information about the distance but the chemical nature of the atom as well.

5.2.2 Cluster search Module

In three dimensional atomic reconstruction maps, phases differing in composition can easily be distinguished. However, for early stage of decomposition or small clusters it is extremely difficult to distinguish them from the matrix. For the detail characterization of the clusters and early stages of the decomposition an algorithm based on TAP data has been developed by Kluthe, Wolde and Heinrich [Kluthe03, Wolde03, Heinrich03] in the Institut für Materialphysik, Universität Göttingen.

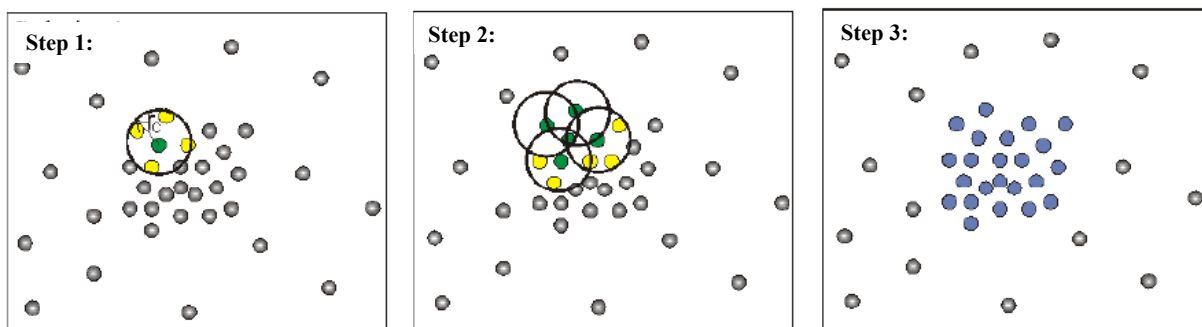


Figure 5.10 Different steps for assigning the cluster using cluster search module [kluthe03]

To process the cluster search module, a critical distance is assigned for cluster search, then an atom is chosen as the start atom in the selected volume, as soon as another atom falls within this critical

distance, it marks it as a part of a cluster (see Fig. 5.10 green atom in step 1). The algorithm searches again for the next atom from that atom i.e., yellow atoms. The procedure is repeated till there comes no more atoms in the radial vicinity of the critical radius. After the whole procedure, all atoms marked green are assigned to one cluster (blue in step 3). Other parameters that can be selected for the cluster search are minimum number of atoms exceeding which, one can assign the agglomerate as a cluster (a threshold value). The threshold value is another parameter to identify statistically significant clusters correctly. It is also highly recommended to verify the results from the cluster search module by characterizing samples with other high resolution techniques such as HRTEM or CFIIT etc. More details are given elsewhere [Heinrich01, Kluthe03, Wolde01].

5.2.3 “Radial Distribution Function” Module

After reconstruction of the analysed volume from the TAP data, the three dimensional atomic position of each detected atom is known. Heinrich developed an algorithm to calculate the radial distribution function from this data. The algorithm developed to determine the radial distribution function is relatively simple. First atom in a selected volume is selected as the start atom (see Fig. 5.11).

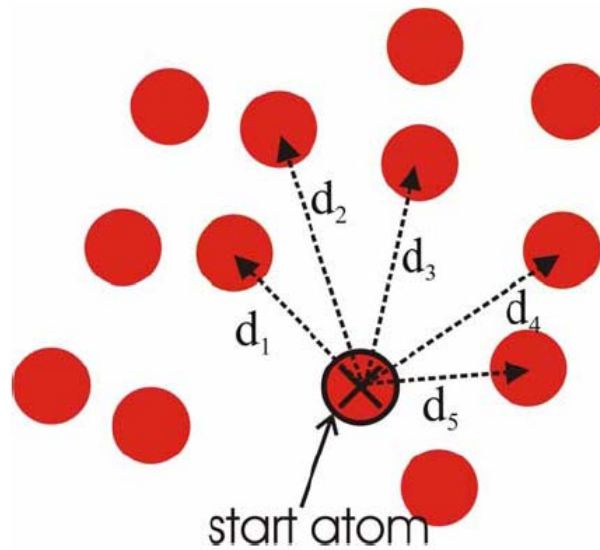


Figure 5.11 The basic principle of “radial distribution function” algorithm.

The distances of all other atoms to the start atom are then calculated. Thereafter, all atoms are sorted out in ascending order according to the distance to the start atom. In the next step, next atom (to the start atom) is selected and the same procedure is repeated. The algorithm is processed for all the atoms in the selected volume. The out come of the complete cycle of the algorithm is that the distances from each atom to all other atoms are known. Then occurrence of atoms for any distance can easily be calculated. The frequency of finding the atoms at an interval of 0.01 nm distance is calculated. This is analogous to putting a spherical shell around each atom and calculating the frequency of finding another atom. The main advantage of such a module is the calculation of a RDF for any multi-

component system. In addition, elemental selection is possible to calculate partial radial distribution functions. A detailed explanation is given by Heinrich [Heinrich05].

5.3 TAP data treatment mainly on compositional considerations

5.3.1 Composition profile

One of the most common forms of data representation is composition profile (also known as concentration profile). These profiles are used for detecting a second phase present in the analysed volume; to estimate concentration differences, to detect the solute segregation and/or to study the diffusion in the layered structures. The volume of interest is selected within the three dimensional analysed volume. The size of the selected volume depends on the feature of interest. This volume is then divided into smaller slices perpendicular to one of the axes of the selected volume. The slice size can be defined as a fixed number of atoms (called block size) or distance. This information can be presented in a number of ways such as, composition as a function of blocks or number of ions or depth of the analysis. A suitable block size has to be chosen depending on the feature of interest. A large block size reduces the statistical errors. However, it should be small enough to elaborate significant changes in composition rather than smoothing it. Too small block size leads to statistical errors making the interpretation difficult.

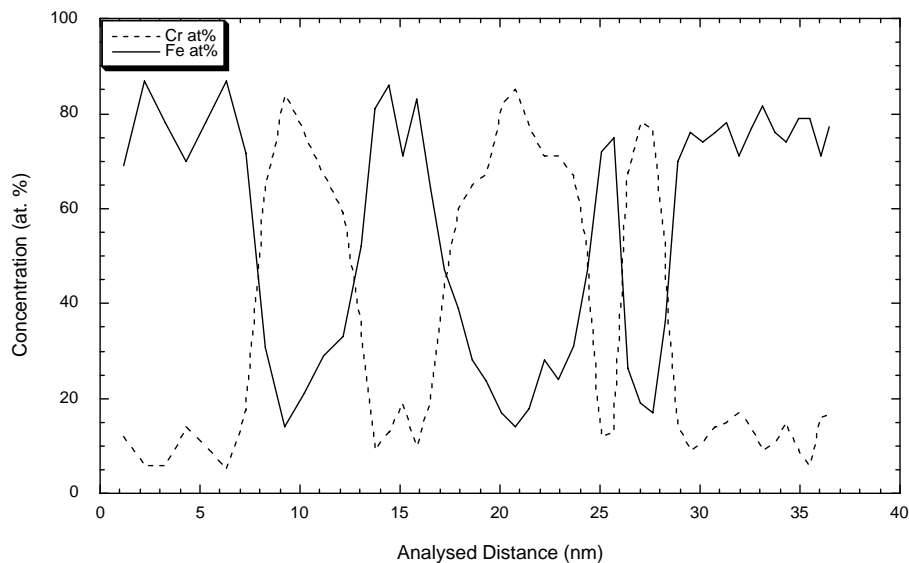


Figure 5.12 A composition profile of Fe-29% Cr superduplex stainless steel aged at 450°C for 243hrs showing the variation of Fe rich α and Cr rich α' phases due to the spinodal decomposition [shariq03].

An example of a composition profile is shown in Fig. 5.12. The figure shows the variation of Fe and Cr concentration as a function of the analysed distance with a block size of 100 ions. Concentration profiles can thereby be used to reveal information regarding composition and distribution of a particular phase or average wavelength and amplitude of compositional modulations.

The analyzed distance in the composition profile is calculated on the basis of the equation 4.3. The value of k_f varies from specimen to specimen, hence can result in some inaccuracy in the calculation of the analyzed distance. The correct distance can be determined by taking TEM images of the same specimen before and after analysis and measure the difference. This, however, calls for an interruption of the analysis before the specimen flashes, which is often difficult to achieve in practice.

The concentration of an element “A” in atomic fraction is given by:

$$c_A = \frac{N_A}{N} \quad (5.6)$$

Where N_A is number of ions of element A and N is total number of collected ions.

The standard deviation σ is given as under:

$$\sigma = \sqrt{\frac{c_A(1-c_A)}{N}} \quad (5.7)$$

Where c_A = mean concentration of solute atom A.

5.3.2 Frequency distribution & a comparison with the binomial distribution

Large-scale variations can easily be interpreted from the composition profiles. However, for small-scale variations it is difficult to use concentration profiles to interpret any variations. A frequency distribution (FD) of the concentration profile might reveal fine scale features such as very early stages of decomposition or any inhomogeneity present. If the atoms in a solid solution are distributed randomly, the probability of finding an ion being species A is the same as the concentration of A in the material. Hence, a frequency distribution from a random solid solution follows the binomial distribution (BD). Frequency distribution for n solute atoms, $F(n)$ in terms of probability $P(n, N_b)$ of detecting n solute atoms in blocks containing N_b atoms is given by:

$$F(n) = n_F P(n, N_b) = n_F \binom{N_b}{n} p^n q^{N_b-n} = n_F \frac{N_b!}{n!(N_b-n)!} p^n q^{N_b-n} \quad (5.8)$$

Where n_F is the total number of fixed size blocks, p is probability of success estimated from the mean solute concentration and $q=1-p$. For materials having some concentration variations e.g. spinodal decomposition, segregation, clustering or some precipitates, the frequency distribution will become broader compared to the binomial distribution. For very high variations it can even consist of well-separated peaks corresponding to different phases. Frequency distributions of the ordered materials on the other hand will be narrower than the binomial distribution. Apart from the information extracted from the shape of frequency distribution, the mode (most numerous) and median concentrations may be directly determined from this distribution (i.e., Fig 5.13 reveal that the Cr depleted phase α has Cr concentration ~15% against Cr rich phase i.e., α' ~75%). To construct a frequency distribution, the obtained data is divided into smaller blocks as for concentration profiles. A histogram chart is then plotted presenting the frequency of finding a certain amount of an element in each block as a function

of concentration of that element. Such a plot for materials showing phase-separation caused by spinodal decomposition is shown in Fig 5.13.

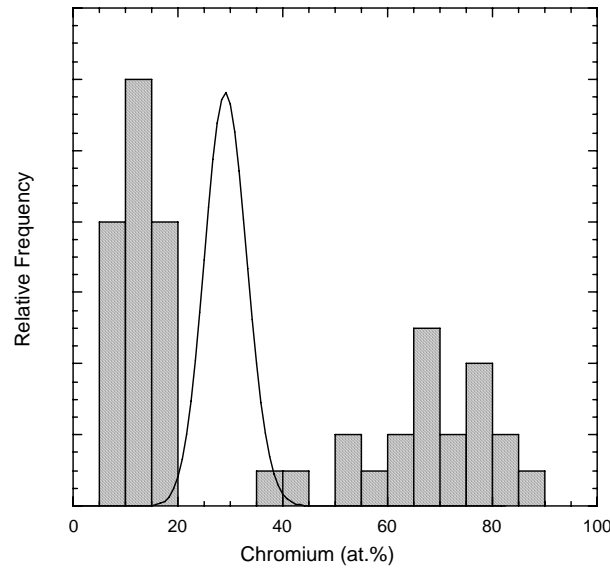


Figure 5.13 Frequency distribution of the chromium concentration of 100 ion blocks of atoms from Fe 29% Cr sample (same sample as for Fig 5.8) aged for 243 hrs at 450°C, with a superimposed binomial distribution of the Medium N material. [shariq03]

5.3.3 χ^2 - Test

The extent to which the distribution is far from the binomial distribution (i.e., homogeneous or heterogeneous) can be ascertained by calculating the χ^2 -test. It can be calculated as:

$$\chi^2 = \sum_{n=0}^{n'} \frac{(F(n) - B(n))^2}{B(n)} \quad (5.9)$$

Where $F(n)$ is experimentally observed frequency distribution of a class, $B(n)$ is binomial distribution (expected distribution from a random solid solution) of a class and n' is number of classes. For a reliable statistical analysis, the expected number of observations ($B(n)$) in each class should be sufficiently large. To fulfil this requirement, the classes with smaller $B(n)$ values are combined into one class (both the experimental and the expected observations should be combined).

For a random solid solution, the null hypothesis is that the observed distribution $F(n)$ is consistent with the hypothesized binomial distribution. The null hypothesis is rejected if the value of χ^2 exceeds the tabulated α percentile of χ^2 of the same degree of freedom ($n'-1$) which means that the sample is not homogeneous. Where α is the level of the significance chosen for testing the hypothesis, 5% was chosen in this work. The value of calculated χ^2 greater than tabulated χ^2 value means that atoms are not distributed homogeneously.

Chapter 6

Results and Discussion

This chapter is dedicated to experimental findings, related to structural, thermodynamical and magnetic properties of different amorphous states. The first section deals mainly with Pd based bulk amorphous alloys; an ideal amorphous material for a detailed inquest into different attributes of the novel next neighbourhood evaluation module¹ developed and implemented during the course of this research work. The next section reveals intriguing results from the studied Fe based metallic glass. The next neighbourhood evaluation module enabled us to characterize primordial stages of the devitrification. The final section divulges copious, albeit, enumerated results of thermodynamical, microstructural and magnetic investigations of the $Zr_{53}Co_{23.5}Al_{23.5}$ amorphous alloys.

6.1 Pd₅₅Cu₂₃P₂₂ Bulk Amorphous Alloys

6.1.1 Thermal characterization by DSC

The thermal stability of the investigated Pd₅₅Cu₂₃P₂₂ amorphous alloy was revealed by the DSC scan; a glass transition temperature (T_g) at 263°C and the onset crystallization temperature (T_x) around 317°C depicted from the Fig. 6.1. A single but pronounced crystallization peak (T_p) is recorded at 332°C. These temperatures are in a good comparison with the DSC experiments carried out by Miller on Pd₅₀Cu₃₁P₁₉ amorphous alloy with slightly different composition. He has reported a T_g at 269°C and start of crystallization T_x at 315°C [Miller03].

¹ Described in detail in chapter 5 § 2.1.

6.1.2 Structural characterization by TAP microscopy

A uniform field ion micrograph of the as cast $\text{Pd}_{55}\text{Cu}_{23}\text{P}_{22}$ bulk amorphous alloy is illustrated in Fig. 6.2. No crystalline poles, typical for the crystal structure, were recorded in the FIM micrograph.

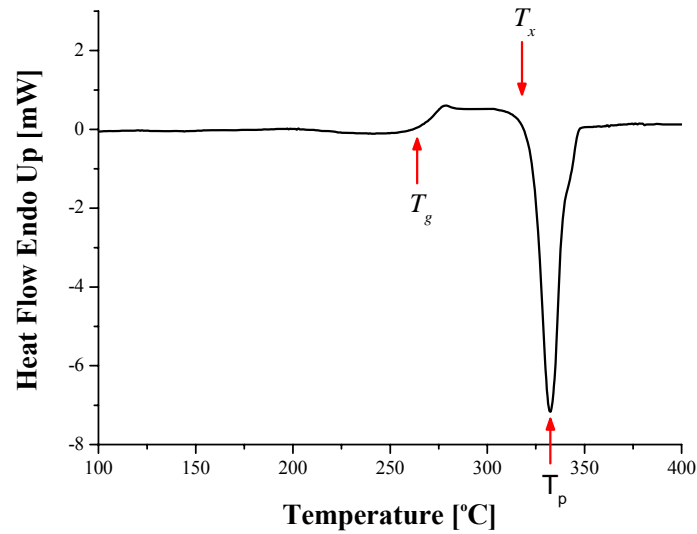


Figure 6.1 DSC trace for $\text{Pd}_{55}\text{Cu}_{23}\text{P}_{22}$ bulk amorphous alloy, taken at a heating rate of $20^\circ\text{C}/\text{min}$.

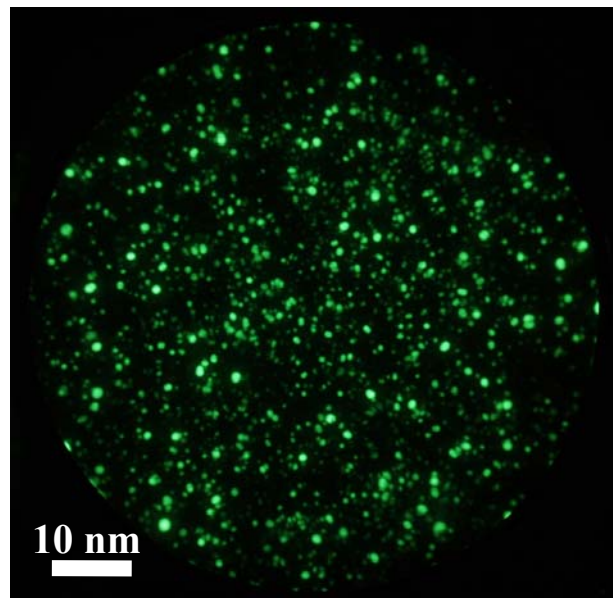


Figure 6.2 Field ion image of the $\text{Pd}_{55}\text{Cu}_{23}\text{P}_{22}$ bulk amorphous alloy.

Fig. 6.3 reveal the three dimensional atomic reconstructions of the as cast $\text{Pd}_{55}\text{Cu}_{23}\text{P}_{22}$ bulk amorphous alloy. Apparently, it exhibits a single homogeneous randomly distributed phase which is also quite evident from the concentration profile drawn in Fig. 6.4. Mean concentration value of each constituent (\bar{c}) and respective 2σ values are also indicated in the respective profiles. There is no palpable concentration variation recorded in the compositional profile for any element. To corroborate the homogeneous distribution, χ^2 test has been processed on the analysed volume. Table 6.1 reveals the χ^2 values calculated for each constituent element, alongside the χ^2 alpha values with 0.05 significance level of alpha.

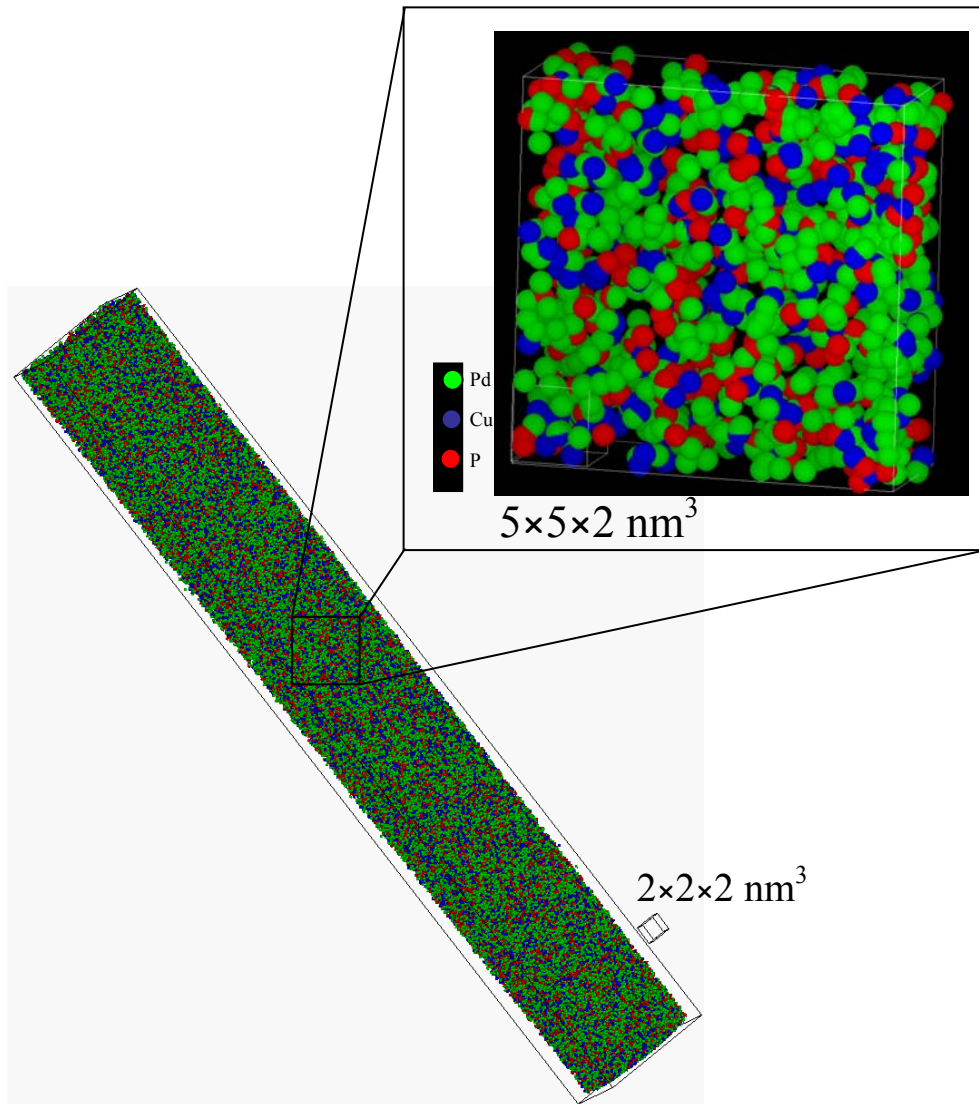


Figure 6.3 Three dimensional atomic reconstruction of $12.3 \times 12.3 \times 94 \text{ nm}^3$ analysed volume for $\text{Pd}_{55}\text{Cu}_{23}\text{P}_{22}$ bulk amorphous alloy.

A graphical comparison of the frequency distribution of the experimental data and that from a binomial distribution with the same mean concentration is plotted in Fig. 6.5. The experimental frequency distribution for each constituent follow the corresponding binomial distribution scaled for similar concentration and reveals no pronounced deviation from a random solid solution, as also corroborated by the χ^2 values presented in the table 6.1. The χ^2 values for each constituent element are smaller than the corresponding χ^2 alpha values, divulging the probability of a homogeneous elemental distribution.

Table 6.1 Summary of the calculated χ^2 values for the $\text{Pd}_{55}\text{Cu}_{23}\text{P}_{22}$ bulk amorphous alloy. The value of χ^2 alpha is also given for comparison, with the significance level of alpha i.e., 0.05.

	Pd	Cu	P
χ^2	27.7	27.1	35.7
χ^2 alpha	43.8	37.6	37.6
Degree of freedom	30	25	25

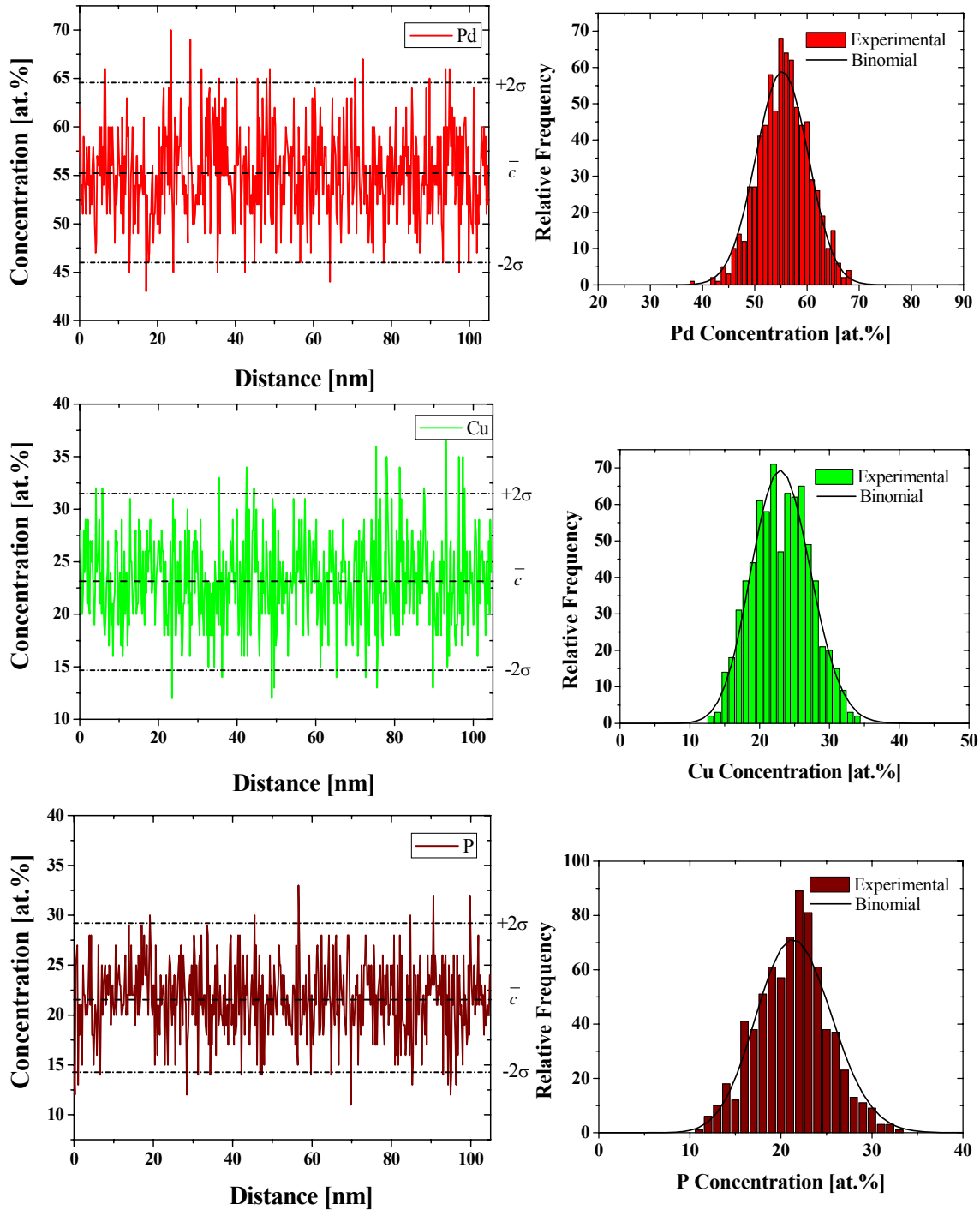


Figure 6.4 Concentration profiles for each constituent element of $\text{Pd}_{55}\text{Cu}_{23}\text{P}_{22}$ bulk amorphous alloy.

Figure 6.5 Comparison of the experimental frequency distribution to the binomial distribution of the same concentration for each constituent element.

6.1.3 Next Neighbourhood Evaluation Module

The NNE algorithm is processed for a $10 \times 10 \times 10 \text{ nm}^3$ volume chosen from the centre of the analysed volume. Albeit, the gallium ion damage to the specimen during the ion milling is limited to first 10-20 nm, the selection of a volume from the centre ensures that the irradiation damage do not effect the local chemical order. Selecting only Cu-Cu elemental correlation in the analysed volume, the

experimental histograms are drawn for the first five neighbours as shown in Fig. 6.6 (only first five neighbours are chosen for simplicity).

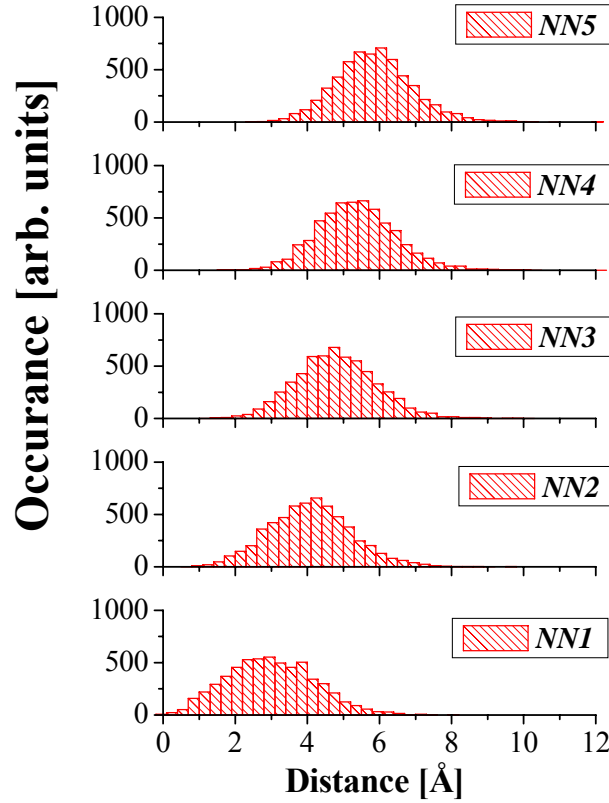


Figure 6.6 Histogram showing the distance distribution of first five next neighbours for Cu-Cu correlation.

The distribution of the distances of the next neighbouring atoms presented in the histograms is denoted as NN_i . The occurrence of the distances for all neighbours follows a Gaussian distribution. This distribution provides the information about the probability of finding the first five neighbouring Cu atoms at certain distances. Fig. 6.6 also reflects the experimental errors in positioning where the peaks are broadened considerably in comparison to the expected ideal peak distribution. Since the inter-atomic distances in a given reconstructed volume may as well depend on the detection efficiency, a slight shift in the position of the peak would also occur as a consequence.

If $P(r)$ is a true distribution of the 1st neighbour distance and $P^o(r)$ is its apparent distribution due to the experimental broadening, then the relation can be described mathematically as

$$p^o(r) = \int d^3 r' s(\bar{r} - \bar{r}') p(r') \quad (6.1)$$

Where, $s(\bar{r} - \bar{r}')$ represents the experimental broadening of the atomic distribution. As a matter of fact, two atoms cannot occupy a position less than their average diameter, the distribution of the 1st neighbour should start from a critical distance r_c rather than from 0 as shown in Fig. 6.7 for next neighbour (NNI).

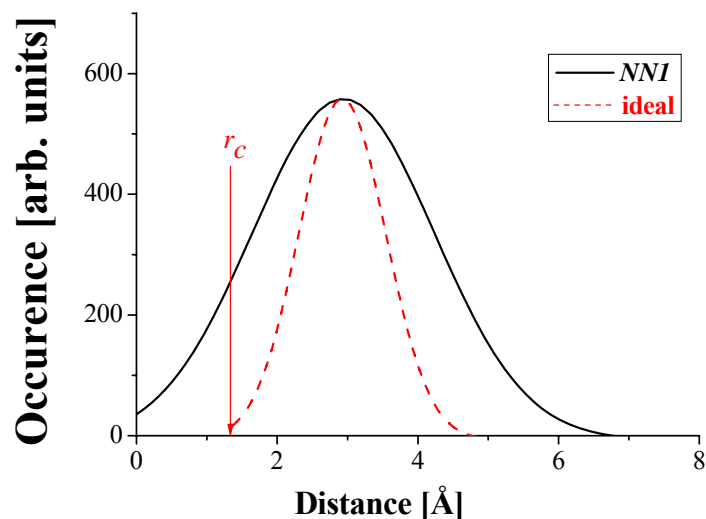


Figure 6.7 Schematic illustration of the experimental peak broadening and an ideal distribution for the *NNI*.

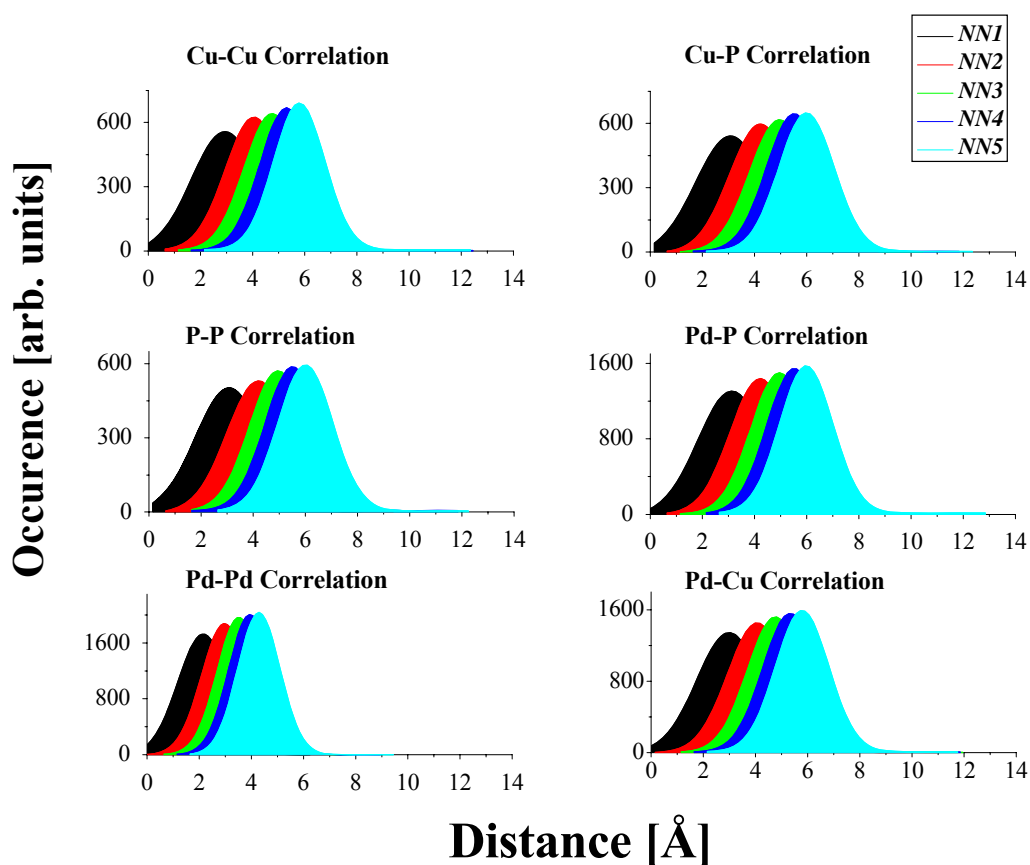


Figure 6.8 Distance distribution of first five *NNs* for all correlations after Gaussian fit. The distances assigned as *NNI* shows the distance distribution of next neighbouring atom for the respective correlation. Each graph presents the probability of finding the first five *NNs* of the respective correlation.

Another important parameter is the value of the full width at half maximum (FWHM). The experimental broadening, $s(\bar{r} - \bar{r}')$ leads to a higher value of the FWHM than reality. One of the major factors leading to the experimental broadening is detection efficiency (i.e., 50%). Higher

detection efficiency will result in higher number of atoms in total, to which the averaged *NNs* will be more precise, as represented by the ideal distribution in the Fig. 6.8. Nevertheless, the peak positions in these distribution plots give important information about the distances of the next neighbours.

The Gaussian fit for each histogram gives the probability of finding first five neighbouring Cu atoms at certain distances as shown in Fig. 6.8. This figure is a reproduction of Fig. 6.6, after a Gaussian fit, though, also includes the subsequent Gaussian fits to other correlations. The maximum of Cu-Cu distribution peak gives us the maximum probability of finding relative Cu atoms which is the same as the average of all the distances of the first neighbour atoms. Similarly, Fig. 6.8 also depicts the distribution of the next neighbouring atoms for other elemental correlations calculated by processing this algorithm. All other correlations follow a likewise trends to the Cu-Cu correlation, shown in Fig. 6.6. The full width at half maximum (FWHM) for each correlation shows the following trend

$$\text{FWHM for } NN1 > NN2 > NN3 > NN4 > NN5$$

This relation reveals that the distribution for *NN5* has the smallest error among all of them. The experimental limitations in TAP analysis (i.e., detection efficiency, depth and lateral resolution, localised effect of field evaporation, etc.) result in smearing individual next neighbouring atomic distributions leading to strong overlapping (see Fig. 6.8). Albeit, there is no problem in differentiating individual *NN* distributions that is evident from Fig. 6.6 (i.e., experimental histograms), the smearing effect however pose greater uncertainty in differentiating coordination shells in the RDFs, discussed in detail in the next section. A comparison of FWHM among the different correlations results the FWHM in the following order for Pd-Pd < Cu-Cu < P-P, that depends on the respective concentration of different species in the analysed volume. Averaging over larger number of atoms of a certain element (i.e., higher concentration) will lead to smaller values of FWHM. The distances of maximum occurrence of each distribution give the maximum probability of finding a respective atom at those distances. The results for all correlations are summarized in the table 6.2.

Table 6.2 Summary of the average distances of the first ten next neighbour atoms for different correlations, calculated by processing the NNE algorithm to TAP data. The distances are in Å.

Next Neighbour distances in Å	Pd-Pd	Cu-Cu	Pd-Cu	Cu-P	P-P	Pd-P
<i>NN1</i>	2.21	3.01	3.08	3.15	3.16	3.19
<i>NN2</i>	3.02	4.09	4.13	4.26	4.25	4.27
<i>NN3</i>	3.56	4.80	4.85	4.99	5.00	5.02
<i>NN4</i>	3.98	5.37	5.41	5.58	5.58	5.60
<i>NN5</i>	4.33	5.85	5.88	6.08	6.08	6.08
<i>NN6</i>	4.63	6.27	6.29	6.50	6.50	6.51
<i>NN7</i>	4.91	6.64	6.66	6.89	6.89	6.89
<i>NN8</i>	5.16	6.98	6.99	7.23	7.24	7.24
<i>NN9</i>	5.39	7.30	7.30	7.55	7.56	7.56
<i>NN10</i>	5.59	7.58	7.59	7.84	7.86	7.86

6.1.4 Radial Distribution Functions²

Heinrich had utilized RDF tool to calculate atomic correlation of different species in crystalline alloys [Heinrich05]. This tool has also been utilized during the course of this research work to calculate the RDFs analogues in definition to the RDFs calculated using scattering techniques. Subsequently, P-P partial radial distribution function is calculated and presented in Fig 6.9a. Albeit, graph reveals a parabolic $\approx r^2$ dependence, no detailed sub-nanometre features that can be attributed to short range ordering present in the amorphous structure is revealed. In order to corroborate the functionality of RDF module for the TAP data, well established RDF^T tool utilized by the Theoretical Materials Physics group³ (Institute of Material physics, Göttingen University, Germany) has been processed on the same data set. The corresponding P-P partial radial distribution function calculated using RDF^T is shown in Fig. 6.9b. The resultant correlation follows the same trend as that in Fig. 6.9a. No detail on the short range ordering can be elicited from both radial distribution functions.

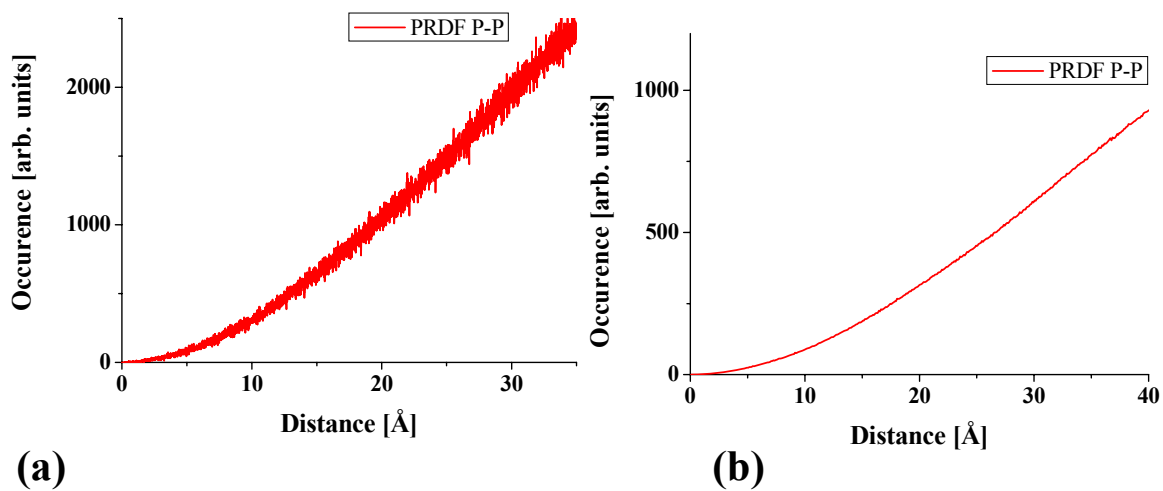


Figure 6.9 Partial radial distribution functions calculated utilizing a) RDF module developed to treat TAP data and b) calculated utilizing well established RDF^T tool in the theoretical group in Institute of Material Physics, Göttingen University by Guerdane.

Lucid explanation of inability to elucidate any information exploiting RDF modules is the overlaps in subsequent next neighbour positions evident from Fig. 6.8. Owing to the broadening of the FWHM of each peak leads to the observed smearing out effect. This overlap is elaborated in the NNE distribution for P-P correlation shown in the Fig. 6.10. Dashed line follows the distribution of the first *NNI*, which has a palpable overlap with the distribution of the subsequent *NNs*. When the number of atoms are averaged at a definite distance, say at a distance indicated by a yellow line i.e., at 3.15 Å, the atoms

² Described in detail in chapter 5 § 1.1.

³ Guerdane from theoretical group, IMP, Uni. Göttingen has developed and extensively utilized the stated RDF^T tool. He has kindly processed the RDF tool, the results of which are presented in Fig. 6.9b.

from all five NNs contribute to the averaging and hence smear out any peak that can be attributed to short range order. A likewise comparison provides RDFs and PRDFs for all other correlations calculated exploiting both tools, reveal same trends; absence of any particular that can be attributed to short range features.

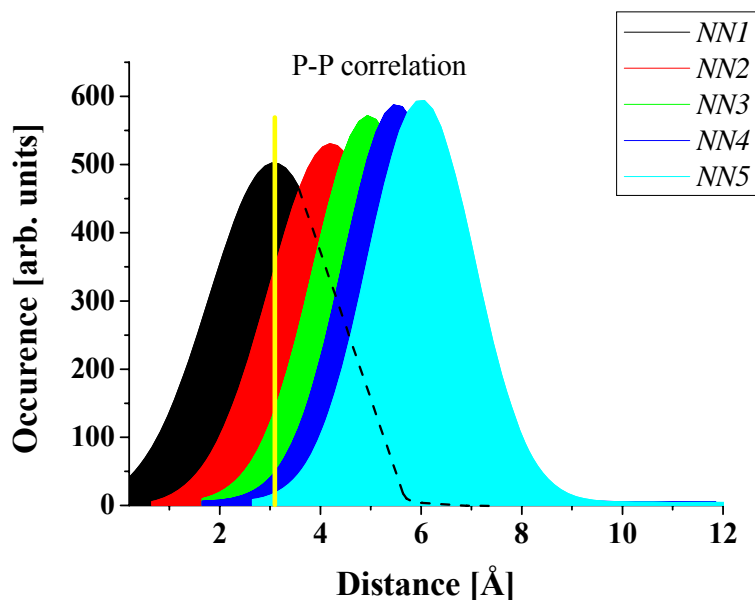


Figure 6.10 Distance distribution of first five NNs for P-P correlations. The distances assigned as NNi shows the distance distribution of the i^{th} next neighbouring atom.

6.1.5 Discussion

Miller has reported nanometre scale copper enriched/phosphorous-depleted regions and vice versa in Pd-Cu-P bulk amorphous alloys with different compositions [Miller03]. However, our studies reveal a homogeneous distribution, the plausible explanation for the diverse results are different thermal histories (cooling rate during sample preparation) in addition to the differences in composition of the investigated materials.

Comparison with the diffraction results

Table 6.2 illustrates the next neighbourhood distances for the first ten atoms of all correlations in the studied system. The order of finding atoms next to each other is the same as that shown in this table, i.e., Pd-Pd, Cu-Cu, Pd-Cu, Cu-P, P-P & Pd-P.

Since, the partial radial distribution functions of the material analysed from scattering techniques are not yet reported, a comparison is made with already available data in the literature. Albeit, the referred experiments were done mostly on binary alloys except (Pd-Ni-P), it provides somewhat analogous

information for a comparison. The Pd-Pd correlation reported by Duine [Duine94] is reproduced in Fig 6.11. The arrows pointing towards the abscissa indicate the next neighbour atomic positions deduced from the present work. It seems that $NN1$ and $NN2$ contributes to the first coordination shell while $NN3 - NN10$ are contributing to the second coordinate shell.

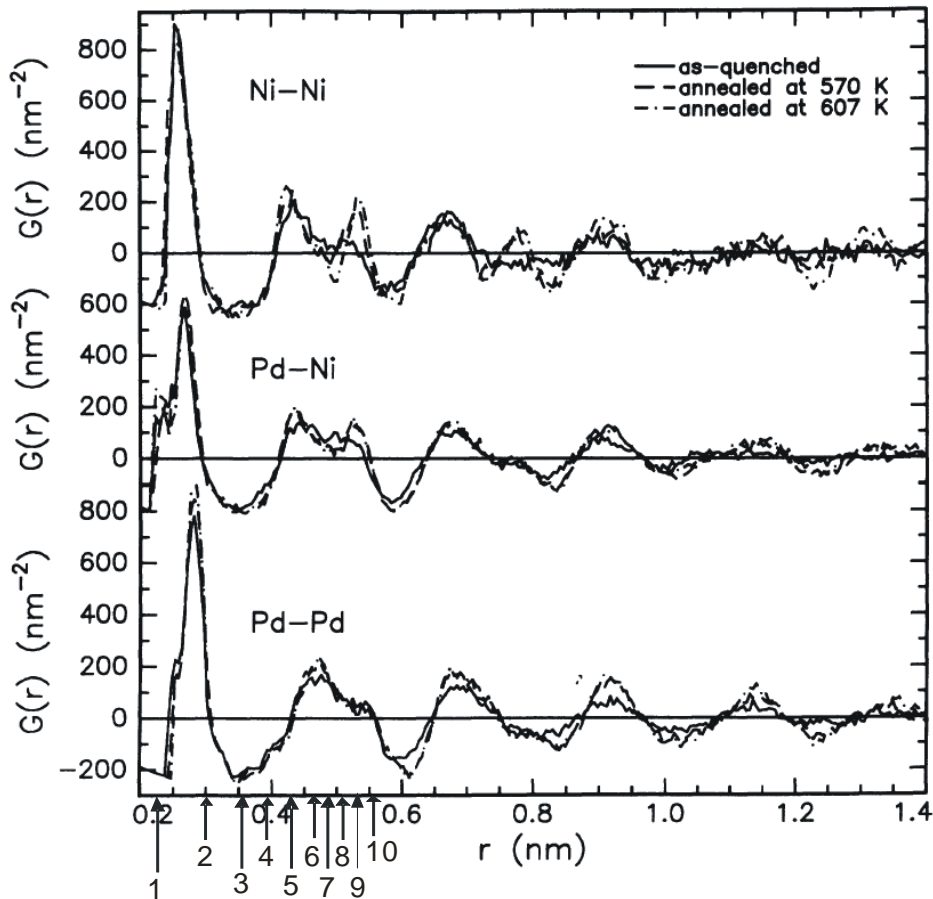


Figure 6.11 Reduced partial RDF's of amorphous $\text{Pd}_{52}\text{Ni}_{32}\text{P}_{16}$ alloy for the as quenched and annealed states calculated by Duine [Duine94]. The arrows indicated along the abscissa are the distances of first ten next neighbours for Pd-Pd correlation, calculated by processing the NNE algorithm in the present work.

Taking the average of the corresponding neighbouring distances i.e., for $NN1$ & $NN2$ for the first shell gives a distance of 2.6 \AA while other neighbours contributing to the second coordinate shell, i.e. average of $NN3$ to $NN10$ gives an average distance of 4.7 \AA , these values are in a very good agreement with the corresponding peaks in Pd-Pd partial radial distribution function. A similar comparison is shown in Fig. 6.12 for Cu-Cu [Maret87] and in Fig. 6.13 for P-P correlation [Sadoc76]. The first neighbour for P-P is found at a distance of 3.16 \AA as compared to the expected distance of 2.12 \AA (covalent diameter of P) which means, two P atoms are rarely neighbours to each other as reported earlier [Wong81,Gaskell83].

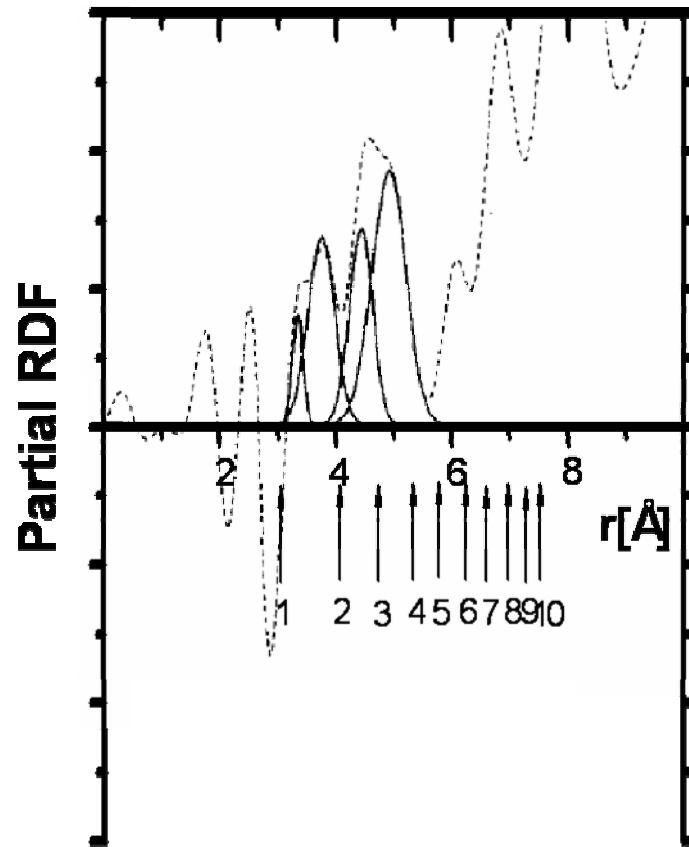


Figure 6.12 Partial RDF's of $\text{Cu}_{33}\text{Y}_{67}$ glass and Gaussian components of the nearest neighbour region, characterized by Maret [Maret87]. The arrows indicated along the abscissa are the distances of first ten next neighbours for Cu-Cu correlation, calculated by processing the NNE algorithm in the present work.

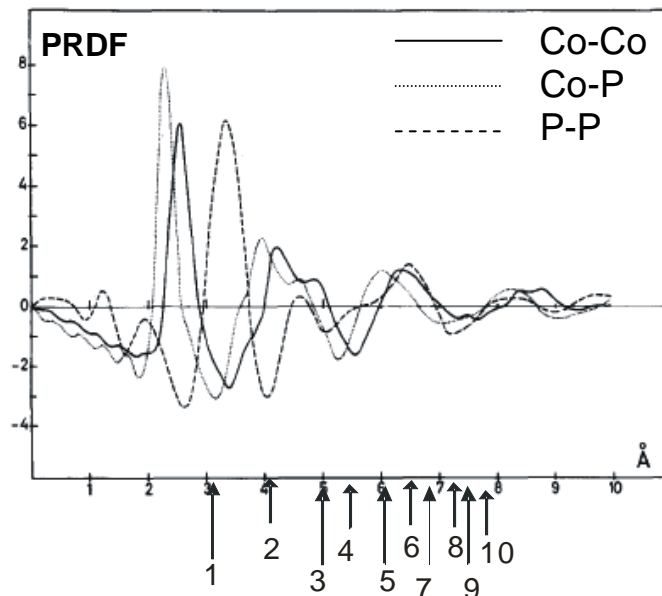


Figure 6.13 Reduced partial RDF's of $\text{Co}_{80}\text{P}_{20}$ amorphous alloy characterized by Sadoc [Sadoc76]. The arrows indicated along the abscissa are the distances of first ten next neighbours for P-P correlation, calculated by processing the NNE algorithm in the present work.

Dependence of evaluation data on evaporation field at tip surface (F_o) and geometrical field factor (K_f)

A comparison of the next neighbouring atomic distances calculated by processing the NNE algorithm on atomic reconstructions for different F_oK_f factors [Miller89] is given in table 6.3. The estimated F_oK_f value used for this alloy system is 24 V/Å. The next neighbouring distances are almost unaffected for smaller deviations in the estimated value of F_oK_f . However, there are pronounced differences for larger ($> \pm 5$ V/Å) F_oK_f variations especially for the smaller values of F_oK_f (e.g. for the distance distribution of Pd-Pd and P-P). A lower F_oK_f value than the estimated one results in larger next neighbour atomic distances and vice versa.

Table 6.3 Comparison of the average distances of the first five next neighbour atoms for different correlations, calculated for different F_oK_f values. The distances are in Å.

F_oK_f [V/Å]	Pd-Pd					Cu-Cu		
	30	25	24	23	15	25	24	23
<i>NN1</i>	2.20	2.20	2.21	2.23	2.27	3.01	3.01	3.03
<i>NN2</i>	3.02	3.01	3.02	3.05	3.07	4.07	4.09	4.11
<i>NN3</i>	3.55	3.54	3.56	3.59	3.60	4.79	4.80	4.82
<i>NN4</i>	3.99	3.96	3.98	4.01	4.02	5.36	5.37	5.38
<i>NN5</i>	4.35	4.31	4.33	4.36	4.37	5.84	5.85	5.86

F_oK_f [V/Å]	Cu-P			Pd-P			Pd-Cu		
	25	24	23	25	24	23	25	24	23
<i>NN1</i>	3.12	3.15	3.19	3.12	3.19	3.22	3.03	3.08	3.12
<i>NN2</i>	4.18	4.26	4.30	4.20	4.27	4.32	4.09	4.13	4.16
<i>NN3</i>	4.93	4.99	5.03	4.92	5.02	5.07	4.80	4.85	4.87
<i>NN4</i>	5.51	5.58	5.61	5.49	5.60	5.65	5.36	5.41	5.43
<i>NN5</i>	5.99	6.08	6.10	5.97	6.08	6.13	5.83	5.88	5.90

F_oK_f [V/Å]	P-P				
	30	25	24	23	15
<i>NN1</i>	3.15	3.10	3.16	3.25	3.22
<i>NN2</i>	4.25	4.19	4.25	4.31	4.32
<i>NN3</i>	4.99	4.93	5.00	5.05	5.07
<i>NN4</i>	5.59	5.51	5.58	5.63	5.64
<i>NN5</i>	6.11	6.00	6.08	6.12	6.13

A comparison of the next neighbouring atomic distances calculated by processing the NNE algorithm on atomic reconstructions for different average atomic volumes (Ω_{av}) [Miller89] manifests the strong dependence of the next neighbouring atomic distances on the Ω_{av} values (Appendix B). A slight increase in the average atomic volume results in a remarkable increase in the next neighbour distances and vice versa. Hence, wrong Ω_{av} and F_oK_f parameters can result in a shift of all distributions to higher or lower distances. The variation of the *NNs* with respect to different values of Ω_{av} and F_oK_f also reflect the dependence on both depth and lateral resolution. These parameters affect differently both

depth and lateral scaling, hence, resulting in different average NVs . These results corroborate the influence of the reconstruction parameters as reported in detail elsewhere [Bas95, Vurpillot03].

Structural features down to next neighbouring atoms

In order to find out any correlation among the distances of different neighbours, a normalization should be made by a certain factor, e.g. normalizing with the diameter of respective atoms. The distance of the respective first neighbour NNi is used for normalizing, firstly because it contains the average diameter of both atoms and secondly because of the difficulties in accessing the exact diameter of the atoms in amorphous states. The normalized distances are summarized in table 6.4. Surprisingly, the resultant ratios after normalization are similar for all elemental correlations, showing that there is a steric relationship rather than chemical. A steric dependence can also be inferred from the radial distribution functions. In the case of the RDFs, the neighbouring coordination shells follow a certain periodicity on the other hand our finding shows that even neighbouring atoms are arranged at certain definite order. Häussler suggests the repetitive coordination shells, as illustrated in Fig 6.14, based on Friedel oscillation [Häussler85]. However, Teichler found such a relation in RDFs calculated from the pair potential simulations, justified purely by steric considerations [Teichler06]. Nevertheless, for both cases, the coordination shells follow a certain periodicity. The findings from the present results, however, reveal such an atomic ordering/periodicity even exists down to those next neighbouring atoms which are responsible for the coordination shells in RDFs.

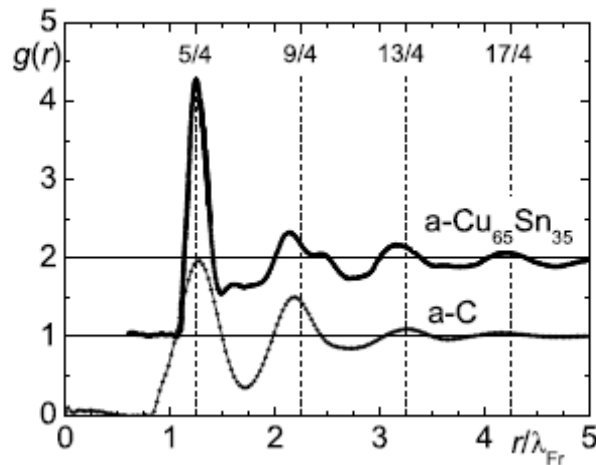


Figure 6.14 Pair distribution of $a\text{-Cu}_{65}\text{Sn}_{35}$ and $a\text{-C}$, normalized on the r -scale by λ_{Fr} , the Friedel wavelength, showing coordination shell repetition at certain distances [Häussler04].

Table 6.4 The ratio for different elemental correlations after normalizing the average distances of the first ten next neighbours by the average distance of first neighbouring atom. The distances are in Å.

	Pd-Pd	Cu-Cu	Pd-Cu	Cu-P	P-P	Pd-P	Average ratio
<i>NN2/NN1</i>	1.36	1.36	1.34	1.35	1.34	1.34	1.35 ± 0.02
<i>NN3/NN1</i>	1.61	1.60	1.57	1.59	1.58	1.57	1.59 ± 0.02
<i>NN4/NN1</i>	1.80	1.79	1.75	1.77	1.77	1.76	1.77 ± 0.04
<i>NN5/NN1</i>	1.96	1.95	1.91	1.93	1.92	1.91	1.93 ± 0.04
<i>NN6/NN1</i>	2.10	2.09	2.04	2.07	2.06	2.04	2.06 ± 0.04
<i>NN7/NN1</i>	2.22	2.21	2.16	2.19	2.18	2.16	2.19 ± 0.04
<i>NN8/NN1</i>	2.33	2.32	2.27	2.30	2.29	2.27	2.30 ± 0.06
<i>NN9/NN1</i>	2.44	2.43	2.37	2.40	2.39	2.37	2.40 ± 0.06
<i>NN10/NN1</i>	2.53	2.52	2.46	2.49	2.49	2.47	2.49 ± 0.06

6.1.6 Conclusion

The DSC traces exhibited by Pd₅₅Cu₂₃P₂₂ bulk amorphous specimens show a palpable T_g and a single crystallization exothermic peak. Three dimensional atomic reconstructions of as cast samples reveal a single homogeneous phase. The homogeneity of the investigated material is also corroborated by the results from statistical χ^2 tests; a comparison of different elemental frequency distributions with the binomial distributions of a perfectly random solid solution. The χ^2 values less than χ^2 alpha values do not exclude the probability that all elements are homogeneously distributed.

The NNE algorithm is exploited to elicit the next neighbourhood atomic vicinity in Pd₅₅Cu₂₃P₂₂ bulk amorphous specimens from the data, analysed using TAP. First ten next neighbours for all elemental correlations were evaluated alone from the TAP data, which for multi-component systems is difficult, otherwise. A comparison of the FWHM among different elemental correlations in Fig. 6.8 reveals the following trend, FWHM for Pd-Pd < Cu-Cu < P-P due to the compositional dependence (a higher concentration leads to a smaller FWHM). The distribution of next neighbouring atomic distances shows that for this system, the Pd-Pd atoms have the highest probability to be the next neighbours to each other. The fact that P is not a direct next neighbour to another P atom is also lucid from these results. The distances for the first ten next neighbours of different elemental correlations are in good agreement with the data available in literature. The findings from the present work enables for the first time to assign the atoms responsible for the coordination peaks in RDFs. Normalizing the distances by the first next neighbour distance *NN1* yields a ratio similar for all elemental correlations showing that there exist a certain order among the atoms, irrespective of the chemical nature of the atoms. Such an atomic ordering is already known for the coordination peaks in RDFs [Häussler85, Teichler06]. Hence, algorithm developed in the present work allows specifying atom positions and chemical identities of

the next neighbouring atoms for amorphous materials in real space which are difficult to access alone from RDFs.

6.2 $\text{Fe}_{40}\text{Ni}_{40}\text{B}_{20}$ Glassy Ribbons

6.2.1 Thermal characterization by DSC

The DSC scans of both as quenched and 1 hour annealed state of the investigated $\text{Fe}_{40}\text{Ni}_{40}\text{B}_{20}$ metallic glass are presented in Fig. 6.15. A comparison shows no palpable difference in the thermodynamic kinetics of both samples and the both DSC scans reveal a pronounced single crystallization peak (T_p) at 440°C. The DSC scans suggests that there is no major difference in the structure of the as quenched and annealed state.

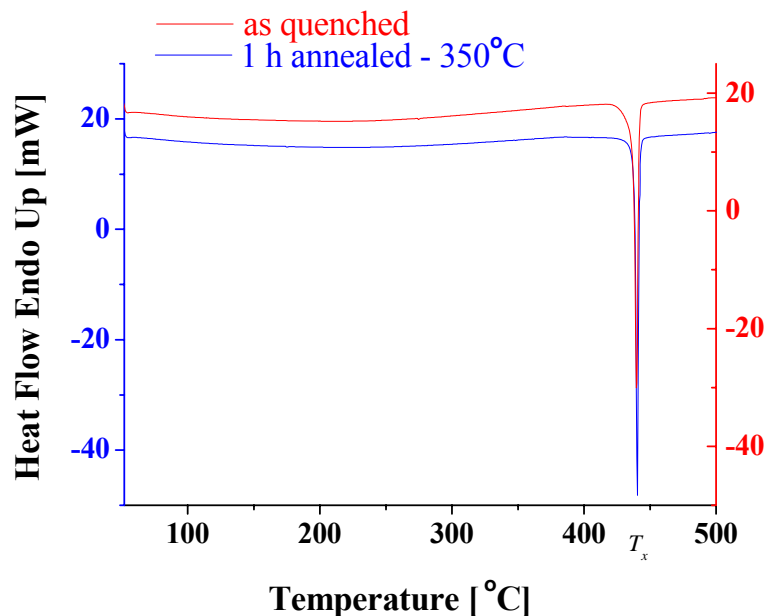


Figure 6.15 Comparison of the DSC traces of $\text{Fe}_{40}\text{Ni}_{40}\text{B}_{20}$ metallic glass for as quenched and 1 hour annealed at 350°C, taken at a heating rate of 0.33 K/s.

6.2.2 Diffraction study by X-Rays

The XRD patterns reveal no different results than deduced from the DSC scans. Fig. 6.16 shows the comparison of the XRD patterns both for the as quenched and annealed state. Albeit, first order and second order humps⁴ are evident in both patterns, no additional crystallization peaks are revealed for the annealed state. Comparing both patterns it's very difficult to deduce any palpable difference between both states.

⁴ The presence of the first order and second order humps don't rule out any nanoscale crystalline inclusions, it is because of the resolution limit of the XRD.

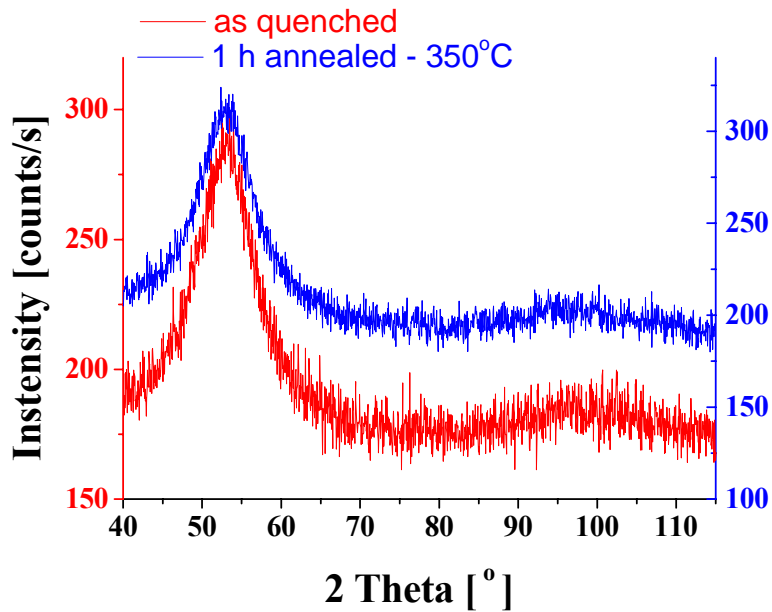


Figure 6.16 XRD pattern of as quenched sample and sample annealed for 1 h at 350°C $\text{Fe}_{40}\text{Ni}_{40}\text{B}_{20}$ metallic glass. Both curves shows first order and second order humps typical for amorphous structure.

6.2.3 Structural characterization by TAP microscopy

The field ion micrograph of the as quenched $\text{Fe}_{40}\text{Ni}_{40}\text{B}_{20}$ glassy ribbon exhibit no major pole that can be attributed to crystalline phase. A uniform atomic distribution is also depicted in the FIM micrograph of the annealed state (i.e., 1 h @ 350°C) in the Fig. 6.17⁵.

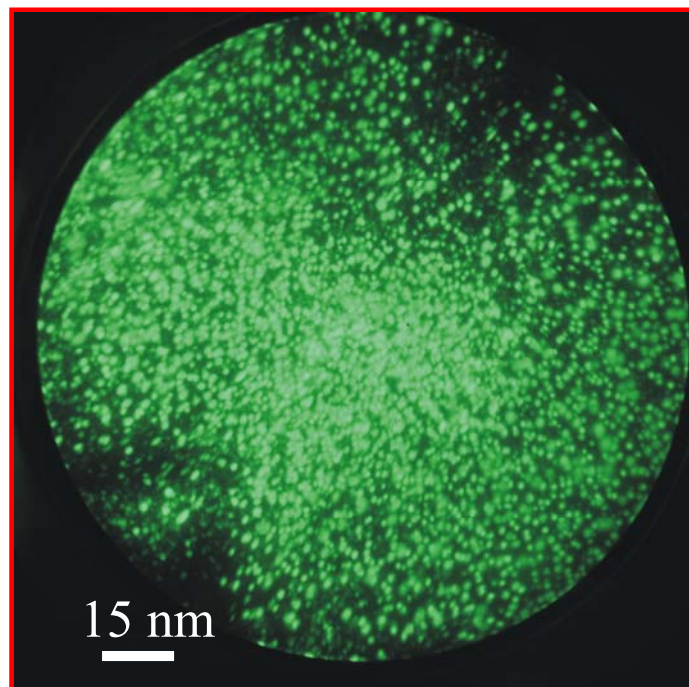


Figure 6.17 Field ion image of the $\text{Fe}_{40}\text{Ni}_{40}\text{B}_{20}$ glassy ribbons annealed for 1 hour at 350°C.

⁵ The darker region in the FIM micrograph represent undeveloped TAP tip.

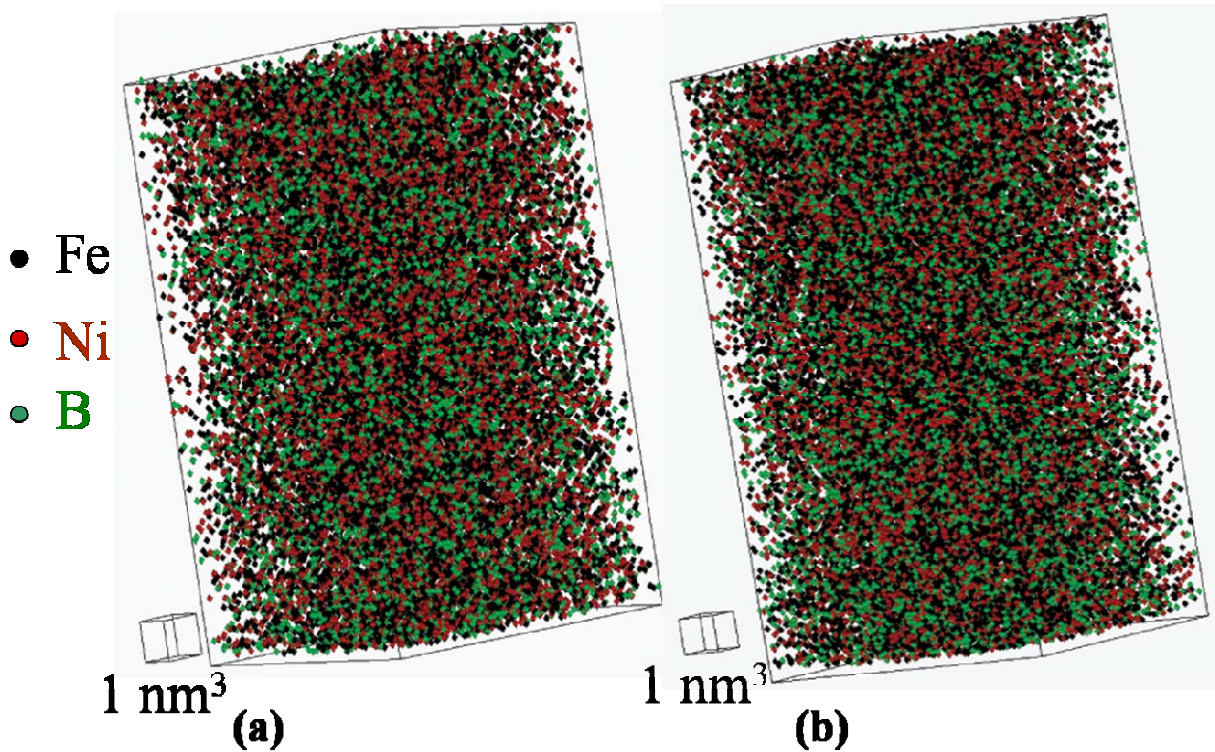


Figure 6.18 Three dimensional elemental atomic reconstruction for a) as quenched and b) sample annealed for 1 hour at 350°C of the $\text{Fe}_{40}\text{Ni}_{40}\text{B}_{20}$ glassy ribbons. Each dot represents atomic position of the relative element distinguished by different colours.

Fig. 6.18 depicts the comparison of the three dimensional atomic reconstructions of as quenched $\text{Fe}_{40}\text{Ni}_{40}\text{B}_{20}$ glassy ribbon and annealed ribbon. Visually, both samples exhibit a single homogeneous randomly distributed phase. Fig. 6.19 depicts the three dimensional atomic reconstruction of the individual elements in order to elaborate the stereological representation of atoms for the heat treated samples.

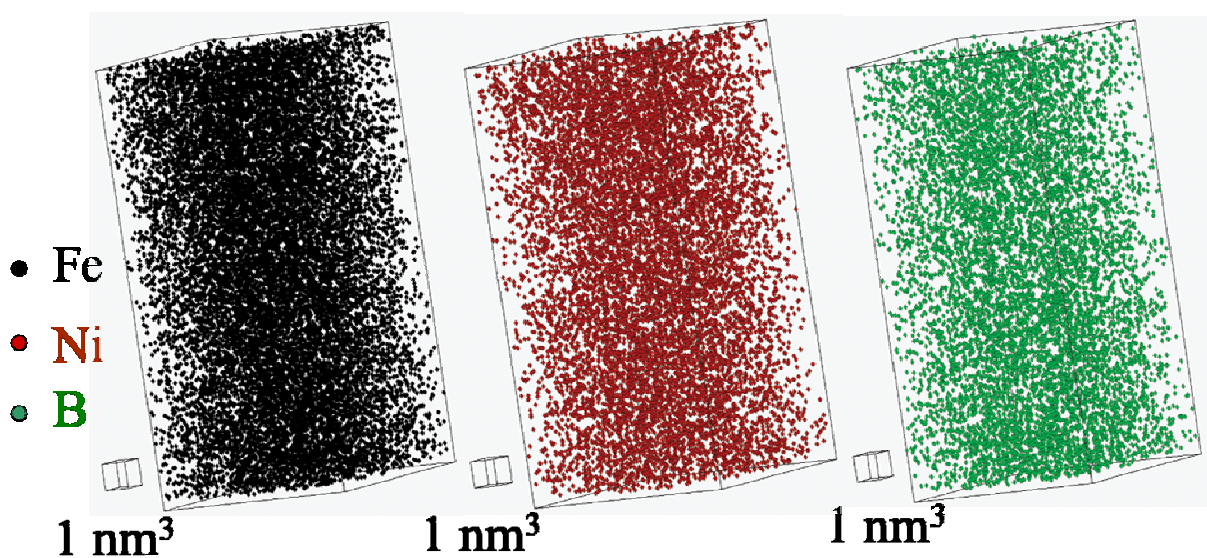


Figure 6.19 Three dimensional atomic reconstruction for individual elements for sample annealed for 1 hour at 350°C of the $\text{Fe}_{40}\text{Ni}_{40}\text{B}_{20}$ glassy ribbons. Each dot represents atomic position of the relative element distinguished by different colours.

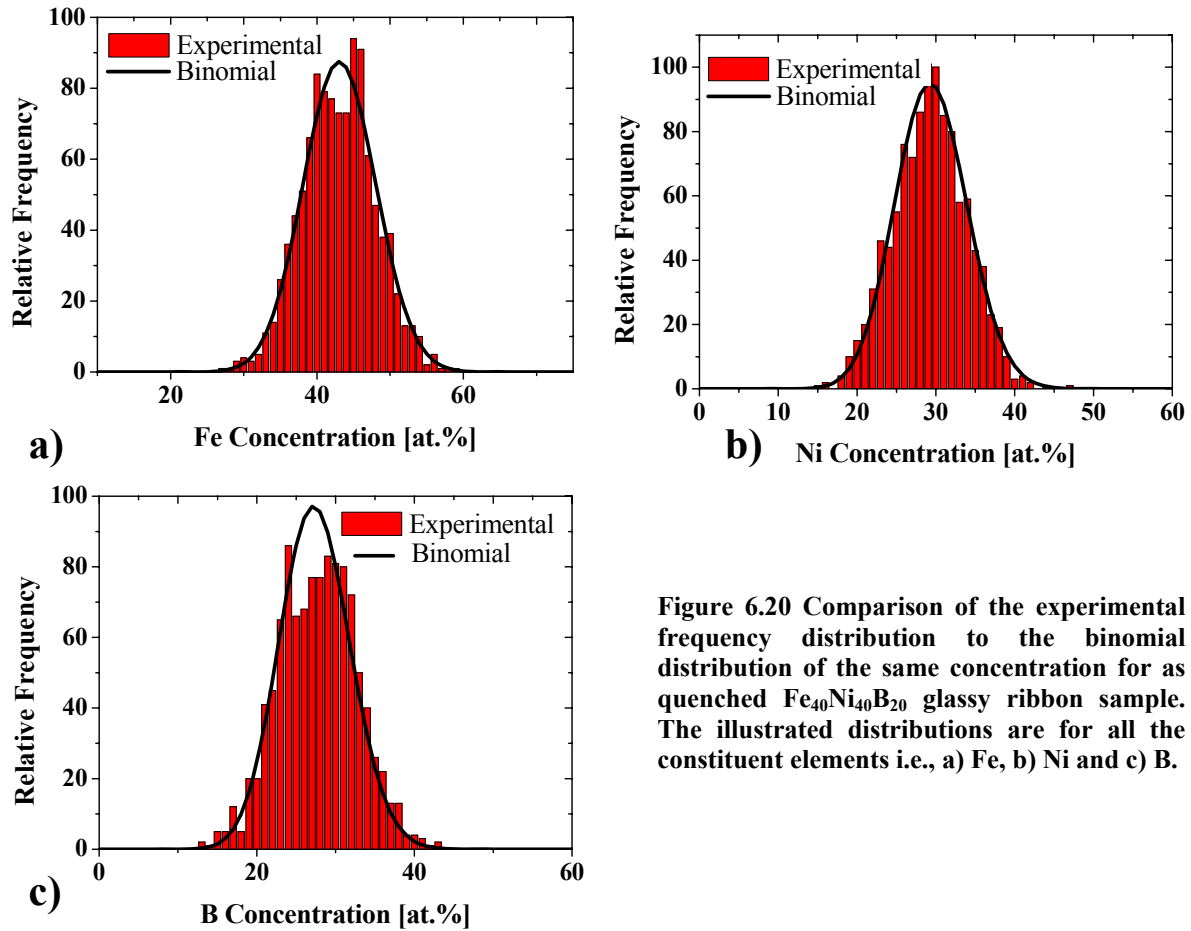


Figure 6.20 Comparison of the experimental frequency distribution to the binomial distribution of the same concentration for as quenched $\text{Fe}_{40}\text{Ni}_{40}\text{B}_{20}$ glassy ribbon sample. The illustrated distributions are for all the constituent elements i.e., a) Fe, b) Ni and c) B.

The statistical tool χ^2 test has been processed to check the homogeneity in both samples. Fig. 6.20 illustrates a comparison of the frequency distribution of the experimental data and that from a binomial distribution with the same mean concentration for each constituent of as quenched $\text{Fe}_{40}\text{Ni}_{40}\text{B}_{20}$ glassy ribbons. For the as quenched sample both the binomial and experimental frequency distributions for Fe and Ni depict no deviation. However, very slight hints of deviation present between the experimental and binomial distribution of the B element.

Table 6.5 Summary of the calculated χ^2 values for both as quenched and annealed $\text{Fe}_{40}\text{Ni}_{40}\text{B}_{20}$ glassy ribbon. The value of χ^2 alpha for the stated degree of freedom is also given for comparison, with 0.05 significance level of alpha.

$\text{Fe}_{40}\text{Ni}_{40}\text{B}_{20}$	As quenched			1 hour @350°C		
	Fe	Ni	B	Fe	Ni	B
χ^2	27	23	72.4	64.4	84	393.18
χ^2 alpha	45	41	41	45	43	41
Degree of freedom	31	28	28	31	29	28

Table 6.5 gives a comparison of the χ^2 values calculated for each constituent element and the χ^2 alpha values with 0.05 significance level of alpha, for both as quenched and annealed samples. It is evident

that the calculated χ^2 values for Fe and Ni are reasonably less than χ^2 alpha values; showing the possibility that the Fe and Ni are distributed homogeneously. However, for B the calculated χ^2 value exceeds the χ^2 alpha value; some inhomogeneity may be present for B distribution.

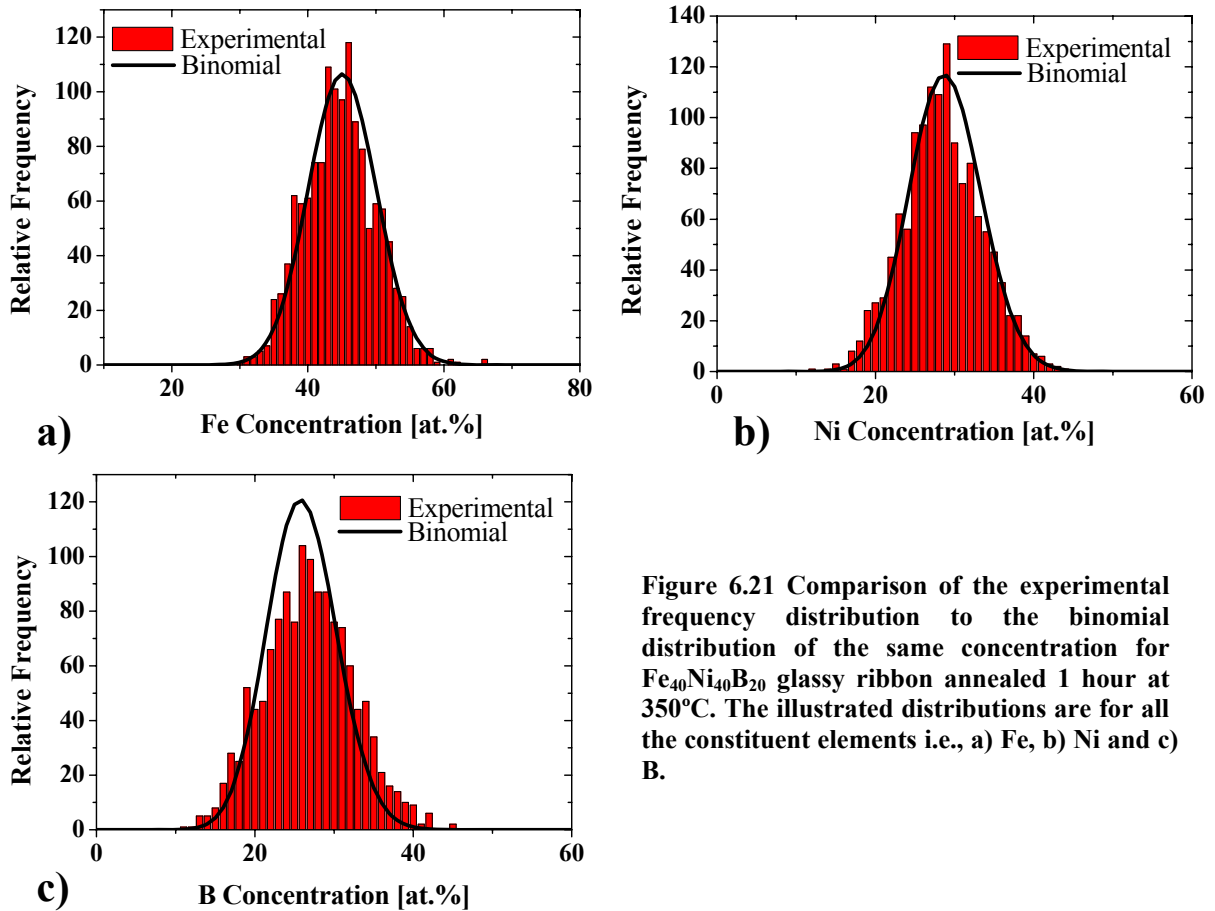


Figure 6.21 Comparison of the experimental frequency distribution to the binomial distribution of the same concentration for $\text{Fe}_{40}\text{Ni}_{40}\text{B}_{20}$ glassy ribbon annealed 1 hour at 350°C . The illustrated distributions are for all the constituent elements i.e., a) Fe, b) Ni and c) B.

Fig. 6.21 illustrates a similar comparison of the experimental and binomial distributions for the annealed sample and subsequent χ^2 , χ^2 alpha values and degree of freedom are summarized in the table 6.5. The χ^2 values for all elements for the annealed sample exceeds the reference χ^2 alpha values, rulling out any homogenous distribution of the constituent elements, especially for B distribution for which palpable difference is recorded between the two values.

6.2.4 Next Neighbourhood Evaluation Module

The NNE algorithm is processed to elucidate the fine details attributed to the short range ordering for both as quenched and annealed $\text{Fe}_{40}\text{Ni}_{40}\text{B}_{20}$ glassy ribbon. Subsequently, table 6.6 depicts the average distances of first thirty NNs for each elemental correlation, calculated by processing the aforementioned algorithm on the TAP data of as quenched $\text{Fe}_{40}\text{Ni}_{40}\text{B}_{20}$ glassy ribbon.

Table 6.6 Summary of the average distances of the first thirty next neighbour atoms for different correlations, calculated by processing the NNE algorithm to TAP data for the as quenched Fe₄₀Ni₄₀B₂₀ glassy ribbon. The distances are in Å.

<i>NNi</i>	Fe-Fe	Ni-Ni	Fe-Ni	Ni-B	B-B	Fe-B
<i>NN1</i>	2.27	2.56	2.57	2.65	2.7	2.75
<i>NN2</i>	3.04	3.44	3.45	3.53	3.66	3.67
<i>NN3</i>	3.56	4.02	4.05	4.11	4.29	4.3
<i>NN4</i>	3.96	4.49	4.5	4.58	4.79	4.79
<i>NN5</i>	4.29	4.88	4.89	4.97	5.21	5.21
<i>NN6</i>	4.59	5.22	5.23	5.31	5.57	5.57
<i>NN7</i>	4.85	5.52	5.53	5.61	5.9	5.89
<i>NN8</i>	5.09	5.8	5.8	5.88	6.19	6.18
<i>NN9</i>	5.3	6.05	6.06	6.13	6.47	6.45
<i>NN10</i>	5.51	6.28	6.29	6.37	6.72	6.7
<i>NN11</i>	5.7	6.5	6.51	6.59	6.95	6.93
<i>NN12</i>	5.87	6.7	6.72	6.79	7.17	7.15
<i>NN13</i>	6.04	6.9	6.91	6.99	7.38	7.36
<i>NN14</i>	6.21	7.09	7.1	7.17	7.57	7.56
<i>NN15</i>	6.36	7.26	7.28	7.35	7.76	7.75
<i>NN16</i>	6.51	7.44	7.45	7.52	7.94	7.93
<i>NN17</i>	6.65	7.6	7.61	7.69	8.12	8.11
<i>NN18</i>	6.79	7.75	7.77	7.85	8.29	8.27
<i>NN19</i>	6.92	7.91	7.92	8	8.45	8.43
<i>NN20</i>	7.05	8.06	8.07	8.14	8.6	8.59
<i>NN21</i>	7.17	8.2	8.21	8.29	8.76	8.75
<i>NN22</i>	7.29	8.34	8.35	8.43	8.91	8.89
<i>NN23</i>	7.41	8.48	8.48	8.56	9.05	9.03
<i>NN24</i>	7.52	8.61	8.61	8.69	9.19	9.17
<i>NN25</i>	7.63	8.73	8.74	8.81	9.33	9.31
<i>NN26</i>	7.74	8.86	8.87	8.94	9.46	9.44
<i>NN27</i>	7.85	8.98	8.99	9.05	9.59	9.57
<i>NN28</i>	7.95	9.1	9.11	9.17	9.72	9.7
<i>NN29</i>	8.05	9.21	9.22	9.29	9.84	9.82
<i>NN30</i>	8.15	9.33	9.33	9.4	9.96	9.94

The algorithm was processed for a 10×10×10 nm³ volume chosen from the centre of the analysed volume for both as quenched and annealed ribbons. Table 6.6 divulges the probability of finding the elemental correlation as follows:

Fe-Fe<Ni-Ni<Fe-Ni<Ni-B<B-B<Fe-B

Corresponding, average distances for first thirty *NNs* for each elemental correlation for annealed Fe₄₀Ni₄₀B₂₀ glassy ribbon are presented in table 6.7. Annealing for 1 hour at 350°C doesn't make any difference on the order of elemental correlation. Radial distribution functions calculated from the TAP data by processing the RDF algorithm (for both as quenched and annealed samples) are presented in Appendix B.

Table 6.7 Summary of the average distances of the first thirty next neighbour atoms for different correlations, calculated by processing the NNE algorithm to TAP data for the Fe₄₀Ni₄₀B₂₀ glassy ribbon annealed for 1 hour at 350°C. The distances are in Å.

<i>NNi</i>	Fe-Fe	Ni-Ni	Fe-Ni	Ni-B	B-B	Fe-B
<i>NN1</i>	2.18	2.5	2.52	2.55	2.68	2.79
<i>NN2</i>	2.92	3.37	3.39	3.42	3.65	3.7
<i>NN3</i>	3.42	3.95	3.97	4.02	4.28	4.33
<i>NN4</i>	3.82	4.41	4.43	4.48	4.77	4.83
<i>NN5</i>	4.14	4.79	4.8	4.86	5.19	5.24
<i>NN6</i>	4.43	5.12	5.13	5.19	5.54	5.59
<i>NN7</i>	4.68	5.42	5.43	5.48	5.86	5.91
<i>NN8</i>	4.91	5.69	5.69	5.76	6.15	6.2
<i>NN9</i>	5.12	5.93	5.94	6	6.42	6.46
<i>NN10</i>	5.31	6.16	6.16	6.23	6.68	6.71
<i>NN11</i>	5.49	6.38	6.38	6.44	6.91	6.95
<i>NN12</i>	5.66	6.58	6.58	6.65	7.14	7.17
<i>NN13</i>	5.82	6.77	6.77	6.84	7.35	7.37
<i>NN14</i>	5.98	6.95	6.95	7.02	7.54	7.57
<i>NN15</i>	6.12	7.12	7.12	7.19	7.73	7.76
<i>NN16</i>	6.26	7.28	7.29	7.36	7.92	7.94
<i>NN17</i>	6.4	7.44	7.45	7.51	8.1	8.11
<i>NN18</i>	6.53	7.6	7.6	7.67	8.26	8.28
<i>NN19</i>	6.65	7.75	7.75	7.82	8.43	8.44
<i>NN20</i>	6.77	7.89	7.9	7.96	8.59	8.6
<i>NN21</i>	6.89	8.03	8.03	8.1	8.74	8.75
<i>NN22</i>	7.01	8.16	8.17	8.24	8.89	8.89
<i>NN23</i>	7.12	8.3	8.3	8.36	9.03	9.04
<i>NN24</i>	7.23	8.42	8.43	8.49	9.17	9.18
<i>NN25</i>	7.33	8.55	8.55	8.62	9.31	9.31
<i>NN26</i>	7.43	8.67	8.67	8.74	9.44	9.44
<i>NN27</i>	7.54	8.79	8.79	8.85	9.57	9.57
<i>NN28</i>	7.63	8.91	8.91	8.97	9.69	9.7
<i>NN29</i>	7.73	9.02	9.02	9.08	9.81	9.82
<i>NN30</i>	7.82	9.13	9.13	9.19	9.94	9.94

6.2.5 Discussion

The characterization of sub nano-scale transformations, more precisely, short range ordering was limited because of the resolution limits of many characterization techniques in the past decades. Lewis has though enunciated that the alloys that crystallise initially to a bcc phase e.g. Fe-based alloys, or to an hcp phase, e.g. Co-based alloys and Ti based metallic glasses (Metglas 2204), embrittle prior to crystallisation. Thus, slight short range rearrangements to incipient bcc or respective groupings may occur in the glassy state, giving rise to embrittlement [Lewis79]. For alloys containing high metalloid concentrations segregation of the metalloid(s) may occur, perhaps leading also to the establishment of incipient metal-metalloid groups and/or regions of high concentrations of metalloid(s) which render the alloy brittle. Further, since the metalloid content of glassy alloys clearly determines the mode of crystallisation, high metalloid concentrations leading to eutectic or polymorphic crystallisation, an

alloy of high metalloid content may form incipient groupings involving brittle boride phases that lead to embrittlement. Focus of the present work was characterization of the aforementioned primordial stages of transformation in these alloys before crystallization.

Albeit, the DSC and XRD measurements shows no difference in the structure of the as quenched and annealed $\text{Fe}_{40}\text{Ni}_{40}\text{B}_{20}$ glassy ribbon, TAP results depict a change in the structure on the very fine sub nanometre scale: the deviation reveal by both χ^2 test and NNE module. This clearly shows that the change of structure is beyond the resolution limilts of these conventional charcterization techniques.

Though χ^2 test depict a homogeneous distribution of Fe and Ni, however, the χ^2 value for B is slightly higher than the χ^2 alpha value suggesting that there may present some inhomogeneity even in as quenched state. Nevertheless, this inhomogeneity is more pronounced for the annealed state for B distribution and a slight deviation from homogeneity is also present for other constituent elements.

The NNE module reveals the atomic distances of first thirty next neighbours for both as quenched and annealed state. The atomic and covalent radii (in Å) of each element reported in literature are given below;

Element	Atomic radius	Covalent radius
Fe	1.26	1.17
Ni	1.24	1.15
B	0.98	0.82

The covalent diameter of Fe, Ni and B are 2.34 Å, 2.3 Å and 1.64 Å. The first neighbour distances calculated from NNE algorithm for Fe, Ni and B are 2.27 Å, 2.56 Å and 2.7 Å for as quenched state. Larger next neighbour distance than covalent and atomic radii for B are revealed from the present study for this alloy system; understandably there will be some differences in the bonding nature and thereby resultant diameter in amorphous state.

Comparison with the diffraction results

Sietsma had enunciated three partial reduced radial distribution functions of $\text{Fe}_{40}\text{Ni}_{40}\text{B}_{20}$ metallic glasses revealed by neutron diffraction experiments; three partial RDFs [Sietsma87] were calculated by applying isotopic substitution [Wagner80] from $\text{Fe}_{40}\text{Ni}_{40}^{11}\text{B}_{20}$, $\text{Fe}_{40}^{60}\text{Ni}_{40}^{11}\text{B}_{20}$, $\text{Fe}_{40}^{62}\text{Ni}_{40}^{11}\text{B}_{20}$ samples. Moreover, for the calculations it was assumed that $S_{\text{FeFe}}(Q) = S_{\text{NiNi}}(Q)$. Resultant partial reduced RDFs are reproduced in Fig. 6.22.

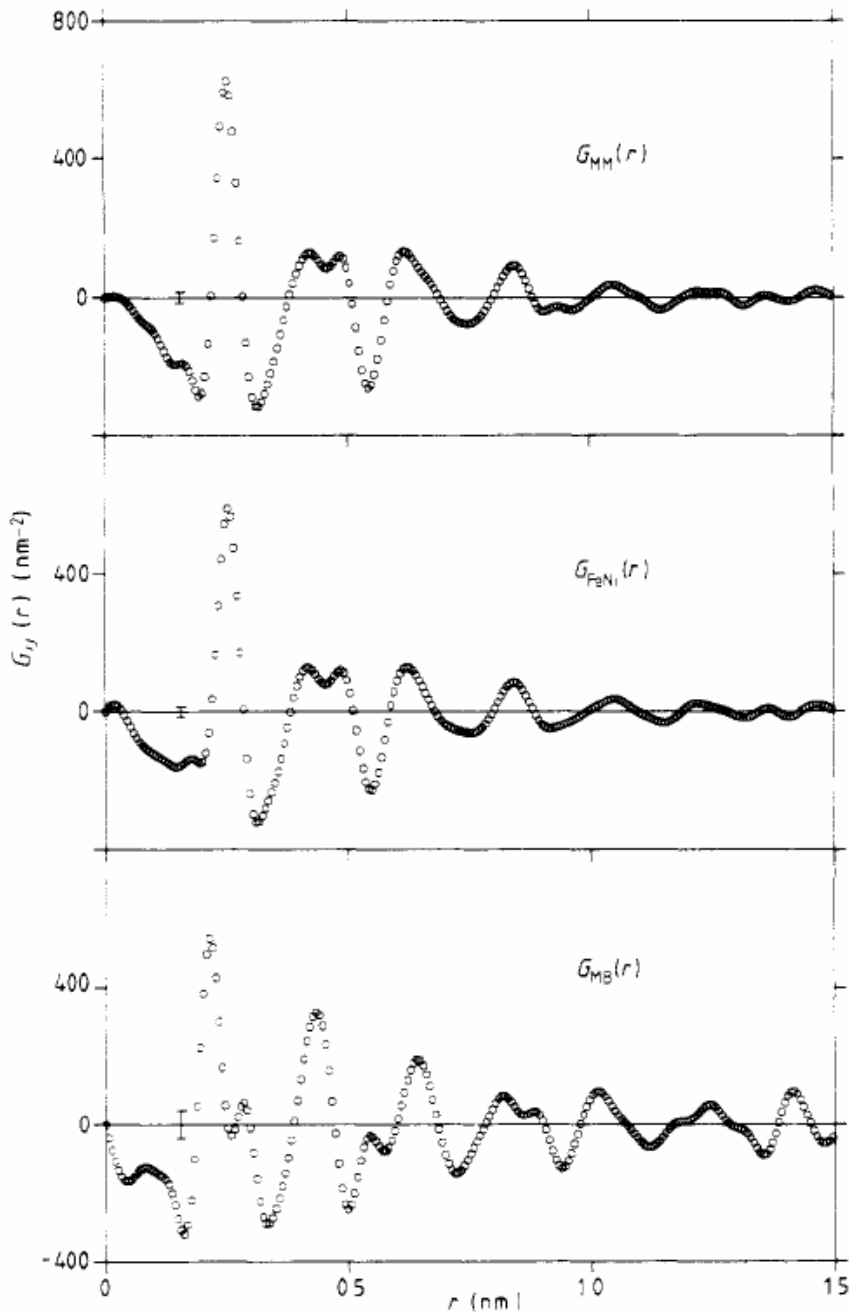


Figure 6.22 Three partial reduced radial distribution functions calculated based on the assumption that $S_{FeFe}(Q) = S_{NiNi}(Q) = S_{MM}(Q)$ for $Fe_{40}Ni_{40}^{11}B_{20}$ [Sietsma87].

Corresponding peak positions of the coordination shells for three partial reduced radial distribution functions i.e., for Fe-Fe, Ni-Ni (denoted as MM), Fe-Ni, and Fe-B, Ni-B (denoted as MB), along with the results revealed by processing NNE module (as quenched state) are summarized in table 6.8. The plausible methodology adapted for a comparison with the reduced radial distribution function⁶ calculated from the scattering techniques, is to take the average of NNs having same distance range as

⁶ As explained in detail in chapter 5 § 1.1.

that of the corresponding coordination peak/sub peak. For example, for Fe-Ni correlation, only $NN1$ has comparable distance to that of the first peak in the corresponding PRDF (r_1^1), hence considered. Subsequently, $NN2$ - $NN4$ corresponds to the sub-peak1 of the second peak in the corresponding PRDF (i.e., r_2^1) and hence averaged.

Table 6.8 Summary of the distances of the peak position of the coordination shells of the partial reduced radial distribution functions for $Fe_{40}Ni_{40}B_{20}$ metallic glasses [Sietsma87] and a comparison with the present results calculated exploiting NNE module for as quenched state. Distances are given in Å.

	$Fe_{40}Ni_{40}B_{20}$ (Sietsma87)			$Fe_{40}Ni_{40}B_{20}$ (Present Work)				
	M-M	Fe-Ni	M-B	Fe-Fe	Ni-Ni	Fe-Ni	Ni-B	Fe-B
r_1^1	2.52	2.53	2.15	2.66	2.56	2.57	2.65	2.75
r_1^2			2.83					
r_2^1	4.23	4.18	4.34	4.1	3.98	4	4.3	4.25
r_2^2	4.85	4.85		4.97	5.05	5.06		

The comparison is summarized in table 6.8, all values corroborate the results from Sietsma, though, the calculated values from the NNE module have slightly higher values. It should be noted that Sietsma enunciated for the transition metal-metalloid (Fe-B, Ni-B) correlation; first coordination peak with two sub peaks, however, from our results none of the NNE lies in distance range of first sub peak but in the range of the second sub-peak ($NN1$), we have thus assigned it to only one coordination peak without any sub-peak. Moreover, it's lucid that utilizing alone TAP, it is possible to reveal all different elemental correlations regardless of the number of the constituent elements which is a great challenge to calculate, otherwise.

Comparison between quenched and annealed state

To elaborate the structural change between as quenched and annealed state of the $Fe_{40}Ni_{40}B_{20}$ glassy ribbon, a difference between corresponding elemental correlations is presented in table 6.9. Generally, the NN distances of the annealed samples reveal comparatively a relaxed structure. The well established phenomenon of the structural relaxation, leads to decrease in the atomic distances for all correlations except that of Fe-B, evident from the positive values of the differences shown in table 6.9.

Table 6.9 Differences in Å for the average distances of first thirty next neighbour atoms between as quenched and annealed state of Fe₄₀Ni₄₀B₂₀ glassy ribbons. (*q* denotes as quenched and *a* denotes annealed state)

	Fe-B	B-B	Fe-Ni	Ni-Ni	Fe-Fe	Ni-B
<i>NN1_q-NN1_a</i>	-0.04	0.02	0.05	0.06	0.09	0.1
<i>NN2_q-NN2_a</i>	-0.03	0.01	0.06	0.07	0.12	0.11
<i>NN3_q-NN3_a</i>	-0.03	0.01	0.08	0.07	0.14	0.09
<i>NN4_q-NN4_a</i>	-0.04	0.02	0.07	0.08	0.14	0.1
<i>NN5_q-NN5_a</i>	-0.03	0.02	0.09	0.09	0.15	0.11
<i>NN6_q-NN6_a</i>	-0.02	0.03	0.1	0.1	0.16	0.12
<i>NN7_q-NN7_a</i>	-0.02	0.04	0.1	0.1	0.17	0.13
<i>NN8_q-NN8_a</i>	-0.02	0.04	0.11	0.11	0.18	0.12
<i>NN9_q-NN9_a</i>	-0.01	0.05	0.12	0.12	0.18	0.13
<i>NN10_q-NN10_a</i>	-0.01	0.04	0.13	0.12	0.2	0.14
<i>NN11_q-NN11_a</i>	-0.02	0.04	0.13	0.12	0.21	0.15
<i>NN12_q-NN12_a</i>	-0.02	0.03	0.14	0.12	0.21	0.14
<i>NN13_q-NN13_a</i>	-0.01	0.03	0.14	0.13	0.22	0.15
<i>NN14_q-NN14_a</i>	-0.01	0.03	0.15	0.14	0.23	0.15
<i>NN15_q-NN15_a</i>	-0.01	0.03	0.16	0.14	0.24	0.16
<i>NN16_q-NN16_a</i>	-0.01	0.02	0.16	0.16	0.25	0.16
<i>NN17_q-NN17_a</i>	0	0.02	0.16	0.16	0.25	0.18
<i>NN18_q-NN18_a</i>	-0.01	0.03	0.17	0.15	0.26	0.18
<i>NN19_q-NN19_a</i>	-0.01	0.02	0.17	0.16	0.27	0.18
<i>NN20_q-NN20_a</i>	-0.01	0.01	0.17	0.17	0.28	0.18
<i>NN21_q-NN21_a</i>	0	0.02	0.18	0.17	0.28	0.19
<i>NN22_q-NN22_a</i>	0	0.02	0.18	0.18	0.28	0.19
<i>NN23_q-NN23_a</i>	-0.01	0.02	0.18	0.18	0.29	0.2
<i>NN24_q-NN24_a</i>	-0.01	0.02	0.18	0.19	0.29	0.2
<i>NN25_q-NN25_a</i>	0	0.02	0.19	0.18	0.3	0.19
<i>NN26_q-NN26_a</i>	0	0.02	0.2	0.19	0.31	0.2
<i>NN27_q-NN27_a</i>	0	0.02	0.2	0.19	0.31	0.2
<i>NN28_q-NN28_a</i>	0	0.03	0.2	0.19	0.32	0.2
<i>NN29_q-NN29_a</i>	0	0.03	0.2	0.19	0.32	0.21
<i>NN30_q-NN30_a</i>	0	0.02	0.2	0.2	0.33	0.21

Only exception to the relaxation trend, is the difference of Fe-B correlation, exhibiting somewhat increase in the interatomic distances after annealing. The tendency of elemental preference upon annealing revealed from the present results is as following;

$$\mathbf{Fe-B < B-B < Fe-Ni < Ni-Ni < Fe-Fe < Ni-B}$$

It shows that Fe-B has a slight tendency to move away from each other, contrary to the Ni-B which has the highest attraction to each other in the annealed state. Does it show that the Ni boride is more favourable than Fe boride? To answer this, the Gibb's free energies of both borides are considered and given as under [TAPP2.2];

NiB	-98.76 KJ/mol
FeB	-69.49 KJ/mol

Thus the Gibbs free energy for NiB being more negative than that of the FeB give a plausible explanation for the tendency of B to move towards the Ni.

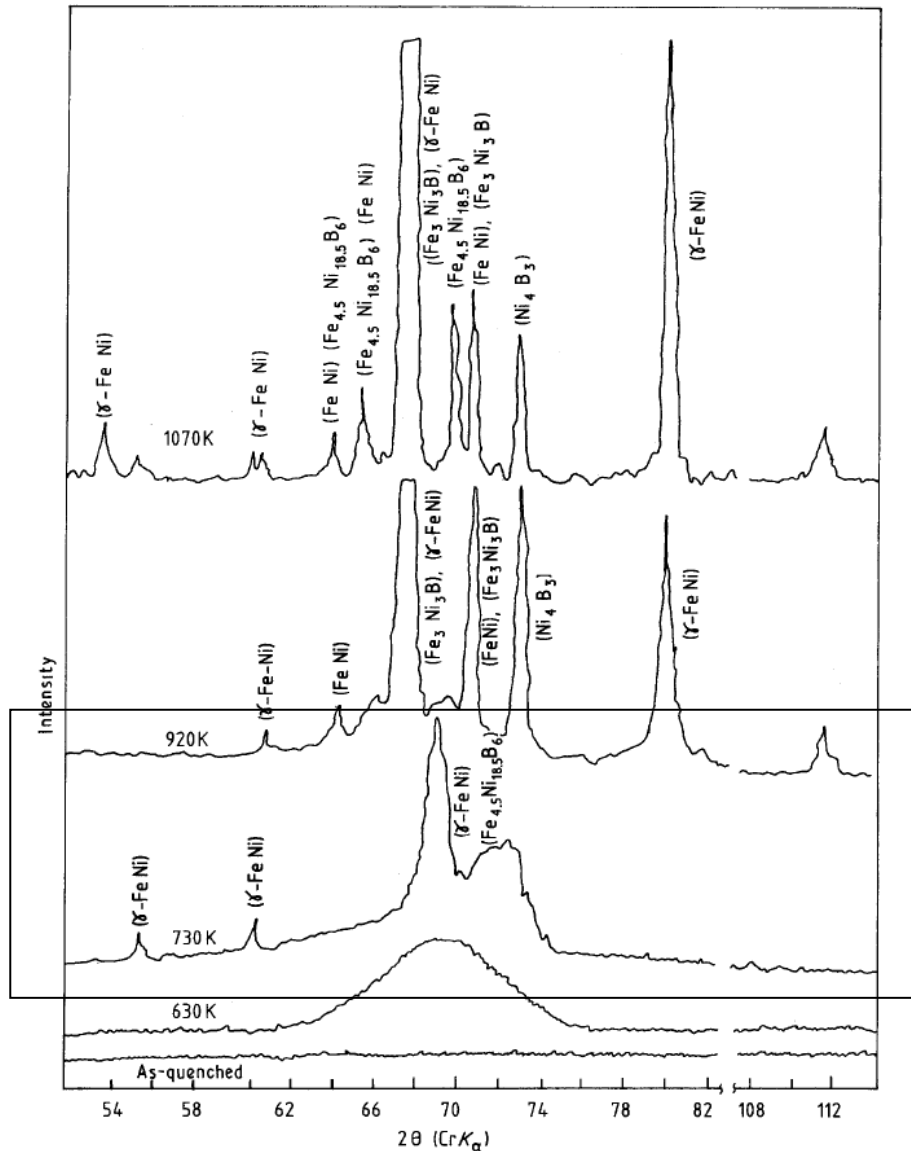


Figure 6.23 X-ray diffractograms of $\text{Fe}_{40}\text{Ni}_{40}\text{B}_{20}$ metallic glass annealed at different stated temperatures for 30 min [Mitra92]. The rectangle shows early stages of crystallization for sample annealed at 457°C .

Different stages of crystallization had earlier been investigated by Mitra and it revealed for early stages (though at higher temperature i.e., 457°C as elaborated by a rectangle in Fig. 6.23) a solid solution of FeNi alongside the $\text{Fe}_{4.5}\text{Ni}_{18.5}\text{B}_6$ and Ni_4B_3 [Mitra92]. Diffraction reveals that further crystallization leads to the formation of Ni_4B_3 , $\text{Fe}_{4.5}\text{Ni}_{18.5}\text{B}_6$ and $\text{Fe}_3\text{Ni}_3\text{B}$ compounds.

Present results reveal the tendency of the incipient grouping of Ni and B that may be is either, directly to yield the aforementioned Ni rich boride, i.e., Ni_4B_3 or is a step towards the formation of ternary Ni-rich $\text{Fe}_{4.5}\text{Ni}_{18.5}\text{B}_6$. For the formation of the $\text{Fe}_{4.5}\text{Ni}_{18.5}\text{B}_6$, B has to move away from the Fe and towards the Ni to meet the required ratio explains the tendency evident from NNE results. It also corroborates the theory proposed by Lewis that slight short range rearrangements for alloys containing high

metalloid concentrations may occur by segregation of the metalloid(s), perhaps leading also to the establishment of incipient metal-metalloid groups and/or regions of high concentrations of metalloid(s) which render the alloy brittle.

Steric periodicity of atomic distribution

To elaborate any structural periodicity, a normalization is made analogous to the one described earlier in section 6.1.5. The distance of the each *NN* is normalized by the first *NN* of corresponding correlation. The normalized distances are summarized in table 6.10. Last column in the table depicts the average ratio of the *NN* of annealed sample for comparison. The resultant ratios after normalization are similar for all elemental correlations, showing that there is a steric relationship rather than chemical. Such a correlation is also reported for Pd based amorphous sample during the course of this research work [Shariq06b].

Table 6.10 The ratio for different elemental correlations after normalizing the average distances of the first fifteen next neighbours by the average distance of first neighbouring atom for as quenched state. Averaged ratio for the annealed state is also given for a comparison. The distances are in Å.

	Fe-Fe	Ni-Ni	Fe-Ni	B-B	Fe-B	Ni-B	Average as quenched	Average annealed
<i>NN2/NN1</i>	1.34	1.35	1.34	1.36	1.33	1.34	1.34 ± 0.02	1.35 ± 0.02
<i>NN3/NN1</i>	1.57	1.58	1.57	1.6	1.56	1.56	1.56 ± 0.03	1.58 ± 0.03
<i>NN4/NN1</i>	1.75	1.76	1.75	1.78	1.74	1.74	1.74 ± 0.03	1.76 ± 0.03
<i>NN5/NN1</i>	1.89	1.91	1.9	1.94	1.89	1.88	1.88 ± 0.04	1.91 ± 0.04
<i>NN6/NN1</i>	2.02	2.04	2.03	2.07	2.02	2.02	2.02 ± 0.04	2.04 ± 0.05
<i>NN7/NN1</i>	2.14	2.16	2.15	2.19	2.14	2.13	2.13 ± 0.04	2.16 ± 0.05
<i>NN8/NN1</i>	2.24	2.27	2.26	2.3	2.24	2.23	2.23 ± 0.05	2.26 ± 0.05
<i>NN9/NN1</i>	2.34	2.37	2.36	2.4	2.34	2.33	2.33 ± 0.05	2.36 ± 0.05
<i>NN10/NN1</i>	2.43	2.46	2.45	2.5	2.43	2.42	2.42 ± 0.06	2.45 ± 0.05
<i>NN11/NN1</i>	2.51	2.55	2.53	2.58	2.51	2.5	2.5 ± 0.06	2.53 ± 0.06
<i>NN12/NN1</i>	2.59	2.63	2.61	2.66	2.59	2.58	2.58 ± 0.06	2.61 ± 0.06
<i>NN13/NN1</i>	2.66	2.71	2.69	2.74	2.67	2.65	2.65 ± 0.07	2.69 ± 0.07
<i>NN14/NN1</i>	2.74	2.78	2.76	2.81	2.74	2.72	2.72 ± 0.07	2.76 ± 0.07
<i>NN15/NN1</i>	2.8	2.85	2.83	2.88	2.81	2.79	2.79 ± 0.07	2.83 ± 0.07

Such an atomic periodicity independent of the elemental correlation, reveal that the underlying principle responsible for periodicity is rather steric: the arrangement of atoms according to the constraint of filling the three dimensional space contrary to the one suggested by Häussler [Häussler85].

6.2.6 Conclusion

The XRD and DSC, the conventional characterization tools don't show any structural transformation for 1 hour annealed $\text{Fe}_{40}\text{Ni}_{40}\text{B}_{20}$ metallic glass at 350°C . TAP results, however, depict a change in the structure on the very fine sub nanometre scale. Albeit, χ^2 test reveal pronounced inhomogeneity for the annealed state, there were slight hints of inhomogeneity for B distribution even for the as quenched $\text{Fe}_{40}\text{Ni}_{40}\text{B}_{20}$ glassy ribbon.

The state of art NNE algorithm successfully reveals first thirty next neighbours for both as quenched and annealed state. The distances for the next neighbours of different elemental correlations are in a very good agreement with the data available in literature. The distance distributions of next neighbouring atoms show that Fe-Fe atoms have the highest probability to be the next neighbours to each other. A steric periodicity of the atoms is also depicted by normalizing the NV distances by the first next neighbour distance NNI ; yielding a ratio similar for all elemental correlations showing that there exist a certain order among the atoms, irrespective of their chemical nature. A comparison of the NV atomic distribution for as quenched and annealed state reveals accumulation of Ni and B. It also shows the tendency of Fe and B to move slightly away from each other. These findings are in good agreement with the Gibbs free energies for Ni- and Fe boride formation; a Ni rich boride formation is also enunciated by Mitra [Mitra92]. Lucid evidence of the aforementioned boride formation corroborate Lewis's postulate about the change in short range ordering, a primordial step to boride formation, which causes embrittlement of the $\text{Fe}_{40}\text{Ni}_{40}\text{B}_{20}$ metallic glass even before the crystallization temperature.

6.3 $\text{Zr}_{53}\text{Co}_{23.5}\text{Al}_{23.5}$ Amorphous Alloys

Results and Discussion

This section essentially deals with a detailed study of the $\text{Zr}_{53}\text{Co}_{23.5}\text{Al}_{23.5}$ glassy system. Both, bulk amorphous alloys and metallic glasses are investigated during the course of this work. In addition to microstructural investigations utilizing DSC, XRD, SEM, HR/TEM, EFTEM, TAP, CFIIT and FIM, SQUID has been utilized to determine the magnetic properties. Apart from the microstructural features in the as cast/quenched state, heat treated samples are also characterized in order to depict the crystallization kinetics and subsequent effect on the magnetic properties.

6.3.1 As cast $\text{Zr}_{53}\text{Co}_{23.5}\text{Al}_{23.5}$ bulk amorphous alloys

Diffraction study by X-rays

The XRD was utilized for a microscopic glance to reveal, if the bulk amorphous alloy is pure amorphous or constitutes some crystalline inclusions and thereby forming a composite structure. Fig. 6.24 shows the XRD patterns for the $\text{Zr}_{53}\text{Co}_{23.5}\text{Al}_{23.5}$ bulk amorphous alloy. Apart from the typical first

order and second order humps⁷, no additional crystallization peaks are present for the as cast state. Absence of crystalline peaks depicts that the bulk samples are X-ray amorphous, a term widely adapted, more recently.

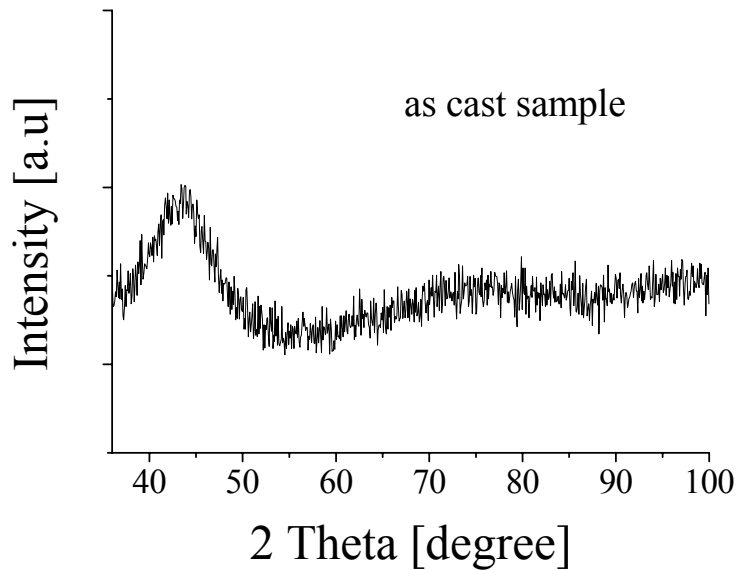


Figure 6.24 X-ray diffractogram of $Zr_{53}Al_{23.5}Co_{23.5}$ bulk sample for as cast state.

Thermal characterization by DSC

The DSC scan of $Zr_{53}Co_{23.5}Al_{23.5}$ bulk amorphous alloy is illustrated in Fig. 6.25. It essentially features a glass transition temperature T_g at 510°C and the onset temperature of crystallization T_x is at 563°C. The intriguing features exhibited are two well defined crystallization peaks at 568°C and 586°C. These two peak temperatures are assigned as T_{p1} and T_{p2} , respectively as manifested in the Fig. 6.25.

The reason for multiple-peaks in the DSC scan observed can be explained in a number of ways:

- Multiphase amorphous alloy in which each phase contribute a separate exothermic peak [Mattern05].
- Multi-step crystallization, a transformation from amorphous phase further to a metastable phase and then to a stable phase e.g., transformation into quasicrystalline phase and a subsequent decomposition [He03].
- Amorphous-crystalline composite material.
- During the course of crystallization, the composition of the remaining phase can vary remarkably from the nominal composition and hence can result in an additional crystallization peak or a shoulder [Cahn96].

To evince the rationale for two crystallization peaks, further investigations were carried out utilizing SEM, SQUID and TEM.

⁷ Due to the limited resolution of XRD, it is difficult to state with surety that the sample is pure amorphous.

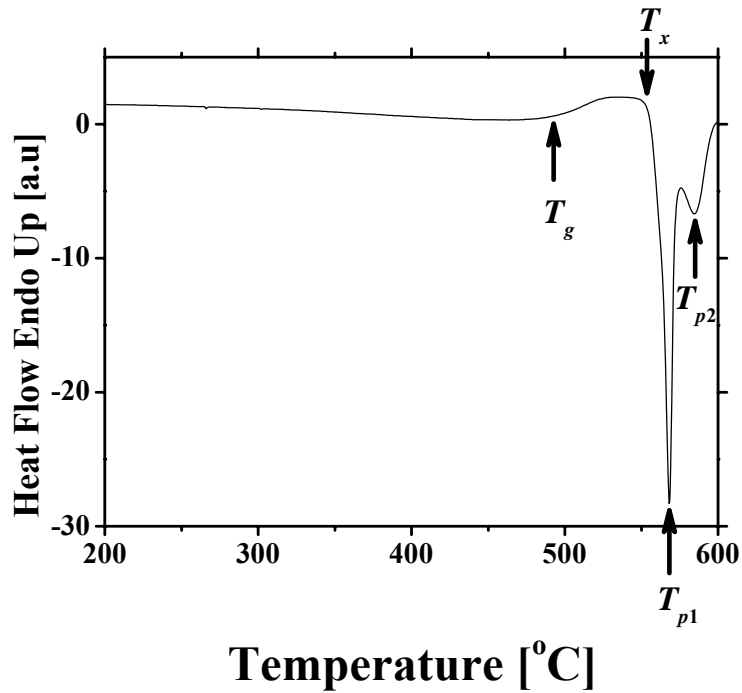


Figure 6.25 DSC scan of as cast $Zr_{53}Co_{23.5}Al_{23.5}$ bulk sample (Heating rate is $20^{\circ}C/min$).

Microstructural investigations by SEM

Fig. 6.26 depicts the SEM micrograph of the as cast sample. The SEM investigation shows a homogeneous structure of the amorphous alloy with no phase contrast that can be attributed to any phase separation. The elongated lines in the SEM micrograph are due to the grinding of the sample. A compositional SEM-EDX line scan for as cast sample is illustrated in Fig. 6.27, demonstrates rather a homogeneous structure. However, the resolution of the chemical analysis of EDX in SEM limits due to the larger size of the interaction volume (μm) of the electron beam on the specimen surface.

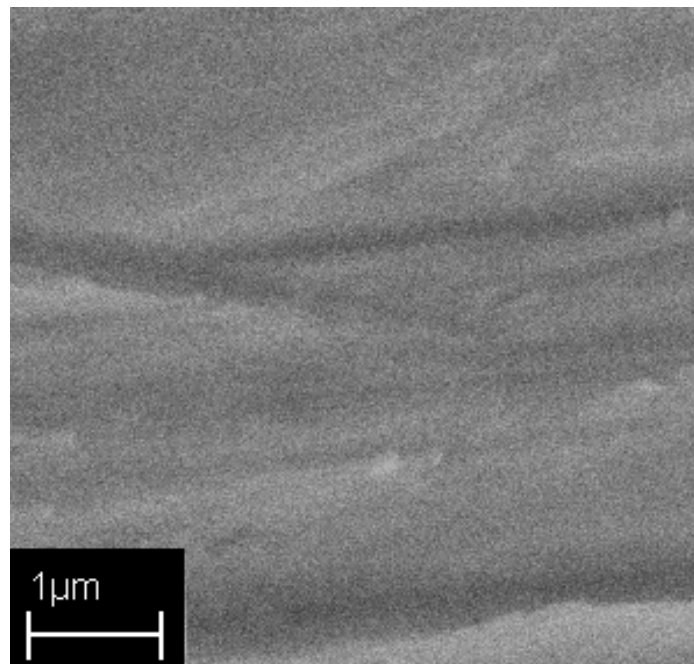


Figure 6.26 SEM micrograph of as cast $Zr_{53}Co_{23.5}Al_{23.5}$ bulk sample.

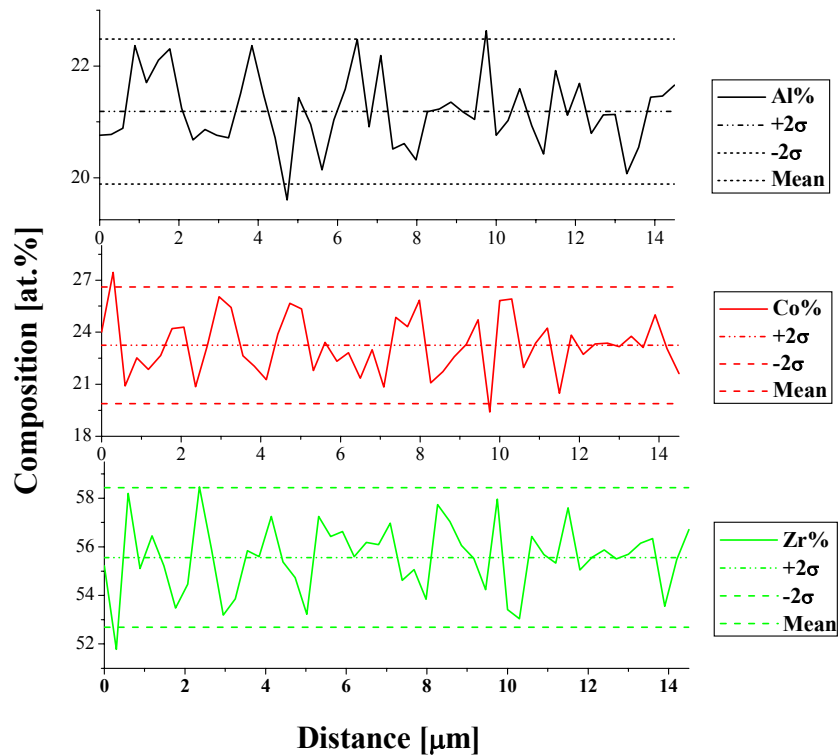


Figure 6.27 SEM-EDX, compositional line scan of as cast $Zr_{53}Co_{23.5}Al_{23.5}$ bulk sample.

A comparison of the nominal composition and composition calculated utilizing SEM-EDX is depicted in table 6.11. The composition calculated utilizing EDX scan is within the error bars, except that of Al concentration. Slightly low concentration of Al than nominal concentration reflects to the inaccuracy of the SEM-EDX analysis.

Table 6.11 A comparison of the nominal and calculated composition of the as cast $Zr_{53}Co_{23.5}Al_{23.5}$ bulk sample.

Element	Nominal composition	SEM-EDX
Zr at. %	53	55.6 ± 2.8
Co at. %	23.5	23.2 ± 1.3
Al at. %	23.5	21.2 ± 1.3

Microstructural investigations by HRTEM

Owing to the limited resolution of the XRD and SEM, conventional and high resolution TEMs are utilized for detailed microstructural study of the as cast $Zr_{53}Co_{23.5}Al_{23.5}$ bulk samples. Fig. 6.28 depicts different HRTEM micrographs. Fig. 6.28a illustrates an overview of the overall microstructure of the bulk sample. Fig. 6.28b & c illustrate the bright field images in order to elaborate any phase contrast, if present at all.

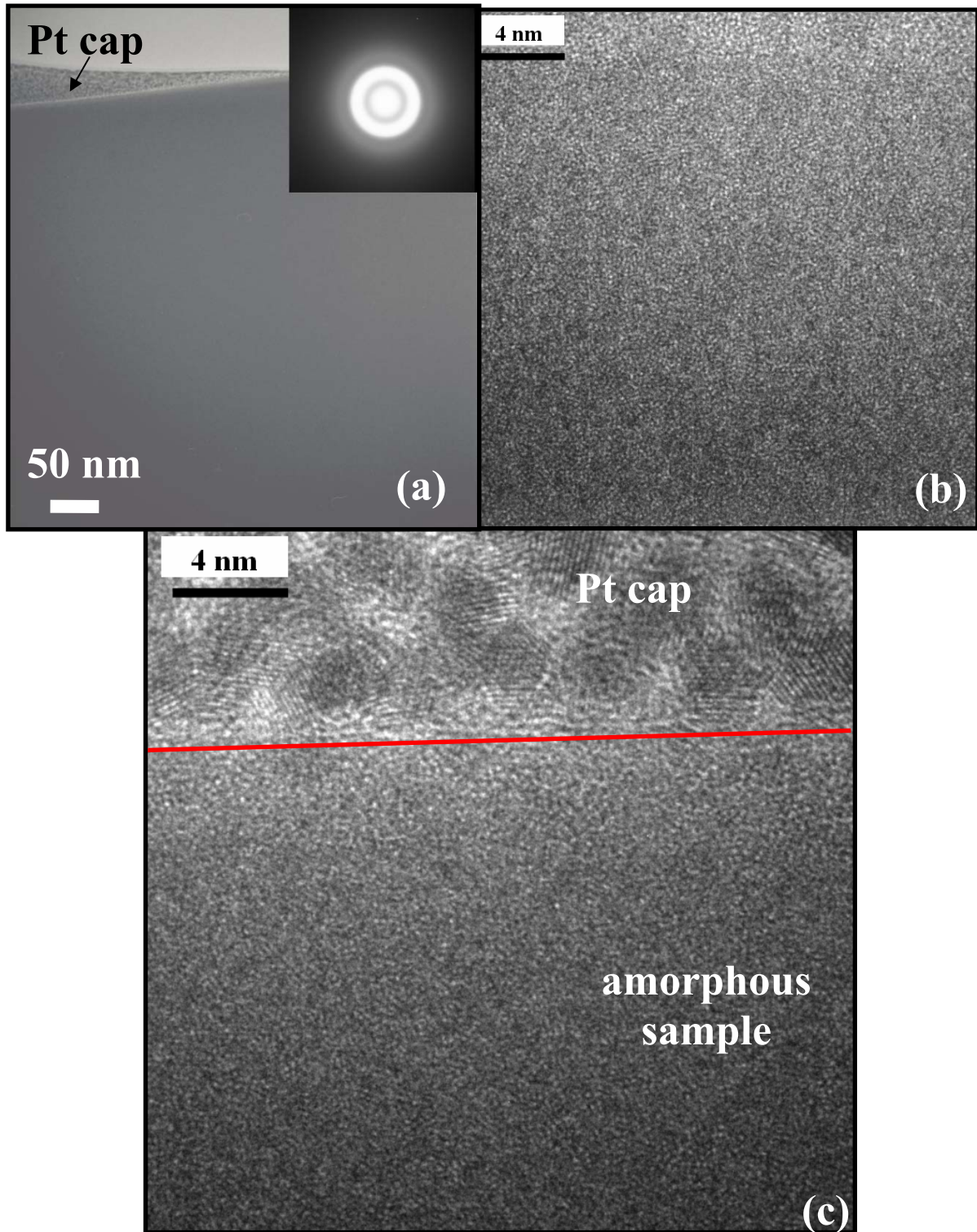


Figure 6.28 HRTEM micrographs (a) bright field image of the as cast $Zr_{53}Co_{23.5}Al_{23.5}$ bulk sample, along with the SAD of the amorphous sample, (b) HRTEM bright field image of the amorphous matrix, (c) HRTEM bright field image of the amorphous matrix along with Pt layer deposited to save the sample from sever ion beam interaction during the sample preparation.

No phase contrast is evident from the TEM micrograph neither from bright field images nor from dark field images⁸. Selected area diffraction pattern of the amorphous matrix shown in the inset of Fig.6.28a demonstrates rings typical for an amorphous structure. Fig. 6.28b shows the HRTEM

⁸ Dark field images are not shown here.

micrograph of the amorphous matrix, no crystallites are resolved in this image and the structure of the sample insinuates to be amorphous at such extreme resolutions. Fig. 6.28c depicts lucidly the structural differences of amorphous and a nano-crystalline structure. It contains a micrograph of the bulk sample containing the Pt layer (cap) deposited on the sample to obviate from unwanted ion/electron beam interaction with the sample, during the sample preparation by ion beam milling. Nano-crystallites of ~ 2 nm size are evident in the e-beam deposited Pt layer with lucid lattice planes. The line on the micrograph is a rough indication of the interface between the sample and the deposited layer. However, no phase contrast or lattice planes are evident from the amorphous sample below the line separating the amorphous matrix from the Pt cap.

6.3.2 Heat treated $Zr_{53}Co_{23.5}Al_{23.5}$ bulk amorphous alloys

Thermal characterization by DSC

Albeit, microstructural investigations by XRD, SEM and TEM are carried out, the underlying reason for two exothermic peaks evident in the DSC scan (Fig. 6.25) of the bulk sample is still quite ambiguous. Among different aforementioned rationales, no phase separation or crystalline inclusions are revealed by microstructural investigations. To further delve this issue, the effect of the aging at high temperature on the two peaks is further investigated.

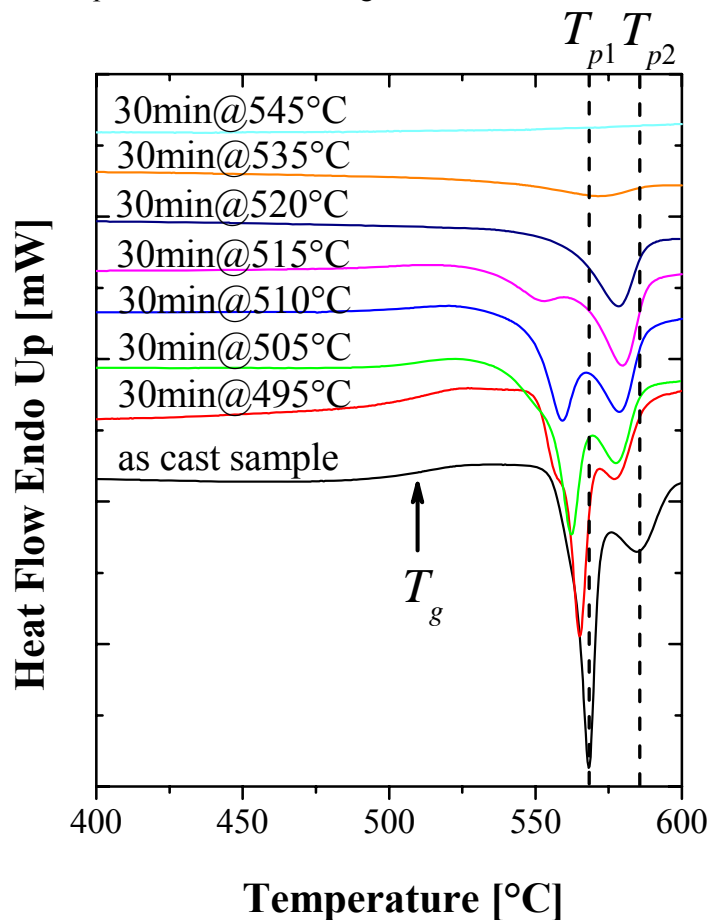


Figure 6.29 DSC scans of as cast $Zr_{53}Co_{23.5}Al_{23.5}$ bulk sample and samples heat treated at different temperatures from 495-545°C for 30 minutes (Heating rate is 20°C/min).

Bulk samples are heat treated in a temperature range of 495°C - 545°C for 30 minutes. The heat treatment was carried out inside a DSC furnace under Ar flow to obviate from oxidation. The sample preparation for heat treatment was similar as that of DSC samples⁹. Fig. 6.29 depicts the DSC curves for as cast bulk sample and bulk samples heated for 30 minutes at different temperatures from 495°C - 545°C. The peak temperatures shift to the lower temperature by the heat treatment, as evident from the dashed line indicating the original peak positions. However, both peaks show a different behaviour to the heat treatment. The area under peak I decreases with increasing the temperature indicating that for the highest temperature of heat treatment the exothermic reaction (i.e., crystallization) in the sample makes no palpable difference that can be recorded by DSC anymore. Contrarily, the area under peak II increases first, followed by a decrease. To elaborate aforementioned behaviour, the difference in the heat of enthalpies as a function of temperature, are presented in Fig. 6.30.

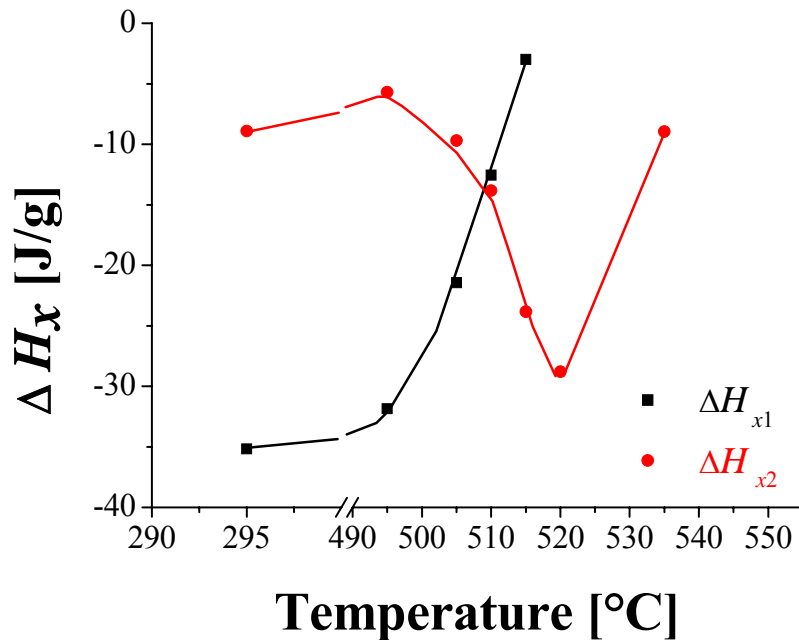


Figure 6.30 Variation of ΔH_x as a function of heat treated temperature for $Zr_{53}Co_{23.5}Al_{23.5}$ bulk samples.

The magnitude of enthalpy change for the phase responsible for peak I decreases with the increase in heat treated temperature, on the other hand for the phase responsible for peak II first increases with a subsequent decrease. This behaviour shows that the phase responsible for the second peak needs still higher temperature for a complete transformation.

Fig. 6.31 represents the glass transition temperature T_g and both peak temperatures (i.e., T_{p1} and T_{p2}) as a function of heat treated temperatures. The glass transition temperature remains constant for samples heat treated till 505°C followed by a sudden decrease. The sample with the heat treatment at 520°C and higher shows no glass transition that can be recorded by the DSC.

⁹ See chapter 5 § 1.

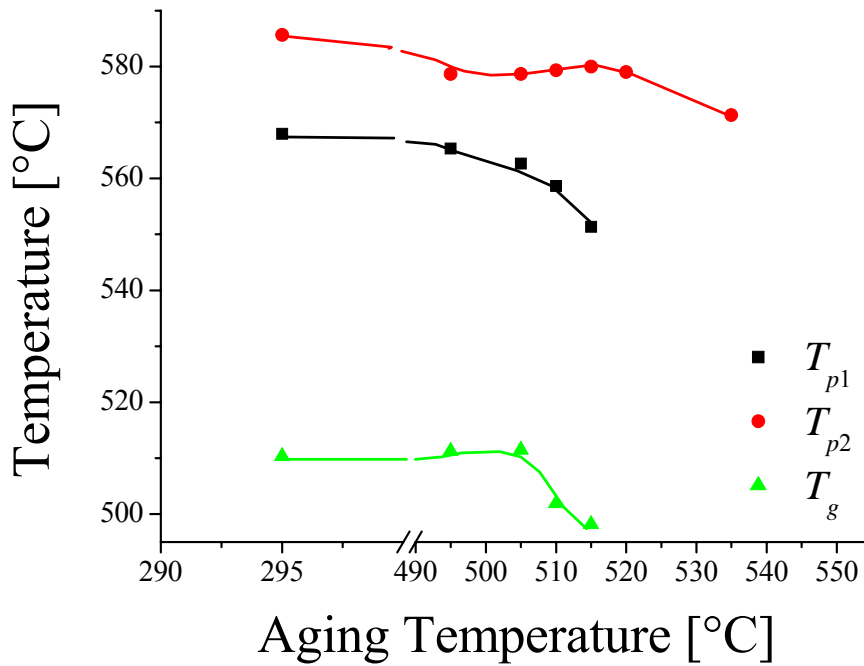


Figure 6.31 Variation of the glass transition temperature and crystallization peak temperatures as a function of heat treated temperature for $Zr_{53}Co_{23.5}Al_{23.5}$ bulk samples.

The crystallization peak temperature, T_{p1} decreases gradually with the increase in the heat treatment temperature and crystallization of this phase completes before 520°C. The crystallization peak temperature, T_{p2} decreases a bit after the first heat treatment at 495°C and then a sudden rise is recorded followed by a subsequent drop. This change in T_{p2} with respect to aging temperature is lucid from Fig. 6.29. The crystallization of this phase completes around 545°C. The intriguing finding from these DSC scans is that the crystallisation seems to start already around 495°C and finishes around 545°C when heat treated for 30 minutes, against a glass transition temperature of 510°C and crystallization onset temperature of 563°C. The fact that the crystallization starts already at 495°C hints that may be the bulk sample is a composite of a very small amount of crystalline phase embedded in amorphous phase leading to crystallization even below the glass transition temperature. However, no phase separation or composite structure is evident from the microstructural investigations. It is also not plausible to attribute two peaks to multi-step crystallization process during the DSC, as clearly the peak position and extent of heat of enthalpy changes with the change in the heat treatment even for low temperatures, which should be in principle same for same DSC parameters. Moreover, a decrease in the glass transition temperature and subsequent diminishing attributes to a phenomenon responsible after crystallization in amorphous alloys.

6.3.3 Magnetic properties of the as cast and heat treated $Zr_{53}Co_{23.5}Al_{23.5}$ bulk samples

The most commercial and sensitive instrument, SQUID, has been utilized to delve the magnetic properties of the $Zr_{53}Co_{23.5}Al_{23.5}$ bulk samples and subsequent effect of crystallization on these properties. Fig. 6.32 illustrates the typical hysteresis curve obtained from the SQUID for the as cast

bulk sample. The bulk sample reveals very soft ferromagnetic properties with very small amount of hysteresis, showing a remanent magnetization, M_r , of around 3.9×10^{-4} emu/g and coercivity, H_c of 25 Oe is required to return the magnetization back to zero. The trend line of hysteresis curve of as prepared bulk sample seems to have the saturation fields much larger than 2T.

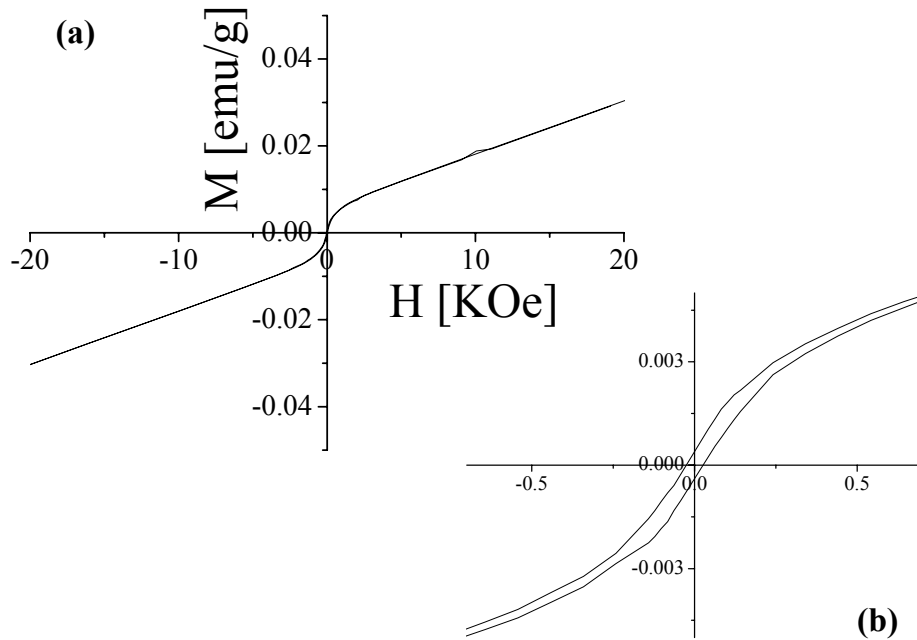


Figure 6.32 (a) Hysteresis loop measured at room temperature for as cast $Zr_{53}Co_{23.5}Al_{23.5}$ bulk sample, (b) a magnified portion of the hysteresis loop at low magnetic field, H.

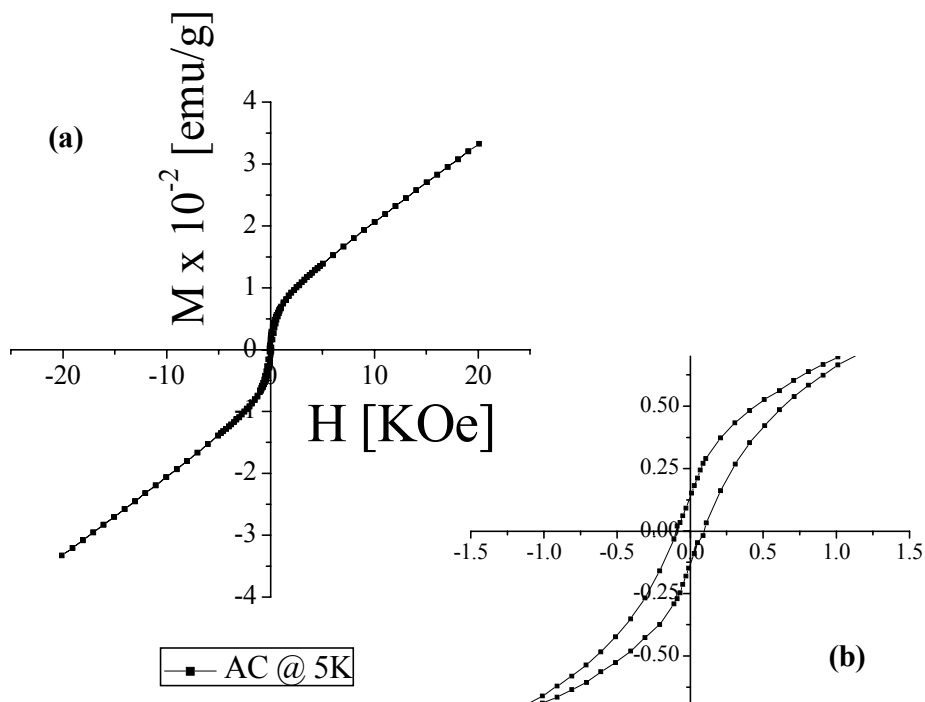


Figure 6.33 (a) Hysteresis loop measured at 5K for as cast $Zr_{53}Co_{23.5}Al_{23.5}$ bulk sample, (b) a magnified portion of the hysteresis loop at low magnetic field, H.

As a matter of fact, that the atomic vibrations and fluctuations are least at deep temperatures and hence, will lead to a higher magnetization, correspondingly saturation magnetization might reach at lower applied fields. Fig. 6.33 illustrates the hysteresis loop of the as cast bulk sample at 5K. Albeit, an increase in net magnetization is revealed at this temperature, no saturation is yet attained till 2T and trend line of the hysteresis loop indicates that the saturation is far from occurring.

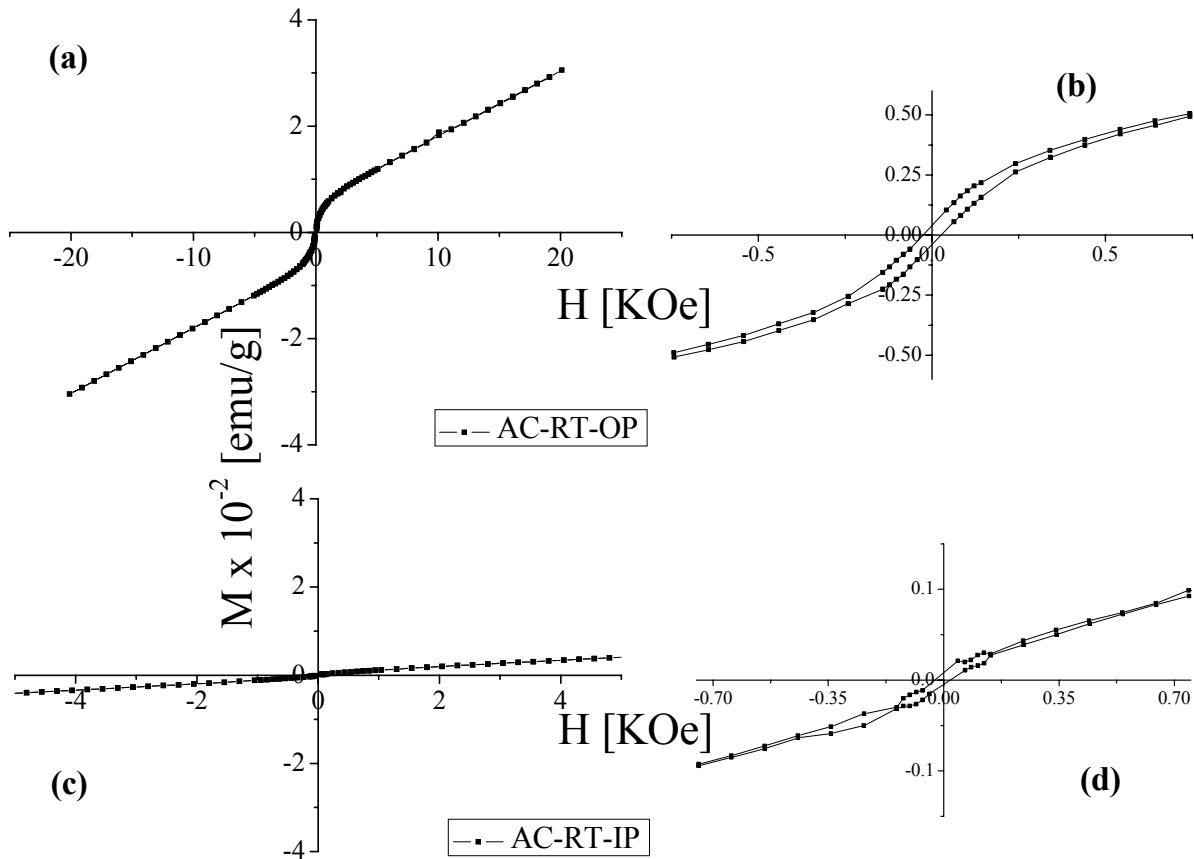


Figure 6.34 Hysteresis loops measured at room temperatures for as cast $Zr_{53}Co_{23.5}Al_{23.5}$ bulk samples a) out of plane to the direction of the applied field, (b) a corresponding magnified portion of hysteresis loops for low fields, (c) in plane to the direction of applied field in SQUID and (d) a magnified portion of hysteresis loops for low fields.

Fig.6.34 illustrates the hysteresis of the as cast bulk sample recorded in plane and out of the plane to the direction of the applied field in the SQUID. The hysteresis loops lucidly illustrates the magnetic anisotropy; as shown in Fig. 6.34a & b. The net magnetization for sample out of plane to the applied field is higher than in plane sample at room temperature, ruling out the shape anisotropic effect. For non-spherical geometry of the specimen, long axis is easy to magnetize as compared to that of short axis [Cullity72]. Along the short axis the magnetized specimen will produce magnetic charges or poles at the surface. This surface charge distribution, acting in isolation, is itself another source of a magnetic field, called the demagnetizing field because it acts in opposition to the magnetization that produces it, resulting in reduction of the net magnetization along short axis. However, in this case the

net magnetization is less for the long axis. Hence, the decrease in net magnetization isn't explainable by shape anisotropy. Another plausible explanation, is the presence of the crystalline phase in the as cast bulk sample that can lead to a magnetic anisotropy. This aspect is dealt in detail in the next section.

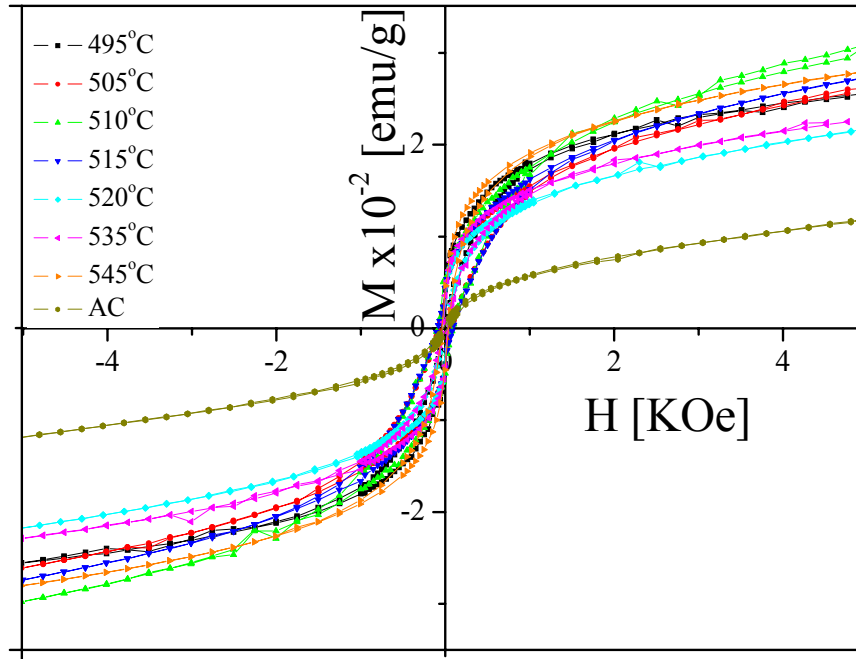


Figure 6.35 Hysteresis loops measured at room temperature for as cast $Zr_{53}Co_{23.5}Al_{23.5}$ bulk sample and bulk samples heat treated at different temperatures for 30 minutes.

A comparison of the hysteresis curves of as cast sample and samples heat treated at different temperatures for 30 minutes is shown in Fig. 6.35. The net magnetization is higher for all heat treated samples than the as cast bulk sample, showing that there is a change in the structure of the samples even after first heat treatment at 495°C for 30 minutes. Fig. 6.36 illustrates the coercivity and remanent magnetization as a function of heat treated temperature, for a better comparison and quantitative illustration of the differences among as cast sample and samples heat treated at different temperatures. The coercivity increases to almost 90% by the first heat treatment i.e., heat treating at the 495°C for 30 minutes in bulk samples with a corresponding increase of 925% in the remanent magnetization M_r . The temperature regime for the changes in coercivity and remanent magnetization are consistent with the thermodynamical attributes of the heat treated samples from the DSC scans (Fig. 6.30 and Fig. 6.31). Hence, the crystallization and subsequent growth of the phase responsible for T_{p1} contributes to an increase in both coercive field and remanent magnetization. Contrarily, the phase responsible for the second peak i.e., for T_{p2} has an opposite effect on both the coercive field and remanent magnetization though hints for a slight increase during the growth. The remanent magnetization M_r is a strong function of specimen magnetic history and the fact that small amounts of field were applied to properly adjust the specimen in SQUID, the magnetization at 0,5T is also compared with the aging temperatures and reveals the same trend as that of remanent magnetization, hence showing the effect is

not owing to magnetic field but rather because of the structure of the bulk sample. Herzer enunciated somewhat similar dependence of the soft ferromagnetic properties on the structure of the Fe based amorphous system [Herzer90].

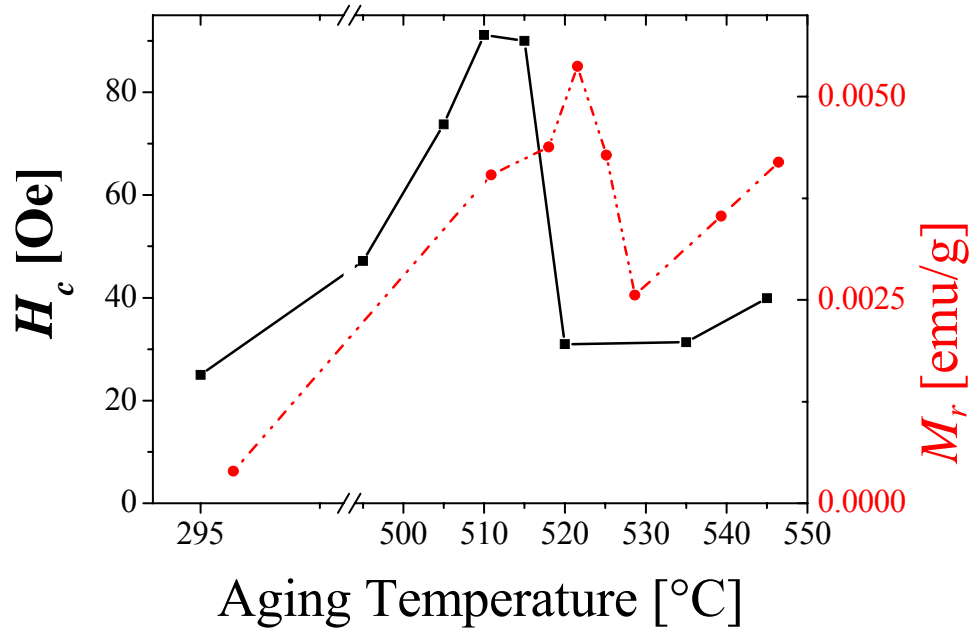


Figure 6.36 Variation of the remanent magnetization, M_r and coercivity, H_c as a function of heat treated temperature for $Zr_{53}Co_{23.5}Al_{23.5}$ bulk sample. The dashed line represents the remanent magnetization M_r while solid line depicts the variation of the coercivity H_c .

Microstructural investigations by TEM

In order to study the microstructural changes upon heat treatment, the TEM lamellas were prepared for the sample heat treated at 545°C for 30 minutes. The sample shows a multiphase structure under TEM, containing crystalline phases as well. Fig. 6.37 depicts corresponding TEM micrographs obtained under different operating conditions. Fig. 6.37a shows ambiguous phase contrast, this micrograph was obtained with both beams i.e., direct incident beam and diffracted beam, the Pt layers deposited during TEM sample preparation are also evident.

However, the phase contrast elaborates considerably, under bright field imaging condition. The morphology of different grains reveal from these micrographs is rather complex and it is evident that different grains are not having lucid interfaces rather are diffuse into each other. The SAD patterns from the sample, shown in the Figs. 6.37a & b are obtained utilizing convergent beam and parallel beam, respectively. The diffraction spots decorated alongside the rings are indication of crystalline phase and are relatively sharp in the parallel beam selected area diffraction pattern than the other one. Palpable amounts of crystalline phases were also perceived from the respective DSC scans, where no more crystallization exothermic peak is detectable. Moiré fringes, typical for the crystalline phase, are lucid from Figs. 6.37a & b; an indicative of the presence of the crystalline phase.

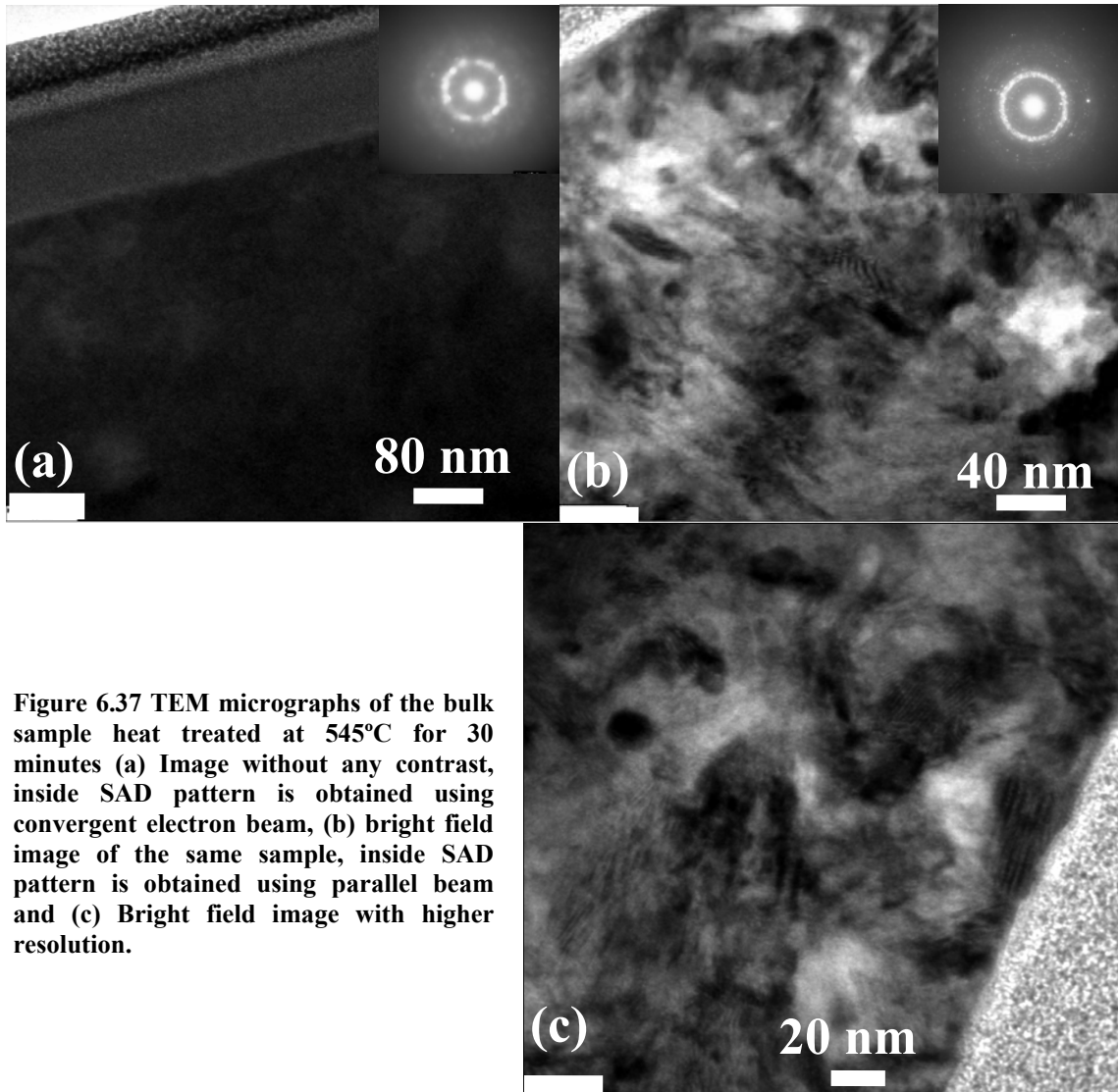


Figure 6.37 TEM micrographs of the bulk sample heat treated at 545°C for 30 minutes (a) Image without any contrast, inside SAD pattern is obtained using convergent electron beam, (b) bright field image of the same sample, inside SAD pattern is obtained using parallel beam and (c) Bright field image with higher resolution.

The grain morphology is quite evident from the phase contrast from bright field images, depicted in Fig. 6.37. To demonstrate the concentration variations EDS scan were carried out and the corresponding scans are illustrated in Fig. 6.38. The bright field image for which the EDS scan was carried out is shown in Fig. 6.38a. On the other hand, Fig. 6.38b, c & d shows the corresponding, EDS scans for Co, Al and Zr, respectively. Dark and bright regions of Co depleted and Co enriched phase are lucid in the Fig. 6.38b. The Co depleted phase which is dark in Fig. 6.38b (indicated by arrows), is enriched in Al concentration as indicated by arrows in Fig. 6.38c, regions that are bright. For Zr concentration, the scan is unanimously bright that's because of the higher concentrations of Zr throughout the sample.

A comparison of the bright filed image and the EDS scans, also reveal that the phase appeared bright in the bright field image is Co depleted and Al enriched as marked by arrows in Fig. 6.38. It means that the bright spots in the bright field micrographs presented in Fig. 6.37, also represent Al enriched and Co depleted phase.

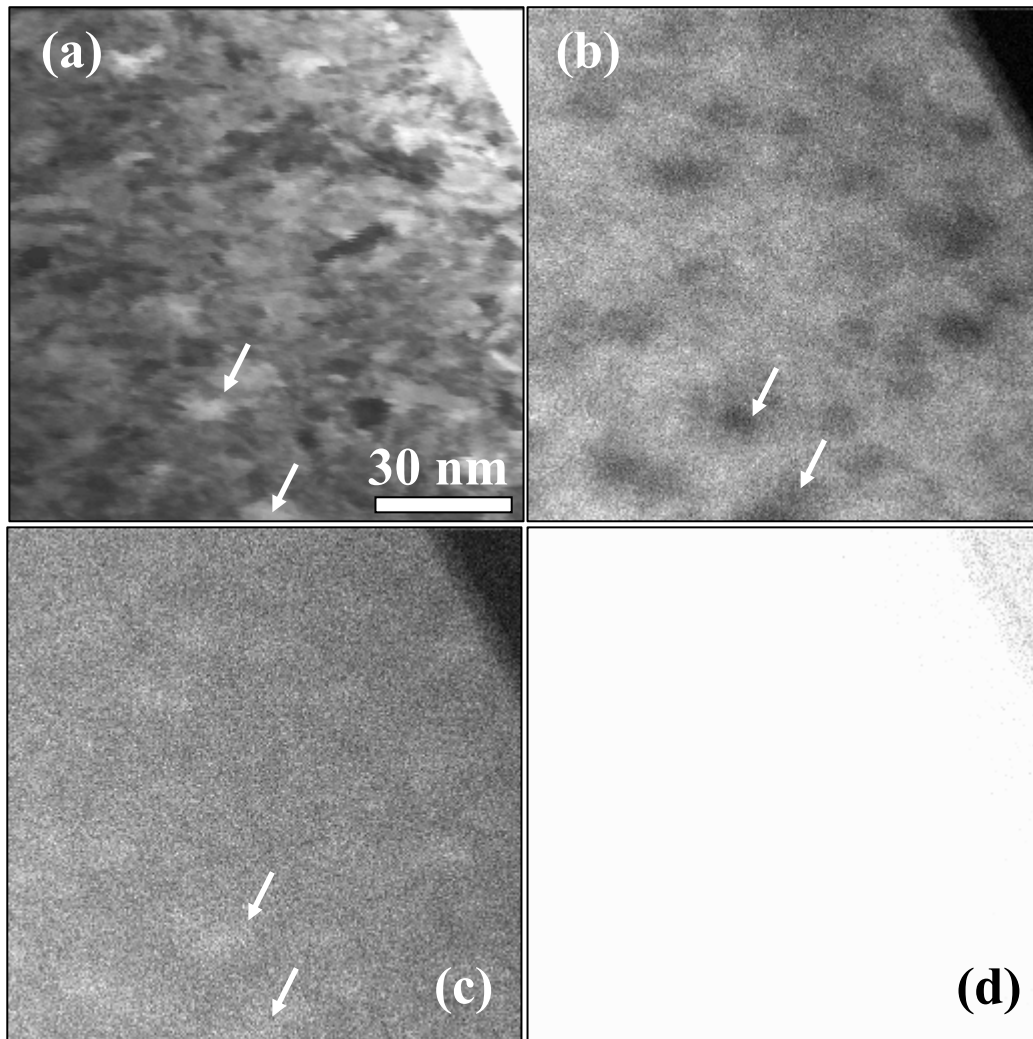


Figure 6.38 (a) Bright field TEM micrograph and corresponding EDS scans for (b) Co, (c) Al and (d) Zr concentrations of the bulk sample heat treated at 545°C for 30 minutes.

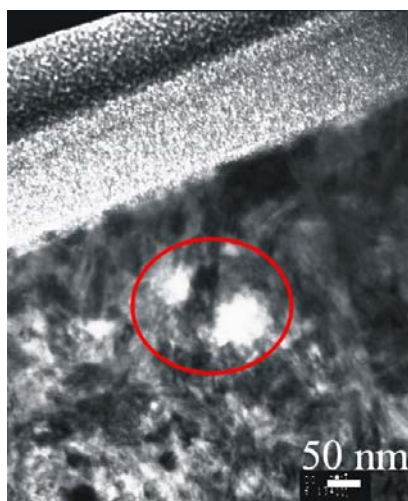


Table 6.12 Chemical composition of different regions obtained by TEM-EDS

	Zr at. %	Co at. %	Al at. %
Bright	61.8	3.7	34.5
Grey	62.1	11.6	26.3
Dark	60.6	9.4	30
Bright	61.8	5.3	32.9
Grey	60.8	10.3	28.9

Figure 6.39 TEM micrograph, encircled region is utilized for obtaining chemical composition utilising EDS.

To corroborate it, EDS analysis on each individual phase was carried out. Fig. 6.39 shows the bright field image and the encircled region is further exploited for chemical analysis. Table 6.12 summarizes the resultant phase composition from the bright, grey and dark regions in the encircled area. The bright regions are depleted in Co and both grey and dark regions are enriched in Al concentration and vice versa.

The above stated composition is a rough estimate as the electron beam interaction may overlap the next region. Moreover, as the thickness of the TEM specimen is between 80-100 nm, larger than some grains revealed in the TEM micrographs, there is a chance that a grain of a phase is overlying the other one along the depth of the specimen. In such case the electron beam interaction in depth may give signals from the lower grains as well.

To conclude, the heat treated sample comprises of grains of different size but less than 100 nm, and are quite complex in morphology with inter-diffused interfaces, as revealed by the phase contrast in TEM micrograph. In addition, Al enriched phase appear as brightest phase in the TEM micrographs. Co rich regions present in the heat treated sample, would therefore explain the increase in the net magnetization in heat treated samples.

6.3.5 $Zr_{53}Co_{23.5}Al_{23.5}$ metallic glass (splat quenched)

The microstructural investigations on the $Zr_{53}Co_{23.5}Al_{23.5}$ bulk amorphous alloys lead to an ambiguous conclusion, the DSC and SQUID investigations show rather a composite structure than a homogeneous single phase structure revealed from SEM and HRTEM investigations. For a comparison of the thermodynamic and magnetic behaviour of the bulk sample, stoichiometrically identical metallic glasses are prepared by splat quenching. It will not only help to elicit the effect of faster cooling rate on the thermodynamics of this system, but also to elucidate the subsequent effect on magnetic properties after heat treatment.

Diffraction study by X-rays

Fig. 6.40 shows a theta-2theta plot obtained from XRD for the $Zr_{53}Co_{23.5}Al_{23.5}$ splat sample, bearing typical first and second order humps for amorphous structure. Such a diffractogram is analogous to the one obtained for bulk sample; no crystalline peaks are evident for the as quenched state as per perception for a splat sample fabricated with comparatively higher cooling rates.

Thermal characterization by DSC

Fig. 6.41 depicts the DSC trace of the as quenched $Zr_{53}Co_{23.5}Al_{23.5}$ splat sample. Contrary to the bulk sample, the splat sample exhibit a single exothermic peak though contains a meek pro-shoulder (pro-shoulder). Cahn and Greer have enunciated such an extension as an after affect of crystallization

leading to a remaining matrix with a different composition than the nominal composition, thereby crystallizes at slightly different temperature [Cahn96].

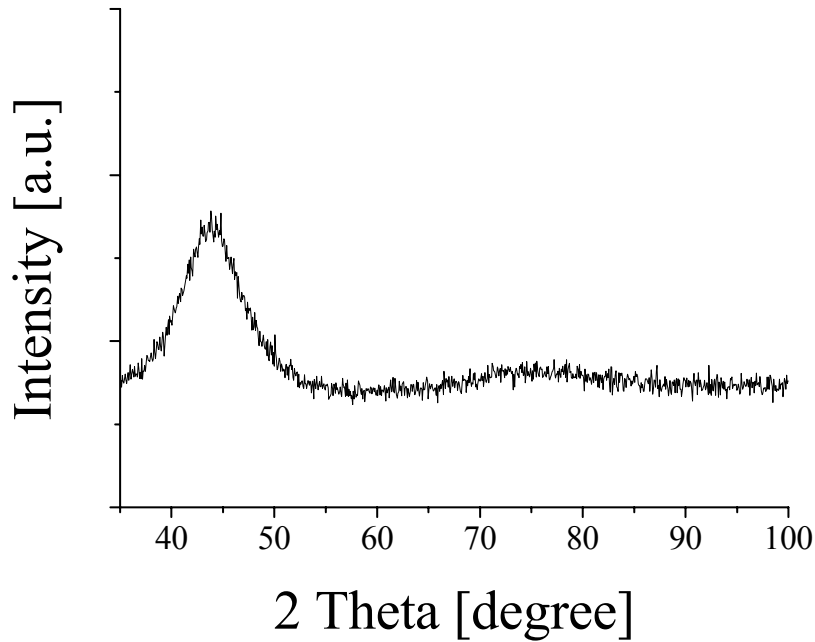


Figure 6.40 X-ray diffractogram of $Zr_{53}Al_{23.5}Co_{23.5}$ splat sample.

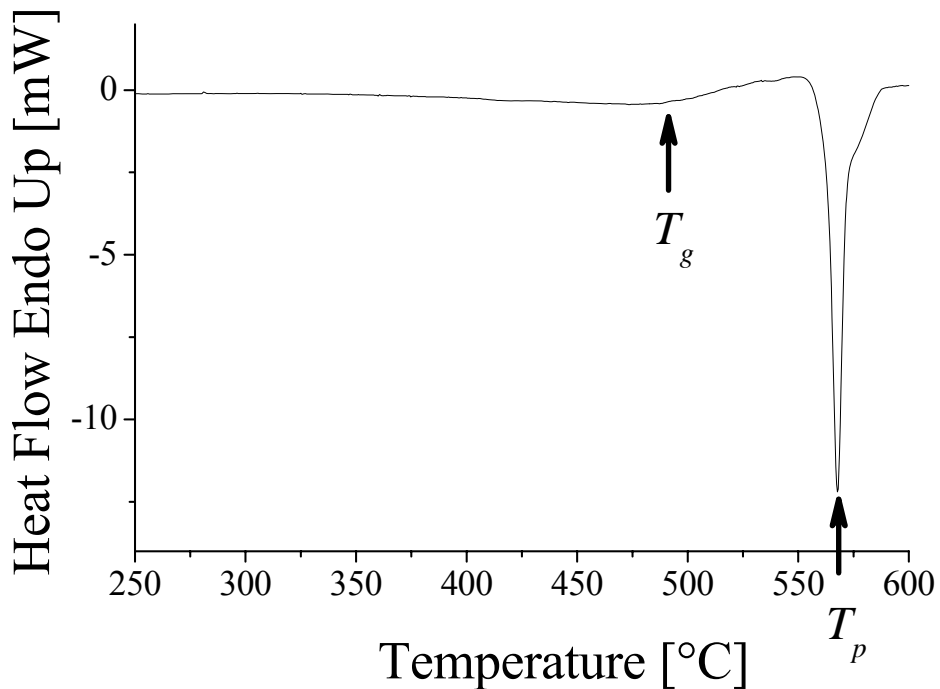


Figure 6.41 DSC scan of as cast $Zr_{53}Co_{23.5}Al_{23.5}$ splat sample (Heating rate is $20^{\circ}C/min$).

Other attributes related to the DSC scan of the splat quenched sample are a glass transition temperature T_g at $492^{\circ}C$, onset of crystallization at $551^{\circ}C$ and crystallization peak temperature T_p at $568^{\circ}C$. The absence of second peak suggests that the splat constitutes of rather a single amorphous

phase contrary to the bulk sample. A defiant exothermic peak for the same heating rate of the splat sample also rule out the fact that two peaks in the DSC scan of the as cast bulk sample might be multi-step crystallization caused during the DSC run. Albeit, for different cooling rates of splat and bulk samples, stoichiometrically identical alloys exhibit somewhat identical crystallization scenario for same heating rates in the DSC scan.

Magnetic properties of the as quenched and heat treated $Zr_{53}Co_{23.5}Al_{23.5}$ splat samples

The hysteresis loop of the as quenched $Zr_{53}Co_{23.5}Al_{23.5}$ splat sample is shown in Fig. 6.42. It reveals very soft ferromagnetic properties with very small amount of hysteresis, showing a remanent magnetization, M_r of around 3.13×10^{-4} emu/g and coercivity, H_c of 47 Oe is required to return the magnetization back to zero.

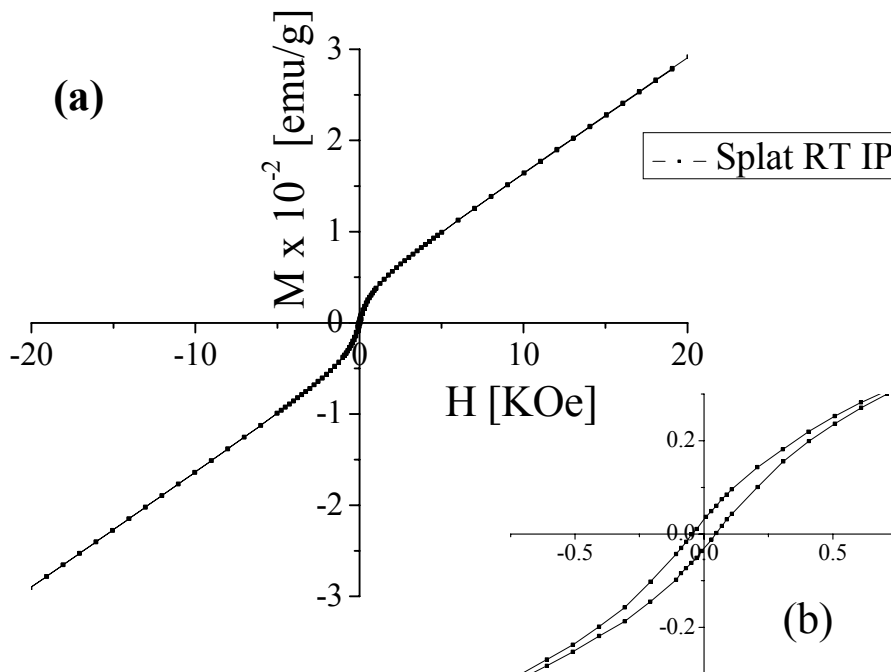


Figure 6.42 (a) Hysteresis loop measured at 5K for as cast $Zr_{53}Co_{23.5}Al_{23.5}$ splat sample, (b) a magnified portion of the hysteresis loop at low magnetic field, H .

These values are comparable to the bulk sample, showing that faster cooling rate don't affect the magnetic properties palpably. The trend line of magnetisation of as quenched sample seems to have the saturation fields much larger than 2T. Intriguingly, there is no difference recorded in net magnetization of the as quenched sample in out of plane and in plane direction to the applied field in the SQUID¹⁰. This behaviour corroborates the rationale that the magnetic anisotropy present in the bulk sample is magneto-crystalline anisotropy i.e., the crystalline phase present in as cast bulk samples. However, for as quenched splat samples, a meek magnetic anisotropy is revealed from the hysteresis loop recorded at deep temperature i.e., 5K, illustrated in Fig. 6.43. However, it is analogous to

¹⁰ Not shown here.

geometric anisotropy i.e., net magnetization in plane direction is higher than net magnetization in out of plane to the applied field in the SQUID. It also enunciates that geometric anisotropy revealed at low temperature for the splat sample is far less pronounced to be recorded at high temperatures. The atomic vibrations even at room temperature are high enough to hide out the extent of magnetic anisotropy present.

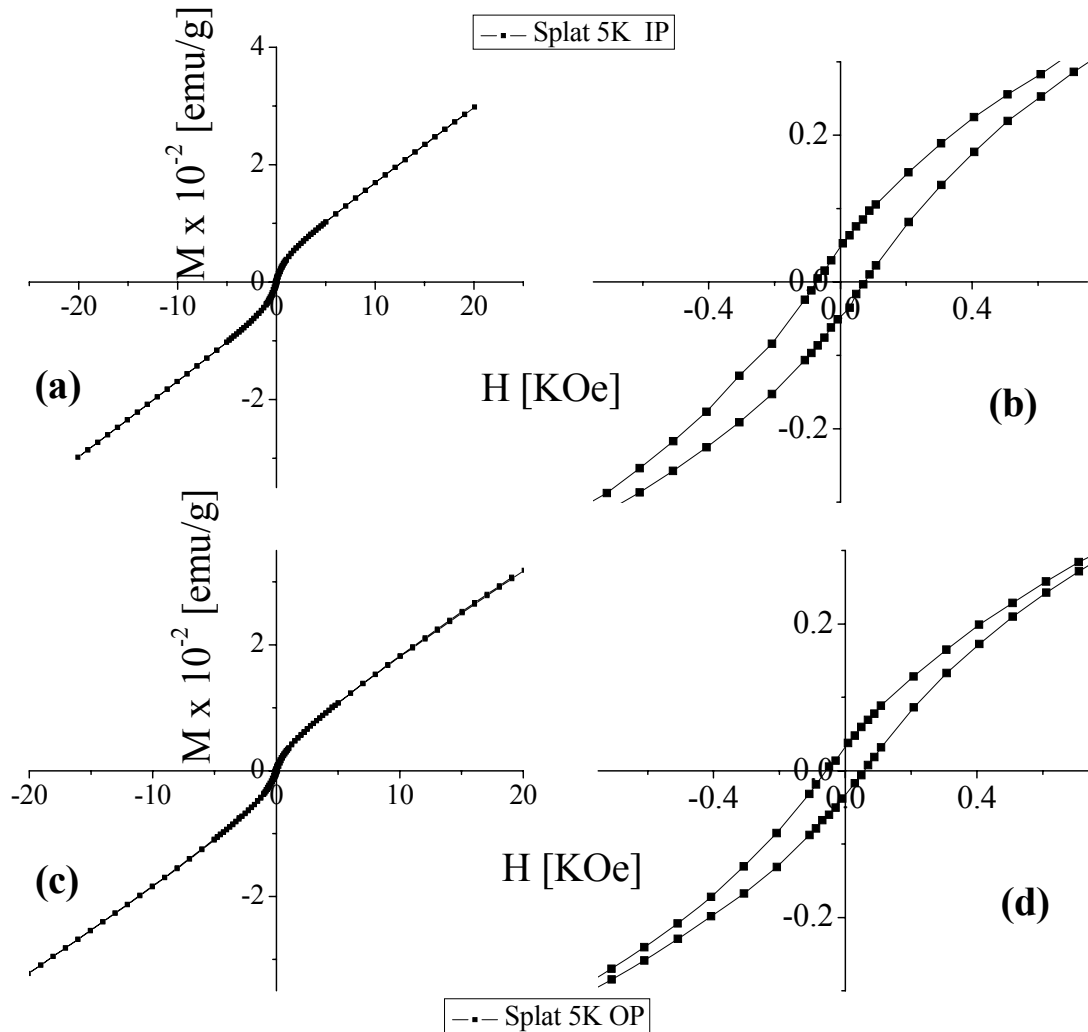


Figure 6.43 Hysteresis loops measured at 5K for as cast $Zr_{53}Co_{23.5}Al_{23.5}$ splat samples a) in plane to the direction of the applied field, (b) a corresponding magnified portion of hysteresis loops for low magnetic fields, (c) out of plane to the direction of applied field in SQUID and (e) a magnified portion of hysteresis loops for low magnetic fields.

The splat sample heat treated at 560°C shows very good soft ferromagnetic properties as illustrated in a comparison to that of as quenched splat sample in Fig. 6.44. The hysteresis curve of heat treated splat sample almost approaches saturation already at the field of 3T. The remanent magnetization of heat treated splat is 36 times higher than the as quenched splat.

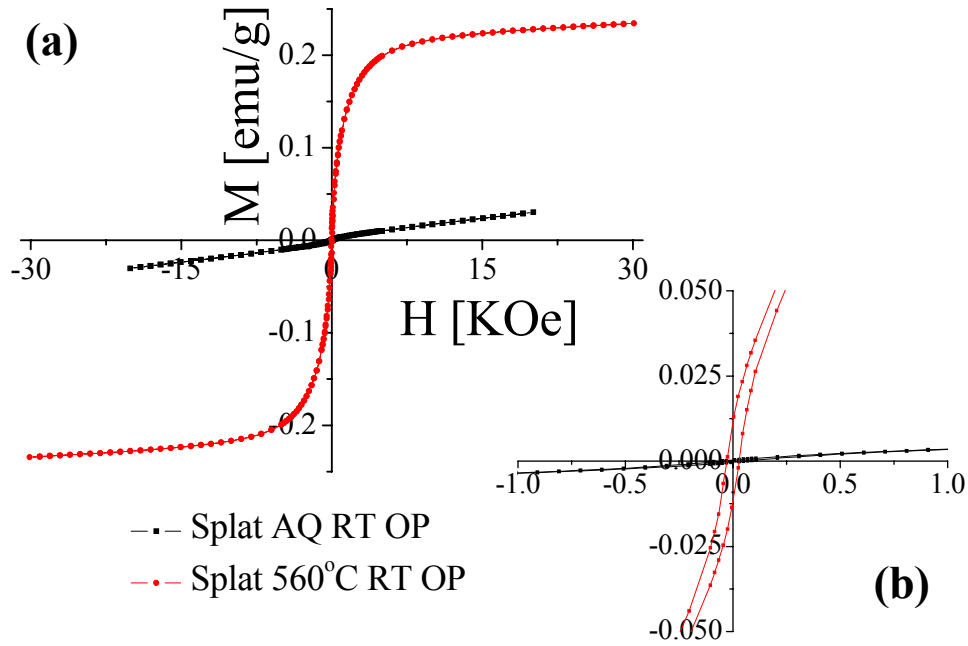


Figure 6.44 (a) Comparison of the hysteresis loops measured at room temperature for as quenched $Zr_{53}Co_{23.5}Al_{23.5}$ splat samples and splat sample heat treated at 560°C for 30 minutes, **(b)** a corresponding magnified portion of hysteresis loops for low magnetic fields.

Hysteresis loop at 5K for the heat treated splat sample, as depicted in Fig. 6.45, reveals that the saturation point is almost approached already at 1T at such a deep temperature. Correspondingly, the net magnetization is also higher as compared to the hysteresis at room temperature.

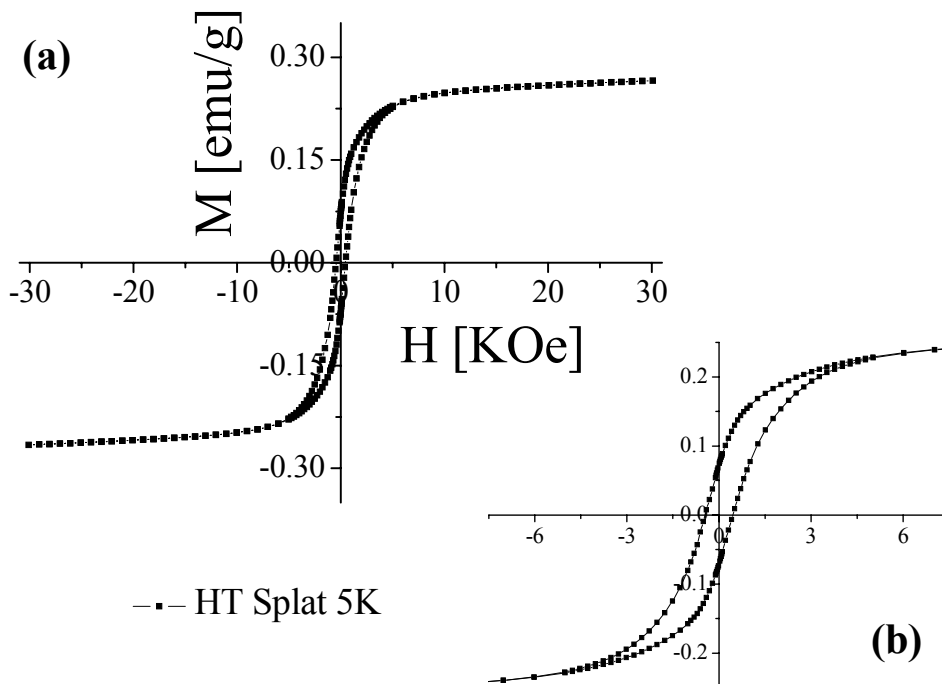


Figure 6.45 (a) Hysteresis loop measured at 5K for as quenched $Zr_{53}Co_{23.5}Al_{23.5}$ splat sample, **(b)** a magnified portion of the hysteresis loop at low magnetic field, H .

Table 6.13 present the summary of the magnetic properties of the as cast $Zr_{53}Co_{23.5}Al_{23.5}$ bulk alloy and splat samples. Moreover, the corresponding values of heat treated splat samples are also given. Lucidly, the heat treated splat sample offers very good soft ferromagnetic properties, some order of magnitude higher than as quenched splat and as cast bulk samples. The intriguing increase in the net magnetization after crystallization revealed from the present study, are somewhat analogous to the superior magnetic properties of amorphous alloys after crystallization enunciated by Yoshizawa and Herzer [Yoshizawa88, Herzer90].

Table 6.13 A comparison of different magnetic attributes for $Zr_{53}Co_{23.5}Al_{23.5}$ splat and bulk samples.

	M_r room temp. [emu/g]	H_c room temp. [Oe]	M_r 5K [emu/g]	H_c 5K [Oe]
Bulk sample, as Cast Out of Plane	3.9×10^{-4}	25	1.4×10^{-3}	96
Splat sample, as Quenched	3.1×10^{-4}	47	3.23×10^{-4}	58.7
Splat sample 30 min@560°C	0.0112	28.3	0.074	454

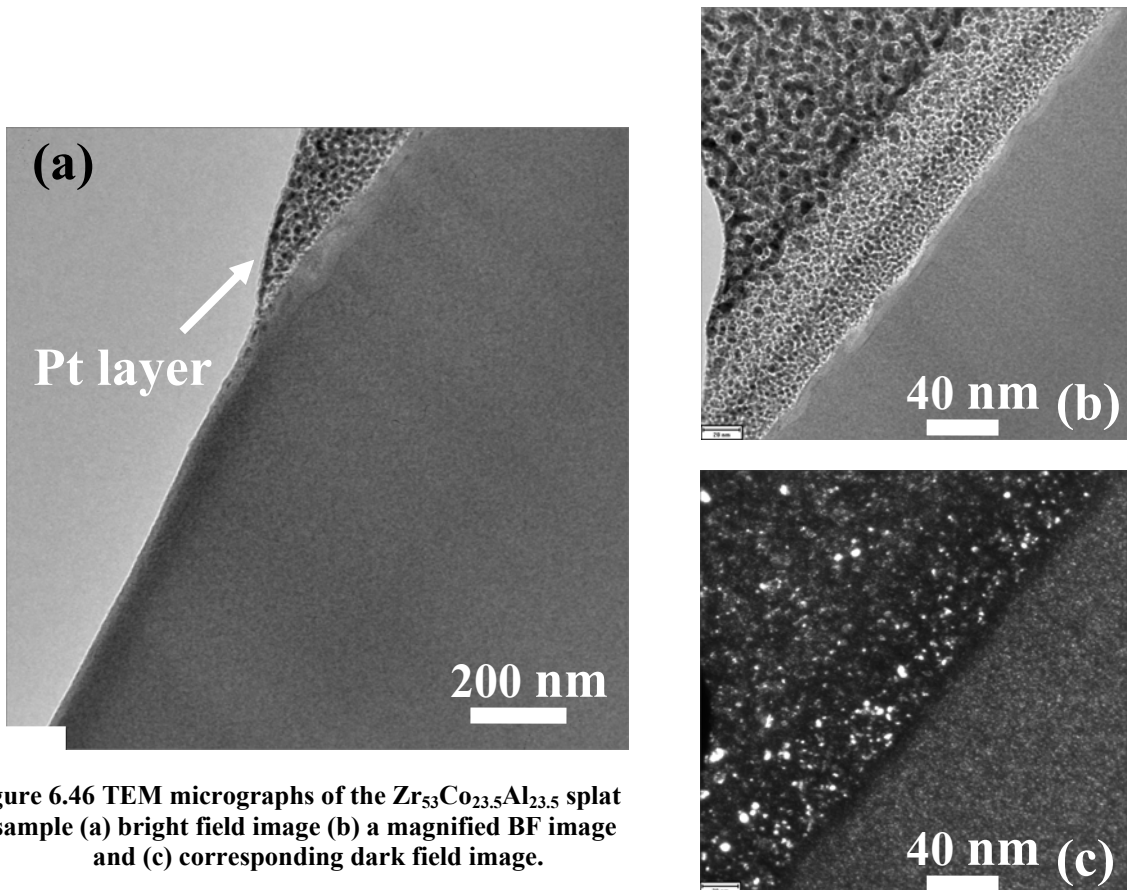


Figure 6.46 TEM micrographs of the $Zr_{53}Co_{23.5}Al_{23.5}$ splat sample (a) bright field image (b) a magnified BF image and (c) corresponding dark field image.

Microstructural investigations by TEM

TEM investigations reveal a single phase amorphous microstructure. Fig. 6.46 depicts the bright field and dark field images of the $Zr_{53}Co_{23.5}Al_{23.5}$ splat sample. The Pt layer is deposited during the sample preparation by ion beam milling. The amorphous matrix bears no phase contrast for both bright field image and dark field image.

To conclude about the microstructural investigations on the $Zr_{53}Co_{23.5}Al_{23.5}$ splat samples, TEM investigations exhibit a single homogeneous amorphous phase that is also expected for such a high cooling rate during splat preparation. The DSC scan and absence of any magnetic anisotropy also corroborate these results. The trend of better magnetic properties after heat treatment continues for $Zr_{53}Co_{23.5}Al_{23.5}$ metallic glass. The resultant magnetic properties are even better than revealed by the corresponding crystalline bulk samples.

6.3.6 Reconsidering microstructural investigations of the as cast $Zr_{53}Co_{23.5}Al_{23.5}$ bulk amorphous alloys

The magnetic anisotropy and two exothermic peaks in the DSC scan for $Zr_{53}Co_{23.5}Al_{23.5}$ bulk samples are not yet explainable, by the microstructural investigations. Another rationale for inability to demonstrate any thing else than a homogeneous phase from TEM analysis might be is a thick TEM specimen and the structural features are in sub nanometre range. However, even then one should observe some structural variations in high resolution transmission electron microscopy. Energy filtering transmission electron microscopy has also been utilized to elaborate any structural difference present in the bulk specimen.

Microstructural investigations by EFTEM

To produce the elemental map images, images for three energy windows were obtained, two energy filtered images before the edge (pre-edge windows) and one image after the edge (post-edge window) of the element of interest in the corresponding EELS spectrum. The energy filtration was done for Co element. Fig. 6.47 depicts the EFTEM image for Co element; reveal a single phase homogeneous structure. The lower right corner of the EFTEM image manifest the Pt layer deposited during sample preparation. Despite this layer, the structure doesn't contain any Co variation that can be deduced from this micrograph. The EFTEM analysis also ruled out any presence of different phases that can explain the magnetic anisotropy and two exothermic peaks in the DSC scans for the as cast $Zr_{53}Co_{23.5}Al_{23.5}$ bulk samples.

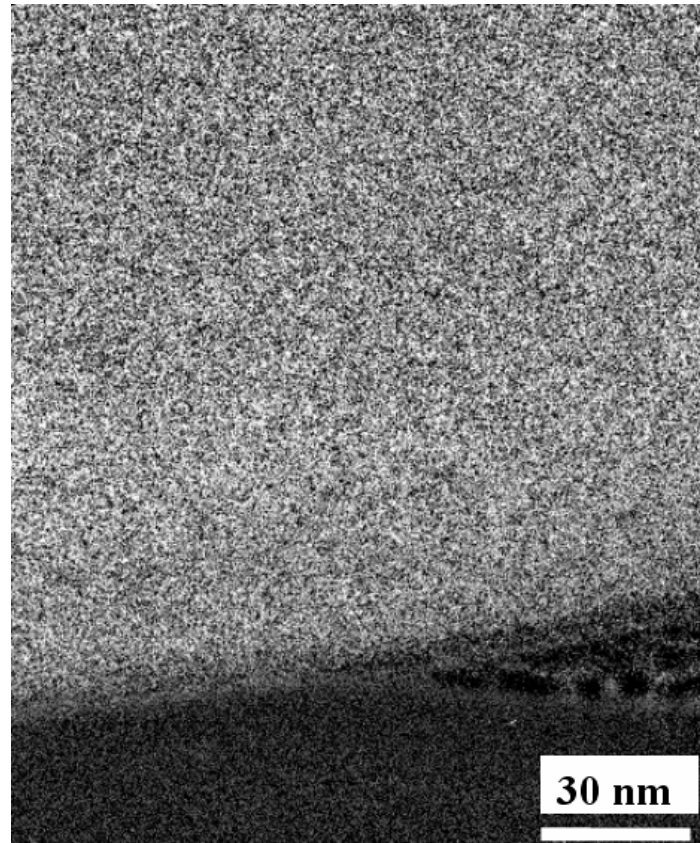


Figure 6.47 EFTEM micrograph for Co element of as cast $Zr_{53}Co_{23.5}Al_{23.5}$ bulk sample.

TEM sampling

All samples prepared for the TEM analysis, were taken within the vicinity of the centre of the discs cut by EDM machine from the $Zr_{53}Co_{23.5}Al_{23.5}$ bulk rods. The cooling rate is supposed to be the slowest in the centre of the bulk sample rod, being at the maximum distance from the heat sink (i.e., water cooled Cu mould). Any phase transformation is thought to occur would be in the centre of the $Zr_{53}Co_{23.5}Al_{23.5}$ bulk rods due to the slowest cooling rate.

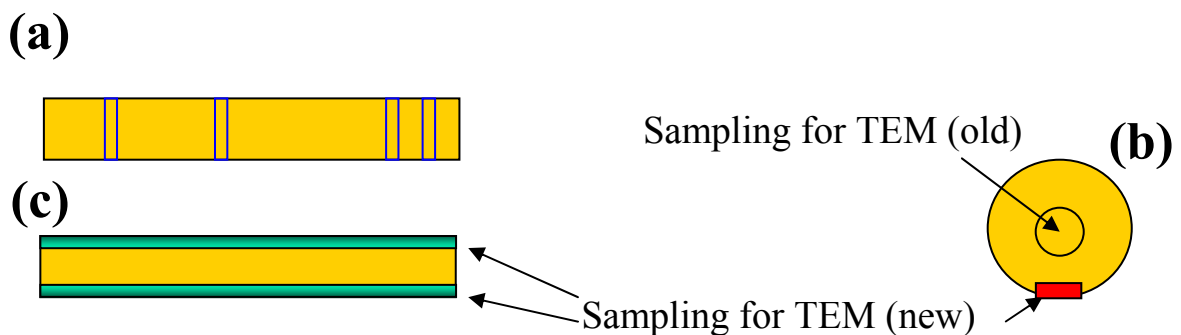


Figure 6.48 (a) sampling for the DSC, XRD, SQUID and TEM analyses (b) Top view of the disc, encircles region in the middle of the disc shows the area from where TEM samples were fabricate using FIB, the rectangle shows the area for new sampling for TEM analysis and (c) side view of the $Zr_{53}Co_{23.5}Al_{23.5}$ bulk rods.

Fig. 6.48 illustrates the sampling for DSC, XRD, SQUID and TEM investigations. In order to see if heterogeneous nucleation plays any role during the vitrification, new samples are prepared from very near to the edge ($\sim 10 \mu\text{m}$ from the outer edge) of the disc. Fig. 6.48b illustrates the areas chosen for previous TEM sample i.e., encircles area in the middle of the disc and rectangle manifests the area for new TEM samples.

Phase variation evident from FIB/SEM in the edge sample

A phase contrast is already evident from aforementioned edge sample even during the course of the TEM sample preparation inside FIB/SEM. Fig. 6.49 depicts a SEM micrographs during the TEM sample preparation for the $\text{Zr}_{53}\text{Co}_{23.5}\text{Al}_{23.5}$ bulk edge sample; reveal dark regions of varying size up to 450 nm. However, these regions were only evident when the sample was too thin after milling.

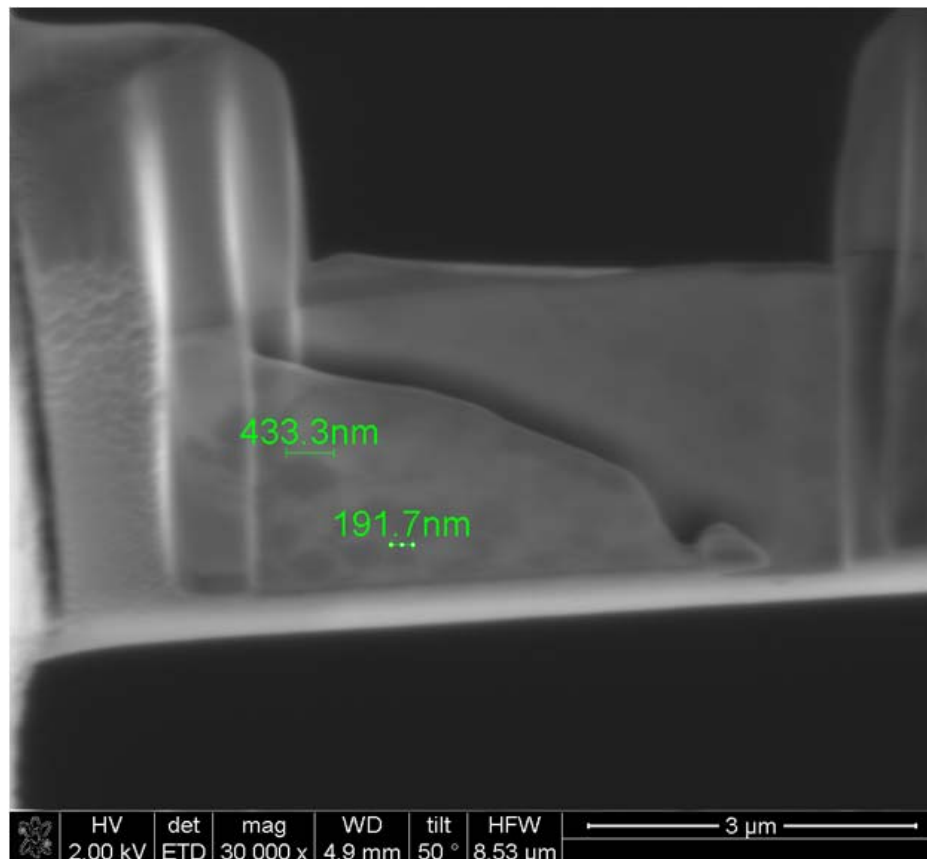


Figure 6.49 SEM micrograph, during the ion milling for the TEM sample preparation of the $\text{Zr}_{53}\text{Co}_{23.5}\text{Al}_{23.5}$ bulk edge sample.

Microstructural investigations of the edge sample by TEM

Fig. 6.50 illustrates the bright field images of the $\text{Zr}_{53}\text{Co}_{23.5}\text{Al}_{23.5}$ bulk edge sample. Bright field image lucidly reveal different phases, present in the as cast state. The grain size varies for different grains. The brightest grain has a size in a range from 10-450 nm, contrary to the phase appearing as dark, has a grain size in a range of 5-100 nm. Hence, the $\text{Zr}_{53}\text{Co}_{23.5}\text{Al}_{23.5}$ bulk samples undergo heterogeneous

nucleation. The morphology appears to be quite complex. Fig.6.50b depicts a structure analogous to the cross-sectional view of a dendrite arm. However, larger bright grains are evident from this micrograph. Fig.6.50b shows relative smaller grains < 100 nm, Fig.6.50c & d demonstrates the grain morphology with higher magnification. Moiré fringes, typical for the crystalline phase, are revealed in Fig.6.50d.

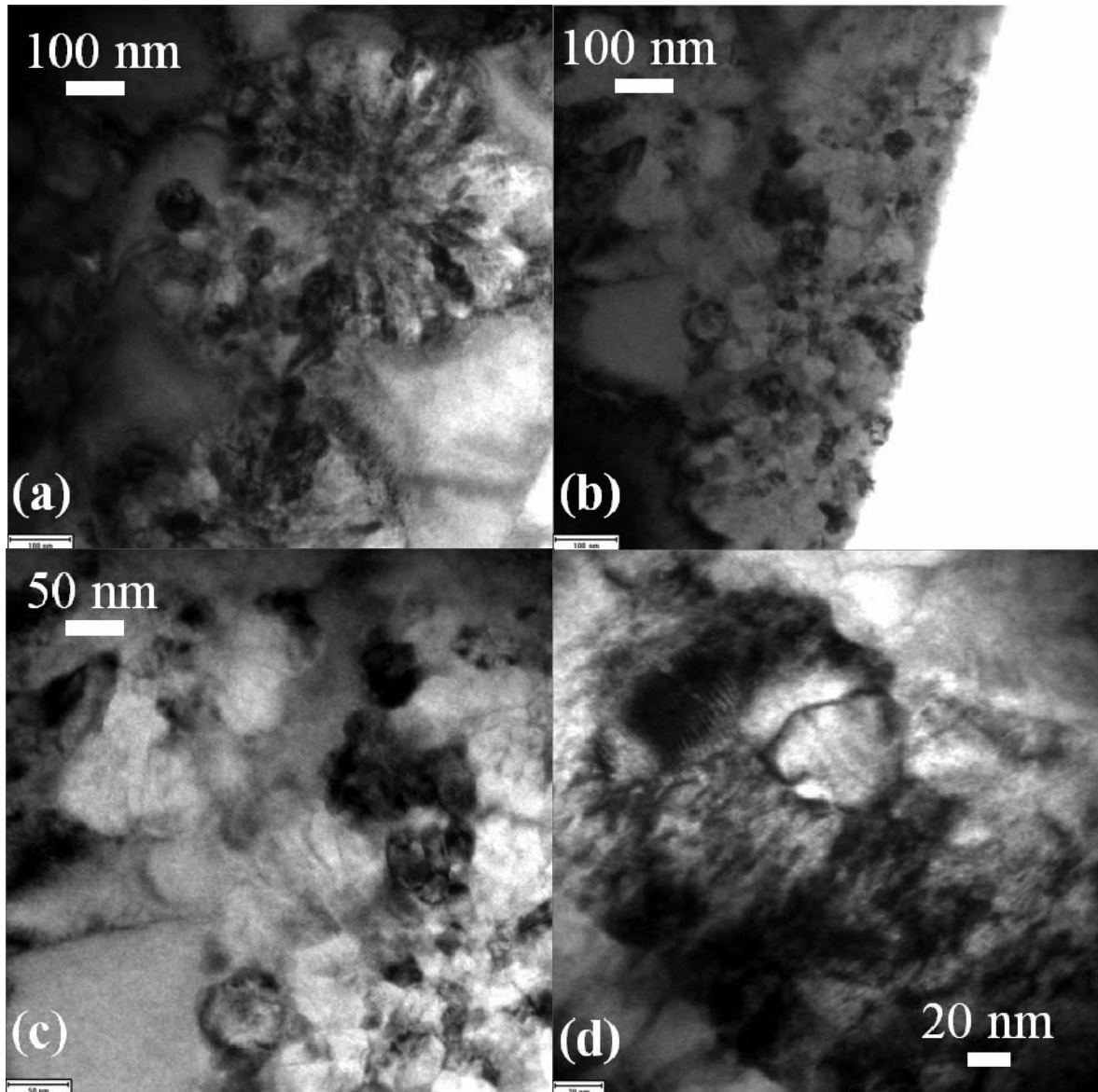


Figure 6.50 TEM bright field images of the $Zr_{53}Co_{23.5}Al_{23.5}$ bulk edge sample.

6.3.7 Microstructural investigations by APT

Field ion imaging and tomography

Fig. 6.51 illustrates the FIM image of the as cast $Zr_{53}Co_{23.5}Al_{23.5}$ bulk edge sample. It features poles, a lucid evidence of the crystalline inclusions in the bulk sample. Presence of the poles, corroborate the results from the TEM edge sample. In addition, regions of the brighter and dark contrast are also

present in the FIM image that may arise due to the compositional variations in different phases or from the interface of different phases. Fig. 6.51b represents the CFIIT image of single plane to manifest presence of more than one pole.

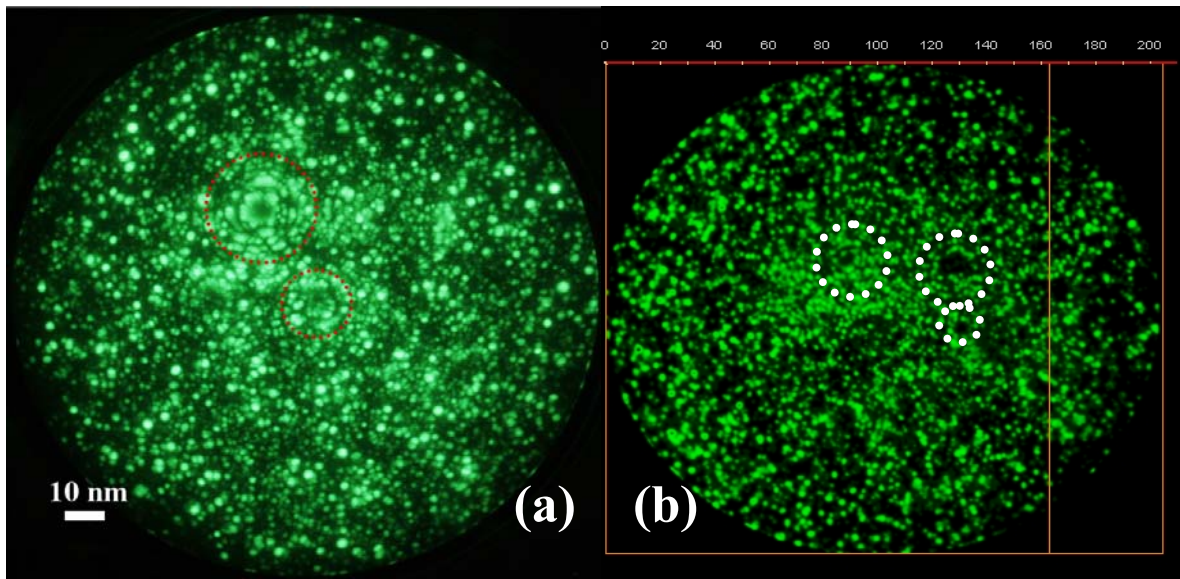


Figure 6.51 (a) FIM image of the $Zr_{53}Co_{23.5}Al_{23.5}$ bulk edge sample, (b) CFIIT image of a single plane to manifest poles of different grains. Encircled regions are poles representative of crystalline phases.

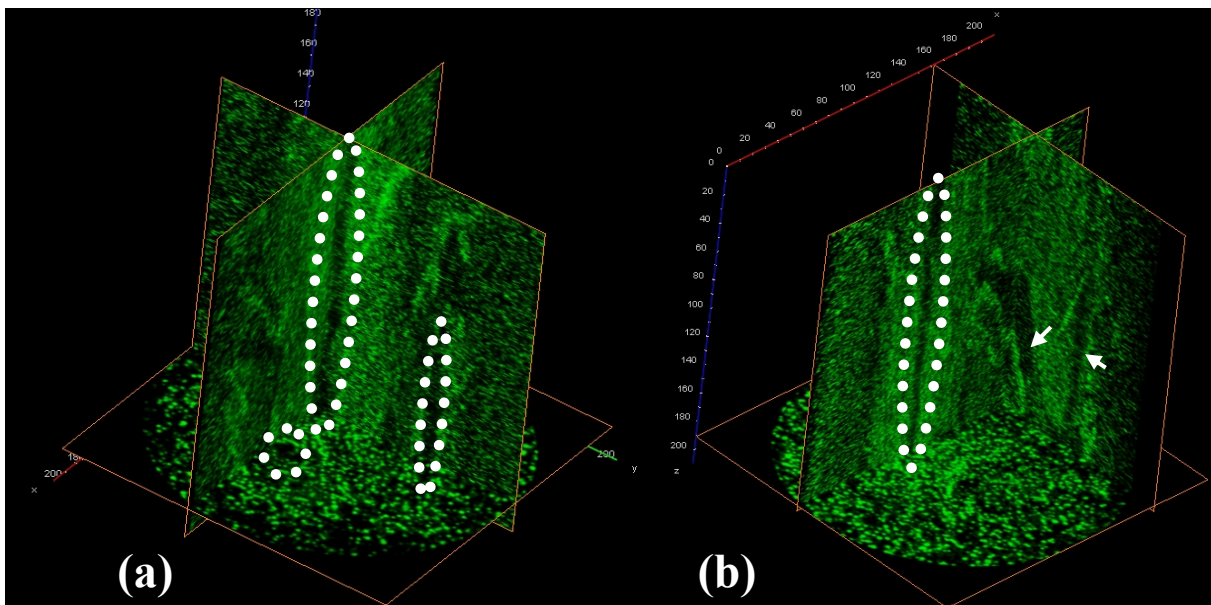


Figure 6.52 Three dimensional CFIIT images of the $Zr_{53}Co_{23.5}Al_{23.5}$ bulk edge sample, encircled regions are poles typical for the crystalline phases.

Fig. 6.52 shows the atomic distributions of $200 \times 200 \times 200 \text{ nm}^3$ as cast $Zr_{53}Co_{23.5}Al_{23.5}$ edge sample by computer assisted field ion image tomography (CFIIT) with three slices. The main advantage of CFIIT is a higher field of view as compared to the TAP analysis. It is essentially a step further to the FIM imaging, extending its x and y coordinates in the z direction. One of the poles, encircled, in Fig. 6.52a

crosses throughout the analysed volume; hence, the corresponding phase has a size greater than 200 nm, which is also evident from the TEM analysis of the edge sample. Fig. 6.52b depicts one of the slices exactly on one of the major pole evident in Fig. 6.52a showing that the crystalline region passes through out the analysed volume. Furthermore, a strong contrast elaborated by arrows can arise because of the phase boundaries. A phase with the higher evaporation field will protrude from the specimen surface and field ionization will preferentially occur above this region, resulting in a bright area in the FIM image. The estimated field of evaporation for Co atoms is higher than that of the other elements hence the Co rich phase should be imaged as bright region in the FIM micrographs.

Stereological phase morphology and Quantification by APT

Fig. 6.53 (a-c) depicts three-dimensional atomic reconstruction of each element in the $Zr_{53}Co_{23.5}Al_{23.5}$ as cast edge sample analysed by the tomographic atom probe. The three-dimensional atomic reconstruction lucidly illustrates distinct regions of compositional variation in the analysed volume.

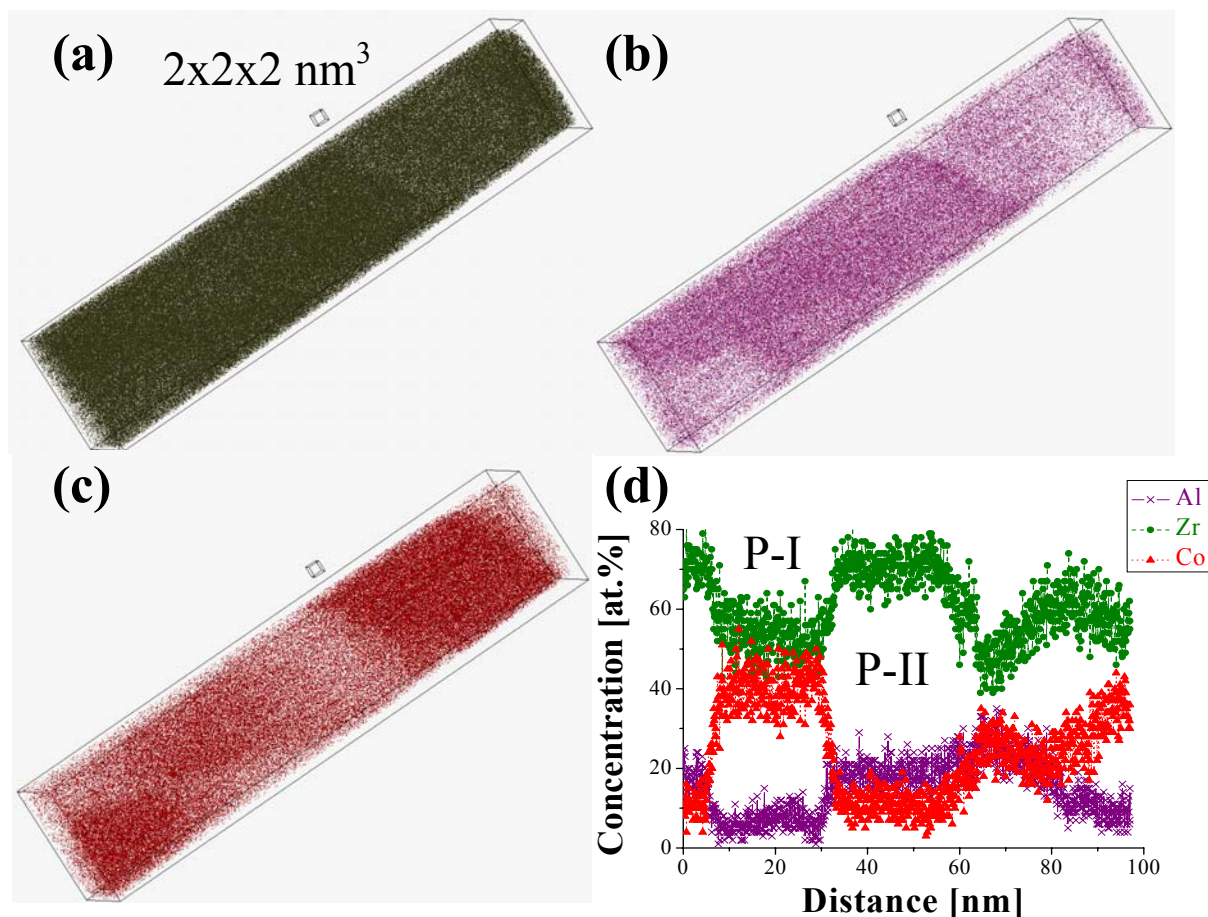


Figure 6.53 Three dimensional atomic reconstruction of $Zr_{53}Co_{23.5}Al_{23.5}$ bulk edge sample, (a) Zr atoms, (b) Al atoms, (c) Co atoms and (d) Concentration profile through the centre of the aforementioned 3-D atomic reconstruction.

A pronounced difference in Al rich and Al depleted phase is evident in Fig. 6.53b. The regions that are depleted in Al concentration are Co rich, when compared with the same region in Fig. 6.53c. A similar comparison with Fig. 6.53a manifests that the phase depleted in Co concentration is enriched in Zr concentration and vice versa. A concentration profile is a more precise and quantitative approach that gives the compositional variations as a function of the distance in the analysed volume. Fig. 6.53d illustrates the concentration profile of 8 nm diameter cylinder passing through the centre of the analysed volume (shown in Fig. 6.53 a-c). The analysis starts from Zr & Al rich phase marked as phase II reaches the Co rich phase assigned as phase I. As the analysis proceeds further, Phase II is reached again and finally at the end features the grain boundary. The composition of both phases is summarized in table 6.14.

Table 6.14 Composition of two phases of $Zr_{53}Co_{23.5}Al_{23.5}$ as cast edge sample.

	Zr at. %	Co at. %	Al at. %
P-I	54.82 ± 5.78	38.38 ± 6.30	6.8 ± 3.33
P-II	70.82 ± 4.31	10.76 ± 3.26	18.42 ± 3.72

Composition of the aforementioned two phases revealed from the TAP, is far from the nominal composition of the alloy (i.e., $Zr_{53}Co_{23.5}Al_{23.5}$). These phases must likely form by heterogeneous nucleation from the mould wall.

A complex phase morphology is difficult to assess alone from the three dimensional atomic reconstructions (as presented in Fig. 6.53). To delve the morphology of these two phases, iso-concentration slices are, hence, utilised. Fig. 6.54 depicts three perpendicular Zr concentration slices through the analysed volume that can be moved with in the analysed volume to observe the morphology of different phases in detail, as a colour scale map. It shows clearly the variation of the Zr concentration which is not that evident in Fig. 6.53a because of higher concentration of Zr.

Fig. 6.55 illustrates the same representation in the analysed volume for the variations of Co concentrations. One of the slices, marked by an

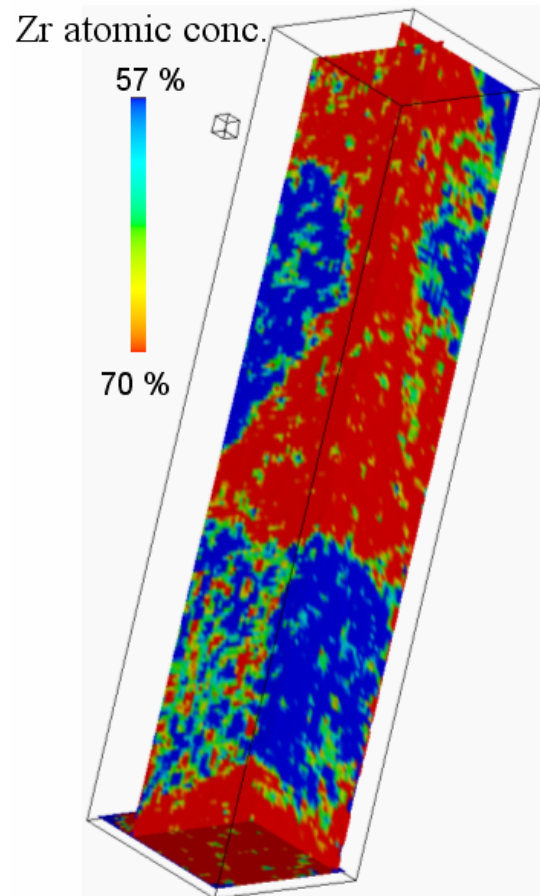


Figure 6.54 Zr concentration variations scaled as a colour map, in the analysed volume of $Zr_{53}Co_{23.5}Al_{23.5}$ bulk edge sample. Small cube represent 8 nm^3 volume.

arrow, in Fig. 6.55a, is moved from left to right to follow the Co concentration variation. As the slice moves from left to right in Fig. 6.55 (a-d), the encircled Co rich phase increases in volume. Another Co rich region starts appearing as manifested by a smaller circle in Fig. 6.55e. As the slice moves to right, the first Co rich region which appeared in Fig. 6.55a starts decreasing, while the second one grows. Fig. 6.55h depicts the two Co rich regions intersecting each other, and thereafter, the first region starts diminishing and this persists till the other end of the analysed volume. The compositional colour scale maps, in the Fig. 6.55, show that the morphology of two phases has an interconnected and rather a complex network, which explains the faint contrast of the grain boundaries revealed from the corresponding TEM micrographs in Fig. 6.50. The size of two phases varies from 5 nm to greater than 30 nm (exceeding the analysed dimensions in the x and y directions).

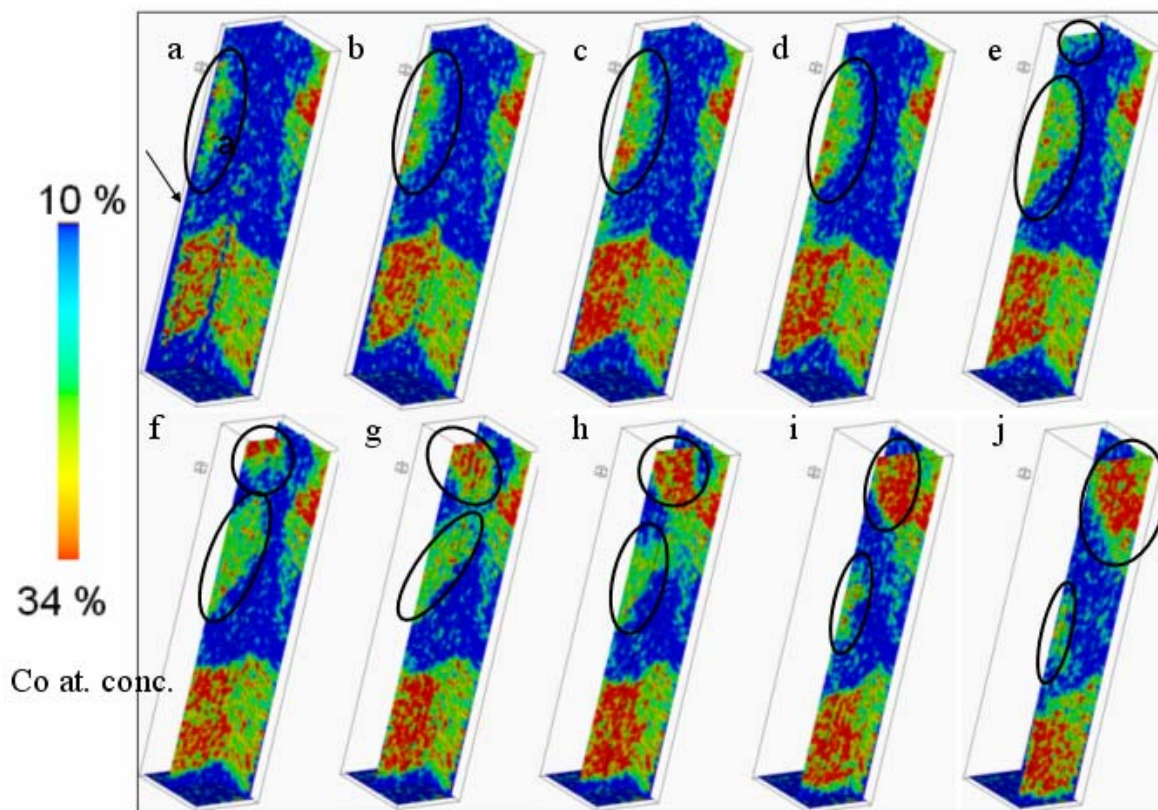


Figure 6.55 Co concentration variations, between 10-34 at. %, scaled as a colour map in the analysed volume of $Zr_{53}Co_{23.5}Al_{23.5}$ bulk edge sample. A slice (marked by an arrow in Fig. a), is moved from left to right at predefined steps from, Fig. a-j, depicting the concentration variation in 3-D. Small cube represent 8 nm^3 volume.

Hence, the crystalline phases, demonstrated by the TEM and TAP, near the edge of the bulk as cast sample explains the mysteries of the magnetic anisotropy and two peaks in the DSC scan of the corresponding samples. The presence of different phases explains two exothermic peaks in the DSC scans of the as cast sample. Albeit, the absence of any crystalline inclusion in the middle of the as cast bulk rods (after TEM analysis), the edge sample reveal crystalline inclusions that is thermodynamically explained by the heterogeneous nucleation. The underlying theory to explain why the crystallization starts on the mould wall is explained in detail in chapter 2. Howbeit, for the same

critical nucleus radius r^* , the Gibbs free energy for heterogeneous nucleation ΔG_{het}^* is smaller than the Gibbs free energy for homogeneous nucleation ΔG_{hom}^* , hence the crystallization starts at the mould walls.

6.3.8 Conclusion

A detailed microstructural investigation has been carried out on the $Zr_{53}Co_{23.5}Al_{23.5}$ bulk amorphous alloys and metallic glasses in as cast/quenched state and heat treated state. Moreover, subsequent effects on the magnetic properties are also delved during the course of this research work. To our best knowledge these are the first microstructural investigations on the $Zr_{53}Co_{23.5}Al_{23.5}$ system. The as cast bulk sample reveal an amorphous structure, when analysed by XRD and SEM, though, two exothermic crystallization peaks depicted by the DSC scans and magnetic anisotropy revealed by the SQUID measurements shows that the as cast alloy is not a single phase homogeneous structure. Hence, extensive HRTEM investigations were carried out to elicit the underlying reasons. The TEM micrographs from the samples fabricated from the centre of the as cast $Zr_{53}Co_{23.5}Al_{23.5}$ bulk sample, however, divulge a single phase homogeneous amorphous structure that is even corroborated by the EFTEM Co images. The HRTEM images also depict a homogeneous amorphous single phase.

The TEM samples fabricated from the edge of the as cast sample, however, show egregious phase contrast from the bright field images. The corresponding diffraction pattern contains the diffraction spots that suggest that the sample clearly constitutes certain crystalline phase(s). TEM micrographs show regions of different phase sizes. Some regions have grains size less than 50 nm and the phases have intermixed morphology, on the other hand some regions show rather larger grains with the grain size up to 450 nm. The three dimensional atomic reconstruction by TAP reveals two phases and allow quantifying these phases. The phase that is rich in Zr and Al concentration is depleted in Co concentration while the phase that is rich in Co concentration is depleted both in Zr and Al. A vivid representation of two phase morphology is done by presenting the concentration difference as a colour map and moving a slice through the analysed volume (Fig. 6.55). Such a representation shows that two phases are interconnected and show rather a complex stereological network with a phase distribution in the range of 5 to +30 nm (exceeding the analysed volume), which also explains the inter-diffused grains revealed from the corresponding TEM micrographs. Inquest into the magnetic anisotropy and two exothermic peaks depicted by the DSC scans for bulk sample show that the heterogeneous nucleation hampers the vitrification and subsequently results in crystalline phase(s) on the outer edge of the $Zr_{53}Co_{23.5}Al_{23.5}$ bulk rods.

The presence of the crystalline phase(s) is also lucid from the prominent poles depicted by the micrographs attained exploiting FIM and rather a new technique known as CFIIT. CFIIT not only reveal the crystallographic information but also helps to investigate larger volume as compared to the TAP. Two phases give rise to a different contrast in the CFIIT micrographs and the extension of the

pole throughout the 200 nm analysed volume reveal that the crystalline phase has a grain size higher than 200 nm that is also evident from the TEM investigations. Therefore, as cast bulk sample is rather a composite, constituting amorphous and crystalline phases.

Contrary to the as cast bulk sample, the DSC scan of the splat sample depicts a single exothermic crystallization peak. The splat sample exhibits a different T_g as compared to that of as cast bulk sample. The corresponding TEM investigations showed that the splat sample constitutes a single homogeneous amorphous phase. Hence, the faster cooling rate during splat preparation was good enough to form an amorphous structure.

Both, $Zr_{53}Co_{23.5}Al_{23.5}$ bulk sample and splat sample exhibit very soft ferromagnetic properties. The heat treatment of as cast bulk sample results in an increase in net magnetization. The crystallization kinetics during the heat treatment, effects the remanent magnetization, M_r and coercivity, H_c accordingly. The isotropic magnetic properties of splat samples measured in plane and out of plane in SQUID corroborate that the anisotropic magnetic properties of bulk samples arise from the crystalline phase present in the as cast bulk samples. This very fact also explains the start of crystallization at a lower temperature than the crystallization onset temperature and a subsequent effect of the first heat treatment (for a temperature even less than the T_g) on magnetic properties is lucid (Fig. 6.35). Even the first heat treatment results in a defiant increase in the net magnetization. Intriguingly, there is a remarkable increase in the soft ferromagnetic properties of the splat sample by the heat treatment as compared to the bulk samples. To sum up, the magnetic properties of the $Zr_{53}Co_{23.5}Al_{23.5}$ alloys especially for the splat samples can egregiously be enhanced by the heat treatment.

Chapter 7

Summary and Outlook

A novel algorithm, “Next Neighbourhood Evaluation (NNE)”, is enunciated during the course of this work, to elucidate the next neighbourhood atomic vicinity from the data, analysed using tomographic atom probe (TAP). These are the first ever investigations on the amorphous materials to study the next neighbourhood evaluation using TAP. The NNE algorithm allows specifying atom positions and chemical identities of the next neighbouring atoms for multicomponent amorphous materials in real space which are difficult to access alone from scattering techniques (e.g., radial distribution functions, RDFs). It enables to delve the short range ordering, an essential phenomena, in the structural description of the amorphous materials. Pd and Fe based glassy materials are characterized with an emphasize on exploiting the NNE algorithm.

For the Pd₅₅Cu₂₃P₂₂ bulk amorphous alloy, first ten next neighbours for all elemental correlations are enunciated alone from the TAP data, which for a multi-component system is difficult, otherwise. The distribution of next neighbouring atomic distances shows that for this system, the Pd-Pd atoms have the highest probability to be the next neighbours to each other. Moreover, P-P correlation corroborates earlier investigations with scattering techniques that P is not a direct next neighbour to another P atom. The findings from the present work enables for the first time to assign the atoms responsible for the coordination peaks in RDFs obtained by scattering techniques. Normalizing the distances by the first next neighbour distance yields a ratio similar for all elemental correlations showing that there exists a certain order among the atoms, irrespective of the chemical nature of the atoms.

Fe₄₀Ni₄₀B₂₀ metallic glass ribbons are characterized in the as quenched state and for a state heat treated at 350°C for 1 hour. The conventional characterization tools i.e., XRD and DSC don't reveal any structural transformation for the heat treated state. TAP investigations, however, insinuate a change in the structure on the sub-nanometre scale. By applying the statistical tool, χ^2 test, a pronounced elemental inhomogeneity is perceived for the annealed state, though, it also depicts glimpse of a slight inhomogeneity for B distribution even for the as quenched sample. The distance distribution of first

thirty atomic neighbours is elicited by the state of art NNE algorithm for both as quenched and annealed state. The distances for the next neighbours of different elemental correlations are in a very good agreement with the data available in literature. Moreover, the NNE algorithm also evinces a steric periodicity of the atoms when the next neighbour distances are normalized by the first next neighbour distance. The resultant ratio is similar for all elemental correlations showing that this steric periodicity is independent of the chemical nature of the atoms. A comparison of the NN atomic distribution for as quenched and annealed state shows accumulation of Ni and B. Moreover, it also reveals the tendency of Fe and B to move slightly away from each other, an incipient step to Ni rich boride formation. Hence, the structural changes attributed to the short range ordering in $\text{Fe}_{40}\text{Ni}_{40}\text{B}_{20}$ metallic glasses are able to be characterized by the TAP.

Finally, comprehensive microstructural investigations have been carried out on the $\text{Zr}_{53}\text{Co}_{23.5}\text{Al}_{23.5}$ amorphous alloys. To our best knowledge, these are the first microstructural investigations on the $\text{Zr}_{53}\text{Co}_{23.5}\text{Al}_{23.5}$ system. Different characterization techniques such as DSC, XRD, SEM, SEM-EDX, HRTEM, EFTEM, TAP, FIM and CFIT are utilized to study the amorphous structure. Moreover, SQUID was exploited to depict the magnetic properties of the investigated material. Intensive TEM and TAP investigations evince that the as cast bulk samples constitutes a composite structure of an amorphous phase and crystalline phase(s). The crystallization is essentially triggered at the mould walls due to heterogeneous nucleation. The crystalline phase(s) on the edge of the bulk rod lead to the magnetic anisotropy and two exothermic crystallization peaks in the DSC scans. The three dimensional atomic reconstruction maps of the analysed volume, by TAP, demonstrate lucidly two phase region. The phase that is rich in Zr and Al concentration is depleted in Co concentration while the phase that is rich in Co concentration is depleted both in Zr and Al. Moreover, TAP investigations reveal that the two phases are interconnected and exhibit rather a complex stereological network.

CFIT and FIM micrographs depict prominent poles manifesting the presence of the crystalline phase(s) in the as cast bulk edge samples. CFIT not only shows the crystallographic information but also helps to investigate larger volume as compared to the TAP. $\text{Zr}_{53}\text{Co}_{23.5}\text{Al}_{23.5}$ glassy splat samples exhibit a single exothermic crystallization peak contrary to the as cast bulk sample with a different T_g temperature. A single homogeneous amorphous phase revealed by TEM investigations depict that the faster cooling rate during splat quenching are good enough for the vitrification of this alloy system.

$\text{Zr}_{53}\text{Co}_{23.5}\text{Al}_{23.5}$ bulk samples and splat samples, both exhibit very soft ferromagnetic properties. The heat treatment of as cast bulk sample results in an increase in net magnetization. The crystallization kinetics during the heat treatment, effects both the remanent magnetization, M_r and coercivity, H_c accordingly. Intriguingly, a salient increase in soft ferromagnetic properties is recorded for the heat treated splat samples. Hence, the magnetic properties of the glassy $\text{Zr}_{53}\text{Co}_{23.5}\text{Al}_{23.5}$ alloys especially for the splat quenched samples can be enhanced by a controlled heat treatment.

Several further investigations are suggested considering the results of this work. Firstly, as the NNE enables to investigate the short range ordering in detail, an amorphous alloy especially Pd based can be investigated just below the glass transition temperature T_g , in between the supercooled region, and just below the crystallization onset temperature T_x , to elicit the structural differences among these stages. Pd based amorphous alloys are suggested because of the stability of the samples during the TAP analysis.

Secondly, to produce the $Zr_{53}Co_{23.5}Al_{23.5}$ bulk amorphous alloys, the heterogeneous nucleation is necessary to avoid. Different parameters can be checked during the specimen preparation i.e., super clean Cu mould, or even trying to produce rods by water quenching analogous to the Vit. 1 alloy vitrification but in dimensions between 2-3 mm or coating a very thin layer of graphite on the walls of the Cu mould.

Thirdly, other salient aspects keeping in mind purely the magnetic properties, especially for metallic glasses, are to inquire into the primordial steps of the crystallization and their subsequent effect on the magnetic properties for potential industrial applications.

Finally, a focus on the statistical tools based on the TAP data should continue further. A next step can be the calculation of the different parameters that hamper to extract accurately the radial distribution function. If the deconvolution is somehow possible, it will open up a vast field of unsolved problems in the materials physics especially to resolve the sub-nanometre structural mystery of the amorphous state.

Appendix A

Vitreloy 1 ($\text{Zr}_{41.2}\text{Ti}_{13.8}\text{Cu}_{12.5}\text{Ni}_{10}\text{Be}_{22.5}$) bulk metallic glass

The results from the investigation of the vit1 alloy utilizing atom probe tomography (APT) are revealed in this section. Additionally, the reasons to continue further investigations on other alloy systems (Pd-based and Fe-based) are also explained.

Microstructural characterization by TAP microscopy

Fig. 1 illustrates a FIM image of vit1 alloy in the as quenched state. A uniform image that exhibits no characteristic features indicative of the presence of crystalline phases i.e., poles. However, since the FIM image is not sensitive to the partial crystallization or the small compositional fluctuation, the FIM image does not provide sufficient evidence for the chemical homogeneity in the amorphous alloy. Hence, three-dimensional atom maps were obtained using the TAP. TAP analyses were carried out at 100 K, 60 K and 50 K with a pulse fraction of 15% between pulse voltage and permanently applied voltage. Vit1 exhibits extremely brittle behaviour both for higher pulse fractions than 15% and for lower temperatures.

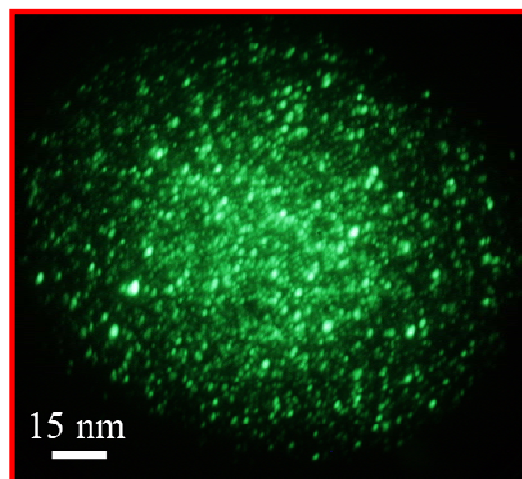


Figure 1 Field ion image of vitreloy 1: showing no characteristic feature for crystalline inclusion.

Fig. 2 shows three dimensional atomic reconstructions of all elements, as well as for each individual element. The atomic reconstruction reveals that the atomic distribution of all elements is homogeneous and random. Statistical tools are processed on the TAP data because of the difficulties to extract any information simply from three dimensional representations.

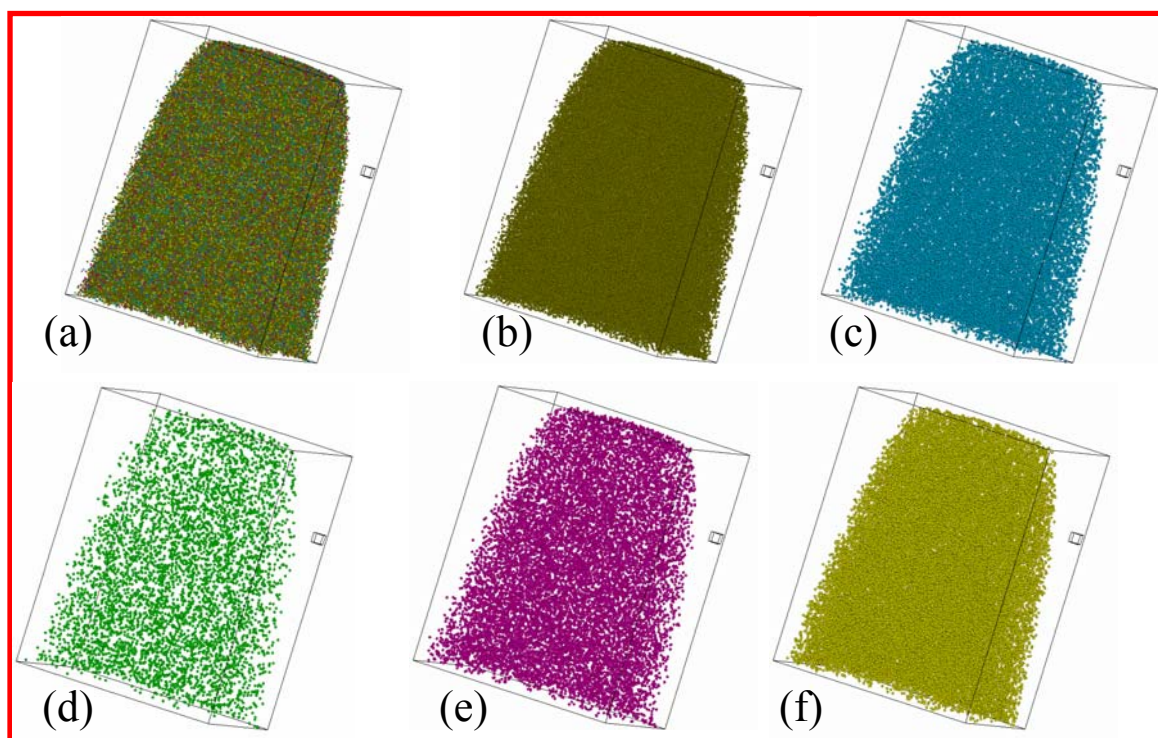


Figure 2 Three dimensional atomic reconstruction of a) all elements, b) Zr atoms, c) Ti atoms, d) Cu, e) Ni atoms and f) Be atoms. Small cube represents 1 nm^3 .

Albeit, the reported difficulties in the evaluation of cluster search module for an alloy with higher concentrations of constituent elements ($> 6 \text{ at. \%}$), just to check different attributes related to cluster search module: it has been processed for different search radii for each element. Numbers of clusters having atoms greater than 9 are plotted against critical circular search diameter and presented in Fig. 3. The dotted line shows an ideal case if the material have clustering for low concentration of constituent elements [Heinrich05].

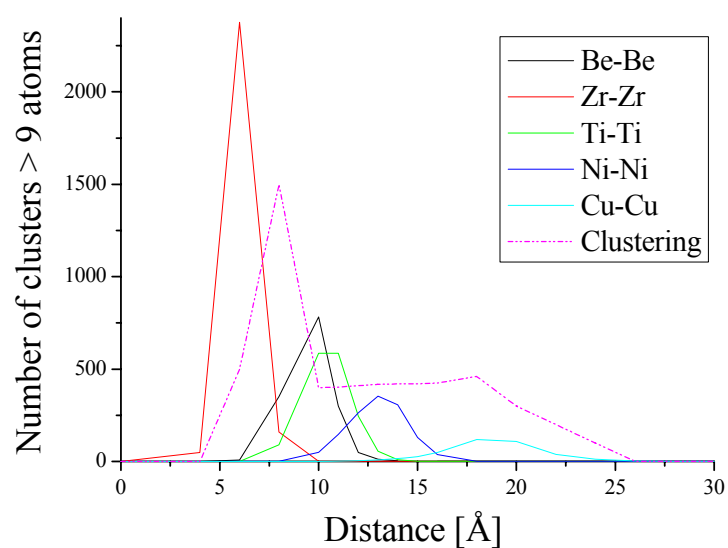


Figure 3 Number of clusters (consisting more than 9 atoms) as a function of cluster search diameter for vit1 alloys in as quenched state.

The minimum of the plateau gives the mean critical diameter for cluster search module. However, no such plateau was found for any constituent element of the vit1 alloy, which is explained by the intensive super saturation of alloy constituents.

Discussion

Previous investigations have suggested phase separation responsible for the formation of nano-scale crystalline phases at early stages of the crystallization. This feature is somewhat unexpected from a good glass forming metallic glass; an amorphous phase with a large supercooled liquid region is supposed to be considerable resistant to crystallization and hence, nuclei formation rate is retarded as corroborated by the presence of large size nuclei in Pd-Ni-P system by Drehman [Drehman84]. Phase separation has been reported to be responsible for such nano scale devitrification in vit1 alloy even in as cast state [Busch95]. However, later studies claimed to refute earlier work and stated that a primary crystallization of *i*-phase is responsible for such nano-scale crystallization [Martin04].

The χ^2 test, as a well established statistical tool, has been applied to check the homogeneity of the investigated vit1 alloy. Fig. 4 illustrates a comparison of the frequency distribution of the experimental data and that from a binomial distribution with the same mean concentration for each constituent reveals no palpable deviation from the random solid solution. The corresponding χ^2 values calculated are summarized in table 1. The χ^2 values for each constituent element are smaller than the corresponding χ^2 alpha values, hence, divulges rather a homogeneous structure for all constituents of vit1 alloy. χ^2 values rule out any clustering or inhomogeneities that can be inferred from the cluster search module and corroborate previous findings that it's difficult to reveal any structural feature using the cluster search module for high concentration constituent elements.

Moreover, radial distribution function module was also applied to the reconstruction volume from the TAP data, showing no details of structural feature (see Appendix B). A detailed description on RDF tool and its finding from TAP data are discussed in chapter 6 § 1.4.

Table 1 Summary of the calculated χ^2 values for vit1 bulk amorphous alloy. Degree of freedom and values of χ^2 alpha are also given for a comparison, with the significance level of alpha i.e., 0.05.

	<i>Zr</i>	<i>Ti</i>	<i>Be</i>	<i>Ni</i>	<i>Cu</i>
χ^2 value	39	23.86	24.82	15.34	7.44
χ^2 alpha	46	35	37.65	26.29	16.91
Degree of freedom	32	23	25	16	9

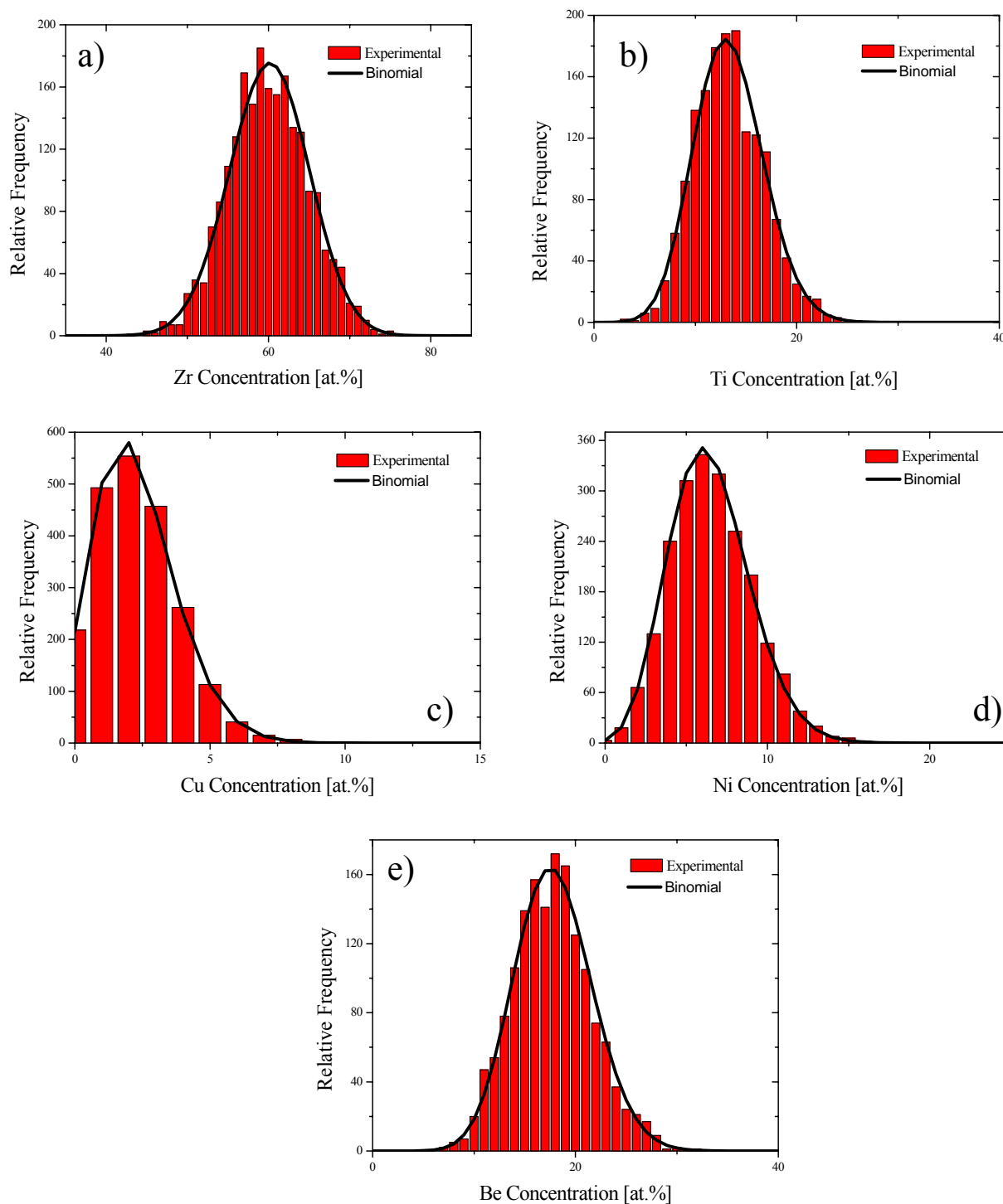


Figure 4 Comparison of binomial and experimental frequency distributions for the vit1 bulk amorphous alloys: for a) Zr, b) Ti, c) Cu, d) Ni, and e) Be.

Conclusions

The present investigations limited to the as cast state showed a randomly distributed homogenous structure. Albeit, such a homogenous structure was ideal to proceed further with the statistical tools developed to investigate the short range ordering in amorphous structure; one of the prime objectives

of this research work, different critical issues inhibit to proceed further investigations with this alloy system. These critical factors are enumerated as under:

- Strong overlap between Ni^{+2} and Zr^{+3} at 30 a.m.u. Fig. 5 illustrates a mass spectrum obtained from TAP. It evinces an overlap of Ni^{+2} and Zr^{+3} at a.m.u. 30. This peak was assigned to Zr for avoiding missing any particular atom, which strongly affects the results from cluster search and RDF modules, though it contributes to higher concentration of Zr than present. Apart from this overlap there are also other minor overlaps for Ti^+ with Zr^{+2} at 46, 47 and 48.
- The differences in field of evaporation of the constituent elements results in a preferential evaporation. Preferential evaporation can be suppressed by running TAP analysis at very deep temperatures and higher pulse fraction; however, it was difficult to perform TAP analysis at deep temperatures for this alloy system because of its extremely brittle nature.
- Performing TAP analysis at higher temperatures gave rise to hydride formation at the apex of the specimen. Hence, Be and Zr comes as respective hydrides, complicating a lucid interpretation of the data.
- Intensive contamination of the tip after electropolishing during sample preparation makes it very difficult to perform TAP analysis.
- Furthermore, crystallization renders further brittleness, and hence will be difficult to make TAP analysis on the heat treated states.

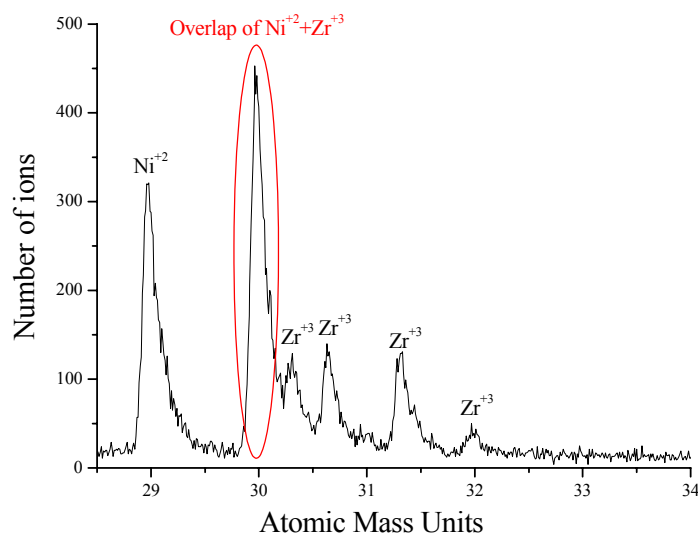


Figure 5 Mass spectrum elaborating the overlap of Zr^{+3} and Ni^{+2} ions.

Above stated difficulties obviates from continuing further investigations on this alloy system. Thereby, Pd-Cu-P bulk amorphous alloy has been investigated utilizing TAP (chapter 6 § 1): a system free from any overlap among the constituent elements and comparatively more stable to surface oxide formation.

Appendix B

Radial distribution function calculated by TAP

This section shows the radial distribution functions calculated utilizing the atom probe data for different glassy materials analysed during this research work. The broadening of atomic distributions of next neighbours as explained in detail in § 1.4 in chapter 6, hamper to reveal any information from radial distribution functions.

Vitreloy1 ($\text{Zr}_{41.2}\text{Ti}_{13.8}\text{Cu}_{12.5}\text{Ni}_{10}\text{Be}_{22.5}$)

Frequency of occurrence of atoms as a function of distance known as radial distribution function is illustrated in Fig. 1 for vit1 bulk amorphous alloy.

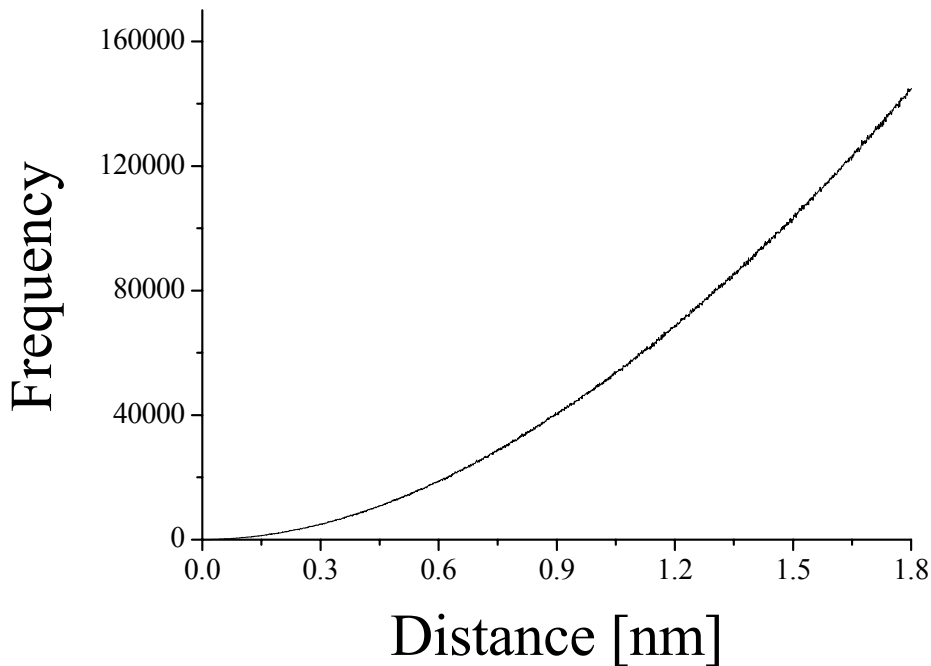


Figure 1 Radial distribution function for vitreloy 1.

The plot of the radial distribution function shows homogeneous distribution for the constituent alloying elements. This graph follows the characteristic Gaussian distribution. Similarly partial radial

distributions are also obtained for Zr, Be and Ni to elicit corresponding elemental distributions and are depicted in Fig. 2. However, no detailed features on account of short range ordering can be extracted from these graphs.

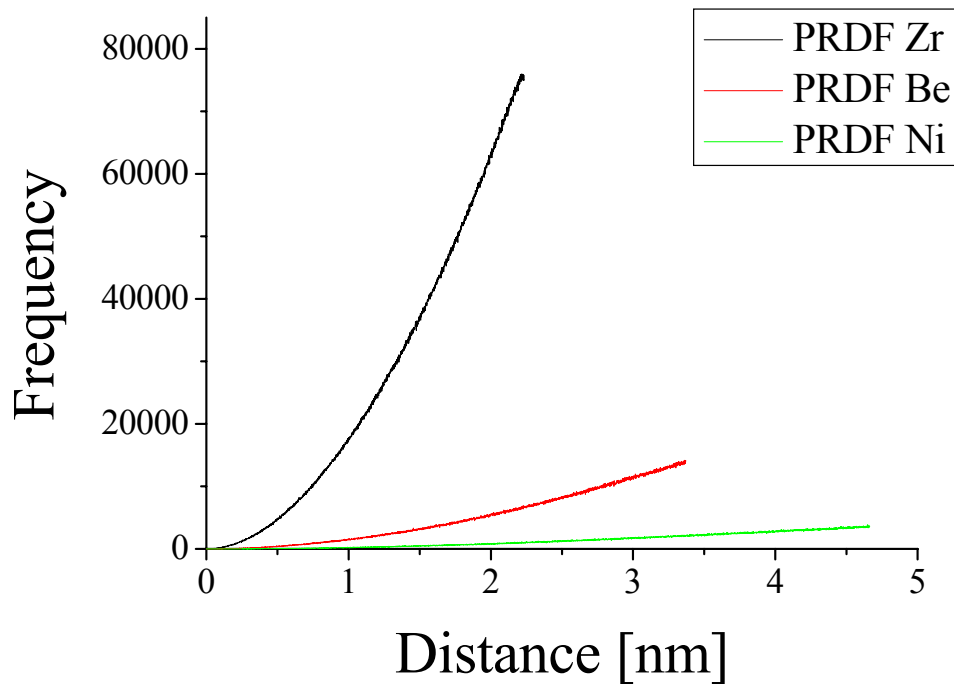


Figure 2 Partial radial distribution functions for Zr, Be and Ni.

$\text{Fe}_{40}\text{Ni}_{40}\text{B}_{20}$ glassy ribbons

Fig. 3 depicts the radial distribution function and similarly partial radial distribution functions for Fe-Fe, B-B and Ni-Ni correlations for as quenched $\text{Fe}_{40}\text{Ni}_{40}\text{B}_{20}$ glassy ribbon utilizing the radial distribution function module based on the TAP data.

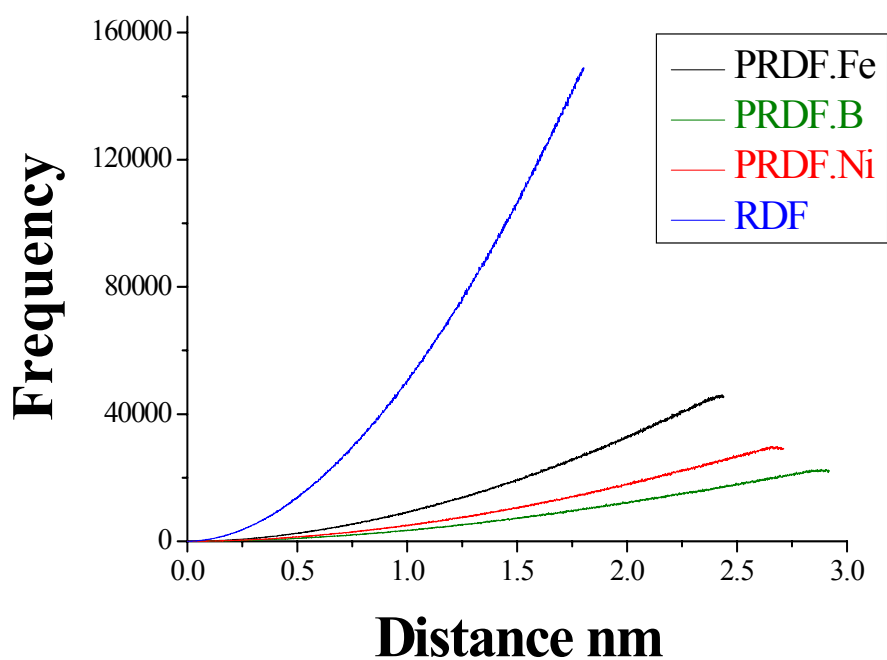


Figure 3 RDF and PRDFs of as quenched $\text{Fe}_{40}\text{Ni}_{40}\text{B}_{20}$ glassy ribbon.

The parabolic curves show that the structure is rather homogeneous however no fine details that can be attributed to short range ordering are evident.

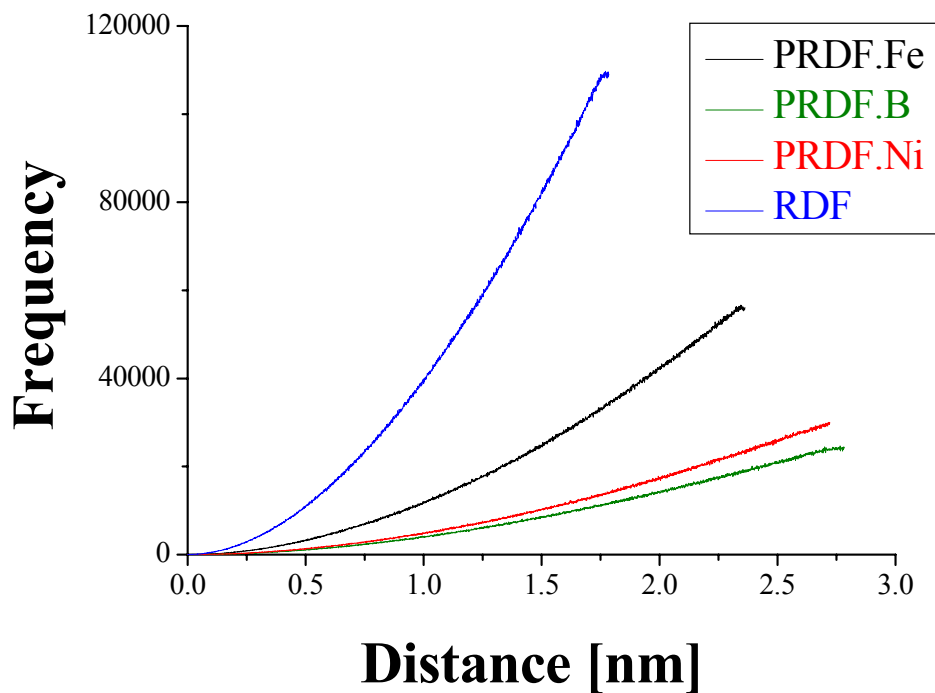


Figure 4 RDF and PRDFs for $\text{Fe}_{40}\text{Ni}_{40}\text{B}_{20}$ glassy ribbon annealed at 350°C for 1 hour.

Similarly Fig. 4 represents the radial distribution function and partial radial distribution functions for Fe-Fe, B-B and Ni-Ni correlations for $\text{Fe}_{40}\text{Ni}_{40}\text{B}_{20}$ glassy ribbon annealed for 1 hour at 350°C . Inability to resolve short range ordering is described in detail in § 1.3 & 1.4 of chapter 6.

Appendix C

Next neighbourhood evaluation as function of average atomic volume

The next neighbour distribution calculated utilizing the TAP data strongly depends on the experimental parameters as well as on the reconstructional parameters utilized for interpreting the TAP data. The effects of some of the parameters are well described in § 1.5 in chapter 6. Here a comparison of the atomic distributions of Pd-Pd, Cu-Cu and P-P elements calculated by processing the next neighbourhood evaluation module on the atomic reconstructions for different atomic volumes (Ω_{av}) for Pd₅₅Cu₂₃P₂₂ bulk amorphous alloys is given. Table 1 present the atomic distribution of first ten next neighbours calculated by NNE module for different atomic volumes (Ω_{av}). The next neighbour atomic distances are directly proportional to the average atomic volume (Ω_{av}). A slight change in the atomic volume (Ω_{av}) leads to a palpable deviation in the next neighbour distances. Hence, a careful selection of the experimental as well as reconstruction parameters is essential for successful evaluations.

Table 1 Comparison of the first ten next neighbours for Pd-Pd, Cu-Cu and P-P correlations calculated for different average atomic volumes. The distances are in Å.

	Pd-Pd	Pd-Pd	Pd-Pd	Pd-Pd	Pd-Pd
Av.At.Vol [Å units]	20	16	14	12	10
NN1	2.47	2.31	2.21	2.11	1.98
NN2	3.38	3.16	3.02	2.87	2.70
NN3	3.98	3.73	3.56	3.37	3.17
NN4	4.45	4.17	3.98	3.77	3.54
NN5	4.85	4.53	4.33	4.11	3.85
NN6	5.20	4.85	4.63	4.39	4.12
NN7	5.50	5.13	4.91	4.65	4.35
NN8	5.77	5.38	5.16	4.88	4.57
NN9	6.03	5.61	5.39	5.10	4.77
NN10	6.27	5.83	5.59	5.29	4.96

	Cu-Cu	Cu-Cu	Cu-Cu	Cu-Cu	Cu-Cu
Av.At.Vol [Å units]	20	16	14	12	10
NN1	3.37	3.17	3.01	2.86	2.67
NN2	4.58	4.27	4.09	3.88	3.65
NN3	5.41	5.03	4.80	4.57	4.29
NN4	6.06	5.61	5.37	5.11	4.79
NN5	6.59	6.10	5.85	5.56	5.20
NN6	7.05	6.54	6.27	5.95	5.56
NN7	7.47	6.92	6.64	6.28	5.89
NN8	7.85	7.26	6.98	6.60	6.18
NN9	8.19	7.58	7.30	6.89	6.44
NN10	8.50	7.88	7.58	7.16	6.69

	P-P	P-P	P-P	P-P	P-P
Av.At.Vol [\AA units]	20	16	14	12	10
NN1	3.59	3.28	3.16	2.96	2.82
NN2	4.81	4.44	4.25	4.01	3.79
NN3	5.63	5.19	5.00	4.69	4.45
NN4	6.28	5.78	5.58	5.21	4.96
NN5	6.83	6.30	6.08	5.68	5.38
NN6	7.31	6.74	6.50	6.08	5.74
NN7	7.73	7.13	6.89	6.44	6.08
NN8	8.13	7.49	7.24	6.76	6.38
NN9	8.49	7.82	7.56	7.06	6.65
NN10	8.83	8.12	7.86	7.34	6.91

Bibliography

- Alkassab03 Al-Kassab, T., Wollenberger, H., Schmitz, G., Kirchheim, R., in: High Resolution Imaging and Spectrometry of Materials, ed. F. Ernst and M. Rühler, SVB, pp.274-320. 2003.
- Angell95 Angell, C. A., Science, 267, 5206, 1924-1935, 1995.
- Ashby06 Ashby, M. F., Greer, A. L., Scripta Mater. 54, 321-326, 2006.
- Bas95 Bas, P., Bostel, A., Deconihout, B., Blavette, D., Appl. Surf. Sci., 87/88 (1995) 298-304.
- Bernal64 Bernal, J. D., Proc. R. Soc. (Lond.) A284, 299, 1964.
- Blavette88 Blavette, D., Grancher, G., Bostel, A., J. de Physique, Tome 49, P. C6-433-438, Nov 1988.
- Blavette93 Blavette, D., Deconihout, B., Bostel, A., Sarrau, J.M., Bouet, M., Menand, A., Rev Sci Instrum, 64, 10, 2911-2919, 1993.
- Bostel Bostel, A., Blavette, D., Menand, A., Sarrau, J.M., J de Phys C8, 50, 501, 1989.
- Bracchi04 Bracchi, A., Ph.D. Thesis, Universität Göttingen, 2004.
- Busch95 Busch, R., Schneider, S., Peker, A., Johnson, W. L., Appl, Phys. Lett. 67 -11, 1544-47, 1995.
- Cahn96 Cahn, R. W., Haasen, P., Physical metallurgy, 4th edition, Elsevier Science BV, 1996.
- Cargill70 Cargill, G. S., J. Appl. Phys. 41, 12, 1970.
- Chen69 Chen, H. S., Turnbull, D., Acta Metall. 17, 1021, 1969.
- Chen74 Chen, H. S., Acta Metall., 22, 1505-11, 1974.
- Chen76 Chen, H. S., Mater. Sci. Eng., 26, 79-82, 1976.
- Chen80 Chen, H. S., Rep. Prog. Phys., 43, 354-432, 1980.
- Chen03 Chen W, R., Wang, Y, M., Qiang, J, B., Dong, C., Acta Meter., 51, 1899, 2003.
- Chuang86a Chuang, Y, -Y., Chang, Y, A., Schmid, Lin, J, -C., Met. Trans., 17A, 1361, 1986.
- Chuang86b Chuang, Y, -Y., Hsieh, C, -C, Chang, Y, A., Met. Trans., 17A, 1373, 1986.
- Cullity67 Cullity, B.D., Elements of X-Ray diffraction, third edition, AWP, 1967.
- Cullity72 Cullity, B.D., Introduction to magnetic materials, Addison-Wesley publication company, 1972.

- Dixmier76 Dixmier, J., Sadoc, J. F., Structural models, Metallic glasses; Materials science seminar, American Society for Metals, Metals Park, Ohio, (1976).
- Drehman82 Drehman, A.J., Greer, A.L., Turnbull, D., Appl. Phys. Lett., 41, 716, 1982.
- Drehman84 Drehman, A. J., Greer, A. L., Acta Mater. 32, 323, 1984.
- Dubey84 Dubey, K.S., Rao, C.R., Acta Metall., 32 P.91-96, 1984.
- Dubois85a Dubois, J. M., Gaskell, P. H., Caer, G. Le., Rapidly Quenched Metals (V) eds. Steeb, S. and Warliimont, H., North-Holland, Amsterdam, p. 567, 1985.
- Dubois85a Dubois, J. M., Caer, G. Le., Dehghan, K., Rapidly Quenched Metals (V) eds. Steeb, S. and Warliimont, H., North-Holland, Amsterdam, p. 197, 1985.
- Duine94 Duine, P. A., Sietsma, J., Thijsse, B. J., Phys. Rev., B 50 -18,13240-13249, 1994.
- Duwez76 Duwez, P., Annu. Rev. Mater. Sci., 6, 83-117, 1976.
- Elliott90 Elliott, S. R., Physics of amorphous materials, second edition, Longman Group UK limited, (1990).
- Fenny83 Finney, J. L., Amorphous metallic alloys, ed. Luborski, F. E., Butterworths, London, Ch. 4, 1983.
- Gaskell79 Gaskell, P. H., J. Non-Cryst. Solids 32, 207, 1979.
- Gaskell83 Gaskel, P. H., in: Amorphous Materials: Modelling of Structure and Properties, ed. Vitek, V. The Metallurgical Society, Warrendale, PA., p. 47, 1983.
- Gaskell83 Gaskell, P. H., in: Glassy Metals II; Atomic Structure and Dynamics, Electronic Structure and Magnetic Properties, Topics in Applied Physics Vol. 53, eds. Beck, H., and Güntherodt, H.-J., Springer-Verlag BHNVT, pp.5-50, 1983.
- Giannuzzi04 Giannuzzi, L. A., Stevie, F. A., Intoduction to focused ion beams: Instrumentation, Theory, Techniques and practice, Springer Inc., 2004.
- Giannuzzi99 Giannuzzi, L. A., Stevie, F. A., Micron 30, P. 197, 1999.
- Greer82 Greer, A. L., Acta Metall., 30, 171-192, 1982.
- Greer95 Greer, A. L., Science, 267, 1947-1953, 1995.
- Haasen96 Haasen, Peter, Physical metallurgy, Cambridge university press, 1996.
- Harms03 Harms, U., Schwarz, R. B., Shen, T. D., Phil. Mag. Lett., 83-8, 503-509, 2003.
- He98 He, Y., Shen, T., Schwarz, R. B., Met. and Mater. Trans. 29A, 7, 1795-1804, 1998.
- He03 He, G., Löser, W., Eckert, J., Scripta Materialia 48, 1531-1536, 2003.
- Heinrich01 Heinrich, A., Diplome Thesis, Universität Göttingen, 2001.
- Heinrich03 Heinrich, A., Al-Kassab, T., Kirchheim, R., Mat. Sci. Eng. A 353, Iss. 1-2, P.92-98, 2003.
- Heilmaier00 Heilmaier, M., Eckert, J., JOM, 52-7, pp. 43-47, 2000.
- Herlach94 Herlach, D. M., Material Science and Engineering, R12, P.177-272, 1994.
- Herzer90 Herzer, G., IEEE Trans. Magn. 26, 1397, 1990.
- Heinrich05 Heinrich, A., PhD Thesis, Universität Göttingen, 2005.

- Häussler04 Häussler, P., *Phys. Stat. Sol. (c)* 1, No. 11, 2879–2883, 2004.
- Häussler85 Häussler, P., *J. Physique (Paris)*, C8 361, 1985.
- Höhne96 Höhne, G.W.H., Hemminger, W., Flammersheim, H.-J., *Differential Scanning Calorimetry; An introduction for practitioners*, SVB, 1996.
- Inoue00 Inoue, A., *Acta Mater.* 48, 279-306, 2000.
- Inoue88 Inoue, A., Ohtera, K., Kita, K., Masumoto, T., *Japan J. appl. Phys.*, 27, L2248, 1988
- Inoue91 Inoue, A., Zhang, T., Masumoto, T., *Mater. Sci. Eng. A*, 134,1125, 1991.
- Inoue93 Inoue, A., Zhang, T., Masumoto, T., *J. Non-cryst Solids*, 156-158, pp. 473-480, 1993.
- Inoue95 Inoue, A., *Mater. Trans. Jpn. Inst. Met.* 36, 866-877, 1995.
- Inoue99 Inoue, A., *Non-equilibrium processing of materials*, Elsevier Science, ch 14, 1999.
- Johnson99 Johnson, W. L., *MRS Bull.* 24 – 10, 42, 1999.
- Kawashima85 Kawashima, A., Asami, K., Sato, T., Hasimoto, K., *Rapidly quenched metals V*, North Holland, Amsterdam, p-1671, 1985.
- Kellogg87 Kellogg, G. L., *Rev. Sci. Instrum.*, 58, P.38, 1987
- Kluthe03 Kluthe, C., Ph.D. Thesis, Universität Göttingen, 2003.
- Krohn61 Krohn, V.E., *Progr. Astronautics R P* 73, 1961.
- Larson98 Larson, D. J., Foord, D. T., Petford-Long, A. K., Anthony, T. C., Rozdilsky, I. M., Cerezo, A., Smith, G. D.W., *ultramicroscopy*, 75, P. 147, 1998.
- Larson99 Larson, D. J., Foord, D. T., Petford-Long, A. K., Liew, H., Blamire, M. G., Cerezo, A., Smith, G. D.W., *ultramicroscopy*, 79, P. 287, 1999.
- Lewis79 Lewis, B. G., Davies, H. A., Ward, K. D., *Scripta Metall.*, 13, 313-317, 1979.
- Li77 Li, J. C. M., in: *Metallic Glasses*, ASM, Metals park, Ohio, pp.224-246, 1977.
- Luborsky80 Luborsky, F. E., in: *Ferromagnetic materials*, ed. Wohlfarth, P., N-H, Amsterdam, 1980.
- Liebermann83 Liebermann, *Amorphous metallic alloys*, ed. Luborski, F. E., Butterworths, London, Ch. 3, 1983.
- Masumoto76 Masumoto, T., Kimura, H. M., Inoue, A., Waseda, Y., *Mater. Sci. Eng.*, 23, 141, 1976.
- Masumoto82 Masumoto, T., *Materials science of amorphous metals*, Ohmu publ. Tokyo, 1982.
- Mattern05 Mattern, N., Kühn, U., Gebert, A., Gemming, T., Zinkevich, M., Wendrock, H., Schultz, L., *Scripta Materialia* 53, 271-274, 2005.
- McElfresh94 Mc-Elfresh, M., *Fundamentals of magnetism and magnetic measurements: Quantum Design's magnetic measurement system*, Quantum Design. 1994.
- Maret87 Maret, M., Chieux, P., Hicter, P., Atzmon, M., Johnson, W. L., *J. Phys. F: Met. Phys.*, 17, 315-333, 1987.
- Martin04 Martin, I., Ohkubo, T., Ohnuma, M., Deconihout, B., Hono, K., *Acta Mater.* 52, 4427-4435, 2004.
- Miller00 Miller, M. K., *Atom Probe Tomography: Analysis at the atomic level*, KA/PP, 2000.

- Miller03 Miller, M. K., Shen, T. D., Schwarz, R. B., *J. Non-Cryst. Solids*, 317, 10-16, 2003.
- Miller05 Miller, M. K., Russell, K. F., Thompson, G.B., *ultramicroscopy*, 102, P.287, 2005.
- Miller89 Miller, M. K., Smith, G. D. W., *Atom Probe Microanalysis: Principles and Applications to Materials Problems*, Materials Research Society, Pittsburgh (Pennsylvania), 1989.
- Miller96 Miller, M. K., Cerezo, A., Hetherington, M. G., Smith, G. D. W., *Atom Probe Field Ion Microscopy*, Clarendon Press, Oxford, 1996.
- Mitra92 Mitra, A., Rao, S., Pramanik, S., Mohanty, O. N., *J Mat. Sci.*, 27, 5863-5868, 1992.
- Müller51 Müller, E. W., *Z. Physik*, 131, 136, 1951.
- Nagel75 Nagel, S, R., Tauc, J., *Phys. Rev. Lett.*, 35, 380, 1975.
- Ohsaka98 Ohsaka, K., Chung, S. K., Rhim, W. K., *Acta Mater.* 46, 4535, 1998.
- Orloff02 Orloff, J., Utlaut, M., Swanson, L., *High resolution focused ion beams: FIB and its applications*, Kluwer Academic/ Plenum Publishers, 2002.
- O'Handley87 O'Handley, R.C., *J.Appl.Phys.*62-10, P.R15-R45.
- Pang02 Pang, S., Zhang, T, Asami, K., Inoue, A., *Acta Mater.* 50, 2002.
- Peker93 Peker, A., Johnson, W. L., *Appl. Phys. Lett.*, 63, 17, 1993.
- Piller82 Piller, J., Haasen, P., *Acta Metall.*, 30, 1-8, 1982.
- Polk70 Polk, D. E. *Scr. Metall.* 4, 117, 1970.
- Porter01 Porter, D.A., Easterling, K.E., *Phase transformation in metals and alloys*, second edition, Nelson Thornes Ltd., 2001.
- Sadoc76 Sadoc, J. F., Dixmier, J., *Mater. Sci. Eng.*, 23 (1976) 187-192.
- Sailimion2004 Salimon, A. I., Ashby, M. F., Bréchet, Y., Greer, A.L., *Mater. Sci. Eng. A* 375-377, 385-388, 2004.
- Schneider01 Schneider, S., *J. Phys.: Condens. Matter* 13, 7723-7736, 2001.
- Shariq03 Shariq, A., Master thesis; A microstructural investigation of spinodal decomposition in super duplex stainless steels, Chalmers university of Technology, 2003.
- Shariq06a Shariq, A., Al-Kassab, T., *Proceedings of the SCANDEM2006*, P 40, 2006.
- Shariq06b Shariq, A., Al-Kassab, T, Kirchheim, R., *Ultramicroscopy*, accepted, 2006.
- Shen98 Shen, T. D., He, Y., Schwarz, R. B., *J. Mater. Res.*, 14-5, 2107-2115, 1998.
- Sietsma87 Sietsma, J., Thijsse, B. J., *J. Phys. F: Met. Phys.*, 17, 1-17, 1987.
- Steinhardt83 Steinhardt, P.J., Nelson, D. R., Ronchetti, M., *Phys. Rev. B*, 28, 784, 1983.
- Smith93 Smith, C. H., *Rapidly solidified alloys*, edited by Liebermann, Dekker, New York, Ch. 19, 1993.
- TAPP2.2 TAPP, Database of thermodynamic and physical properties, Version 2.2.
- Teichler06 Teichler, H., Unpublished data, Private communication, Institut für Materialphysik, Universität Göttingen, (2006).
- Temkin73 Temkin, R. J., Paul, W., Connell, G. A. N. (1973), *Adv. Phys.* 22, 581, 1973.

- Turnbull49 Turnbull, D., Fisher, J.C., *J. Chem. Phys.*, 17, P. 71, 1949.
- Turnbull69 Turnbull, D., *Contemp. Phys.*, 10 (1), P. 473, 1969.
- Vennström04 Vennström, M., Höwing, J., Gustafsson, T., Andersson, Y., *J. of solid state chem.*, 177, 1449-1455, 2004
- Vurpillot03 Vurpillot, F., Renaud, L., Blavette, D., *Ultramicroscopy*, 95, 223-229, 2003.
- Wagner80 Wagner, C. N. J., Lee, D., *J. Physique Coll.*, 41-C8, 242-245, 1980.
- Wagner83 Wagner, C. N. J., *Amorphous metallic alloys*, ed. Luborski, F. E., Butterworths, London, 1983.
- Walter78 Walter, J. L., Luborsky, F. E., *Mater. Sci. Eng.*, 33, 91-94, 1978.
- Wang03 Wang, Y. M., Qiang, J. B., Wong, C. H., Shek C. H., Dong, C., *J Mater. Res.*, 18, 642, 2003.
- Wang04 Wang, Y., Zhang, F., Qiang, J., Wang, Q., Wang, D. H., Li, D.J., Shek, C.H., Dong, C., *Scripta Materialia* 50 (2004) 829-833.
- Waseda80 Waseda, Y., *The structure of non-crystalline Materials*, McGraw-Hill, N. Y. 1980.
- Watson64 Watson, E. S., O'Neill, M.J., Justin, J., Brenner, N., *Anal Chem.* 36, 1233-1237, 1964.
- Wilde94 Wilde, G., Görler, G. P., Willnecker, R., Dietz, G., *Appl. Phys. Lett.*, 65-4, 397-399, 1994.
- Williams96 Williams, D. B., Carter, C. B., *Transmission Electrom Microscopy*, Plenum Press, New York, 1996.
- Wolde01 Wolde, D. G., *Diplome Thesis*, Universität Göttingen, 2001.
- Wolde03 Wolde, D. G., Al-Kassab, T., Kirchheim, R., *Mat. Sci. Eng. A* 353, Iss. 1-2, 152-157, 2003.
- Wong81 Wong, J. in: *Glassy Metals I; Ionic Structure, Electronic Transport and Crystallization*, Topics in Applied Physics Vol 46, ed. Güntherodt, H.-J., and Beck, H., Springer-Verlag BHNYS, chapter 4, pp. 45-78, 1981.
- Yao05 Yao, N., Wang, Z. L., *Handbook of microscopy for nanotechnology*, Kluwer Academic publishers, 2005.
- Yoshizawa88 Yoshizawa, Y., Oguma, S., Yamachi, K., *J. Appl. Phys.* 64 6044 1988.
- Zacharissen32 Zacharissen, W. H., *J. Am. Ceram. Soc.* 54, 3841, 1932.
- Zhang04 Zhang, X.F., Wang, Y. M., Qiang, J. B., Wang, Q., Wang, D. H., Li, D.J., Shek, C.H., Dong, C., *Intermetallics*, 12, 1275-1278, 2004.
- Zhang04b Zhang, T., Inoue, A., *Mat. Sci. Eng. A*, 375-377, pp. 432-435, 2004.

Acknowledgements

A cup of coffee shared with Dr. Talaat Al-Kassab, on the terrace of a smoking lounge in Sweden, proved to be the precursor that essentially leads me to join the Institut für Materialphysik, University of Göttingen. The approval of my PhD application, is more than a good reason to incite me for special thanks to Prof. Reiner Kirchheim, for giving me an opportunity to work in this institute and for generous support and guidance thereafter. That, not only helped me to widen my knowledge in materials physics but also gave me an opportunity to get a first hand experience of the versatile German culture.

I would like to particularly thank my supervisor, Dr. Talaat Al-Kassab, as well for all his generous efforts, stimulating discussions and guidance throughout my work. Specially for always being there, with a constructive and positive attitude, to sort out any kind of problem I faced during my stay.

I would also like to thank Prof. K. Samwer for sharing his wide knowledge on amorphous alloys and for being kind enough for allowing me to work in his laboratory. I am thankful to Ms. U. Beta and Dr. D. Bogdanov for their unlimited help during sample preparations and magnetic measurements. I am also thankful to Prof. E. Olsson, Prof. H.O. Andren, Prof. K. Stiller, Dr. E. Keehan and Dr. T. Liljenfors for allowing and helping me to use their facilities in Chalmers University of Technology, Göteborg, Sweden.

I would also take this opportunity to specially thank Dr. R. Schwarz, Prof. C. Dong, Prof. Q. Jianbing and Dr. D.J. Safarik for scientific collaborations, many fruitful discussions and for providing some of the investigated materials.

I am also thankful to Prof. H. Teichler, Prof. W. Felsch and Dr. C. Borchers for many fruitful discussions and for sharing their unlimited knowledge.

My most kind thanks also goes to Dr. P. Wilbrandt, Dr. J. Faupel, T. Schulz, V. Radisch, M. Hahn, D. Plischke, M. Malchow, M. Kanbach, C. Mewes and H.J. Walter for the technical support and for introducing me to TEM, SEM, FIB and other instruments in the institute.

A special thanks to all the present and past staff of the institute (especially to the TAP group and Secretaries Frau Kuba, Frau Saalfeld and Frau Haacke) for generating such a nice working environment. A special thanks to Dr. M. Guerdane, Dr. D.W. Giorgis, Dr. A. Heinrich, Dr. P. Choi, Dr. T. Haramina, A. Meschede, C. Ene, C. Wille, C. Nowak, R. Gemma and C. Eysell for their friendship, humour and many interesting discussions. I am also thankful to the Göttingen Graduate School of Physics for their financial support as Georg-Christoph-Lichtenberg-Stipendium des Landes Niedersachsen.

Finally and the most important, my deepest thanks to my parents, my sisters, my brother and his family for all your love, encouragements, prayers and support. Whatever I have today, without you none of this would ever have been possible.

Lebenslauf

Persönliche Daten

Name: Shariq
Vorname: Ahmed
Geburtsdatum: 05. September 1976
Geburtsort: Lahore, Pakistan
Staatsangehörigkeit: Pakistani
E-Mail: ahmadshariqpk@hotmail.com

Ausbildung

1980 - 1985	Grundschule	Govt. P.M.D.C Model High School, Khewra, Jhelum, Pakistan
1985 - 1992	Gymnasium	Govt. P.M.D.C Model High School, Khewra, Jhelum, Pakistan
1992 - 1995	Studium	Govt. F. C. College, Lahore, Pakistan
1996 - 2000	Ingenieurwissenschaften	Metallurgie und Materialwissenschaft, Universität der Ingenieurwissenschaften und Technologie, Lahore, Pakistan Title: "study of the production of HSLA A615 steel"
2001 - 2003	Masters	Materialwissenschaft, Chalmers Universität der Technologie, Göteborg, Schweden Title: "A microstructural investigation of spinodal decomposition in super duplex stainless steels"
2003-2006	Doktorarbeit	Wissenschaftlicher Mitarbeiter am Institut für Materialphysik der Universität Göttingen. Titel: "Nahordnung und Mikrostruktur- Eigenschaftsbeziehungen in amorphen Legierungen"